KU LEUVEN

ARENBERG DOCTORAL SCHOOL
Faculty of Engineering Science

RELIABLE THERMAL RESISTANCE ESTIMATION OF BUILDING COMPONENTS FROM ON-SITE MEASUREMENTS

An-Heleen Deconinck

Supervisor:
Prof. Dr. Ir. Arch. Staf Roels

Dissertation presented in partial fulfilment of the requirements for the degree of Doctor of Engineering Science (PhD): Civil Engineering

March 2017

Reliable thermal resistance estimation of building components from on-site measurements

---

An-Heleen Deconinck

KU Leuven
Faculty of Engineering Science
Department of Civil Engineering

Reliable thermal resistance estimation of building components from on-site measurements

An-Heleen Deconinck

Dissertation presented in partial fulfilment of the requirements
for the degree of Doctor of Engineering Science (PhD):
Civil Engineering
7 March 2017

KU Leuven
Faculty of Engineering Science
Department of Civil Engineering

Jury: Prof. Dr. Ir. Arch. Herman Neuckermans, *chair*
Prof. Dr. Ir. Arch. Staf Roels, *supervisor*
Prof. Dr. Ir. Arch. Arnold Janssens,
Ghent University
Prof. Dr. Ir. Edwin Reynders,
Prof. Dr. Henrik Madsen,
Technical University of Denmark
Prof. Dr. Ir. Arch. Dirk Saelens

Dit werk kwam tot stand in het kader van een bursaalbeurs (nummer 121167) van het agentschap voor Innovatie door Wetenschap en Technologie (IWT).

Dissertation presented in partial fulfilment of the requirements
for the degree of Doctor of Engineering Science (PhD):
Civil Engineering
7 March 2017

Acknowledgements

It always seems impossible until it's done.

– Nelson Mandela

And now it's done. Of toch bijna. Er rest me enkel nog deze – *nu nog* – lege pagina's te vullen. De laatste, maar ook de belangrijkste, want ik kan er iedereen in bedanken die me gesteund heeft toen dit werk nog *onmogelijk* leek. Zonder hen had dit boekje waarschijnlijk nooit bestaan.

In de eerste plaats wil ik mijn promotor, professor Staf Roels, bedanken. Staf, ik had me geen betere promotor kunnen indenken. Telkens ik dacht geen kant meer uit te kunnen met mijn onderzoek, kon ik je om raad vragen. En telkens kwam ik na zo'n bespreking buiten vol nieuwe ideeën en vol goede moed om er weer tegenaan te gaan. Bedankt om me steeds weer de rode draad te tonen nadat ik me voor de zoveelste keer had blind gestaard op de details. Bedankt ook voor je warme aanpak: je toonde niet alleen vertrouwen in het onderzoek, maar ook in de persoon die erachter zat. Dat heb ik heel erg gewaardeerd.

I sincerely thank all members of the examination committee, for their reading of this work and for their valuable suggestions to improve it.

Toen ik vier jaar geleden toekwam op de afdeling Bouwfysica had ik nooit durven dromen dat ik me er zo goed thuis zou voelen. A warm thank you goes to *all* of my colleagues, for the instructive brainstorms and discussions, for the entertaining coffee and lunch breaks, for the pleasant after-work drinks, for the conference stays worth remembering, etc. Some people deserve a special thank you. Jelena, before I met you in person, I met the cardboard boxes with your belongings on the desk I initially wanted to claim. Luckily, you did not only steal my desk, but also my friendship. It was an honour sharing an office with you – *and brownies and laughs and lots of stories* – and

it was a real support to have someone in the office who *exactly* understood the troubles of doing a PhD. (Christina, sorry for all our complaining. I can say it now: it's worth the while.) Glenn, van jou heb ik veel geleerd. Van in het begin zat je rechts van mij en was je ook figuurlijk mijn rechterhand. Ik had maar mijn hoofd te draaien en ik vond een antwoord op al mijn vragen. Veel vragen. Bedankt om die nooit weg te wimpelen en om me altijd op weg te zetten die vragen ook werkelijk te beantwoorden. Bedankt ook voor alle babbels over de weekendplannen, over het beklimmen van bergen met de fiets, over een huis kopen, etc. Hans, bedankt voor de ervaringen die ik heb mogen opdoen tijdens het begeleiden van de oefenzittingen bouwfysica en om altijd al mijn vragen hierover – en over nog veel meer – te beantwoorden. Liesje en Wouter, bedankt voor de gezamenlijke uren die we in De Molen hebben gespendeerd en voor de gedeelde deadline-stress voor het op tijd verbeteren van de tussentijdse testen voor kerst.

Patricia, Wim en Esther, jullie verdienen een aparte paragraaf. Bedankt om mij jullie *partner in crime* te maken voor het organiseren van de jaarlijkse barbecue, het ineen knutselen van de cadeaus voor collega's, etc. Jullie zijn de drijvende motor van die evenementen en ik ben blij ik dat ik daar deel van heb mogen uitmaken. Patricia en Wim, bedankt ook om mijn testwand in het Vliet met zoveel zorg op te bouwen!

Ook mijn familie wil ik – *nee, moet ik* – bedanken. Mama en papa, bedankt om me zoveel kansen te bieden en om me altijd bij te staan met raad en daad. Bedankt om me te blijven steunen en motiveren ook al was mijn doctoraat een taboe – *sorry mama, ik weet hoe je je hebt moeten inhouden om er niet telkens naar te vragen.* Mama, papa, Katrien, Barbara, Bruno, Celine en Lucas, bedankt voor de vele warme familiemomenten. Bij jullie voel ik me steeds thuis.

Ten slotte, Xavier, heb jij de grootste bijdrage aan dit werk geleverd: zonder jou was dit boekje waarschijnlijk niet klaar geraakt. Ik had het nooit volgehouden als ik niet elke avond had kunnen thuiskomen bij iemand die me altijd weer doet lachen. Bedankt ook om mij telkens opnieuw achter die bureau te krijgen – *Moet jij niet werken?* – en voor je oneindige geduld bij het schrijven van dit boek. Ik besef pas hoeveel ik je alleen gelaten heb als ik zie hoe wij ineens een ingerichte garage hebben, hoe bijna al het oude behangpapier van onze muren verdwenen is en hoe er plots een boom minder staat in onze tuin.

Nu deze pagina's gevuld zijn, is dit boekje klaar. Echt klaar. Ik had het nooit voor mogelijk gehouden. Bedankt allemaal.

An-Heleen Deconinck
7 maart 2017

Abstract

In the current evolution towards energy efficient buildings, the thermal quality of a building's envelope plays an important role. This is reflected in the EPB Directives which impose increasingly stringent specifications to the thermal performance of buildings. Among others, the minimum performance levels of building components have been tightened significantly over the last 10 years. The compelled U-value for walls in Flanders, for instance, has evolved from 0.6 $Wm^{-2}K^{-1}$ in 2006 to 0.24 $Wm^{-2}K^{-1}$ in 2014. Performance levels typically relate to the theoretical performance of building components: they are determined from the thermal properties of a component's constituent material layers. These properties are, however, theoretical values obtained from standards and product information and do not account for the way these materials are applied in the construction. Consequently, the actual thermal performance of building components may deviate significantly from the labelled one. For a better view on the *as-built* performance of our building components, their thermal quality should be determined from on-site measurements. Therefore, reliable in-situ characterisation methods are required.

The presented work investigates several characterisation methods determining the thermal resistance of building components from on-site measurements. Thereby, a distinction is made between semi-stationary and dynamic methods. The first class of methods comprises techniques that rely on the stationary definition of the thermal resistance, such as the commonly used and standardised average method and its extension (ISO 9869). The second class of methods encompasses techniques that rely on inverse modelling. Notably, the more established techniques of Anderlind- and ARX-modelling are considered, as well as the more innovative technique of stochastic grey-box modelling. Since the latter technique is rather new in the specific context of thermal resistance estimation, its possibilities are examined thoroughly. Special attention is given to the physical interpretability of the individual parameters of a

grey-box model structure that is typically used to describe the heat transfer in building components. Next to that, the method's possibilities for identifying and characterising building components with non-linear, apparent thermal resistances are examined. Finally, the performances of the individual characterisation methods are assembled in a large-scale comparative assessment. For various scenarios and boundary conditions, the methods' ability to cope with the constantly varying climatic conditions to which in-situ components are subjected, is studied.

The comparative results demonstrate that semi-stationary methods are easy-to-use, but that their applicability is often limited to winter measurements. The considered dynamic methods, by contrast, prove to be more complex in use, but offer a versatile applicability, meaning that a thermal resistance can reliably be estimated from both winter and summer measurements. Furthermore, a thorough examination of stochastic grey-box modelling demonstrates that the elementary heat flux and surface temperature measurements are often not dynamically informative enough to characterise fully identifiable grey-box models. Although this has no consequence for estimating the total thermal resistance of building components, it neutralises many of the method's advanced (statistical) properties. Hence, it is hard to justify their use, especially when less time-intensive approaches such as Anderlind- and ARX-modelling prove to result in R-estimates of similar quality. Yet, stochastic grey-box models prove to be relevant for the characterisation of variable performance indicators, quantifying for instance cavity walls liable to rotational air looping around their insulation layer.

Samenvatting

De thermische prestatie van de gebouwschil speelt een belangrijke rol in de huidige evolutie naar energie-efficiënte gebouwen. Dit is weerspiegeld in de EPB-regelgeving die steeds striktere eisen stelt aan de thermische prestatie van gebouwen. Zo zijn de minimum prestatie-eisen voor bouwcomponenten aanzienlijk strenger geworden tijdens de laatste 10 jaar. In Vlaanderen is de opgelegde U-waarde voor wanden bijvoorbeeld geëvolueerd van 0.6 $Wm^{-2}K^{-1}$ in 2006 naar 0.24 $Wm^{-2}K^{-1}$ in 2014. Minimum prestatie-eisen zijn echter over het algemeen gerelateerd aan de theoretische prestatie van bouwcomponenten: prestatielabels worden toegekend op basis van de thermische eigenschappen van hun samenstellende materialen. Deze eigenschappen zijn theoretische waardes, afkomstig van productinformatie of standaardwaardes en houden op geen enkele manier rekening met de manier waarop deze materialen in de constructie zijn geplaatst. De werkelijke thermische prestatie van bouwcomponenten kan dan ook behoorlijk afwijken van de gelabelde. Om een betere kijk te ontwikkelen op de *as-built* prestatie van onze bouwcomponenten, zou hun thermische kwaliteit moeten worden bepaald op basis van in-situ metingen. Dit vereist betrouwbare karakterisatiemethodes.

Dit werk onderzoekt verschillende karakterisatiemethodes die de thermische weerstand van bouwcomponenten kunnen bepalen op basis van in-situ metingen. Daarbij wordt een onderscheid gemaakt tussen semi-stationaire en dynamische methodes. De eerste klasse omvat methodes die gebaseerd zijn op de stationaire definitie van de thermische weerstand, zoals de *average method* en al zijn varianten (ISO 9869). De tweede klasse bevat methodes die steunen op de techniek van invers modelleren. Zowel de gevestigde technieken van *Anderlind-* en *ARX-modelling* worden bestudeerd, als de meer innovatieve techniek van *stochastic grey-box modelling*. Aangezien deze laatste methode nieuw is in de specifieke context van thermische weerstands-karakterisatie, wordt ze diepgaand geanalyseerd. Daarbij wordt er speciale aandacht besteed aan de fysische interpreteerbaarheid van de parameters van een typisch toestands-ruimtemodel dat

wordt gebruikt voor het beschrijven van warmtetransport in bouwcomponenten. Daarnaast worden ook de mogelijkheden van deze methode bestudeerd voor het identificeren en karakteriseren van bouwcomponenten met een variable thermische weerstand. Ten slotte worden de prestaties van de verschillende individuele karakterisatietechnieken samengebracht in een grootschalige vergelijkende studie. Daarin worden de methodes bestudeerd naar hun mogelijkheid om om te gaan met de constant variërende klimaatcondities waaraan in-situ bouwcomponenten zijn onderworpen, en dit voor verschillende scenarios en randvoorwaardes.

De vergelijkende studie toont aan dat semi-stationaire methodes gemakkelijk zijn in gebruik, maar dat hun toepasbaarheid vaak beperkt blijft tot wintermetingen. De beschouwde dynamische methodes daarentegen, zijn gecompliceerder in gebruik, maar bewijzen meer algemeen toepasbaar te zijn: ze zijn in staat een betrouwbare weerstand te karakteriseren op basis van zowel winter- als zomermetingen. Voorts wijst een diepgaande studie van *stochastic grey-box modelling* uit dat de elementaire warmtestromen temperatuursmetingen meestal niet voldoende dynamische informatie bevatten om volledig identificeerbare toestands-ruimtemodellen te karakteriseren. Hoewel dit geen gevolgen heeft voor het schatten van de totale thermische weerstand van bouwcomponenten, neutraliseert het wel de (statistische) voordelen. Dit maakt het gebruik van deze methode moeilijk te rechtvaardigen, zeker omdat de minder tijdsintensieve Anderlind- en ARX-modellen tot even betrouwbare R-waardeschattingen leiden. *Stochastic grey-box models* bewijzen wel relevant te zijn voor het karakteriseren van variable prestatieindicatoren om bijvoorbeeld spouwmuren te karakteriseren die beïnvloed worden door rotatiestroming rond hun isolatie.

Contents

Nomenclature

GREEK SYMBOLS

α_j	regression coefficient, $[Wm^{-2}K^{-1}]$
α_S	absorption coefficient, [-]
β_j	regression coefficient, $[Wm^{-2}K^{-1}]$
δT_i	difference between the interior temperature averaged over the 24h prior to a certain reading and the interior temperature averaged over the first 24h of the analysis period, $[K]$
δT_e	difference between the exterior temperature averaged over the 24h prior to a certain reading and the exterior temperature averaged over the first 24h of the analysis period, $[K]$
Δ	difference, $[-]$
Δ_α	the α^{th} quantile of a χ^2-distribution for one degree of freedom, $[-]$
ϵ	residual, $[Wm^{-2}]$
ϵ_L	emissivity, [-]
$\boldsymbol{\epsilon}$	vector of residuals, $[Wm^{-2}]$
$\{\boldsymbol{\epsilon}_{t_k}\}$	white noise process with Gaussian variance $\boldsymbol{S}(\boldsymbol{\theta})$
λ	thermal conductivity, $[Wm^{-1}K^{-1}]$
λ	Lagrange weighting coefficient, $[-]$
Λ	likelihood ratio test, $[-]$
ω_i	standard Wiener process in state i
$\omega_{se}(B)$	polynomial in the backshift operator B corresponding to model input T_{se}

$\omega_{si}(B)$	polynomial in the backshift operator B corresponding to model input T_{si}
$\omega_{se,j}$	coefficient in the polynomial $\omega_{se}(B)$ corresponding to the backshift operator B^j, $[Wm^{-2}K^{-1}]$
$\omega_{si,j}$	coefficient in the polynomial $\omega_{si}(B)$ corresponding to the backshift operator B^j, $[Wm^{-2}K^{-1}]$
$\{\boldsymbol{\omega}_t\}$	Wiener process with incremental covariance $\boldsymbol{\sigma}(\boldsymbol{\theta})$
σ	standard deviation
σ_i	scaling of standard Wiener process ω_i in state i
χ^2_{PL}	two times the negative generalised likelihood ratio test $R(\theta_i)$ of parameter θ_i, $[-]$

ROMAN SYMBOLS

a	scaling factor in the exponential or logistic function formulation
$a_{ij,l}$	l^{th} zero of the ij^{th} element, formulated in zero-pole-gain form, of the transfer function matrix $\boldsymbol{H}_{input}$
$A_1(B)$	polynomial formulated in the backshift operator B
$A_2(B)$	polynomial formulated in the backshift operator B
$\boldsymbol{A}(\boldsymbol{\theta})$	state space matrix formulated in function of the set of parameters $\boldsymbol{\theta}$, $[-]$
$A(B)$	polynomial formulated in the backshift operator B
b	scaling factor in the exponential or logistic function formulation
$b_{ij,l}$	l^{th} pole of the ij^{th} element, formulated in zero-pole-gain form, of the transfer function matrix $\boldsymbol{H}_{input}$
B	backshift operator, $[-]$
$\boldsymbol{B}(\boldsymbol{\theta})$	state space matrix formulated in function of the set of parameters $\boldsymbol{\theta}$, $[-]$
$B(B)$	polynomial formulated in the backshift operator B
c	specific heat, $[Jkg^{-1}K^{-1}]$
C	thermal capacity, $[Jm^{-2}K^{-1}]$ or $[MJm^{-2}K^{-1}]$
$\boldsymbol{C}(\boldsymbol{\theta})$	state space matrix formulated in function of the set of parameters $\boldsymbol{\theta}$, $[-]$
$C(B)$	polynomial formulated in the backshift operator B
C_i	individual model capacitance, $[Jm^{-2}K^{-1}]$ or $[MJm^{-2}K^{-1}]$

C_m	thermal capacitance of material layer m, $[Jm^{-2}K^{-1}]$ or $[MJm^{-2}K^{-1}]$
d	thickness, $[m]$
d	differential operator, $[-]$
d	scaling factor in the exponential or logistic function formulation
$\boldsymbol{D}(\boldsymbol{\theta})$	state space matrix formulated in function of the set of parameters $\boldsymbol{\theta}$, $[-]$
Dif	diffuse solar radiation on a horizontal plane, $[Wm^{-2}]$
Dir	direct solar radiation on a horizontal plane, $[Wm^{-2}]$
F_i	interior thermal mass factor, $[Jm^{-2}K^{-1}]$
F_e	exterior thermal mass factor, $[Jm^{-2}K^{-1}]$
H_{ce}	exterior convective heat transfer coefficient, $[Wm^{-2}K^{-1}]$
$\boldsymbol{H}_{input}$	transfer function acting on the input, $[-]$
$\boldsymbol{H}_{noise}$	transfer function acting on the noise, $[-]$
i	number of state, counting from the exterior (i=1) to the interior (i=n), $[-]$
i	dummy index, $[-]$
I	identity matrix, $[-]$
j	dummy index, $[-]$
k	discrete time point, $[-]$
K_{ij}	gain of the ij^{th} element, formulated in zero-pole-gain form, of the transfer function matrix $\boldsymbol{H}_{input}$
l	dummy index, $[-]$
$L(\boldsymbol{\theta}; \mathcal{Y}_N)$	likelihood function of the parameter set $\boldsymbol{\theta}$ for a given sequence of measurements $\mathcal{Y}_N$, $[-]$
m	number of material layer in a building component, $[-]$
M	total number of material layers in a building component, $[-]$
n	model order, $[-]$
ne	order of the polynomial $\omega_{se}(B)$, $[-]$
ni	order of the polynomial $\omega_{si}(B)$, $[-]$
nq	order of the polynomial $Q(B)$, $[-]$
N	total number of data points in a data set, $[-]$
p	number of historical data points, $[-]$

$p(\boldsymbol{y}_k \mid \mathcal{Y}_{k-1}, \boldsymbol{\theta})$	conditional probability of $\boldsymbol{y}_k$ given the sequence of measurements $\mathcal{Y}_{k-1}$ and the parameter set $\boldsymbol{\theta}$, [−]
$p(\mathcal{Y}_N \mid \boldsymbol{\theta})$	joint probability density of a given sequence of measurements $\mathcal{Y}_N$ for a fixed parameter set $\boldsymbol{\theta}$, [−]
$PL(\theta_i)$	profile likelihood of parameter θ_i, [−]
q, q_{hfm}	heat flux, $[Wm^{-2}]$
$Q(B)$	polynomial formulated in the backshift operator B corresponding to model output q
Q_j	coefficient in the polynomial $Q(B)$ corresponding to the backshift operator B^j, [−]
ρ	density, $[kgm^{-3}]$
R	thermal resistance, $[m^2KW^{-1}]$
R^2	coefficient of determination, or R-squared, [−]
$R(\theta_i)$	generalised likelihood ratio test of parameter θ_i, [−]
R_{app}	apparent thermal resistance, $[m^2KW^{-1}]$
R_{em}	total thermal resistance of all the material layers situated at the outside of layer m, $[m^2KW^{-1}]$
R_i	individual model resistance, $[m^2KW^{-1}]$
R_{im}	total thermal resistance of all the material layers situated at the inside of layer m, $[m^2KW^{-1}]$
$\boldsymbol{R}_{k\mid k-1}$	variance of $\boldsymbol{y}_k$ given the sequence of measurements $\mathcal{Y}_{k-1}$ and the parameter set $\boldsymbol{\theta}$, [−]
R_m	thermal resistance of material layer m, $[m^2KW^{-1}]$
R_{tot}	total thermal resistance, $[m^2KW^{-1}]$
s	Laplace variable, [−]
$\boldsymbol{\theta}$	set of physical parameters, [−]
$\hat{\boldsymbol{\theta}}$	estimated set of physical parameters, [−]
t	time, $[s]$
t_k	time at discrete point k, $[s]$
T	temperature, $[^\circ C]$
T_{ae}	exterior air temperature, $[^\circ C]$
T_{ai}	interior air temperature, $[^\circ C]$

T_i	state temperature, $[^\circ C]$
T_{se}	exterior surface temperature, $[^\circ C]$
T_{si}	interior surface temperature, $[^\circ C]$
$\boldsymbol{u}$	input vector, $[-]$
U	thermal transmittance, $[Wm^{-2}K^{-1}]$
v	number of zeros of the ij^{th} element, formulated in zero-pole-gain form, of the transfer function matrix $\boldsymbol{H}_{input}$, $[-]$
v	velocity, $[ms^{-1}]$
w	number of poles of the ij^{th} element, formulated in zero-pole-gain form, of the transfer function matrix $\boldsymbol{H}_{input}$, $[-]$
$\boldsymbol{x}$	state vector, $[-]$
$\boldsymbol{y}$	output vector, $[-]$
$\boldsymbol{y}_0$	initial value of the output vector, $[-]$
$\mathcal{Y}_k$	a sequence of k observation measurements, $[-]$
$\boldsymbol{y}_k$	output vector at discrete time point k, $[-]$
$\hat{\boldsymbol{y}}_{k\|k-1}$	expected value of $\boldsymbol{y}_k$ given the sequence of measurements $\mathcal{Y}_{k-1}$ and the parameter set $\boldsymbol{\theta}$, $[-]$
z	number of unknown model parameters, $[-]$

ACRONYMS AND ABBREVIATIONS

ACF	AutoCorrelation Function
AIC	Akaike Information Criteria
$AICc$	Akaike Information Criteria with Correction for finite sample size
$ARMAX$	Auto-Regressive Moving Average eXogeneous input
ARX	Auto-Regressive eXogeneous input
CP	Cummulated Periodogram
$EPBD$	Energy Performance of Buildings Directives
EXT	EXTerior
$HVAC$	Heating, Ventilation and Air Conditioning
INT	INTerior

$nZEB$	nearly-Zero Energy Building
ODE	Ordinary Differential Equation
$PRBS$	Pseudo-Random Binary Sequence
$RMSE$	Root Mean Square Error
$ROLBS$	Randomly Ordered Logarithmically Distributed Binary Sequence
SDE	Stochastic Differential Equation

Chapter 1

Introduction and literature review

1.1 Problem statement: the importance of on-site characterisation

This book is about *building components* – elements such as roofs, walls and floors that constitute the building envelope protecting our indoor environments. In the course of the last twenty years, these building envelopes have evolved towards high performance instruments that must effectuate indoor environments meeting up to the increasingly demanding comfort levels, preferably in the most energy efficient way. In the past decades, a growing awareness of energy sustainability has settled. Since modern society is increasingly relying on energy while its primary resource – fossil fuels – is diminishing every day, the recognition aspired that significant energy savings are needed. An extensive survey of the energy use of the European building stock [1] indicated that the built environment is a major user of energy, hence, harbouring large potentials for energy savings. This is recognised worldwide and has motivated many countries to pro-actively promote energy efficiency in the built environment. In Europe, the European Energy Performance of Buildings Directives (EPBD), first published in 2003, compelled its member states to rate the energy performance of buildings and to impose minimum performance levels to new buildings and to buildings that are subjected to major renovations. A revised version, published in 2010, even mandates that all new buildings must be nearly zero-energy buildings (nZEB) by the end of 2020. Hence, huge efforts are required from the building industry.

A large share of the total energy use in buildings concerns the heat losses through the building envelope. Although the thermal performance of the building envelope is only one of the factors determining the actual energy performance of dwellings – other ones

are for example the efficiency of the dwelling's services, the user behaviour, etc. –, it is the most essential factor that can be influenced by the construction industry. Because, as long as a building's envelope has a poor thermal performance, energy will leak into its environment and the benefits of even the most efficient and responsibly operated HVAC system will be negated. Hence, high priority is placed on effectuating sound thermal envelopes. This is reflected in the EPB Directives which impose increasingly stringent specifications to the thermal performance of individual building components and thermal bridges. Among others, maximum values for the thermal transmittance, or *U-value*, of building components are specified. As an illustration, figure 1.1 shows the impact of the evolution of U-values, imposed by the Flemish government, on the thickness of insulated cavity walls throughout the last 10 years.

Figure 1.1 is only one example illustrating that the concept of a legalised energy assessment framework has influenced the building industry substantially. Since its introduction, architects have been forced to integrate the energy aspect already early in the design phase and contractors have been motivated to reinvent certain construction processes. As a result, the building industry is slowly, but vastly, evolving towards a more energy conscious approach. Nevertheless, the current evolution has one main pitfall: it is based on theoretical energy labels that relate to buildings *as designed* rather than to buildings *as constructed*. Hence, the evolution towards energy efficient buildings

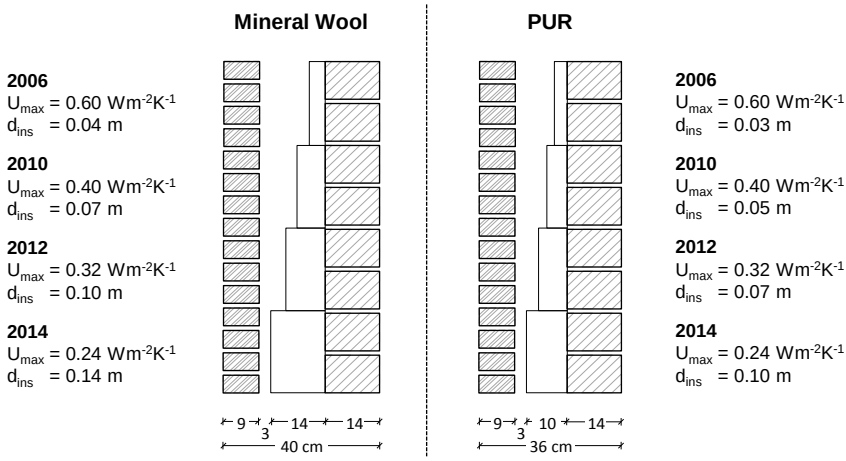

Figure 1.1: Evolution of insulation thickness for mineral wool and PUR insulated cavity walls that correspond to U-values imposed by the Flemish government over the last ten years.

risks to happen only on paper. Indeed, energy labels rely on several crude assumptions: for instance, indoor temperature assumptions are based on standard user behaviour profiles and take no account of actual user preferences, or, heat losses through the building envelope are based on theoretical thermal properties obtained from standards or product information and ignore the way these materials are implemented in the actual construction. Consequently, the actual building performance might deviate significantly from the labelled one. To illustrate this, figure 1.2 shows some pictures taken at construction sites: although all buildings are EPBD approved – meaning that the theoretical U-values of the walls fulfil the requirements – one can question the as-built performance of these building components due to a poor installation of their insulation layer.

Several independent studies [2–6] show that the actual energy use of dwellings after realisation hardly ever measures up to the energy use that was predicted. This discrepancy has multiple possible causes related to the building's fabric, its services or user behaviour, etc. Since this work is about building components, we will focus on the discrepancies caused by the building envelope. Literature shows indeed that on this level significant deviations between the anticipated and real-world performance occur

Figure 1.2: Pictures taken at construction sites. Although all building components are EPBD approved, their as-built performance can be questionned due a poor installation of the insulating layer.

[7–11]. A study in the UK [11], for example, illustrates performance discrepancies at the whole building scale: the study revealed unexpected heat losses through the party walls of 18 newly built dwellings causing building performance discrepancies up to 100 % (see figure 1.3). Next to that, also on the building component scale, research uncovered performance discrepancies. A study conducted at the KU Leuven [9], for instance, illustrates the importance of good workmanship. The work examines the effect of wind velocity on the thermal performance of pitched roofs with both good and poor workmanship (see figure 1.4). Measurements show that poor workmanship decreases the thermal performance of the roof by 200 to 350%. In case of good workmanship, the impact is limited: only at high wind velocities discrepancies are noticed. Next to workmanship issues, other phenomena might contribute to the performance gap on building component level, including unintended air flows in the construction, moisture related issues, the application of other materials than the designated ones, etc.

Currently, knowledge about the performance gap at building component level only stems from small and isolated studies. In order to develop a better understanding of the underlying problems, more data needs to be gathered and analysed. Therein, reliable thermal characterisation methods for on-site measurements are essential. On the one hand, on-site characterisation methods are crucial for research purposes. They enable to identify the actual performance of built components on-site under well-controlled experimental conditions. Hence, common construction methods can be assessed, or, the impact of frequently occurring construction deficiencies can be studied. As such, quantitative data about the thermal integrity of real-world components would be available to sensitise the building industry, where needed, or to enforce better building practices. Next to that, knowledge of actual performance data is also useful for validating existing software packages that predict the thermal performance of building components. A comparison of actual and predicted performance can identify inappropriate simplifications or aspects that are not included in the software's model. On the other hand, knowledge of the actual performance of building components is interesting as a support for the performance labelling practice. One could imagine that performance labels are based on the actual thermal quality of the envelope's constituent components rather than on their theoretical performance. Hence, by relying on measured rather than theoretical values, a major source of uncertainty in the assessment of the thermal quality of building envelopes could be eliminated [12]. Moreover, knowledge of as-built thermal properties could be used repressively to assure qualitative construction methods.

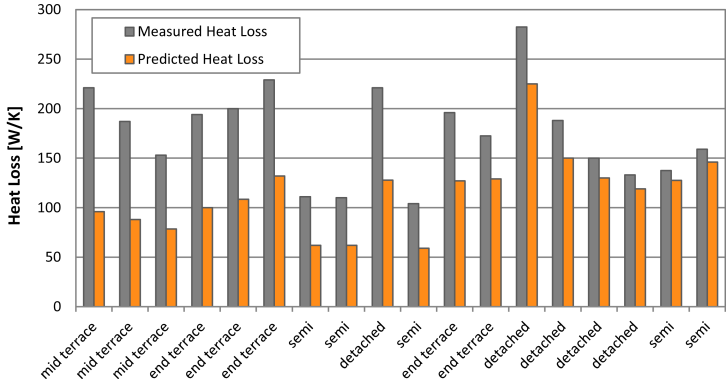

Figure 1.3: Measured versus predicted whole house heat losses (W/K) for 18 newly built dwellings in the UK. None of the houses is able to reach the designed values and deviations may go up to 100%. Source:[11]

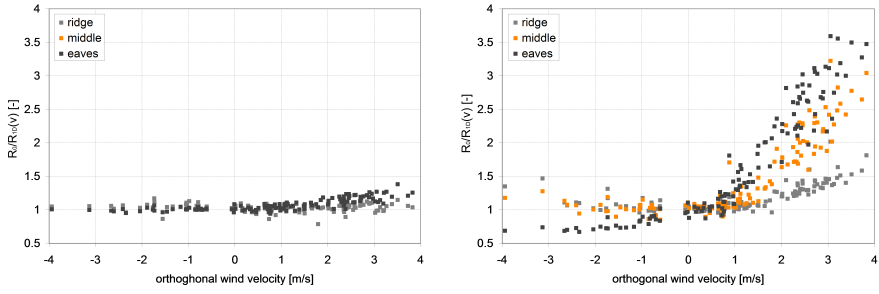

(a) **(b)**

Figure 1.4: Impact of wind velocity on the thermal resistance of a pitched roof with (a) good and (b) poor workmanship. The data points represent the ratio of the R-value at wind velocity v=0 ms^{-1} (R0) and at wind velocity v (R1D(v)). The measurements show that poor workmanship decreases the thermal performance of the roof by 200 to 350%. In case of good workmanship, the impact is limited: only at high wind velocities discrepancies are noticed. Source:[9]

So, essentially, a prerequisite for advancing the real-world thermal integrity of building components is the availability of *reliable thermal characterisation methods*: only when the effective thermal performance of building components can be robustly characterised, the performance gap can be studied and effective solutions can be tailored to reduce the gap between designed and real performance and to ensure that it is kept closed.

1.2 **Research scope and objectives**

Within the framework of the above elaborated problem statement, this work recognises the importance of understanding the actual, as-built performance of building components. It therefore discusses the essential tools enabling on-site performance characterisation. The major aim of this dissertation is

to investigate the reliability of characterisation methods determining the thermal resistance of building components based on on-site measurements.

A major thermal characteristic of building components is their thermal resistance, or equivalently, *R-value*. This quantity is a measure of the component's thermal quality and expresses the temperature difference across the component required to cause one unit of heat flux passing through one unit of area of the element. Put differently, the thermal resistance of a building component expresses the ability to resist a heat flow from one side to the other. The quantity is typically seen as a stationary parameter which, under steady state conditions, regulates a linear temperature distribution across a material layer, i.e. from surface to surface. In a multilayer building component, the total thermal resistance is the sum of the resistances of the individual layers. Each of these resistances is directly linked to the linear temperature profile established in the component under stationary conditions (see figure 1.5 (top)). Under dynamic conditions, however, the temperature distribution in a building component is no longer constant, nor likely to be linear. As a result of the varying surface temperatures and the capacitive working of the materials, the temperature distribution will vary in function of time. The varying surface temperatures of a building component are established by several influencing heat transfer mechanisms (see figure 1.5 (bottom)). At the exterior side, the surface temperature is affected by shortwave radiation from the sun, by longwave radiation from and to the sky, ground and surrounding surfaces and by convection with the surrounding air. In addition, capillary uptake of rain water and drying out by evaporation will also influence the heat balance. At the interior side, the surface temperature is influenced by longwave radiation from and to the

surrounding surfaces and by convection with the adjacent air. To a minor extent, also solar absorption and water vapour evaporation can play a role at the interior surface. In the building component itself, heat is mainly transferred by conduction in the material layers, and by parallel radiative and convective processes in intermediate air layers. Due to the insulating and capacitive properties of building components, an incoming temperature signal at one side of the element will result in a phase-shifted signal with a dampened amplitude at the other side. As a result of all this, the mainly stationary functioning of the thermal resistance is masked, rendering an extraction of this quantity from on-site measurements more difficult than readily apparent.

In this work, the focus lies mainly on the ability of characterisation methods to estimate the thermal resistance of building components and, if possible, an indication of the estimate's accuracy. Additional thermal parameters that may result from the studied characterisation methods are valuable, but they are not essential in this work.

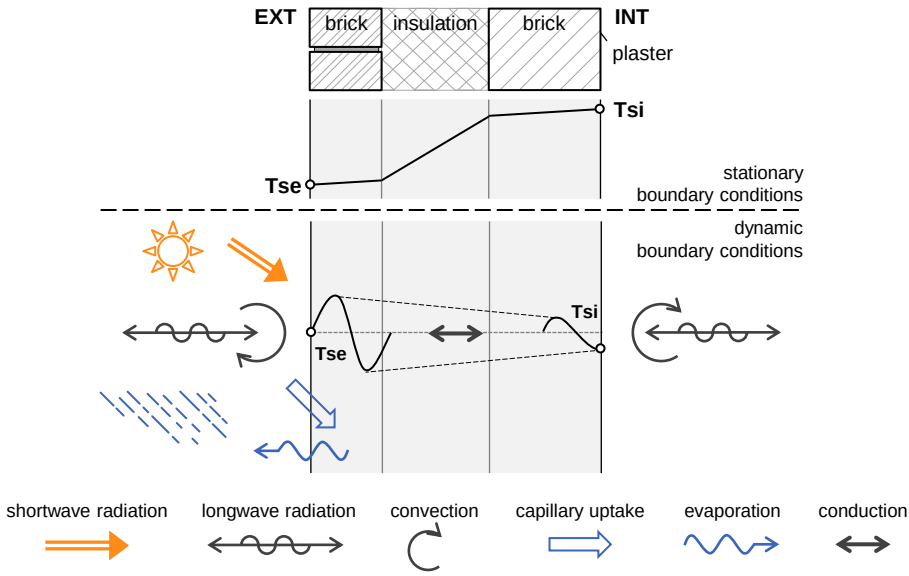

Figure 1.5: Graphical representation of the heat transfer mechanisms affecting a building component. The exterior surface temperature, represented by T_{se}, is influenced by shortwave and longwave radiation, convection, capillary uptake of rain water, evaporation and conduction. The interior surface temperature, represented by T_{si} is mainly influenced by convection and longwave radiation from and to the surrounding surfaces.

Given the overall aim of this dissertation, four main research questions can be formulated:

What are the potentials and limitations of established on-site characterisation methods?
Since the nineteen eighties, characterising the on-site performance of building components has been the interest of many studies [7, 13–26]. Consequently, several methodologies for on-site thermal resistance estimation are available. Various questions about these methods arise in the specific context of this work: What are the basic principles these methods are relying on? How easily applicable are they? What are the limiting factors for the application of these methods? What is the reliability of the estimated thermal resistance and can its physical significance be validated? Etc.

Is stochastic grey-box modelling an appropriate technique for robustly estimating the on-site thermal resistance of building components?
Stochastic grey-box modelling is a dynamic data analysis technique with an impressive track record in identifying systems in various disciplines. Yet, the method's use in building physics is rather new. Therefore, its potentials and limitations for the on-site thermal resistance estimation of building components are to be studied. Among others, the following questions should be asked: Is the method actually able to estimate the thermal resistance from on-site measurements? Which stochastic grey-box models are best suited for this purpose? Are the thermal model's parameters identifiable? Can a general framework be developed for a robust in-situ thermal resistance estimation procedure? Etc.

Which characterisation method most reliably estimates the thermal resistance of building components and under what circumstances?
The existence of several characterisation methods, handling the R-estimation problem in various ways, encourages the following questions: Which method leads to the most accurate and reliable results? Does the reliability of the methods depend on the indoor or outdoor boundary conditions? Which circumstances enhance or hinder the methods' accuracy? How does the measurement length influence the accuracy of the R-estimates? Etc.

Can stochastic grey-box modelling be deployed to characterise variable thermal properties that might result from workmanship induced heat transfer mechanisms?
Due to poor workmanship, phenomena such as wind washing or rotational air flowing can be induced in the construction, affecting the building component's intended heat transfer mechanisms. Often, these disturbing phenomena result in a thermal resistance that is no longer stationary, but time dependent. The question can be raised whether the technique of stochastic grey-box modelling is able to characterise an equivalent, variable thermal resistance indicator.

1.3 Proposed methodology and outline

To establish a precise and extensive understanding of the potentials and limitations of characterisation methods for on-site building components, the research questions, as formulated above, are treated one-by-one. Since many of the questions relate to the methods' application, an exemplary case study is considered throughout this dissertation. Simulated measurement data of an insulated cavity wall is used to demonstrate the functionalities of the different characterisation methods. In a later stage, also a lightweight building component and actual measurement data are considered to prove the generality of the findings.

This dissertation answers the four above-mentioned research questions subsequently and is hence organised in four main chapters, preceded by an introduction and literature review and closed by a summarising chapter. The separate chapters of this work are elaborated in the following outline.

In literature, several characterisation methods have been presented for the specific purpose of determining the on-site thermal resistance of building components. Chapter 2 gives an overview of these *established* characterisation methods and distinguishes thereby between semi-stationary and dynamic techniques. The methods' analysis procedures are discussed together with their potentials and limitations. Alongside, their application is demonstrated for the exemplary case study.

Recently, an important newcomer to the dynamic characterisation methods has been introduced in literature, notably, stochastic state space modelling. Since it is a rather new approach in the context of thermally characterising building components, chapter 3 thoroughly examines its possibilities for the specific aim of thermal resistance estimation. The chapter addresses the formulation of an appropriate grey-box model structure for this purpose and demonstrates its application for the cavity wall case study. Furthermore, a major part of the study in this chapter focusses on the physical interpretability of the thermal models' parameters, an aspect that is closely linked with the concept of practical identifiability. Indeed, the physical interpretability of a model's parameters can be judged by examining whether the assumed model parametrisation can be uniquely defined from the available measurement data. Such interpretability analyses are conducted for different sets of typical measurement data of the studied cavity wall. In addition, several model validation criteria are studied. Since stochastic grey-box modelling is rooted in statistical time series analysis, an extensive set of statistical validation tests is available. It is examined which validation criteria are useful to validate the estimated models and how they have to be interpreted to assure reliable R-estimates. Based on these investigations, the chapter formulates a general framework for the application of stochastic grey-box modelling specifically aiming at

characterising the on-site thermal resistance of building components from dynamic measurements.

The main challenge of on-site characterisation methods is to handle the influences from outdoor weather conditions in the measurement data. Since the outdoor climate is intrinsically dynamic, it complicates the estimation of the in essence stationary thermal resistance. Besides, climatic perturbation signals have a seasonally different appearance, therefore demanding versatilely applicable analysis methods. Essentially, the extent to which the characterisation methods are able to cope with the varying climatic conditions determines their practical applicability. The latter is examined in chapter 4 for all discussed characterisation methods by performing a large-scale comparative assessment. Thereby, special attention is given to the reliability of the methods' thermal resistance estimates when confronted with data sets of limited measurement time spans and different seasonal boundary conditions.

In reality, the thermal resistance of building components is often a time-dependent variable. This can result from temperature or moisture dependent thermal material properties. But, more importantly, it can result from poor workmanship issues inducing phenomena such as wind washing or buoyancy driven flows that interact with the intended heat transfer mechanisms of building components. Chapter 5 investigates a specific example of this: due to poor installation of hard insulation panels in a cavity wall, air looping around the panels can occur, which substantially alters the insulating quality of the cavity wall. In order to study this phenomenon, measurement data of a cavity wall with deliberately poorly installed insulation panels is considered. Chapter 5 then examines whether stochastic grey-box models are able to identify the presence of this phenomenon from local measurement data. Next to that, it studies whether specific grey-box model formulations can be found that define a variable thermal resistance indicator.

Chapter 6 concludes this dissertation by summarising the major findings of the previous chapters. Hereby, a critical view on the potentials and shortcomings of characterising building components on-site is given. Furthermore, the added value of this work is formulated, as well as suggestions for a logic continuation of the initiated research.

1.4 Literature review: the evolution of on-site characterisation methods

The vast amount of literature on on-site thermal characterisation proves that it is an important topic in building physics. The subject has been studied in a wide variety of contexts, addressing the characterisation of various building constructions.

However, against the background of this dissertation, the literature review will solely concentrate on essential studies about how to determine the thermal resistance of building components from on-site measurements.

As pointed out by Stamatiou [23] and Fazio and Zmeureanu [17], these on-site characterisation methods can be classified as either *active* or *passive*. The former class comprises methods that impose an artificial and controlled power as exterior boundary condition, whereas the latter class relies on actual outdoor weather conditions. Active methods obviously require specialised equipment to establish an artificial environment over a sufficient area of the building component. Therefore, generally, portable guarded hot boxes are used. In the early nineteen eighties, much attention was paid to these active methods, as can be seen from works as [27–29]. But also recently, an active approach for the thermal characterisation of building components resurfaced in the work of Rasooli, Itard, and Ferreira [30]. According to Modera et al. [29], active methods have the advantage that the measurements are theoretically independent of the weather conditions and that the frequency spectrum of the perturbation signals can be controlled. Nevertheless, they also admit that the method is rather complex and cumbersome to use in the field. Even more, as mentioned by Fazio and Zmeureanu [17], active methods are bounded to the artificial environments that they establish: dynamic thermal properties that are estimated from such measurements represent the component's response under these imposed controlled conditions rather than that they represent the component's behaviour under real-world conditions.

Passive methods, on the other hand, are completely subjected to outdoor weather conditions. Controlled exterior conditions are thus abandoned. Hence no cumbersome equipment is needed and simple experimental set-ups satisfy. For instance, some attempts have been made to determine the thermal resistance of building components by a simple hand-held infra-red camera, although Treado and Burch [31] demonstrated that this approach leads to considerably inaccurate R-estimates. Almost all other passive characterisation methods involve measurements of the surface temperatures at both sides of the studied building component, together with measurements of the heat flux passing through it. This set of measurements is also of main focus in this dissertation. Because of the simplicity of the experimental set-up required to measure these quantities, this research focusses solely on the ability of passive characterisation methods to determine a reliable thermal resistance from these measurements. Generally, it is the heat flux at the interior face of the construction that is measured, since it is very hard to obtain reliable heat flux measurements at the exterior surface, as explained by McIntyre [20]. Actually, it is already cumbersome to obtain error-free measurements of the interior heat flux. Several studies have been dedicated to this subject. Trethowen [32], for example, investigated the accuracy and stability of differ-

ent heat flux sensors and Flanders [8] formulated guidelines on how to calibrate them when used to measure heat fluxes through building components. Provided that the sensors are carefully placed and appropriately calibrated, Flanders [8] demonstrated that reliable measurements are possible. Therefore, in this dissertation, no further attention is given to the reliability of the measurements themselves; the focus lies on the reliability of the methods' data interpretation.

Based on heat flux and temperature measurements, several passive characterisation methods have been developed to identify a building component's thermal resistance. The first strand of methods stayed close to the concept of the thermal resistance, which is, under stationary conditions, defined as the temperature difference over a component divided by the heat flux across it. However, since stationary conditions are never encountered on-site, a thermal resistance calculation from instantaneous flux and temperature measurements can not provide accurate R-estimates, as is demonstrated by Modera et al. [24]. Hence, to deal with the transient effects in on-site measurements, the majority of the early characterisation methods assumed time-integrated flux and temperature measurements to determine a component's thermal resistance. It was only in 1994 that this approach was adopted as the *average method* in the international standard ISO 9869, although a survey by Anderson [16] already called for a harmonisation in the mid nineteen eighties since many independent studies had been reporting on this approach. McIntyre [20], for example, discussed the physical principles behind the average method and demonstrated the well-functioning of the method in the light of an example. Also Brown and Schuyler [26] applied the average method on measurements of several case studies and proved that the approach enables the estimation of the on-site thermal resistance of building components with reasonable accuracies ($\pm$ 10%). However, the average method also has its limitations, as was pointed out by several other studies. Modera et al. [24], for instance, studied the errors that are associated with the method's data analysis. The study concluded that the test length, required to obtain a certain level of accuracy, mainly depends on the magnitude of the average indoor-outdoor temperature. Hence, since summer data is typically characterised by reduced indoor-outdoor temperature differences, the technique's application is often restricted to winter months, as appointed by McIntyre [20] and Anderson [16]. Also Roulet et al. [25] studied the limitations of the average method. They examined the performance of the average method by assessing its results for nine different building components, from very light to very heavy, subjected to different boundary conditions. From those experiments, they observed that massive building components require much longer integration periods than lightweight elements, due to their increased heat storage capacities. Hence, the analysis method might require long measurement time spans in order to obtain reliable R-estimates. In one case, even 50 days were required.

Furthermore, they observed that the average method might lead to R-estimates that seem to converge to a stable, but, erroneous value, which is a main drawback of the method. This occurs when a significant change in heat storage in the wall takes place during the measurements. The latter phenomenon is further studied by Anderson [33]. By means of harmonic analyses, he studied the problem and suggested to correct the heat flux measurements for storage effects. This correction was later included in the international standard ISO 9869. Both the average method and its correction for storage effects are further referred to as *semi-stationary methods*, since their analysis relies on stationary principles.

Due to the many restrictions of the semi-stationary analysis techniques, a parallel stream of methods was developed focussing on dynamic data analysis. In contrast with the semi-stationary methods, these techniques include the weather induced fluctuations of on-site measurements in their analysis rather than to cancel them out. One of the first methodologies to dynamically analyse heat flux and temperature measurements was proposed by Aittomäki [14], but also Kupke [19] and Ahvenainen et al. [13] reported on this method. Their suggested approach models the heat flux through a studied building component by weighting momentary temperature differences over the component along with surface temperature changes from the past that are lumped together. Since the model formulation is rooted in physics, the thermal resistance can be linked to one of the estimated parameters of the model. This approach was later adopted as the *dynamic analysis method* in Annex B of ISO 9869. A very similar, but more direct, approach relying on the same principles was developed in the works of Anderlind [15, 34]. In [15] the method was successfully applied to determine the thermal resistance of a 0.8 m loose fill glass fibre attic insulation from typical winter and summer measurements. Since Anderlind's approach is documented in more easily accessible papers than the dynamic analysis method of ISO 9869 and since both methods are assumed to result in R-estimates of equal quality because of their common underlying principles, it is the former approach that is further employed in this dissertation.

By the introduction of Aittomäki and Anderlind's methods, one of the first steps towards *inverse modelling* or *system identification* was taken in the context of thermal resistance estimation. In essence, these terms relate to methods that construct data-driven models from available experimental data. Or, in other words, they refer to methods that estimate the parameters of a mathematical model by tuning this model's behaviour to the observed behaviour of the physical system, both subjected to the same boundary conditions. The application of system identification is typically driven by one of the two following intentions: (1) the method aims at identifying the physical properties of the studied system, or, (2) the method aims at identifying the overall

physical behaviour of the system for prediction or control purposes. A modeller always has to keep the intended purpose in mind, since it influences the way identification results need to be interpreted. In the context of this dissertation, it is clear that inverse modelling techniques will be used for *physical properties estimation* purposes.

The term *inverse modelling* or *system identification* covers a multitude of approaches solving the inverse problem. Generally, they are specified (1) by the mathematical model they assume for describing the studied physical object and (2) by the objective function they employ to describe the agreement between model and measurements. Although many different model structures exist for a wide variety of applications, they can, broadly speaking, be subdivided in the following two model classes: so-called *black-box* models which are very general and purely mathematical models without any reference to the physics of the studied system; or, so called *grey-box* models, which are models with a physical structure and hence with physically interpretable parameters. The classification of possible objective functions, by contrast, is more complex. Only some general aspects will be discussed here to give a broad idea on the matter. Generally, objective functions relate to the *residuals* between the measured and modelled values of one or more observed variables. To identify building components, typically the measured surface temperatures are used as inputs to a model that predicts the internal heat flux through the building component as output. The residuals between the modelled and measured heat flux are then subjected to the objective function that quantifies the model's performance. Often, objective functions aim at minimising the sum of squared residuals, although many other approaches exist, such as the maximum likelihood approach for example [35]. A major division in identification methods relates to how a model reckons with information of the model's performance obtained during the estimation procedure itself. When an identification method assumes a model which output is simulated over the whole length of the measurements without any intermediate feedback of the measured observation variable, it is considered an *Output Error Method (OEM)*. When, on the contrary, the identification method assumes a model that includes information on the observed variable from previous time-steps in its consequent predictions, it is considered a *Prediction Error Method (PEM)*. The latter class of methods has the advantage that the residuals are *prediction errors* from one time step to the next rather than *simulation errors*. Hence, they are less likely to be auto-correlated and thus enable the use of various statistical tests for model validation or for pinpointing model deficiencies. This difference between OEMs and PEMs can also be seen as a difference between deterministic and stochastic identification methods. All measured data contains errors, but by accounting for this *noise* in the model itself, the measured data is treated stochastically rather than deterministically. It is actually this stochastic aspect that enables models to include

information of their previous performance in consequent predictions. Very simple noise models, for example, straightforwardly include measured values from previous time steps in the calculation of its consequent prediction, whereas, more sophisticated noise models that differentiate between measurement and system noise, balance the latter two uncertainties to decide to which extent previous measured and modelled observations should be included in new predictions.

The use of system identification in the context of building performance characterisation became widely studied by several collaborative research projects since the late nineteen eighties. The European PASSYS project (1986 - 1989), and later the PASLINK project, addressed the development of dynamic test and analysis procedures to estimate on-site thermal and solar characteristics of building components, as is pointed out by Baker and van Dijk [36]. The focus of these projects was entirely on test cell experiments. Hence, the analysed measurements include in- and outdoor air temperatures as well as the heating demand of the test cell rather than surface temperature and heat flux measurements. Nevertheless, the research that was pursued in this context is also valuable for analysis procedures of the latter set of measurements. The PASSYS collaboration led to the development of two identification packages, notably MRQT and CTLSM [36], which handle the identification problem in very different ways. MQRT implements a deterministic output error method, while CTLSM uses a stochastic prediction error method. MRQT later evolved into the software package LORD [37], that was tailored specifically for interpreting the test cell experiments of the PASLINK project. The latest versions of LORD also included a prediction error method for identifying systems. The package CTLSM, on the other hand, evolved into CTSM and is nowadays available as the R-package CTSM-R (http://ctsm.info/). In parallel with the PASSYS and PASLINK developments, the Joint Research Centre of the European Commission organised several workshops on statistical identification methods for the specific purpose of characterising the thermal performance of buildings. These workshops merely concentrated on the identification procedures themselves and resulted in a book [38] summarising the main stochastic identification approaches. More recently, also the IEA/EBC Annex 58 project (2011 - 2016) grouped a number of international researchers to exchange experience on the development and practical use of on-site characterisation methods in the built environment. The project mainly focussed on the reliability, accuracy and applicability of these methods in real-world and in this context, guidelines [39] were formulated for the specific use of several data analysis methods that characterise the actual thermal performance of whole buildings and building components.

From the aforementioned research projects, two statistical data analysis methods proved promising for reliably characterising building components from on-site heat

flux and temperature measurements, notably ARX-modelling and stochastic grey-box modelling. The use of Auto-Regressive (Moving Average) models with eXogenious inputs, shortly AR(MA)X-models, in this context was first studied by Norlén [22] in the early nineteen nineties. He investigated the method by determining the thermal resistance of the loose fill attic insulation that was also thermally characterised by Anderlind in [15]. Consistent results were obtained. Although the mathematical formulation and estimation procedure of ARX-models is very similar to Anderlind's estimation method, the underlying basics are different: ARX-models are stochastic and black-box instead of deterministic and grey-box. Despite the purely mathematical nature of general ARX-models, the thermal resistance of building components can be estimated by interpreting the static gain of the models [18, 22, 39]. This might not surprise, since the static gain of a model represents the ratio of the magnitude of its steady-state response (or output signal) to the magnitude of a steady-state stimulus (or input signal) applied to it. The thermal resistance can find itself in this description, since it represents the steady-state ratio of a temperature difference over a building component and the heat flux across it. In the work of Naveros et al. [21] the link between the thermal parameters of a building component and an ARX-model is illustrated. Therefore, an ARX-formulation was explicitly derived from a thermal network description of a wall component. Similarly, Bauwens [40] demonstrated the connection between the thermal parameters of a simple building model and an ARX-model, but more clearly indicated the link between the building's thermal parameters and the static gain of the assumed ARX-model. Although the assumed model in [40] describes a *building* rather than a building component, the findings also apply for building components since similar derivations could be made for the latter.

The second approach that showed great promise for building component characterisation is stochastic state space modelling. This method assumes stochastic lumped parameter models to describe the temperature behaviour in dwellings or building components. Such models are essentially thermal Resistance-Capacitance networks (RC-networks) that are expanded with stochastic noise terms. Additional equations then link the observed variable(s) to the parameters of these stochastic models. Typically, stochastic state space models are estimated by a maximum likelihood approach relying on Kalman filtering to calculate the likelihood function. This approach has known a long history and the progress of the technique is described by Young [41] for the period 1958-1980, and by Nielsen, Madsen, and Young [42] for the period 1980-1999. The specific approach used in this work has been developed by Kristensen, Madsen, and Jørgensen and is described thoroughly in [43] and [44]. The technique has been successfully utilised to identify dynamic thermal models of buildings, as is demonstrated in [45–48]. However, this work focusses on the thermal characterisa-

tion of single building components. Also for this purpose, the methodology has been used before. Jiménez, Porcar, and Heras [49] for example, estimated the U-value of a lightweight sandwich panel based on PASSYS test cell measurements. Both deterministic and stochastic state space models were tested. Also Naveros, Bacher, Ruiz, Jiménez, and Madsen [50] estimated the U-value of a PASSYS test cell component, notably a lightweight homogeneous wall, by stochastic state space modelling. Both papers, however, modelled the studied building component from the outdoor to the indoor environment rather than from surface to surface. Hence, the works focussed mainly on the best way to model heat transfer phenomena from the component's surfaces to its environments, such as solar radiation, long wave radiation, heat transfer coefficients, etc. However, when surface temperature and heat flux measurements are regarded, these phenomena are already included in the measurements itself. Consequently, the models that were assumed in the previous works [49, 50] can not be used to analyse flux and temperature measurements. Therefore, models are required that are limited to the description of the internal temperature distribution of the studied component. In literature, there is limited evidence for the use of stochastic grey-box modelling by maximum likelihood estimation for determining the thermal resistance from heat flux and temperature measurements. Only Biddulph, Gori, Elwell, Scott, Rye, Lowe, and Oreszczyn [51] demonstrated this approach, although a maximum a posteriori estimation was used rather than a maximum likelihood approach. The method was applied on measurements of a 0.3 m thick solid brick wall. A fair estimation result was obtained, although it was hard to validate its value since limited information on the thermal properties of the brick was available.

The referred literature proved that the subject of data analysis methods for in-situ thermal resistance estimation of building components has already been studied widely. The potentials and limitations of the semi-stationary methods, of Anderlind's approach and of ARX-modelling have been demonstrated in many works. These methods can hence be regarded as *established* methods. By contrast, stochastic grey-box modelling has only been scanned shallowly in the literature. Therefore, the work at hand studies the method profoundly in order to obtain a better understanding of the technique's possibilities for thermal resistance estimation from on-site measurements. Special attention is thereby given to the identifiability of the individual parameters of grey-box models and its possible influence on the physical interpretation of these parameters. This is an issue that is often disregarded in current works on thermal resistance estimation. Next to that, a comprehensive comparative assessment of the different methods' performance is lacking in the literature. Of course, some studies did compare the performance of their examined method to the performance of other characterisation methods, usually the average method. Roulet et al. [25], for instance, compared the

average method's estimation results with the results of the dynamic analysis method formulated in ISO 9869 for 9 different case studies. Or, Jiménez, Porcar, and Heras [52] juxtaposed the estimation results of several deterministic and stochastic dynamic analysis procedures in order to assess their correspondence. However, as far as known, a large-scale comparison of all techniques' performances in function of the measurement time span and climatic conditions is absent. Therefore, this work assembles the performances of the main characterisation methods for various scenarios and boundary conditions. Based on these results, the methods' ability to cope with the constantly varying climatic conditions to which in-situ building components are subjected, is studied.

Chapter 2

Potentials and limitations of established characterisation methods

Thermal performance characterisation of building components on-site is a recurrent topic in literature. Several characterisation methods have been studied widely since the nineteen eighties. The present chapter gives an overview of the more established characterisation methods that were developed over the past decades. Thereby, a distinction is made between semi-stationary and dynamic techniques. Their analysis procedures are described together with their potentials and limitations. Alongside, their application is demonstrated on a case study. Therefore, simulated measurement data of a south-west oriented insulated cavity wall is used.

2.1 **Case study: massive wall**

Typically, thermal resistance characterisation methods of building components on-site rely on the following measurements:

- the heat flux at the interior face of the building component,
- the interior surface temperature of the building component and
- the exterior surface temperature of the building component.

In this dissertation, several *theoretical* sets of heat flux and temperature measurements of a south-west oriented insulated cavity wall are generated to demonstrate the different methods' functionalities. The data sets are denoted *theoretical* because the heat flux and temperature measurements are simulated data rather than actual measurement

data. Initially, these data sets will serve as input to the characterisation methods so that their estimation performance can be evaluated. The fact that simulated data is used, has its advantages: it implies an exact knowledge of the thermal resistance of the studied building component so that a precise evaluation of the estimated thermal resistance is possible. Furthermore, it enables to focus on the methods' ideal performance excluding all measurement errors or physical aspects possibly jeopardising a proper thermal resistance estimation. At a later stage, the methods' performances will be evaluated for actual measurement data.

As it is a very common massive construction component in the Belgian building stock, an insulated cavity wall is chosen as case study. Later on, also a lightweight building component will be introduced to enable a comparison between the characterisation of both massive and lightweight building components. The theoretical heat flux and temperature measurements of the studied cavity wall are generated with HAMFEM, a finite element program based on the standard partial differential equations of heat, air and moisture transfer in porous building materials [53]. In this dissertation, however, the simulations only consider heat transfer and neglect moisture transfer in the wall. Furthermore, constant thermal properties are assumed to exclude temperature and moisture dependencies of the wall's thermal resistance. As can be seen from figure 2.2, the studied cavity wall consists of four layers: a plastered inner and an outer brick leaf enclosing the polyurethane insulation layer. A fine mesh of 200 elements and 201 nodes is chosen. The thermal properties used for the one-dimensional simulations of the cavity wall with HAMFEM are represented in table 2.1. Note that the insulation layer has an unusual thickness, which is, however, chosen on purpose to result in an easily comparable total thermal resistance of 5.0 m^2KW^{-1}.

The thermal behaviour of the cavity wall is simulated for the moderate climate of Uccle (Belgium). One year has been simulated with a calculation time step of one minute. Climate data of December and January are slightly adapted so that a cyclic year is obtained. Concerning the outdoor climatic data, irradiation and outdoor air temperature data with a time resolution of 1 minute is obtained by Meteonorm v6.1 based on the period of 1981-2000. Other climate data is obtained with a time resolution of 1 hour and is interpolated to minutely data. For the exterior heat balance, the convective heat transfer coefficient is assumed to be function of the wind velocity according to [54]. For the calculation of short and long wave radiation, an absorption coefficient α_S of 0.75 and an emissivity ϵ_L of 0.9 is assumed for the brick façade. This corresponds to a brick with a rather dark colour. Figures 2.1a till 2.1d represent the main outdoor boundary conditions for the whole year.

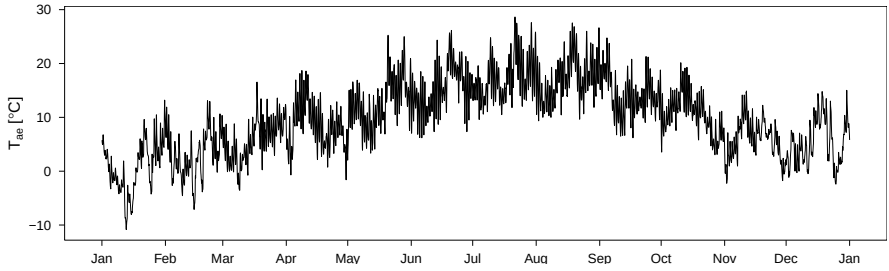

(a) Outdoor air temperature

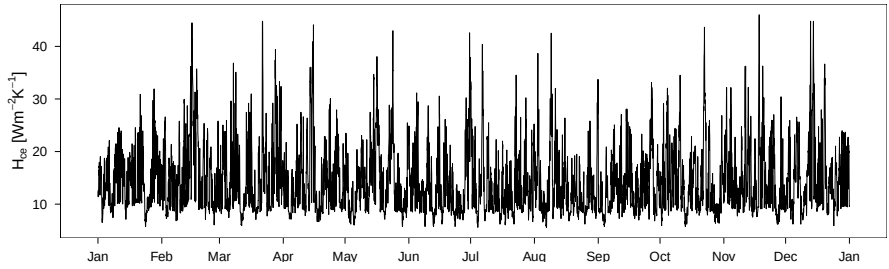

(b) Convective heat transfer coefficient

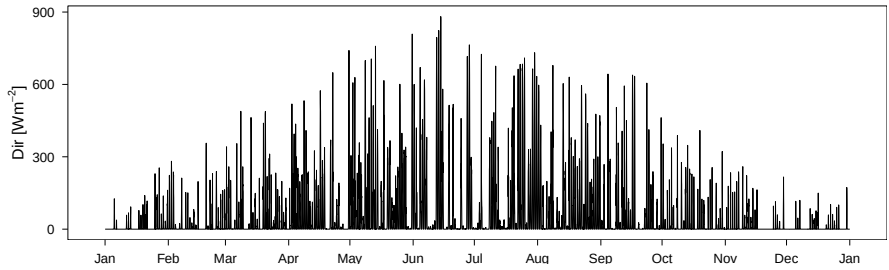

(c) Direct solar radiation on a horizontal plane

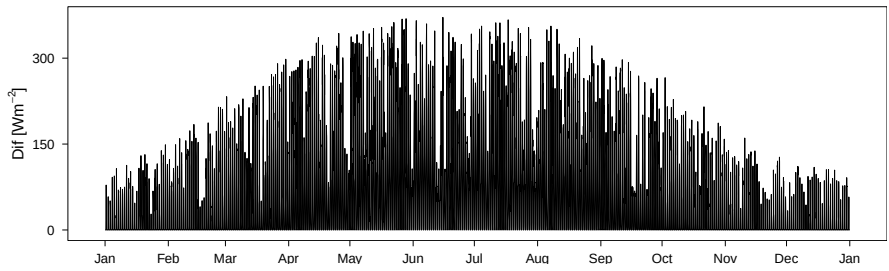

(d) Diffuse solar radiation on a horizontal plane

Figure 2.1: Outdoor weather conditions used for the HAMFEM-simulations of the simulated case studies.

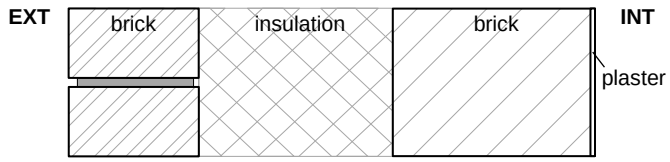

Figure 2.2: Section of the considered massive wall.

Table 2.1: Thermal properties of the considered massive wall.

	d $[m]$	**λ** $[W(mK)^{-1}]$	**ρ** $[kgm^{-3}]$	**c** $[J(kgK)^{-1}]$	**R** $[m^2KW^{-1}]$	**C** $[MJm^{-2}K^{-1}]$
facing brick	0.090	0.850	1744	840	0.106	0.132
insulation layer	0.110	0.024	30	1400	4.582	0.005
building brick	0.140	0.600	1150	840	0.233	0.135
plaster	0.015	0.190	790	1000	0.079	0.012
TOTAL	**0.355**				**5.000**	**0.284**

Concerning the interior heat balance, HAMFEM assumes a constant interior heat transfer coefficient of 8 $Wm^{-2}K^{-1}$ to model the heat transfer from the wall to the indoor temperature node. Regarding the indoor temperature regime, two main scenario's are considered. The **first scenario** assumes a constant indoor temperature of 20°C throughout the whole year, which implies a building with both ideal heating and cooling systems. However, a permanent constant indoor temperature is not very realistic for *in-use* buildings. Nevertheless, in the context of experimental test set ups, this scenario is plausible. Co-heating tests, for example, require a constant indoor temperature in order to determine a building's heat loss coefficient [55]. But, besides that, the assumption is also interesting for research purpose. By assuming a constant temperature, there are no dynamic signals exciting the wall from the inside, but nevertheless, the indoor environment is controlled independently from the outdoor boundary conditions. These are optimal indoor conditions for the semi-stationary analysis methods allowing an assessment of these methods' best performances.

In addition, a more realistic indoor temperature regime is introduced (**second scenario**). A varying indoor temperature is assumed as common in dwellings with a thermostatically controlled heating system. Because HAMFEM does not include such a dwelling model, TRNSYS is used to generate the varying indoor temperature that will be imposed as interior boundary condition in the HAMFEM-simulation. To gen-

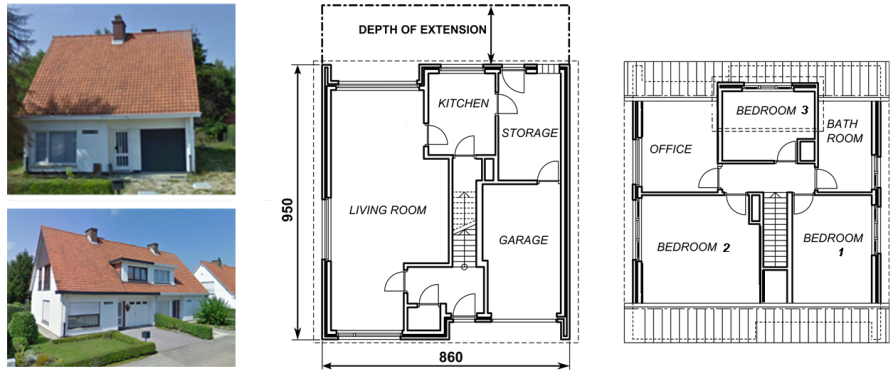

Figure 2.3: Dwelling that is representative for the two zone model used to generate the thermostatically controlled indoor temperature of the second scenario. (Based on [56])

erate the data, an existing two-zone model, developed in [56], is used. The model is based on a real dwelling, depicted in figure 2.3, and assumes ventilation and a day-night/week-weekend heating profile. In summer, no cooling is applied so that the indoor temperature is free-floating rather than controlled. More detailed information on the properties and settings of the dwelling and TRNSYS-model can be found in appendix A. But, in sum, the operative temperature of the day zone that results from the TRNSYS-simulation will be imposed at the indoor temperature node in HAMFEM.

Figure 2.4 depicts the indoor temperatures assumed in HAMFEM for the two considered scenarios. In the rest of this document, the first scenario is denoted *constant*, while the second is denoted *thermostat*.

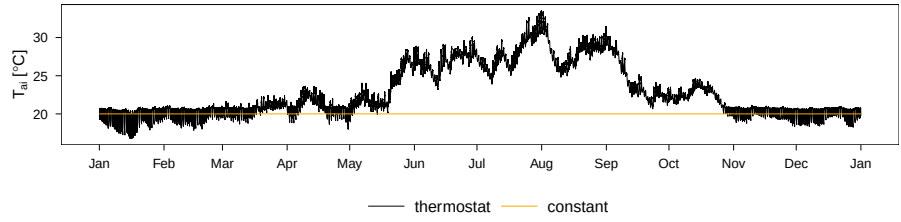

Figure 2.4: Indoor air temperatures of the two scenarios used for the HAMFEM-simulations of building components.

To mimic realistic measurement results, noise is added to the simulated data. A distinction is made between measurement noise and system noise. The former purely relates to the quality or accuracy of the measured signals, while the latter deals with disturbances that are introduced by the system – i.e. the building component – itself. Or, system noise leads to a temperature distribution in the building component that is slightly different than in the *ideal* system. Measurement noise can simply be implemented by adding white noise to the simulated quantities, notably to the exterior surface temperature T_{se}, to the interior surface temperature T_{si} and to the interior heat flux q_{hfm}. System noise, on the other hand, is more complicated to implement, since disturbances in the system's temperature distribution should be introduced. For the cavity wall, this is effectuated by simulating the HAMFEM-model with two sets of boundary conditions: (1) a first *clear* set involving the boundary conditions as specified before (see figures 2.1 and 2.4) and (2) a second *distorted* set including additional random white noise on the indoor and outdoor air temperature, T_{ai} and T_{ae}, and on the direct and diffuse solar radiation, Dir and Dif. Both sets are used to simulate surface temperature and heat flux measurements with HAMFEM. However, a mixed set of these measurements are provided as input to the characterisation methods: surface temperatures resulting from the *clear* simulations are input to the characterisation methods, while heat flux measurements from the *distorted* simulations are used. As such, some of the distortions in the heat flux measurements can not be explained by variations in the surface temperatures, but must be explained by system disturbances. Figure 2.5 schematically represents this and table 2.2 summarises the values of the white noise processes that are added to the variables. Furthermore, it must be mentioned that both system and measurement noise are added to the minutely simulation data. By averaging the data afterwards, the noise levels will decrease. Figure 2.6 represents the noise on the heat flux and surface temperatures for minutely and hourly averaged data for a subset of the year of simulations.

Table 2.2: Properties of the noise models that are added to the data of the simulated case studies.

Variable	Type	White noise	Unit
SYSTEM NOISE			
T_{ae}	absolute	N(0;0.2^2)	$[^\circ C]$
T_{ai}	absolute	N(0;0.2^2)	$[^\circ C]$
Dir	relative	N(0;0.03^2)*Dir	$[Wm^{-2}]$
Dif	relative	N(0;0.03^2)*Dif	$[Wm^{-2}]$
MEASUREMENT NOISE			
T_{se}	absolute	N(0;0.25^2)	$[^\circ C]$
T_{si}	absolute	N(0;0.25^2)	$[^\circ C]$
q_{hfm}	relative	N(0;0.05^2)*q_{hfm}	$[Wm^{-2}]$

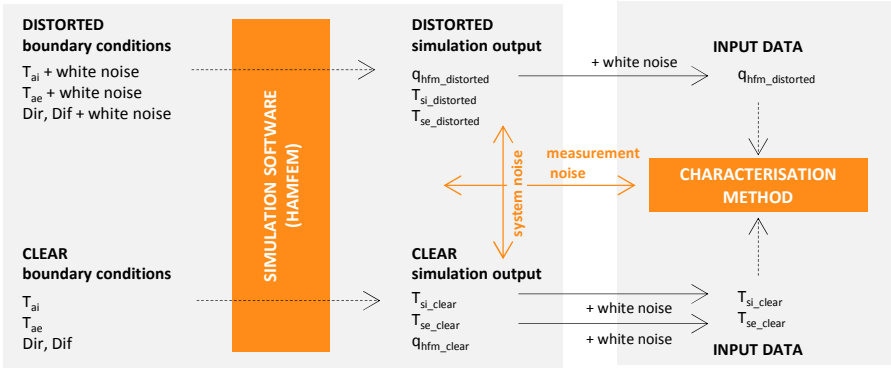

Figure 2.5: Schematic representation of the addition of system and measurement noise to the simulation data.

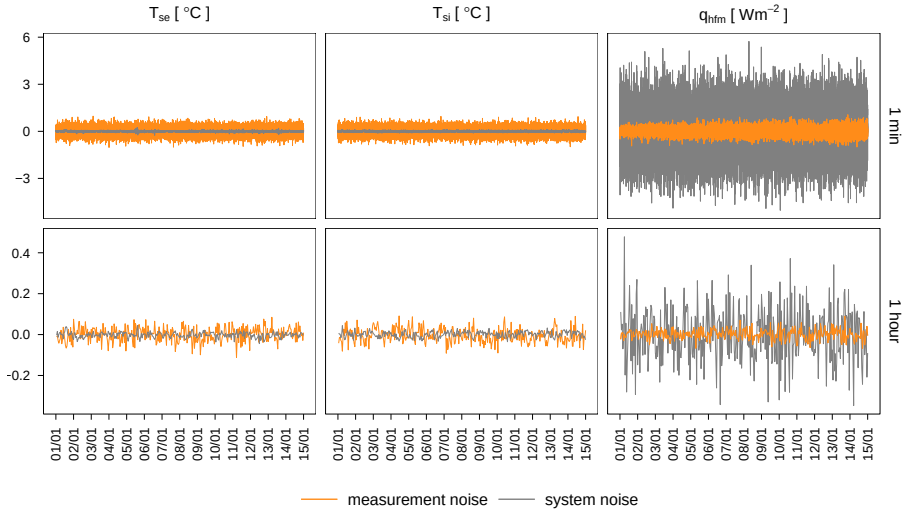

Figure 2.6: Example of the system and measurement noise added to the simulated surface temperatures and heat flux.

In the next sections and in chapter 3 the application of various characterisation methods will be demonstrated for the described cavity wall. To do so, two main data periods of 14 days are selected: a first data set in winter and a second in summer. Both the previously discussed scenarios will be considered. The surface temperatures and interior heat flux, that will serve as inputs to the characterisation methods, are depicted in figure 2.7. When not mentioned differently, hourly averaged data will be used. In this work, data is always averaged by taking the arithmetic mean of the measurements in the non-overlapping intervals that correspond to the new sampling time, without prefiltering the data. This approach can introduce aliasing problems: frequency content higher than the Nyquist frequency (corresponding to half the sampling rate) of the original signal can be wrongly reproduced at lower frequencies, as such contaminating the data. However, the cavity wall data considered in this work contains mainly low frequency content, as will be demonstrated in chapter 3 (section 3.4.1) by depicting the frequency spectra of the input signals. Based on the latter it is assumed that averaging the data with periods up till 6 hours will not introduce significant aliasing problems.

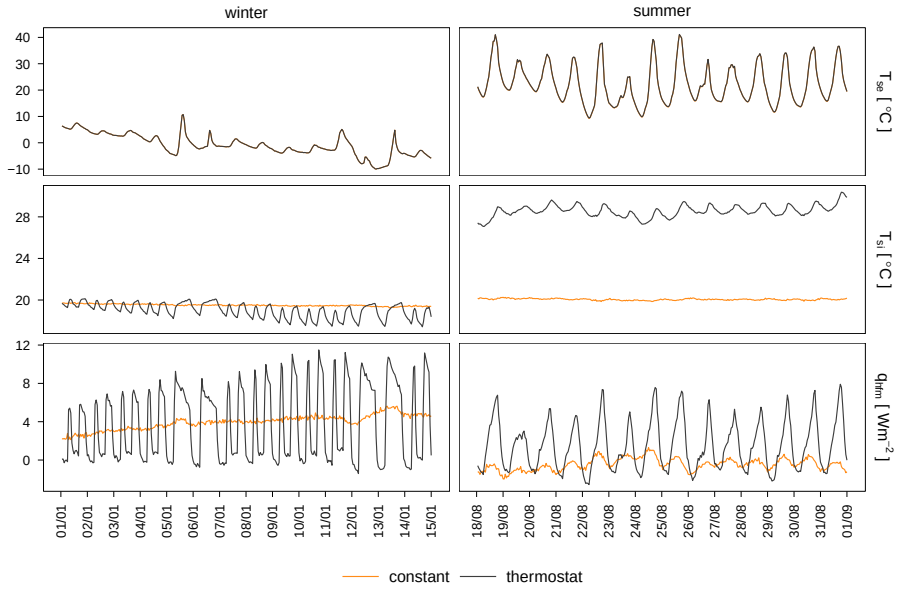

Figure 2.7: The surface temperatures and heat flux of the winter and summer measurements of the two considered scenarios that will serve as inputs to the characterisation methods.

2.2 Semi-stationary methods

2.2.1 Average method

The most generally accepted method for the thermal characterisation of building components on-site is the average method as formulated in ISO 9869 [57]. The method relies on the definition of the thermal resistance of building components which defines the R-value as the temperature difference over the component divided by the heat flux going through the component under stationary conditions. Unfortunately, steady state boundary conditions are never encountered on-site: as-built components are always subjected to the varying outside weather conditions and also the indoor environment is often characterised by a varying temperature. Hence, both the surface temperatures of the building component and the interior heat flux passing through it are fluctuating quantities. Yet, the interior heat flux will not vary in phase with the temperature variations since the thermal mass of the building component will induce a phase shift between these signals. As such, an instantaneously calculated R-value is most likely to be erroneous. To bypass the thermal mass effects, the average method assumes averaged data as an approximation for measurements under stationary conditions. If t_k enumerates the individual measurements, the thermal resistance is calculated as

$$R = \frac{\sum \Delta T}{\sum q} = \frac{\sum_{t_k=1}^{N} (T_{si,t_k} - T_{se,t_k})}{\sum_{t_k=1}^{N} q_{t_k}} \tag{2.1}$$

with R the total thermal resistance of the element $[m^2KW^{-1}]$, T_{si,t_k} the interior surface temperature at reading t_k $[^\circ C]$, T_{se,t_k} the exterior surface temperature at reading t_k $[^\circ C]$, q_{t_k} the interior heat flow rate at reading t_k $[Wm^{-2}]$ and N the number of measured data points $[-]$.

When computed after each recorded measurement, the estimated R-values should converge to an asymptotic value. This value will, however, only coincide with the component's real R-value under particular conditions. First, ISO 9869 specifies that the heat flux meter must not be exposed to direct solar radiation since this is known to be at the origin of large measurement errors [58]. Secondly, the thermal properties of the component's materials should be constant over the range of temperature fluctuations occurring during the test. In reality, however, the thermal conductivity is rarely constant, but is often temperature and moisture dependent. Finally, a last criterion requires that the change of amount of heat stored in the element is negligible when

compared to the amount of heat going through the element. Indeed, the steady state assumption implies that the heat flux measured at the interior surface of the building component passes entirely through the building component. Strictly speaking, this is only the case if there is no net heat or moisture storage in the element during the considered measurement period. Anderson [33] and McIntyre [20] actually demonstrate that pure cyclic temperature variations around a constant mean temperature only ensue oscillations in the R-estimation curve which damp out with time. Theoretically, indeed, there is no net heat storage in a building component when any whole number of the period of the temperatures' variation is considered. By contrast, when there is a change in the building component's mean temperature, a part of the heat flux measured at the interior side of the component will be stored in the element, or, an additional heat flux will be released. If this change in net heat storage is large compared to the heat flux going through the element, then the estimated R-value will be unreliable. ISO 9869 requires that the change in heat stored in the wall is not more than 5% of the heat passing through the wall during the experiment in order to obtain reliable results [57]. This is hard to obtain for structures of high R-value and high thermal mass and, in particular, during summer periods which are characterised by an increased capacitive working of the building's fabric. Hence, the method's practical applicability is often seasonally bounded.

More generally, in order to obtain reliable estimation results, the averages in equation 2.1 should be taken over a sufficiently long period of time so that the dynamic behaviour of the building component is cancelled out. This might limit the applicability of the method, as one usually wants as shortest measurement time spans as possible. A guidance of the measurement durations is provided by ISO 9869. The latter formulates criteria determining, during the course of the measurements, when sufficient data has been recorded to obtain reliable results. These criteria are based on the magnitude of the deviations between the subsequently obtained R-estimates computed after each measurement. So, essentially, the criteria assess the convergence of the estimator. If these criteria are not met, ISO 9869 proposes a correction for storage effects, which is explained in the next section.

To demonstrate the average method's functionality, the R-value of the cavity wall introduced in the previous section is estimated. The wall is characterised from the winter and summer measurements and for the two selected indoor environment scenarios. Figure 2.8 represents the estimated thermal resistances for all considered cases. They are computed gradually with every new obtained data point and are represented as such. The results are shown at the end of the period that is included in the analysis. For example, the estimation result shown at 10/01 includes measurement data from 01/01 up to and including 10/01. The R-estimates computed after each measurement,

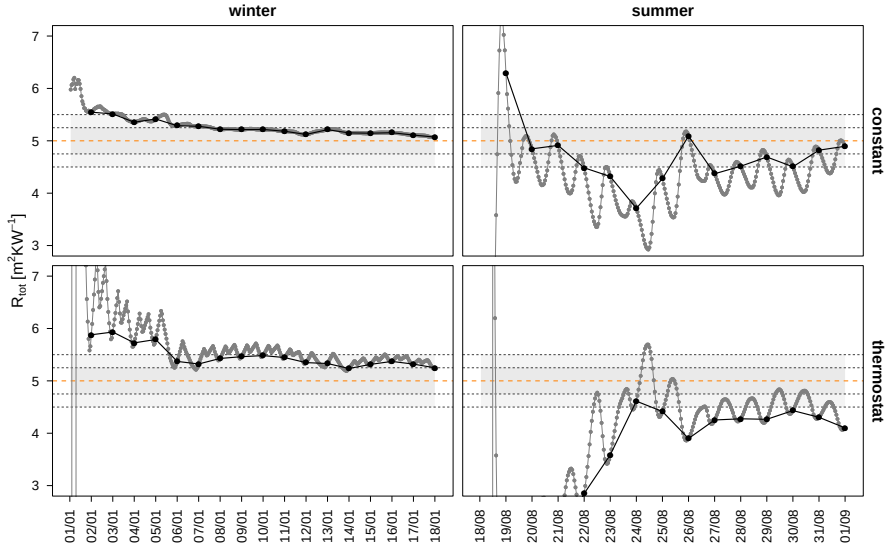

Figure 2.8: The R-estimates obtained by the average method after every hour of obtained data (grey) and after every 24 hours of obtained data (black). The orange dotted line indicates the reference value and the grey dotted lines indicate the 5% and 10% accuracy bands.

i.e. after every hour, are represented in grey. Additionally, the R-estimates computed after every 24 hours are represented in black.

Figure 2.8 demonstrates that it are mainly the winter measurements (top and bottom left) that lead to R-estimates converging towards the real thermal resistance, although a slight overestimation is noticed in both scenarios. The latter is in all probability due to a change in amount of heat stored in the wall. Since figure 2.7 shows a steady fall in outdoor air temperature during the entire winter period, it is justified to assume that the wall is gradually cooling down and as such releasing heat that was previously stored in the wall to the outdoor environment. Furthermore, it is noticed that the overestimation of R is larger in the second scenario. So, it must be the additional variations of the indoor environment that complicate the analysis: the varying indoor temperature of the second scenario leads to an alternation of heating up and cooling down of the inner brick leaf of the wall, which results in the fluctuating R-estimates plotted after every obtained hour of data, clearly visible in figure 2.8 (bottom left). However, since the controlled indoor temperature has a diurnal regime

(with intervention of the weekend days), the change in net heat storage of the capacitive inner layer is rather limited after every cycle. Indeed, the results plotted after every 24 hours of obtained data show less variation.

For the summer measurements, figure 2.8 (top and bottom right) shows less promising results: the R-estimates are not steadily converging towards a reference value, but are still rather unstable after 14 days of measurements. Although, in the first scenario, some R-estimates seem to approach the reference value quite well, for example at 26/08 or at 01/09, the subsequent data points drift away again. In the second scenario, no reliable results are obtained. So again, the additional variations of the interior perturbation signal, now coming from the free-floating indoor temperature, complicate the analysis.

Since *simulated* measurement data is used, the heat storage in the wall can be calculated and, hence, the capacitive working of the wall can be evaluated. Figure 2.9a shows the net amount of heat that is stored in, or released from the wall over the past period, i.e. since the beginning of the measurement period. Positive values indicate heat storage in the wall, while negative values indicate heat release. In winter, heat, previously stored in the wall, is indeed released to the outdoor environment. In summer, the hourly computed values show a cyclic alternation between heat storage in and heat release from the wall. Because these mainly compensate each other, the net heat storage after every cycle is rather limited and even smaller than in winter. However, the same applies for the net heat flux going through the interior face of the wall in summer and hence, the *relative* change in heat storage in summer is large. This can be seen from figure 2.9b showing the net heat that is stored in the wall over the past period as a percentage of the total amount of heat that went through the interior face of the wall in that period. Whereas in winter, with increasing measurement period, the net heat stored becomes smaller compared to the accumulated net heat that went through the wall, in summer this is not the case due to the rapidly changing heat storage and heat transfer. Hence, a robust estimation of the thermal resistance is hindered in summer.

2.2.2 Average method with correction for storage effects

In case that the average method is applied but that the aforementioned convergence criteria are not met, ISO 9869 suggests to apply a correction for storage effects. The latter involves a rectification of the heat flow rates according to the thermal storage capacities of the element and according to the environments' mean temperature change during the measurement period. The following equation represents the adjustment to

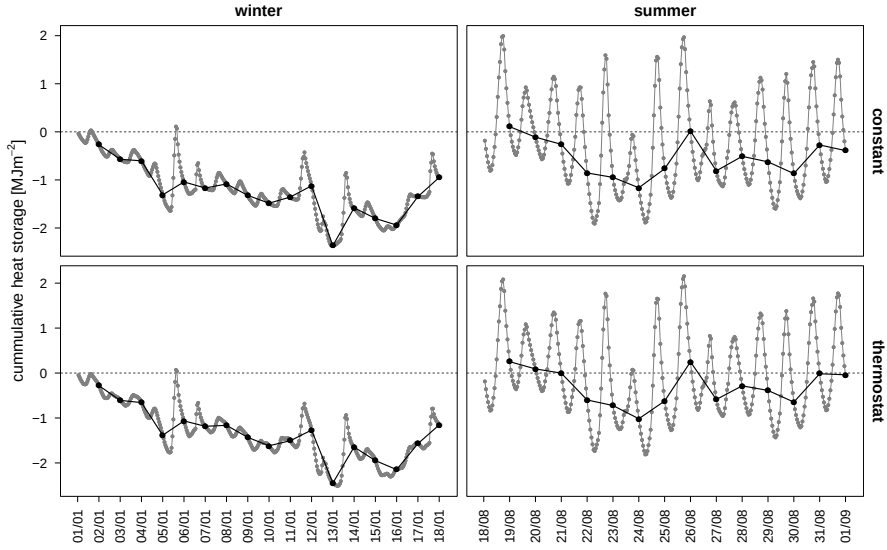

(a)

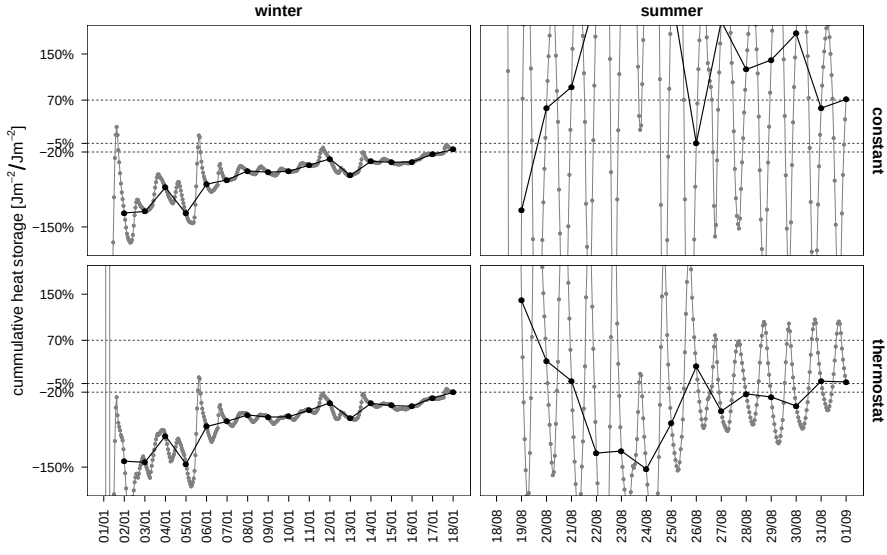

(b)

Figure 2.9: The net heat that is stored in the wall over the past period as such (a) and as a percentage of the total amount of heat that went through the wall in that period (b). Results computed after every hour are represented in grey while results computed after every 24 hours are represented in black.

the measured heat flux at each consecutive data reading t_k.

$$\sum_{t_k=1}^{n} q_{t_k} - \frac{(F_i \delta T_i + F_e \delta T_e)}{\Delta t} \tag{2.2}$$

with F_i and F_e the interior and exterior thermal mass factors, δT_i the difference between the interior temperature averaged over the 24h prior to reading t_k and the interior temperature averaged over the first 24h of the analysis period (K), δT_e the difference between the exterior temperature averaged over the 24h prior to reading t_k and the exterior temperature averaged over the first 24h of the analysis period (K) and Δt the time interval between two readings (s).

For a building component with total thermal resistance R and consisting of M layers, numbered from m=1 to m=M with layer 1 at the interior side of the component, the thermal mass factors F_i and F_e are calculated as

$$F_i = \sum_{m=1}^{M} F_{im} = \sum_{m=1}^{M} C_m \left[\frac{R_{em}}{R} + \frac{R_m^2}{3R^2} - \frac{R_{im} R_{em}}{R^2} \right] \tag{2.3}$$

$$F_e = \sum_{m=1}^{M} F_{em} = \sum_{m=1}^{M} C_m \left[\frac{R_m}{R} \left\{ \frac{1}{6} + \frac{R_{im} + R_{em}}{3R} \right\} + \frac{R_{im} R_{em}}{R^2} \right] \tag{2.4}$$

with (2.5)

$$R_{im} = \sum_{j=1}^{m-1} R_j \tag{2.6}$$

$$R_{em} = \sum_{j=m+1}^{M} R_j \tag{2.7}$$

(2.8)

Hereby R_m $[m^2 K W^{-1}]$ and C_m $[J m^{-2} K^{-1}]$ are the thermal resistances and capacitances, respectively, of each separate layer m. A theoretical background for the derivation of the thermal mass factors can be found in [33].

It should be noted that, although the proposed correction is a meaningful approach to reckon with the thermal mass effects of building components, the application requires foreknowledge about the structure of the building component: the number of layers needs to be known and a good approximation of their thermal properties is required. Given that, the correction for storage effects might be useful for the analysis of known structures, but might be practically inefficient for the analysis of unknown structures.

The efficiency of the *corrected* average method is illustrated by its application on the measurement data of the cavity wall case. The thermal resistance is estimated from the same data considered in the study of the average method in the previous section. The calculation of the storage factors can be found in appendix B. Figure 2.10 shows the results for the selected scenarios and data periods. To enable a comparison, the results from the average method without correction are included after every 24 hours of obtained measurements.

Figure 2.10 shows that the overestimation of the thermal resistance in winter is neutralised by the application of the correction for thermal mass. It can be seen that very robust results are obtained after five days of measurements. Also in summer the results improved, i.e. the curve is shifted towards the goal value. Nevertheless, the consecutively obtained R-estimates still show a rather unstable course, meaning that the continuously heating up and cooling down of the wall still hinders a robust R-estimation.

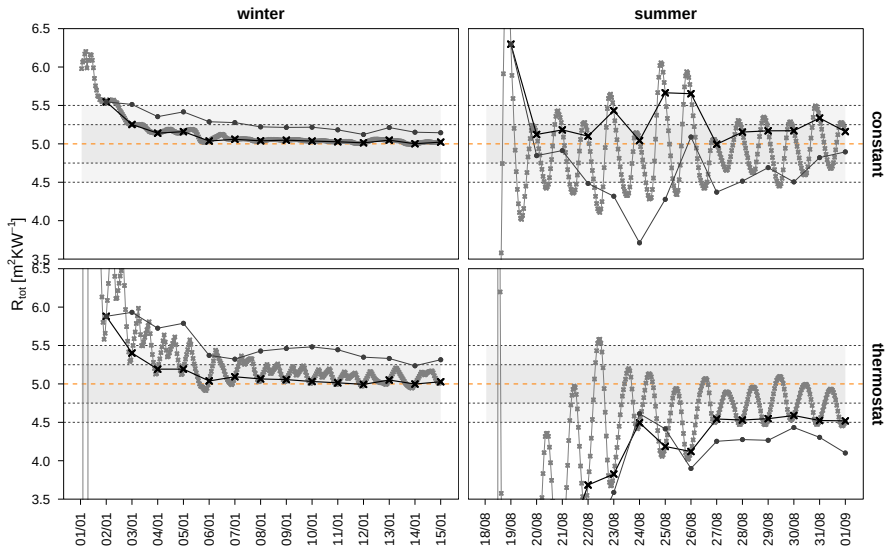

Figure 2.10: The R-estimates obtained by the average method (•) and corrected for storage effects (×) after every hour of obtained data (grey) and after every 24 hours of obtained data (black). The orange dotted line indicates the reference value and the grey dotted lines indicate the 5% and 10% accuracy bands.

It must be said that the demonstrated efficiency of the applied correction is optimal, since the internal structure of the considered wall and its properties are exactly known for the considered building component. To examine how the accuracy of the used thermal properties affect the correction's results, the application of the corrected method is repeated, only, this time with ± 5%, ± 10% and ± 20% deviating thermal properties (thermal conductivity, density and specific heat). Figure 2.11 shows the results. For all tested cases, it can be seen that mistakes up to 20% of the assumed thermal properties diminishes the correction's efficiency, however, only slightly. The results are still better than when no correction is applied. However, the assumed foreknowledge is still large: the composition of the wall and the location of the capacitive insulating elements is still assumed to be known. If a case is considered where the assumed wall composition switches the insulation layer with the outdoor brick layer for the calculation of the thermal mass factors, then the correction does no longer improve the results. This can be seen from figure 2.11, which also includes this test case.

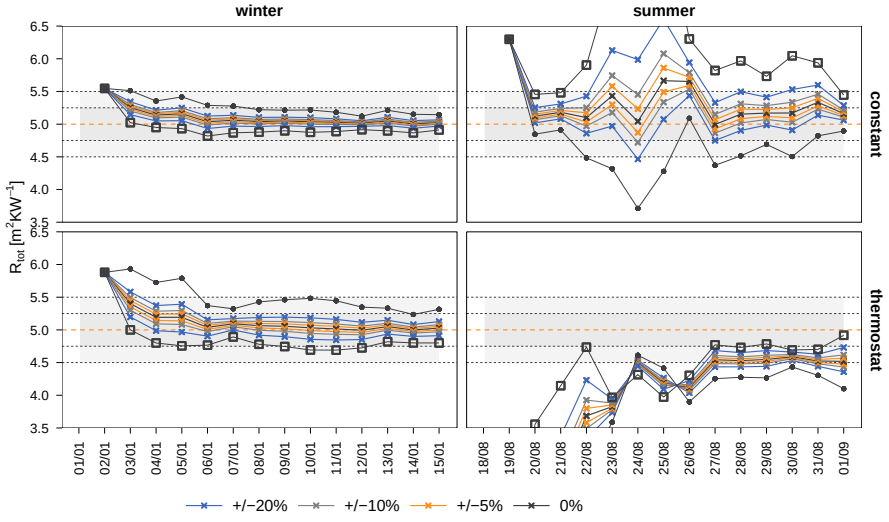

Figure 2.11: The R-estimates obtained by the average method corrected for storage effects (×) with ± 5%, ± 10% and ± 20% deviating thermal properties (thermal conductivity, density and specific heat). The data points indicated by □ represent the R-estimates for a correction assuming an incorrect order of the different thermal layers. Data points indicated by • repeat the estimation results of the average method without correction.

2.2.3 Simple linear regression

Based on the stationary energy balance that was at the origin of the average method, a linear regression model can be formulated. Such a model describes the heat flux through the building component as a linear function of the temperature difference over the component. The slope of the regression line is then the inverse of the thermal resistance. Because of the common basic assumptions, regression models struggle with the same difficulties as the average method, i.e. difficulties provoked by the thermal mass of the building component. Therefore, analogously to the average method, averaged data points are used in the regression analysis. The averaging is performed by taking the arithmetic mean of the measurements in the non-overlapping intervals that correspond to the new sampling time. For the averaged measurement readings at t_k the simple linear regression model is formulated as

$$\bar{q}_{t_k} = \frac{1}{R}(\bar{T}_{si,t_k} - \bar{T}_{se,t_k}) + \epsilon_{t_k} \tag{2.9}$$

with $\bar{q}_{t_k}$ the heat flux, $\bar{T}_{si,t_k}$ the internal surface temperature, $\bar{T}_{se,t_k}$ the external surface temperature and ϵ_{t_k} the residual between the measured and modelled heat flux which is minimised by the regression analysis. Note that the overbar $\bar{}$ indicates averaged values. Since no constant parameter is included in the equation, the regression line is forced through the origin. Typically, the goodness of fit of a linear regression model is assessed by its R-squared value R^2. This quantity is a statistical measure of how close the data are to the fitted regression line. However, in case of a regression line that is forced through the origin, the R^2-value is no reliable indicator of goodness of fit [59] and an interpretation of this value should be avoided. Next to that, however, the regression analysis supplies a standard deviation for the estimated regression coefficient. The standard deviation estimated for the coefficient $\frac{1}{R}$, is denoted $\sigma_{R^{-1}}$. Since the parameter of interest, i.e. the thermal resistance R, is the inverse of the regression coefficient, its standard deviation, denoted by σ_R is calculated based on the rule that $\frac{\sigma_R}{R} = \frac{\sigma_{R^{-1}}}{R^{-1}}$. σ_R then provides an indication for the estimated resistance's accuracy.

The method's primary setting is the averaging period, which must be well chosen in order to obtain reliable R-estimates. According to [60], the optimal averaging period depends on the boundary conditions and on the thermal properties of the studied building component and must hence be determined by trial-and-error. In general, large sampling periods reduce the available number of data points for the regression, whereas short sampling periods risk to retain too much of the transient influences in the data.

The method's application is illustrated for the case study of the cavity wall. Figure 2.12 shows the regression data and the estimated regression line for the 14 days of winter and summer measurements in both scenarios. The regression is performed for hourly, daily, 3-daily and 5-daily averaged data. As can be seen, the hourly averaged data are widespread, especially for the second scenario. From daily averaged data on, the data points are more aggregated so that a more robust regression line can be drawn. Note that in winter, the regression benefits from being forced through the origin. By doing so, the range of present temperature differences is widened. In summer, this is also the case in the second scenario, where, without the addition of the origin, the regression line would have a negative slope. The first scenario in summer does not profit from the addition of the origin, since its data points already lie closely around this point.

The R-values, estimated gradually with increasing measurement length, are represented in figure 2.13. The results are very similar to those obtained by the average method. In winter, a good convergence of the estimates is seen, although, the asymptotic value overestimates the reference value. As was explained before, this results from an outdoor air temperature drop throughout the entire measuring period. In summer, unreliable estimation results are obtained. All the more, because the final estimates including 14 days of measurements, depend on the chosen averaging period. The estimations resulting from the hourly averaged data even lie outside the boundaries of the figure. The poor quality of the summer results are reflected in the large 95% confidence bounds which are included in figure 2.13 and which are calculated as two times the estimated standard deviation resulting from the regression analysis. In winter, the 95% confidence bounds indicate accurate estimation results, especially in the first scenario. Nevertheless, in a lot of cases the confidence levels do not contain the reference value. Hence, although the estimated standard deviation identifies reliable R-estimates, they are no absolute proof of the correctness of the R-estimates. This has to do with the fact that the retrieved standard deviation evaluates the goodness of fit of the model, rather than its physical significance. Or, more specifically, the model performance is assessed based on the deviations between the observed and *estimated* model output, rather than that it is assessed based on the deviations between the observed and *real* (unknown) output. This distinction is often referred to as the difference between variance errors and mean square errors (or bias errors when the variance errors are assumed zero).

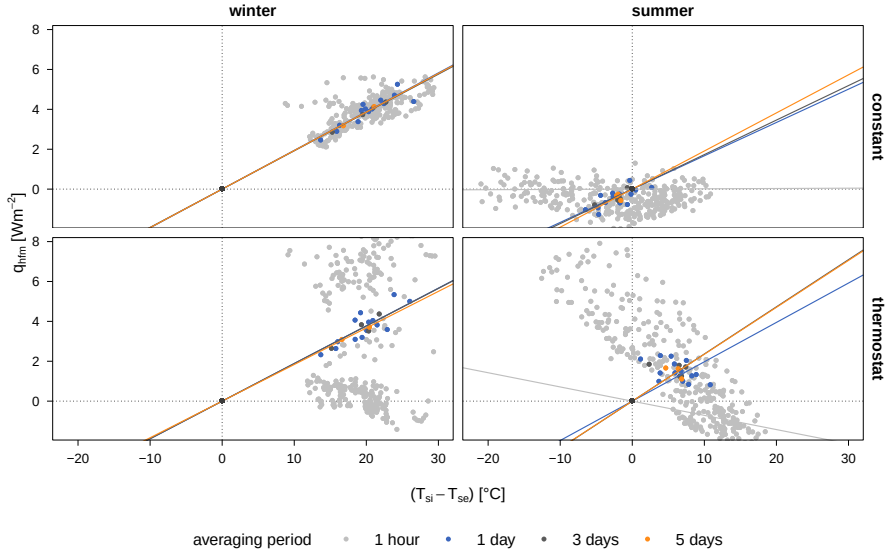

Figure 2.12: Regression line fitted to the regression data of the 14 day periods in winter and summer and for both scenarios. Averaging periods of 1 hour, 1 day, 3 days and 5 days are considered.

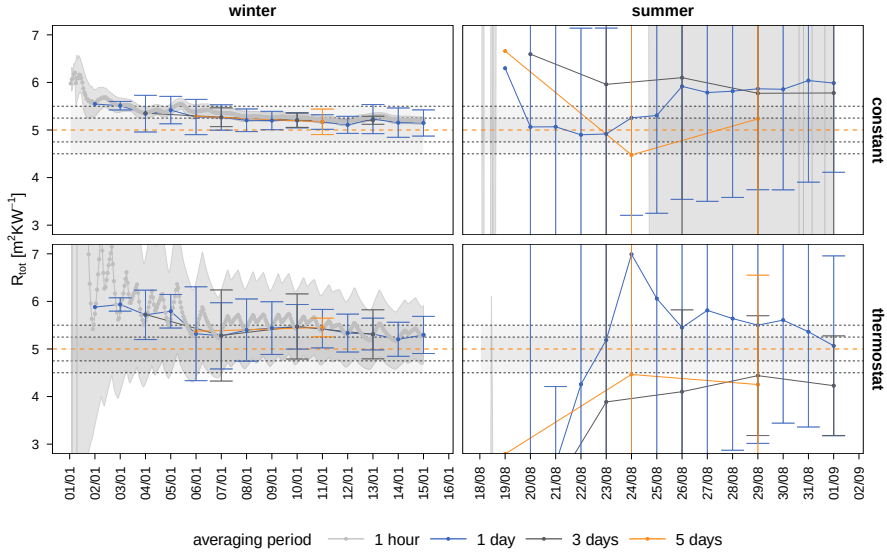

Figure 2.13: The R-estimates obtained by simple linear regression method for averaging periods of 1 hour, 1 day, 3 days and 5 days. The orange dotted line indicates the reference value and the grey dotted lines indicate the 5% and 10% accuracy bands.

2.3 **Dynamic methods**

2.3.1 Anderlind's regression model

In the context of on-site thermal characterisation, one of the first dynamic methods to analyse heat flux and temperature measurements was proposed by e.g. Aittomäki [14], Kupke [19], Roulet et al. [25] and Ahvenainen et al. [13]. This method is also adopted in Annex B of ISO 9869. The proposed technique models the varying heat flux measurements as a function of the temperature difference over the building component and of internal and external surface temperature changes occurring in the past. The latter are lumped together by using a limited number of time constants [57]. Consequently, by means of multiple linear regression, weighting factors are deduced that scale these explanatory variables to match the response variable, i.e. the measured heat flux. The estimated regression coefficient that corresponds to the momentary temperature difference over the building element then contains information on the thermal conductance, or, on the inverse thermal resistance.

A very similar, but more direct approach of this method is developed by Anderlind [15, 34] and is further examined in this dissertation. Anderlind's method similarly assigns the variations in the heat flux measurements to temperature differences over the building element and to temperature changes at the surfaces occurring in the past. These surface temperature changes are, however, not longer lumped together, but are seen as individual explanatory variables. This implies that more regression coefficients are involved, but it also implies that the trial-and-error estimation of (the number of) time constants can be dropped. The increased number of regression parameters is not necessarily a computational drawback since a regression analysis must be applied anyway [15].

Basically, Anderlind's regression equation can be formulated as follows

$$q_{t_k} = \frac{1}{R}(T_{si,t_k} - T_{se,t_k}) + \sum_{j=k-p}^{k-1} \alpha_j (T_{si,j+1} - T_{si,j}) + \sum_{j=k-p}^{k-1} \beta_j (T_{se,j+1} - T_{se,j}) + \epsilon_{t_k} \tag{2.10}$$

with T_{si} the interior surface temperature, T_{se} the exterior surface temperature and $\frac{1}{R}$, α_j and β_j the coefficients which are estimated by means of multiple linear regression and ϵ_{t_k} the residual between the measured and modelled heat flux. The number of *historical* data points that is reckoned with in the analysis is indicated by the number p. The total time that is covered by these past data points is denoted as the *influence time*.

Since these historical data points must be known for the regression and must hence be measured, the actual regression itself can only be established for the measurements after the p first data points, i.e. for the readings $t_k = p + 1, ..., N$, with N the total number of readings.

Although at first sight, the model appears to be a rather black box approach, it is, in essence, purely based on the physical behaviour of building components subjected to varying boundary conditions. The model defines the variations in heat flux as the responses to step temperature changes at the internal and external surfaces of the building component. Basically, under the assumption that the thermal material properties are independent of temperature, the method relies on the superposition principle and hence, describes the variation in heat flux at a given time t_k as the sum of the responses to all previous temperature changes at times $t_{k-p}, ..., t_{k-1}$. Hence, the regression coefficients α_j and β_j are weighting factors that embody these response functions to historical step temperature changes. This transient behaviour, included in the second and third part of equation 2.10, is then combined with the stationary behaviour of the building component, i.e. the first term of equation 2.10. A full physical derivation of Anderlind's model can be found in [34].

Basically, Anderlind's approach relies on the fact that the transient part of the model covers the variations in the heat flux measurements, so that the steady-state behaviour of the wall can be isolated in the stationary part. In this way, the estimated regression coefficient of the momentary temperature differences can be interpreted as the thermal conductance, or the inverse of the thermal resistance. Note that the model assumes a zero intercept and that, in that case, R^2-values are no reliable indicators of goodness of fit [59]. Also, a standard deviation of the estimated conductance can be derived from the multiple linear regression calculations, indicating the accuracy of the estimated parameter. However, also this value is no absolute proof for a physically correct estimate because it evaluates the parameter's fit rather than its physical interpretation.

Application of Anderlind's regression model is very straight-forward. The most important choice that has to be made is how far the method will look back in time. Or, in other words, how many temperature differences from the past will be included in the model. No clear indication for an optimal duration of this influence time is found in literature. In all probability, the optimal duration depends on the studied building component, since every component differs in thermal mass. Furthermore, the optimal influence time will depend on the length of the measurements and on the sampling time. Since historical data points can not be used in the actual fitting process, the choice of the sampling period and influence time must balance between including a sufficient amount of information from the past and including a sufficient amount of information from the present [34].

To illustrate this, Anderlind's model is fitted on the winter and summer measurements of both scenarios of the cavity wall introduced in section 2.1. Figure 2.14 summarises the results for both data periods and both scenarios. Again, the results are calculated gradually with increasing measurement time and are represented as such. The results for the two data periods are ordered column wise and the results for the different scenarios are distinguished from one another by a different colour. For the application of Anderlind's approach, 6 different durations of the influence time are chosen: p = 3 hours, 6 hours, 12 hours, 1 day, 2 days and 3 days. Since hourly sampled data is used, this implies that 3, 6, 12, 24, 48 and 72 historical data points, respectively, are included in the regression model. The results are ordered row wise with increasing influence time. The model was also fitted to data with different sampling times. However, the results were very similar, so only the application on hourly averaged data is represented.

Several things stand out from figure 2.14. First, as opposed to the results of the semi-stationary methods, it is seen that Anderlind's model enables a robust R-estimation from summer measurements (on the condition that an appropriate influence time is selected). Secondly, it is seen that the results from the first scenario (constant) converge faster to the reference value than the results from the second scenario (thermostat). Thus, increased dynamics at the interior surface complicate the R-estimation, but nevertheless, do not hinder a robust R-estimation when sufficient measurements are considered. Next, it is observed that a minimal influence time of 24 hours (p = 1 day) is recommended in order to obtain reliable results. The results for an influence time of 3 and 6 hours clearly show that the R-estimates in summer are erroneous and that the R-estimates in winter are overestimated, although they do converge rather smoothly. An influence time of 12 hours also shows good convergence and leads to accurate R-estimates in winter, but to slightly overestimated R-estimates in summer. Since an influence time of 24 hours leads to a smooth convergence to the real R-value for both winter and summer measurements, this influence time is preferred. Given the diurnal cycle of the perturbation signals, this is also a logical choice from a physical point of view. Nevertheless, as was mentioned previously, the optimal influence time is in all probability case dependent, since every component differs in thermal properties, creating a different phase shifting between signals transferred from one side to the other. Furthermore, figure 2.14 demonstrates that the longer the influence time, the more data points are required for the R-estimates to reach convergence. This results, on the one hand, from the fact that less data points are left over for the actual fitting procedure. So, for the considered data set of 14 days, an influence time of 3 days only permits the first R-estimate to be calculated at the first hour of day 4 of the measurements. But even then, when only the number of days that are included in the actual regression analysis are considered, it is seen that more data is required for

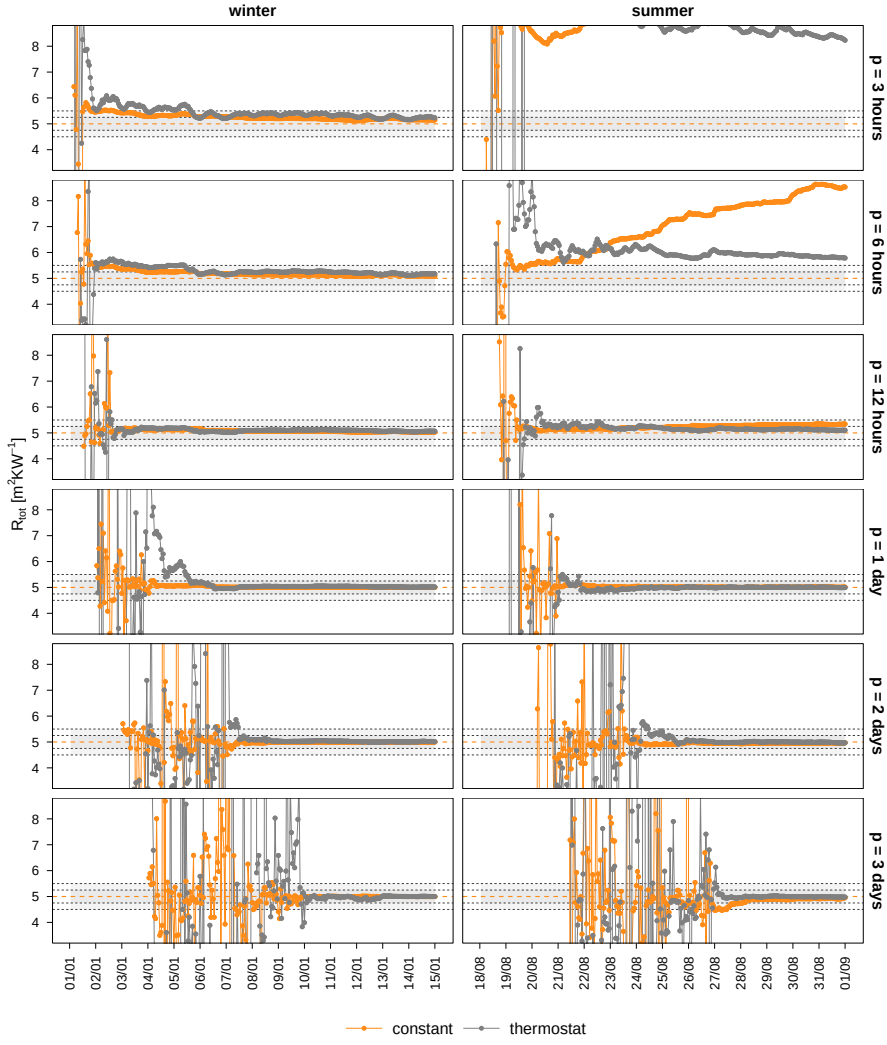

Figure 2.14: The R-estimates obtained by Anderlind's model and computed after every obtained hour of measurements. The results for the different data periods are ordered column wise, while the results for the different influence times p are ordered row wise. The results from the two scenarios are distinguished by a different color.

longer influence times before convergence is reached. This results from the fact that a longer influence time implies more explanatory variables and that, as such, more data points are needed to reliably weight their regression coefficients. In this respect, the recommended minimal influence time of 24 hours is also the maximal one, since an increase in influence time does not improve the estimation result, but does require longer data sets before a robust R-estimate is obtained.

A last thing to examine, is the estimated accuracy of the estimation results. Figure 2.15 selects some of the studied cases and represents their estimation results accompanied by their 95% confidence intervals. The latter are calculated as two times the estimated standard deviation resulting from the multiple linear regression. The figure shows that the large fluctuations occurring in the R-estimates from shorter measurement periods are not accompanied by a standard deviation. This is due to the fact that these measurement periods do not contain enough data points to calculate the regression's covariance matrix. However, next to that, the figure shows that the estimated standard deviations of the results with an influence time of 1 day show the highest accuracies. This counts again in the favour of selecting the influence time of 1 day as the optimal one. Besides that, the summer results for an influence time of 6 hours indicate that the standard deviations can not always be interpreted as the interval in which the true physical R-value lies. As was explained previously, this results from the fact that the variance errors of the model are assessed rather than the mean square errors.

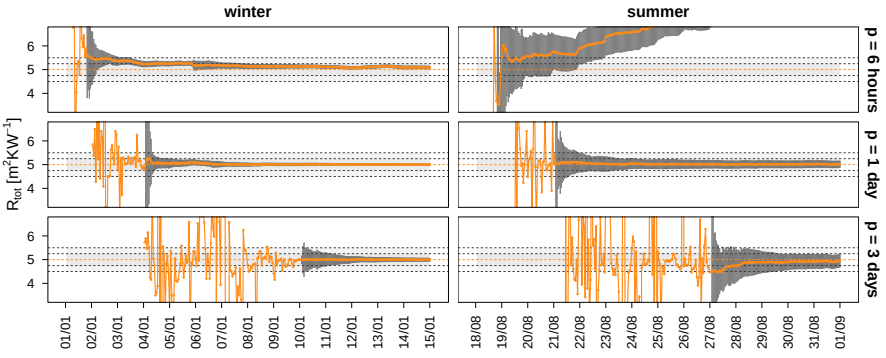

Figure 2.15: The R-estimates (orange) and their estimated accuracy (grey) obtained by Anderlind's approach and computed after every obtained hour of measurements. The results for the different data periods are ordered column wise, while the results for the different influence times p are ordered row wise. The results of the first scenario only are represented.

2.3.2 ARX-modelling

The models formulated thus far all relied on physical principles. When this prior knowledge is left aside, general statistical input-output models can be formulated. This class of models is often referred to as *external* models since they mainly give information on the external relations between the in- and output and not on the internal mechanisms linking them.

Generally, statistical input-output models are formulated in discrete time and can be represented by

$$\boldsymbol{y}_{t_k} = \frac{B(B)}{A_1(B)}\boldsymbol{u}_{t_k} + \frac{C(B)}{A_2(B)}\boldsymbol{\epsilon}_{t_k} \tag{2.11}$$

with $\boldsymbol{y}_{t_k}$ and $\boldsymbol{u}_{t_k}$ the measured outputs and inputs respectively and with $B(B)$, $C(B)$, $A_1(B)$ and $A_2(B)$ the transfer functions' polynomial components containing the backshift operator B. $\{\boldsymbol{\epsilon}_{t_k}\}$ represents white noise errors.

To model the heat dynamics of building components, typically a special case of this general model is considered [18, 21, 39], namely Auto-Regressive models with eXogenous inputs, or abbreviated, ARX-models. They are obtained from the general model in equation 2.11 by assuming that $A_1(B) = A_2(B) = A(B)$ and that $C(B) = 1$.

$$A(B)\boldsymbol{y}_{t_k} = B(B)\boldsymbol{u}_{t_k} + \boldsymbol{\epsilon}_{t_k} \tag{2.12}$$

For the estimation of the thermal resistance from on-site measurements, the ARX-models in this work consider the heat flux q_{t_k} as sole output and the surface temperatures T_{si,t_k} and T_{se,t_k} as inputs. Such Multiple Input Single Output (MISO) ARX-models are represented by

$$Q(B)q_{t_k} = \omega_{si}(B)T_{si,t_k} + \omega_{se}(B)T_{se,t_k} + \epsilon_{t_k} \tag{2.13}$$

with

$$Q(B) = 1 + Q_1B^1 + ... + Q_{nq}B^{nq} \tag{2.14}$$

$$\omega_{si}(B) = \omega_{si,0} + \omega_{si,1}B^1 + ... + \omega_{si,ni}B^{ni} \tag{2.15}$$

$$\omega_{se}(B) = \omega_{se,0} + \omega_{se,1}B^1 + ... + \omega_{se,ne}B^{ne} \tag{2.16}$$

Hereby, ϵ_{t_k} is the simulation error. $Q(B)$ is the output polynomial and $\omega_{si}(B)$ and $\omega_{se}(B)$ are the input polynomials. Each of the latter is characterised by its order: nq for the output polynomial and ni and ne for the input polynomials $\omega_{si}(B)$ and $\omega_{se}(B)$ respectively. The orders basically indicate how many data points from the

past are involved in the description of the heat flux at reading t_k. Note that implicit ARX-models are considered.

Least squares estimation is typically used to determine the parameters of ARX-models. Given the model structure, this basically comes down to applying a multiple linear regression. For example, the first order ARX-model ($nq = ni = ne = 1$) formulated as

$$\begin{aligned} q_{t_k} = &- Q_1 q_{t_{k-1}} + \omega_{si,0} T_{si,t_k} + \omega_{si,1} T_{si,t_{k-1}} \\ &+ \omega_{se,0} T_{se,t_k} + \omega_{se,1} T_{se,t_{k-1}} + \epsilon_{t_k} \end{aligned} \tag{2.17}$$

can be seen as a multiple linear regression model with dependent variable q_{t_k} and with the regressors $q_{t_{k-1}}$, T_{si,t_k}, $T_{si,t_{k-1}}$, T_{se,t_k} and $T_{se,t_{k-1}}$. Since the value of q_{t_k} relates on previous measurements of its own, i.e. $q_{t_{k-1,\ldots,k-nq}}$, ARX-estimates are said to be determined in a one-step ahead prediction setting. Note furthermore, that the estimation relies on historical data points so that the regression itself is limited to the measurements at time steps $k = p+1, ..., N$ with p the maximal polynomial order and N the total number of measurements.

As mentioned before, the model parameters are basically scaling factors that adjust the model output to the measured output [35]. They do not necessarily have a direct physical meaning. Nevertheless, ARX-models are able to estimate the thermal resistance R from measurement data since their static gain reveals information on the stationary behaviour of the observed building component. The gain of an ARX-model can be obtained by setting the back shift operator to 1 [18, 39, 40]. By comparing equation 2.13 for $B = 1$ to the general equation for steady state heat transfer

$$q = \frac{1}{R}(T_{si} - T_{se}) \tag{2.18}$$

two stationary parameters can be distilled: one thermal resistance R_i related to the indoor surface temperature T_{si} and one thermal resistance R_e related to the outdoor surface temperature T_{se}.

$$\frac{1}{R_i} = \frac{\omega_{si}(1)}{Q(1)} \quad ; \quad \frac{1}{R_e} = \frac{-\omega_{se}(1)}{Q(1)} \tag{2.19}$$

Based on a minimum variance weighting, these two estimates can be combined into one estimate of the total thermal resistance [18, 39, 40]

$$\frac{1}{R_{tot}} = \frac{\lambda}{R_i} + \frac{(1-\lambda)}{R_e} \tag{2.20}$$

with λ the value that minimizes the variance of $\frac{1}{R_{tot}}$.

The estimation result is accompanied by a standard deviation giving information on the accuracy of the estimated parameter $\frac{1}{R_{tot}}$. The standard deviation of R, denoted σ_R is then calculated based on the rule that $\frac{\sigma_R}{R} = \frac{\sigma_{R^{-1}}}{R^{-1}}$. Aside the estimation of the thermal resistance, ARX-models also enable the estimation of the time constants of the considered dynamic system. More information about this can be found in [39].

The use of ARX-modelling requires two choices: (1) a proper selection of the polynomial orders and (2) a selection of a feasible averaging time. Both choices must be made in function of the use of the model. In the case of thermal resistance characterisation, the focus is entirely on estimating a stationary parameter. Hence, the higher frequency spectrum corresponding to faster dynamics is of minor importance. Therefore, averaging the measurement data, which corresponds to removing high frequency content, is advised [39].

Before discussing the application of ARX-models, a parallel should be drawn between Anderlind's model and an ARX-model. In essence, Anderlind's model is a specific case of the general ARX-model formulated in this section. For the restrictions that $nq = 0$ and that $ni = ne = p$, the ARX-model of equation 2.13 boils down to the model of Anderlind in equation 2.10. A further comparison of the models' regression coefficients would lead to the equality $\frac{1}{R} = \omega_{si}(1) = -\omega_{se}(1)$, which is very similar to the expressions in equation 2.19. So, although generally ARX-models are seen as black-box models, it is always possible that certain (reduced) formulations relate directly to physics. In those cases, the ARX-formulation can be seen as grey-box. Hence, Anderlind's model could just as well be called a grey-box ARX-model. In this dissertation, however, ARX-modelling is mostly used to indicate the general modelling approach described in this section.

As for the previously discussed characterisation methods, the application of ARX-modelling is demonstrated for the simulated data of the cavity wall. The ARX-models are estimated for different averaging periods of the measurement data: 30 minutely, hourly, 2 hourly, 3 hourly, 4 hourly and 6 hourly averaged data is regarded. Also different influence times are regarded, notably p = 3 hours, 6 hours, 12 hours, 1 day, 2 days and 3 days. Figures 2.16 and 2.17 represent the gradually calculated thermal resistances for the first (constant) and second (thermostat) scenario respectively. The results for the different averaging periods are represented by a different colour while the results for the different influence times p are ordered row wise.

Based on figures 2.16 and 2.17, the following observations are made. First, it is seen that the impact of the different averaging periods on the results is rather limited. In some cases, especially in the second scenario, the estimates from the 30 minutely

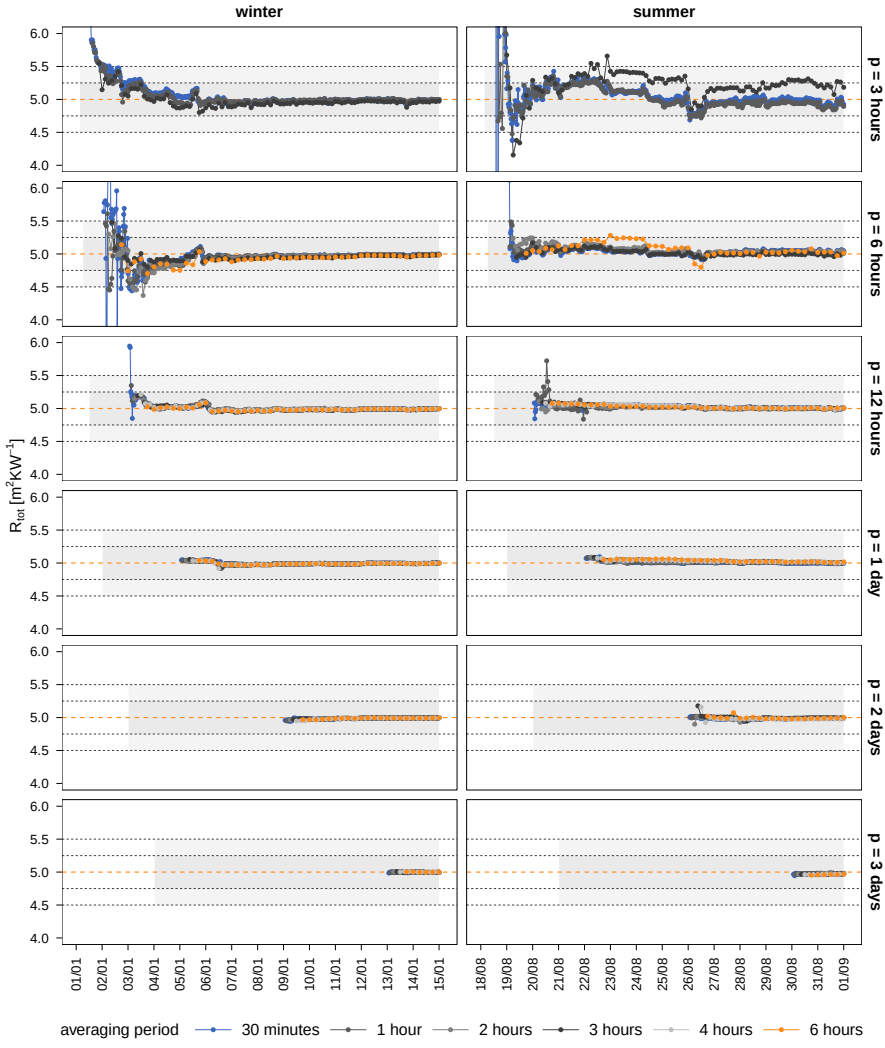

Figure 2.16: The R-estimates obtained by ARX-modeling and computed after every obtained hour of measurements of the first scenario (constant). The results for the different data periods are ordered column wise, while the results for the different influence times p are ordered row wise. The results for different averaging periods are distinguished by a different color.

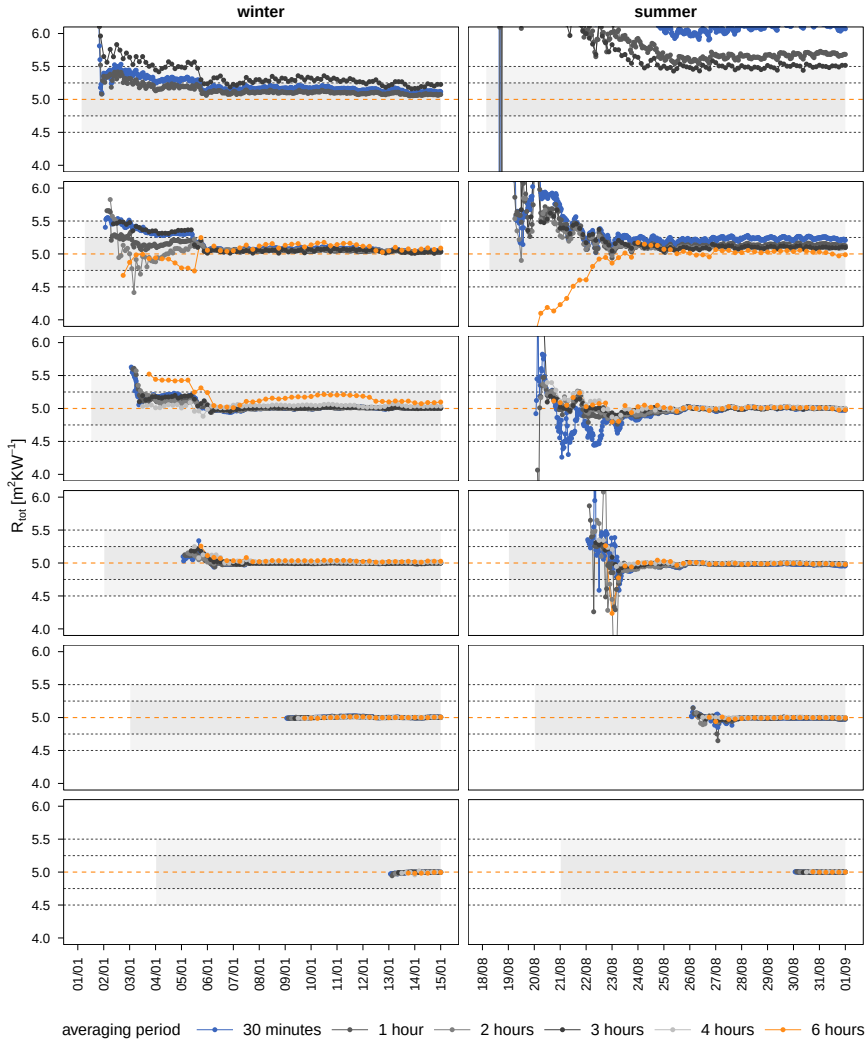

Figure 2.17: The R-estimates obtained by ARX-modeling and computed after every obtained hour of measurements of the second scenario (thermostat). The results for the different data periods are ordered column wise, while the results for the different influence times p are ordered row wise. The results for different averaging periods are distinguished by a different color.

and 6 hourly averaged data behave in a less robust way than the estimates from the other averaged data. Nevertheless, averaging periods from 1 to 4 hours lead to equally robust estimation results so that no preference is given to a specific averaging period. Furthermore, the main observations about ARX-modelling coincide with the remarks made for Anderlind-modelling. More specifically, for ARX-modelling it also applies that short influence times risk to converge to erroneous R-estimates, especially in the second scenario, while influence times from at least 1 day lead to robust R-estimates. Next to that, also for ARX-modelling it is seen that longer influence times require more measurement data before the estimation can be computed and before convergence to the reference value is reached. It is also noticed that the measurements of the first scenario are characterised by a faster convergence to the reference value than the results of the second scenario. Finally, as was seen for Anderlind-modelling, also ARX-modelling enables a robust R-estimation from summer measurements, which was not the case for the studied semi-stationary methods.

Somewhat different from Anderlind's approach, is the estimation of the standard deviation of the estimation results. Although in both cases the noise models are derived from the multiple linear regression analysis, ARX-noise models are more extensively described: its residuals at time t_k depend on historical values of the observed output itself, here the observed heat flux q_{hfm}. Figure 2.18 represents the 95% confidence intervals, i.e. $\pm$ two times the estimated standard deviation, along with the estimation results from the hourly averaged data of the second scenario. At first sight, the confidence bounds accurately assess the physical reliability of the R-estimates. Although, randomly, for some estimates very large confidence intervals are seen whereas the corresponding R-estimates seems robustly estimated. Furthermore, in some cases the confidence intervals do not include the reference value. So, similar to Anderlind's approach and despite the slightly more advanced noise model, the confidence intervals may not be interpreted as absolute bounds for the correct physical R-value. Again this has to do with the fact that the estimated standard deviations of regression models are assessing the model's variance errors rather than its mean square errors.

ARX-models are typically further validated by using statistical tools [39]. For example, the residuals are often tested for being white noise. Since a good model *perfectly* explains the measured heat flux, the remaining residuals should constitute a completely random time series. This can be assessed in the time domain by looking at the autocorrelation function (ACF) of the residuals and in the frequency domain by looking at their cumulated periodogram (CP) [39]. The latter is used to validate some of the fitted ARX-models. A periodogram is calculated as described in [61] and essentially describes the variation of a signal in the frequency domain. For a white

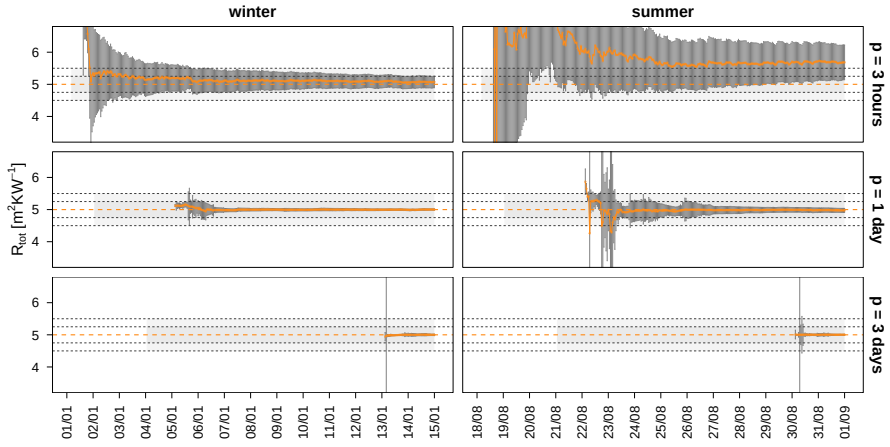

Figure 2.18: The R-estimates and their estimated accuracy obtained by ARX-modelling and computed after every obtained hour of measurements. The results for the different data periods are ordered column wise, while the results for the different influence times p are ordered row wise. The results of the second scenario only are represented.

noise signal, the variation should be uniformly distributed on all frequencies. Or, the cumulated periodogram should increase linearly. If this is not the case, periodicities are still hidden in the noise signal as a result of an inadequate model description of the observed variable(s). Confidence intervals for the cumulated periodogram can be calculated (see [61]). Figure 2.19 depicts the cumulated periodograms for the ARX-models fitted on the entire winter and summer periods with influence times of 3 hours and 1 day and for an averaging period of 1 hour. Both scenarios are regarded. The figure shows that the erroneously estimated R-values resulting from data of the second scenario for a 3 hour influence time are not identified by the periodograms since all considered cases show a linear behaviour indicating white noise. Hence, the erroneous estimation results do not originate from a bad model fit (all variations in heat flux are well explained) but originates from the small sampling time which must conceal part of the stationary behaviour due to the one-step-ahead prediction estimation setting.

Thus far, a fixed model order has been assumed for the input and output polynomials of the estimated ARX-models. For the considered cases, the assumed model order or, equivalently, the assumed influence time, was assessed by comparing the models' estimation results with the reference value. In reality, however, the goal value is not

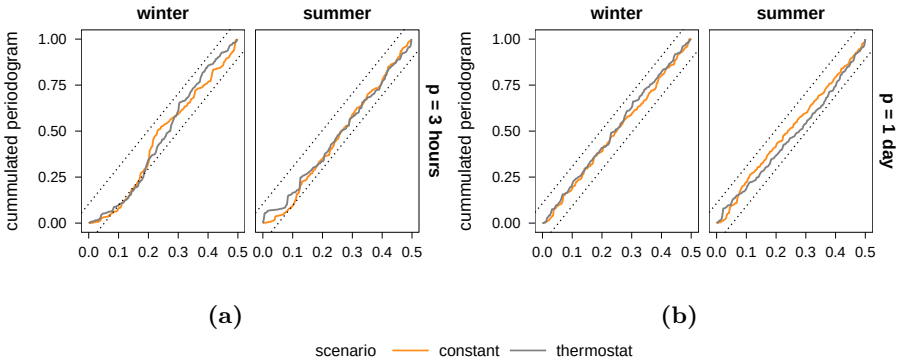

Figure 2.19: The cumulated periodograms of the residuals from the ARX-models fitted on the hourly averaged winter and summer measurements of both scenarios. Influence times of p = 3 hours (a) and p = 1 day (b) are regarded.

known so that the model order selection must rely on other evaluation criteria. In time series analysis, different approaches exist for an automatic model order selection: some of them are based on assessing the overall model performance, using for example the Akaike Information Criterion (AIC) further described in section 3.1.3, or, others are based on significance testing of the individual regression coefficients. All approaches, however, rely on fitting and comparing possible model formulations. Practically, a model with a maximum polynomial order p, has the following possible regressors in its formulation: $T_{si,t_{k=0,1,\ldots,p}}$, $T_{se,t_{k=0,1,\ldots,p}}$ and $q_{hfm,t_{k=1,\ldots,p}}$. An exhaustive selection procedure would estimate all possible regressor combinations and successively identify the optimal formulation based on the chosen criteria. However, the set of combinations to evaluate quickly becomes very large, as such limiting this approach's applicability. Therefore, most selection procedures adopt a stepwise order selection. A forward selection, for example starts from a minimal model formulation, tests the addition of every possible variable using a chosen evaluation criteria and then adds the variable that improves the model the most. This process is repeated until no further improvement is found. Analogously, a backward selection starts from a maximal model, tests the deletion of every variable and consequently deletes the variable that improves the model the most by being deleted. This process is also repeated until no further improvement is found.

It must be noted that literature on model order selection in general is exhaustive. Nevertheless, in the specific context of building component characterisation by ARX-modelling, little has been written. Since the method is considered as an established method, this topic is not largely examined in this dissertation. Only one intuitive

approach is tested for the measurement data of the cavity wall. The considered selection method starts with a full model of order p for all polynomials, $na = ne = ni = p$. It then gradually decreases p, until the highest autoregressive coefficient (the coefficient of the most lagged q_{hfm}-regressor) proves significant by t-testing. Probably, much theoretical arguments can be found to criticise this approach. Nevertheless, it is a simple and intuitive way of reducing the number of regression coefficients that have to be estimated.

The results of this approach are represented in figure 2.20. The ARX-models resulting from the automatic order selection are denoted *reduced* since the models have a reduced order compared to the models with a fixed order. The main difference between both approaches is the fact that less measurement data is required for the reduced ARX-models before an estimation is possible. Furthermore, it is seen that the reduced order models lead to erroneous results (lying outside the boundaries of the figure) in some cases in summer.

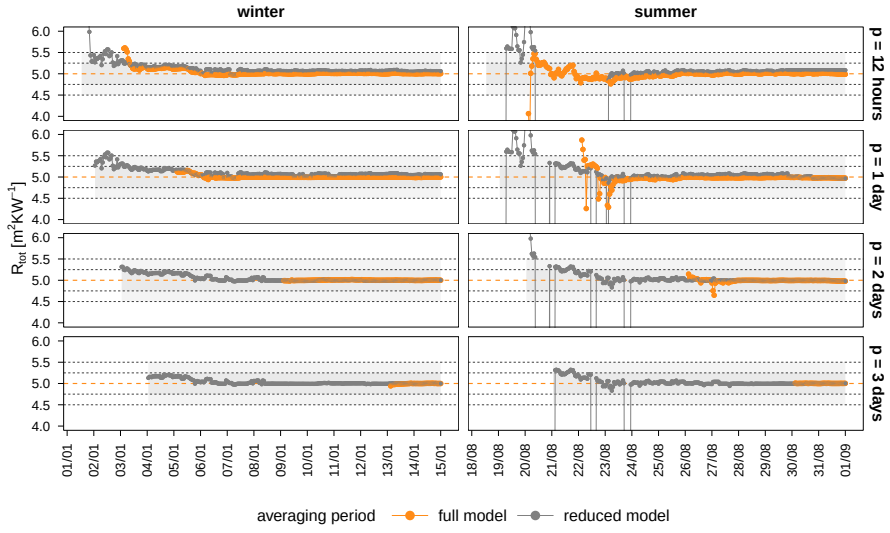

Figure 2.20: The R-estimates obtained by ARX-modeling and computed after every obtained hour of measurements of the second scenario (thermostat). The results for the different data periods are ordered column wise, while the results for the different influence times p are ordered row wise. The R-estimates shown in orange are obtained from ARX-models with a fixed maximum order p. The R-estimates shown in grey are obtained by a backward stepwise order selection starting from a maximum order p.

2.4 Conclusion

The present chapter explored the potentials and limitations of different established characterisation methods developed over the past decades. A distinction was made between semi-stationary and dynamic analysis methods. The former methods, notably the average method with or without a correction for storage effects and the simple linear regression method, originate from the steady state definition of the thermal resistance. They cope with the dynamic boundary conditions by averaging the measured data. By contrast, the dynamic analysis methods, i.e. Anderlind- and ARX-modelling, model the variations in the heat flux rather than to cancel them out. As such, they focus on explaining the influences from the outdoor weather conditions, but without conceding information on the steady state behaviour of the studied building component.

The application of the established methods was demonstrated for the case study of a south-west oriented insulated cavity wall. Based on the results, several aspects related to the methods' implementation were noticed. A first aspect concerns the methods' complexity. From the analyses, it is seen that the average method is the most straightforward to apply, since it relies on simple equations that do not involve time-intensive computations. The same can be said for the average method corrected for storage effects, only now, additional information on the studied building component is required. This information is not always available and therefore limits the method's practical application. Concerning the simple linear regression method, the equations are still fairly simple, but a regression analysis is required to estimate the thermal resistance. Also Anderlind's approach relies on a regression analysis. But more than that, the latter method demands decisions to be made on the fraction of the data that will be used as historical measurements. This *influence time* is often determined by trial-and-error and raises as such the method's complexity. Finally, ARX-modelling is the most complex method to apply. Although the method's implementation is based on a multiple linear regression and very similar to Anderlind's approach, a theoretical understanding of time series analysis and the involved statistics is required in order to deduce the gain of the models. Furthermore, choices about the sampling time and influence time must be made.

The complexity of the methods is indirectly linked to their ability to describe the accuracy of the estimated thermal resistance. Generally, for the considered methods the following counts: the simpler the model, the less information that is available to describe the accuracy of the estimated parameter. The average method, with or without correction, for example, is a purely deterministic method. As such, it does not give any information on the reliability of the estimated thermal resistance. Although ISO 9869 does formulate some convergence criteria for the R-estimates, gradually calculated

during the measurements, these criteria do not provide a standard deviation for every calculated R-estimation. Meanwhile, the methods that rely on simple or multiple linear regression do: simple linear regression models, Anderlind's model and ARX-models all include residuals in their model formulation. Hence, information on the deviation between model and measurements is available and statements on the accuracy of the models' fit can be expressed. Next to that, it must be noted that the noise model in the ARX-case is more extensive than in the other two cases, since its estimation depends on historical values of the output, i.e. the heat flux q_{hfm}, itself. This estimation in a one-step ahead prediction setting allows additional statistical validation criteria such as examining the residuals for white noise. However, it was seen that the latter did not contain absolute proof for the physical interpretability of the estimated parameter. Similarly, it was noted generally that the estimated 95% confidence intervals did not always include the true, physical R-value. Thus, these intervals may not be interpreted as absolute bounds for the physical value of the estimated thermal resistance. This has to do with the fact that the estimated model accuracies relate to the variance errors of the model and not to the mean square errors.

Finally, it must be mentioned that an important newcomer to the dynamic data analysis methods is *stochastic state space modelling*. Since its application is rather complicated and novel in the context of thermally characterising building components, its potentials and limitations have not been discussed in this chapter, but will be thoroughly examined in chapter 3. Next to that, note that the R-estimation performances of the different methods have not been mutually compared yet. It was only remarked that the application of the semi-stationary methods is seasonally bounded whereas this was not the case for the dynamic methods. A final comparison between the methods' performance is reserved for chapter 4. In this chapter, a large-scale comparison of the established estimation methods, introduced in this section, and of the stochastic state space modelling technique is performed. Thereby, special attention is given to the reliability of the methods' estimation results when confronted with data sets of limited measurement time spans and different seasonal boundary conditions.

Chapter 3

What about stochastic grey-box modelling?

Stochastic state space modelling is an approved method for identifying systems in a lot of domains. However, in building physics, it is a rather new approach. Only recently this method has been introduced in the context of the thermal characterisation of buildings or building components [39, 40, 45, 46, 50, 62–68]. In the present chapter, the potentials of this method are examined thoroughly, in particular, when used to characterise the thermal resistance of building components from on-site measurements.

3.1 **Theoretical concepts**

3.1.1 Stochastic state-space models

Stochastic state space models belong to the class of *grey-box models* or *internal models*, meaning that they describe the internal state of the studied system. To be able to do so, appropriate model structures based on physical knowledge are needed. The fact that grey-box models are constructed from a physical background often implies that a direct physical interpretation can be attached to the models' parameters. Needless to say that these models contain much more information about the studied system than the previously discussed black-box models, which only focus on the input-output behaviour of the system. However, the question arises whether this additional information is useful enough to justify the use of grey-box modelling when only the characterisation of stationary parameters is of interest. This is one of the questions addressed in this dissertation.

Stochastic state space models consist of two parts: (1) a part describing the dynamics of the states of the system in continuous time, i.e. the system equation, and (2) a part

describing how these states are related to the observation measurements in discrete time, i.e. the measurement equation. The two parts of a linear stochastic state space model are generally described as

$$d\boldsymbol{x}_t = \big(\boldsymbol{A}(\boldsymbol{\theta})\boldsymbol{x}_t + \boldsymbol{B}(\boldsymbol{\theta})\boldsymbol{u}_t\big)dt + \boldsymbol{\sigma}(\boldsymbol{\theta})d\boldsymbol{\omega}_t \tag{3.1}$$

$$\boldsymbol{y}_{t_k} = \boldsymbol{C}(\boldsymbol{\theta})\boldsymbol{x}_{t_k} + \boldsymbol{D}(\boldsymbol{\theta})\boldsymbol{u}_{t_k} + \boldsymbol{\epsilon}_{t_k} \tag{3.2}$$

where t is time, $\boldsymbol{x}_t$ is the n-dimensional state vector, $\boldsymbol{u}_t$ is the m-dimensional known input vector, $\boldsymbol{y}_{t_k}$ is the l-dimensional vector of measurements at times t_k, $\{\boldsymbol{\omega}_t\}$ is an n-dimensional Wiener process with incremental covariance $\boldsymbol{\sigma}(\boldsymbol{\theta})$, and $\{\boldsymbol{\epsilon}_{t_k}\}$ is an l-dimensional white noise process which is assumed to be Gaussian with variance $\boldsymbol{S}(\boldsymbol{\theta})$. The matrices $\boldsymbol{A}$, $\boldsymbol{B}$, $\boldsymbol{C}$ and $\boldsymbol{D}$ contain elements which are functions of the physical parameters $\boldsymbol{\theta}$. $\boldsymbol{A}$ is an $n \times n$-dimensional matrix describing the dynamical behaviour of the system, $\boldsymbol{B}$ is an $n \times m$-dimensional matrix specifying how the input signals enter the system, $\boldsymbol{C}$ is an $l \times n$-dimensional matrix indicating how the states are related to the observation variables and $\boldsymbol{D}$ is an $l \times m$-dimensional matrix describing the direct feedthrough of the inputs to the observation variables.

Basically, the system equation of a state space model is a set of stochastic differential equations (SDE's); one for each of the states of the system. Note that the system equation (equation 3.1) only differs from a set of ordinary differential equations (ODE's) by its noise terms. Nevertheless, including the latter has a lot of implications. If a set of ODE's would be applied to describe the dynamic behaviour of the observed system, the unknown parameters could be determined by calibrating the model to the measurements. The solution of the ODE's would then be a deterministic function of time, meaning that the model would be able to exactly predict the future states of the system [39]. However, in reality, the states of a system can often not be exactly predicted. Because a model, for example, is always an approximation of the true system and the complexity of the assumed model structure will determine how well the real system's behaviour is imitated. Also, some variables that affect the system may not be included in the model. Or, the input measurement data of the system may be noise corrupted. In all those cases the modelled states will deviate from the real system's states. But, by adding a noise term to the ordinary system equations, SDE's acknowledge and reckon with these differences between the modelled and real states' variations. Even more, it avoids that random effects are absorbed into the parameter estimates. Furthermore, the stochastic framework enables the use of a large set of statistical tools to evaluate the estimated models and their parameters. The latter will be further discussed in subsection 3.1.3.

State space models are useful, especially in the context of physical parameter estimation, because insight into physical mechanisms can easily be incorporated into state-space models [35]. This is also the case for the thermal behaviour of building components, which can easily be modelled by RC-networks consisting of a series of thermal resistances and capacitances [69–71]. The latter models are, in fact, examples of linear time-invariant stochastic state space models. The states of such a model represent the internal temperatures in the modelled building component. If the model should be able to describe the exact temperature distribution of the building component, an infinite number of states would be required. However, for parameter estimation purposes, this would imply too many unknown parameters. Generally, estimation models only consider a small number of temperature nodes, making them so-called lumped parameter models.

Throughout this dissertation, a simple series of model resistances and capacitances is used to model the thermal behaviour of building components. A general representation of the considered model structure is given in figure 3.1. A mathematical description is given in equations 3.3 and 3.4. Note that the SDE's in equation 3.3 are summarized in one equation and have to be repeated for i=1,...,n with n the model order. The same measurements that were used as inputs to the established estimation methods are used for the estimation of these stochastic grey-box models, notably heat flux and surface temperature measurements. The internal and external surface temperatures are used as the model's inputs and the internal heat flux is considered as the observation variable on which the model is calibrated.

$$dT_{i=1,..,n} = \frac{1}{C_i R_i}(T_{i-1} - T_i)dt + \frac{1}{C_i R_{i+1}}(T_{i+1} - T_i)dt + \sigma_i d\omega_i \tag{3.3}$$

$$q_{hfm,t_k} = \frac{1}{R_{n+1}}(T_{n+1,t_k} - T_{n,t_k}) + \epsilon_{t_k} \tag{3.4}$$

with $T_0 = T_{se}$ the exterior surface temperature, $T_{n+1} = T_{si}$ the interior surface temperature, T_i the model states representing the internal temperatures, R_i the model resistances, C_i the model capacitances, t the time, ω_i a standard Wiener process and σ_i the incremental variance of the Wiener process. The total thermal resistance and capacity of the building component are calculated as $R_{tot} = \sum R_i$ and $C_{tot} = \sum C_i$ respectively. The surface temperatures T_{se} and T_{si} are the inputs of the model. The internal heat flux q_{hfm,t_k} is the observed variable with t_k the discrete time point of the measurements and with ϵ_{t_k} the measurement error which is assumed to be a Gaussian white noise process with variance σ^2.

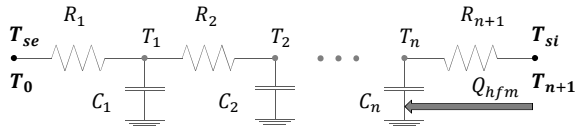

Figure 3.1: A general representation of the stochastic grey-box model of order n typically used to describe the heat transfer in building components.

3.1.2 Maximum likelihood estimation

Stochastic state space models are typically calibrated to measurement data by means of maximum likelihood estimation. Such identification procedure allows to identify the unknown parameters $\boldsymbol{\theta}$ of a given model structure from the considered data. In [43], a maximum likelihood based procedure to identify stochastic grey-box models is discussed. Based on this literature, a summary of the estimation method is given below.

As the name suggests, maximum likelihood estimation relies on the likelihood function. The latter is used to quantify the agreement between the observed measurements and the considered model's outputs. The best agreement, or maximum likelihood, is found for the set of parameters that maximises this objective function. However, before elaborating on the optimisation, lets first consider the likelihood function of a given stochastic state space model with unknown parameters $\boldsymbol{\theta}$.

For a given sequence of observation measurements $\boldsymbol{y}_0, \boldsymbol{y}_1, ..., \boldsymbol{y}_N$ with subsets defined as

$$\mathcal{Y}_k = [\boldsymbol{y}_k, \boldsymbol{y}_{k-1}, ..., \boldsymbol{y}_1, \boldsymbol{y}_0] \tag{3.5}$$

the likelihood function is given by

$$L(\boldsymbol{\theta}; \mathcal{Y}_N) = p(\mathcal{Y}_N|\boldsymbol{\theta}) \tag{3.6}$$

In essence, for a fixed set of model parameters $\boldsymbol{\theta}$, the likelihood function is the joint probability density of $\mathcal{Y}_N$. This joint probability density function can be replaced by conditional probability densities when the general product rule is used.

$$L(\boldsymbol{\theta}; \mathcal{Y}_N) = \Big(\prod_{k=1}^{N} p(\boldsymbol{y}_k|\mathcal{Y}_{k-1}, \boldsymbol{\theta}) \Big) p(\boldsymbol{y}_0|\boldsymbol{\theta}) \tag{3.7}$$

In most general cases, an exact evaluation of the likelihood function as formulated above is possible [72], although, in practice this is typically computationally infeasible. However, under the condition of Gaussian densities, Kalman filtering can be applied to solve the likelihood function. In the case of stochastic state space models, the assumption of Gaussian densities approximating the conditional densities in equation 3.7 is justified because the SDE's in equations 3.1 or 3.3 are driven by Wiener processes which have Gaussian increments.

If the conditional densities in equation 3.7 are considered Gaussian, than they are completely characterised by their mean and covariance

$$\hat{\boldsymbol{y}}_{k|k-1} = E\{\boldsymbol{y}_k|\mathcal{Y}_{k-1}, \boldsymbol{\theta}\} \tag{3.8}$$

$$\boldsymbol{R}_{k|k-1} = V\{\boldsymbol{y}_k|\mathcal{Y}_{k-1}, \boldsymbol{\theta}\} \tag{3.9}$$

Consequently, if $\boldsymbol{\epsilon}_k$ is defined as $\boldsymbol{y}_k - \hat{\boldsymbol{y}}_{k|k-1}$, then the likelihood function can be reformulated as

$$L(\boldsymbol{\theta}; \mathcal{Y}_N) = \Big(\prod_{k=1}^{N} \frac{exp(-\frac{1}{2}\boldsymbol{\epsilon}_k^T \boldsymbol{R}_{k|k-1}^{-1} \boldsymbol{\epsilon}_k)}{\sqrt{det(\boldsymbol{R}_{k|k-1})(2\pi)^l}} \Big) p(\boldsymbol{y}_0|\boldsymbol{\theta}) \tag{3.10}$$

Note that the errors $\boldsymbol{\epsilon}_k$ in the above equation are not simply the deviations between the measured and the modelled output. Since the states of the system are intermediately updated by the Kalman filter, it are the prediction errors from one time step to the next. Basically, the Kalman filter weights the uncertainties of the model predictions and the measurements in order to decide what to trust most: the model or the measurements. Hence, based on the Kalman filter the predicted states of the model are updated at each time step, reckoning with the information obtained during the previous time steps. That is why the method is often said to be functioning in a one-step prediction setting, as opposed to a pure simulation setting.

At this stage, the likelihood function in equation 3.10 can be fully evaluated, since, for any set of parameters $\boldsymbol{\theta}$, $\boldsymbol{R}_{k|k-1}$ and $\boldsymbol{\epsilon}_k$ can be computed by means of Kalman filtering. Subsequently, an optimisation algorithm can be used to identify the parameter set that maximises the likelihood function. Or, analogously, this parameter set can be found by minimising the negative logarithm of the likelihood function. The latter is often preferred since it has improved numerical conditions for the optimisation process. So, the maximum likelihood estimates of a stochastic grey-box model are those parameters minimising the negative log-likelihood function.

$$\hat{\boldsymbol{\theta}} = arg \min_{\boldsymbol{\theta}} \big(- ln(L(\boldsymbol{\theta}; \mathcal{Y}_N) \big) \tag{3.11}$$

This entire procedure of identifying stochastic grey-box models by maximum likelihood estimation and Kalman filtering is implemented in CTSM-R, a toolbox in R developed by DTU (http://ctsm.info/). Throughout this dissertation, the CTSM-R toolbox is used for the thermal characterisation of building components by means of stochastic grey-box modelling.

3.1.3 Statistical model evaluation tools

For the validation of stochastic state space models, the modeller can draw from an exhaustive set of statistical validation tools. In this dissertation, these validation techniques are subdivided into three main groups based on their intended purpose: (1) a first group of techniques focusses on the assessment of the descriptive capabilities of the studied model, (2) a second group is directed towards the assessment of the individual, estimated model parameters and (3) a third group of techniques concentrates on the comparison of different order models or different model structures. Furthermore, as mentioned earlier, the stochastic nature of the state space models allows for the estimation of the models in a prediction error setting. Within this framework, it is possible to pinpoint model deficiencies and their structural origin. The tools that are used for this purpose could be regarded as a fourth group of validation techniques. In this section, the main validation tools that are used throughout this dissertation are introduced.

Assessment of descriptive capabilities

As previously mentioned, a model is estimated by optimising an objective function that describes the agreement between measurements and model. Hence, to assess the overall model performance, the residuals between the modelled and measured output of the observed system can be examined. In essence, the residuals are a measure of the model's descriptive capabilities and its ability to mimic the input-output behaviour of the system.

A model is said to have good descriptive capabilities if the residuals show no significant autocorrelation, i.e. if the residuals are not significantly different from white noise. This can be assessed in the time domain by looking at the autocorrelation function (ACF) of the residuals and in the frequency domain by looking at the cumulated periodogram (CP) [39]. As was mentioned previously, a periodogram describes the variation of a signal in the frequency domain. The latter should be uniformly distributed over all frequencies for a white noise signal [61]. Or, the cumulated periodogram should

increase linearly to indicate white noise. Depending on the intended application of the model, the whiteness of the residuals should be examined in a one-step-ahead prediction setting (where the importance of short-term behaviour prevails) or in a pure simulation setting (where the importance of long-term behaviour prevails) [44]. Furthermore, the whiteness of the residuals can also be checked for a new data set rather than for the data set on which the model was trained. This is denoted by the term cross validation.

In general, if no white-noise residuals are obtained, the model is not able to explain all the dynamics of the input-output characteristic of the observed system. Hence, a higher model order or a different model structure is required [39].

Assessment of individual model parameters

Also on the level of the individual model parameters, statistical properties can be used to evaluate the model estimate. Based on the assumption of the asymptotic Gaussianity of the estimator $\hat{\boldsymbol{\theta}}$ in equation 3.11, the inverse of the Hessian, evaluated at the minimum of the objective function, can be interpreted as the covariance matrix of the model parameters [43, 44]. Hence, an estimate of the uncertainty of the individual parameter estimates can be derived together with the correlations between the estimated model parameters. Actually, these properties are derived from the curvature of a quadratic approximation of the objective function. A model with highly correlated parameters implies that the estimated values of the correlated parameters are interdependent. Hence, high correlations may indicate an over-parametrised model and it is often advised to reduce the model order or the number of parameters in the model [39].

Furthermore, the asymptotic Gaussianity of the estimator in equation 3.11 allows a significance testing of the individual model parameters [44]. A marginal t-test can be performed to examine whether the parameters of a model are significantly different from zero. This test typically results in a p-value, varying between 0 and 1, for every model parameter. This value represents the probability that the null hypothesis – stating that the particular model parameter equals zero – is true. A small p-value thus rejects the null hypothesis, while a large p-value fails to reject it. Different levels of significance can be regarded, however, typically, p-values below 0.05 indicate significant parameters and values bigger or equal to 0.05 indicate insignificant parameters. The latter are seen as unnecessary parameters to adjust the model output to the measurements and are advised to be removed from the model description [39].

Comparison of different models or model structures

When several potential model structures are fitted to measurement data, statistical tests can be used to indicate the best model fit, hereby reckoning with the increased number of parameters of the larger models.

The likelihood ratio test, for example, is typically used to compare the goodness of fit of two *nested* models [39, 46]. The test indicates whether the model with more parameters (the alternative model) performs significantly better than the model with fewer parameters (the null model). The likelihood ratio test is computed as follows

$$\Lambda = \frac{L(\boldsymbol{\theta}_{null}; \mathcal{Y}_N)}{L(\boldsymbol{\theta}_{alternative}; \mathcal{Y}_N)} \tag{3.12}$$

The alternative model will always fit at least as well as the null model. The question is, however, whether the alternative model fits *significantly* better than the null model. Therefore, the method relies on the general property of the likelihood ratio which states that $-2ln(\Lambda)$ is asymptotically χ^2-distributed with a degree of freedom equal to the difference in number of parameters of the alternative and null model [73, 74]. Based on this property, a p-value can be computed. The p-value indicates whether it is more likely that $\mathcal{Y}_N$ is observed with the smaller or larger model. If the null model has to be rejected in favour of the alternative model, than a p-value below a pre-specified limit, usually set to 0.05, must be obtained.

A more general test statistic that can also be used for models that are not nested is the Akaike Information Criterion (AIC) [75]. This test compares the relative quality of different stochastic models, hereby accounting for the complexity of the model. The AIC of a stochastic model is calculated as follows

$$AIC = 2z - 2ln\big(L(\hat{\boldsymbol{\theta}}; \mathcal{Y}_N)\big) \tag{3.13}$$

with z the number of unknown model parameters. The second term of equation 3.13 rewards the goodness of fit whereas the first term is a penalty function that increases with the complexity of the model. From a set of candidate models, the preferred model is selected as the model with the minimum AIC-value.

For univariate, linear models with normally distributed residuals, a correction for finite sample sizes can be considered [76]. The information criterion is then denoted by AICc and calculated by

$$AICc = AIC + \frac{2z(z+1)}{N-z-1} \tag{3.14}$$

with N the number of measurements in the sample. Next to the discussed statistical tests, a model's fit can also be assessed based on its residuals. The RMSE of the residuals of a model are a direct measure of its goodness of fit. Furthermore, a comparison of the RMSE's of different models gives an idea on the accuracy of the candidate models. The preferred model could then be the model with the lowest order that obtains the desired model accuracy. The RMSE of the residuals can be computed in a one-step-ahead prediction setting or in a pure simulation setting, depending on the intended use of the models. Also here, a cross validation can be applied by calculating the RMSEs of the residuals for a new data set instead of for the data set on which the model was trained. This is denoted by the term cross validation.

Pinpointing model deficiencies

Stochastic state space models have the advantage that the noise affecting the system can be decomposed into system noise, i.e. the noise models in the system equation, and measurement noise, i.e. the noise model in the observation equation. Hence, the solution of the SDE's of the system equation, solved by the Kalman filter, provides an estimate of the confidence interval for the estimated nodal temperatures of the model. The estimated standard deviations of these confidence intervals can be examined to pinpoint model deficiencies. The presence of significant parameters among these estimated system noise terms may indicate that the corresponding equation in the SDE's is incorrect [44]. This is valuable information for the modeller since it indicates in which part of the equations the deficiencies occur.

Furthermore, the one-step-ahead residuals of the estimated models contain information on possible model deficiencies. As was previously mentioned, the residuals of an appropriate model fit should be white noise. When this is not the case, the residuals can be analysed to pinpoint the origin of the poor model fit. This is possible since the residuals obtained in a one-step-ahead prediction setting are not auto-correlated [46, 61, 63]. Hence, their cross correlations with the input variable can indicate which phenomena are incorrectly modelled or which input variables should additionally be included in the model.

3.1.4 Identifiability

In this work, stochastic state space modelling is used for *physical parameter estimation* purposes. This means that a physical interpretation is attached to the estimated model parameters. However, it must be questioned whether these estimated values can be trusted. Because, as discussed previously, it must not be forgotten that estima-

tion methods are in essence designed to optimise a goal function that quantifies the agreement between model outputs and measurements. The model parameters that are thereby estimated are merely scaling factors adjusting the model output. Their physical significance is of no importance to the estimation algorithm. The only reason to attach a physical interpretation to the parameters is the modeller's belief that the assumed model structure represents the internal dynamic behaviour of the studied system. Nevertheless, in order to *guarantee* the physical interpretability of the model parameters, the formulation of an appropriate physical model structure is only a first step. Next to that, it is very important that the identified model is the only possible parametrisation explaining the input-output characteristic of the system. Because, if multiple parameter sets lead to the same maximal agreement between model output and measurements, the physical interpretation of those parameter sets is obviously jeopardised.

The question whether the parameters of a model can be uniquely defined from a set of measurement data is a question of identifiability. In literature, the notion of identifiability is twofold [77]. On the one hand, the concept of *structural identifiability*, an intrinsic property of the model, assures that a unique parametrisation is theoretically possible [78]. On the other hand, *practical identifiability* addresses the ability of estimating the unknown parameters uniquely from the available measurement data. Hence, a structural identifiable model can still lead to practically unidentifiable parameters due to a limited amount and/or quality of the measured data. In sum, *physical interpretability* can only be guaranteed for the structurally and practically identifiable parameters of an appropriate physical model.

Structural identifiability

Since structural identifiability is a property of the model structure itself, it can be inspected based on the mathematical description of the model alone. There is no need for quantitative experiments. This implies, however, that the inspection of a model's structural identifiability is based on symbolic computations. The latter can be complex and become very quickly computationally infeasible, even with the use of powerful computer programs nowadays at hand [79]. Literature on the topic is extensive: various approaches are proposed to analyse mathematically complex algebraic expressions [78, 80–83]. However, the stochastic state space models studied in this dissertation have rather simple symbolic equations. As a result, the problem can be approached by a very intuitive method that is based on the essentials of the concept of structural identifiability.

A stochastic state space model is said to be structurally identifiable if, in theory, different sets of parameter values lead to different probability distributions of the output of the system [35]. Or, in other words, a stochastic grey-box model is said to be structurally identifiable if its transfer function can only be generated by one combination of parameters [47]. In the Laplace domain, the output of the state space models defined in equations 3.1 and 3.2, can be written as [47]

$$\boldsymbol{y}(s) = \boldsymbol{H}_{input}(s)\boldsymbol{u}(s) + \boldsymbol{H}_{noise}(s)\boldsymbol{\epsilon}(s) \tag{3.15}$$

It is seen that the output is described as the sum of two transfer functions: one acting on the input and one acting on the noise. Given the scope of this dissertation, it is merely the uniqueness of the transfer function acting on the input that is of interest. The latter can be further developed as

$$\boldsymbol{H}_{input}(s) = \Big(\boldsymbol{C}(\boldsymbol{\theta})(s\boldsymbol{I} - \boldsymbol{A}(\boldsymbol{\theta}))^{-1}\boldsymbol{B}(\boldsymbol{\theta}) + \boldsymbol{D}(\boldsymbol{\theta})\Big) \tag{3.16}$$

with $\boldsymbol{A}$, $\boldsymbol{B}$, $\boldsymbol{C}$ and $\boldsymbol{D}$ the state-space matrices as defined in equations 3.1 and 3.2. The transfer function could also be expressed in discrete-time, however, this would only complicate the notation and the analysis. Generally, it is assumed that sampling the observations only influences the practical identifiability properties of the model and not the structural identifiability [66].

The next step is to verify whether the state-space parameters $\boldsymbol{\theta}$ can be derived uniquely from the given transfer function. Therefore, the elements of the transfer function matrix must be reformulated in their zero-pole-gain form, which is generally represented as

$$H_{input,ij}(s) = K_{ij}\frac{s^v + a_{ij,1}s^{v-1} + ... + a_{ij,v-1}s + a_{ij,v}}{s^w + b_{ij,1}s^{w-1} + ... + b_{ij,w-1}s + b_{ij,w}} \tag{3.17}$$

with K_{ij} the gain, $a_{ij,l}$ the zeros and $b_{ij,l}$ the poles of the ij-th element of the transfer function $\boldsymbol{H}_{input}(s)$ of the system. In order to be identifiable, the transfer function's number of independent zeros, poles and gains must be equal or larger than the number of unknown state-space parameters [47].

As an illustration of the method, let's consider the first order stochastic state-space model, represented in figure 3.2. Its input, output, state, and state-space matrices are given by

$$\boldsymbol{x} = \begin{bmatrix} T_1 \end{bmatrix} \tag{3.18}$$

$$\boldsymbol{y} = \begin{bmatrix} q_{hfm} \end{bmatrix} \tag{3.19}$$

$$\boldsymbol{u} = \begin{bmatrix} T_{se} & T_{si} \end{bmatrix}^T \tag{3.20}$$

$$\boldsymbol{A} = \begin{bmatrix} \frac{-1}{C_1 R_1} & \frac{1}{C_1 R_2} \end{bmatrix} \quad (3.21) \qquad \boldsymbol{B} = \begin{bmatrix} \frac{1}{C_1 R_1} & \frac{1}{C_1 R_2} \end{bmatrix} \quad (3.22)$$

$$\boldsymbol{C} = \begin{bmatrix} \frac{-1}{R_2} \end{bmatrix} \quad (3.23) \qquad \boldsymbol{D} = \begin{bmatrix} 0 & \frac{1}{R_2} \end{bmatrix} \quad (3.24)$$

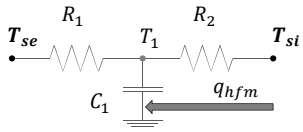

Figure 3.2: Graphic representation of a first order stochastic grey-box model used to describe the heat transfer in building components.

Since the input matrix $\boldsymbol{u}$ consists of two variables, the transfer function is also expressed by two terms. In zero-pole-gain form, those are calculated as

$$H_{input,11}(s) = \frac{-1}{C_1 R_1 R_2} \frac{1}{s + \frac{R_1 + R_2}{C_1 R_1 R_2}} \quad (3.25)$$

$$H_{input,12}(s) = \frac{1}{R_2} \frac{s + \frac{1}{C_1 R_1}}{s + \frac{R_1 + R_2}{C_1 R_1 R_2}} \quad (3.26)$$

The latter result in the following set of five equations

$$K_{11} = \frac{-1}{C_1 R_1 R_2} \quad (3.27) \qquad a_{12,1} = \frac{1}{C_1 R_1} = \frac{K_{11}}{K_{12}} \quad (3.30)$$

$$K_{12} = \frac{1}{R_2} \quad (3.28) \qquad b_{12,1} = \frac{R_1 + R_2}{C_1 R_1 R_2} = b_{11,1} \quad (3.31)$$

$$b_{11,1} = \frac{R_1 + R_2}{C_1 R_1 R_2} \quad (3.29)$$

From the above set of equations it is seen that only equations 3.27, 3.28 and 3.29 are independent. Hence, only three parameters can be uniquely defined by this transfer function. Since the considered first order model contains just three unknown parameters, i.e. C_1, R_1 and R_2, the model is structurally identifiable.

In appendix C, the structural identifiability of the second and third order model of the considered model type is also proven. Apparently, an increase in model order does not lead to structurally unidentifiable parameters. Hence, it is justified to assume that the

considered model type is a structurally identifiable model type. The question whether the model parameters are also practically identifiable requires a data-based analysis.

Practical identifiability

Whereas structural identifiability depends on the model structure alone, practical identifiability depends on both the model structure and the measurement data. In essence, identifiability issues are related to the sensitivity of the objective function of the estimation problem to variations of the model parameters. If a significant change in a certain model parameter does not lead to a significant change in the objective function, than the parameter has identifiability problems. Therefore, identifiability issues are often examined by scanning the objective function for flat manifolds, multiple maxima, etc. in the parameter space. Such an approach has been proposed by Raue et al. [77]. The paper suggests a method that is able to detect both structural and practical identifiable parameters by scanning the profile likelihood function of a given model's parameters for a given set of measurement data. A profile likelihood function basically explores the parameter space of a selected parameter by following the objective function in the direction of its least increase. The main idea is that a flat manifold in this profile indicates a non-identifiable parameter [84]. When the objective function is the likelihood function, the profile likelihood of a parameter θ_i is defined as the likelihood function which is, for each fixed value of θ_i along a chosen interval, re-optimized for all other parameters $\theta_{j\neq i}$. Hence, the profile likelihood returns the highest possible likelihood value for a range of fixed values of θ_i.

$$PL(\theta_i) = \max_{\theta_{j\neq i}} \Big(L(\boldsymbol{\theta}; \mathcal{Y}_N)\Big) \tag{3.32}$$

The profile likelihood can be calculated for all the parameters of interest of a model. Furthermore, the generalised likelihood ratio test of θ_i can be calculated as

$$R(\theta_i) = \frac{PL(\theta_i)}{L(\hat{\boldsymbol{\theta}}; \mathcal{Y}_N)} \tag{3.33}$$

with $L(\hat{\boldsymbol{\theta}}; \mathcal{Y}_N)$ the maximum of the likelihood function after optimisation of all model parameters. A general property of the likelihood ratio test states that $-2ln\Big(R(\theta_i)\Big)$ is asymptotically χ^2-distributed [74]. Therefore, $-2ln\Big(R(\theta_i)\Big)$ is further denoted as χ^2_{PL}. Based on this property, likelihood based confidence intervals [74, 85] can be determined for each parameter θ_i.

$$\left\{\theta_i : \chi^2_{PL} = -2ln\Big(\frac{PL(\theta_i)}{L(\hat{\boldsymbol{\theta}}; \mathcal{Y}_N)}\Big) < \Delta_\alpha\right\} \tag{3.34}$$

with Δ_α the α^{th} quantile of a χ^2-distribution for one degree of freedom. Graphically, the confidence interval of parameter θ_i can be determined by the intersections of χ^2_{PL} and the threshold Δ_α (see figure 3.3).

In [77], structural and practical non-identifiability is linked to the notion of likelihood based confidence intervals. A structurally unidentifiable parameter is defined as a parameter which keeps χ^2_{PL} at a constant level below the desired threshold Δ_α, resulting in an infinite likelihood based confidence interval. The fact that χ^2_{PL} stays at a *constant* level below the desired threshold means that, for every value of θ_i, a set of parameter values $\theta_{j\neq i}$ can be found that optimises the likelihood value. Hence, an infinite number of solutions to the optimisation problem can be found resulting in a structurally unidentifiable parameter θ_i. On the other hand, a practically unidentifiable parameter is defined as a parameter with an infinite or half-infinite confidence interval, meaning that χ^2_{PL} stays below the threshold Δ_α in minimum one direction of θ_i, although χ^2_{PL} may have a minimum. This can be interpreted as follows: although χ^2_{PL} shows a minimum for a certain parameter value of θ_i, for a (half-)infinite range of other values of θ_i, parameter values of $\theta_{j\neq i}$ can be found that lead to χ^2_{PL}-values which are, from a statistical point of view, not significantly different from the minimal value of χ^2_{PL}. Consequently, the present optimum is uncertain and small changes in the measurement data could lead to a totally different optimum. By contrast, an identifiable parameter is defined as a parameter with finite confidence bounds, meaning that χ^2_{PL} crosses the threshold Δ_α in both directions of θ_i. This means that the range of values of θ_i for which χ^2_{PL}-values can be found that are not significantly different from the minimal χ^2_{PL}-value, is limited. As such, the parameter is structurally and practically identifiable. Given the previous information, identifiability issues can be visually assessed by plotting χ^2_{PL} and Δ_α in function of θ_i as is schematically shown in figure 3.3.

3.2 **Physical interpretability analysis**

3.2.1 Methodology

The possibilities of stochastic grey-box modelling for R-estimation purposes highly relate to the *physical interpretability* of the estimated model parameters. The latter is investigated for common stochastic grey-box models in the light of an example. Again, the insulated cavity wall introduced in chapter 2 is considered as an illustration.

As was previously mentioned, a first step towards guaranteeing a model's physical interpretability is the assumption of a *physical model structure*. Such a model structure

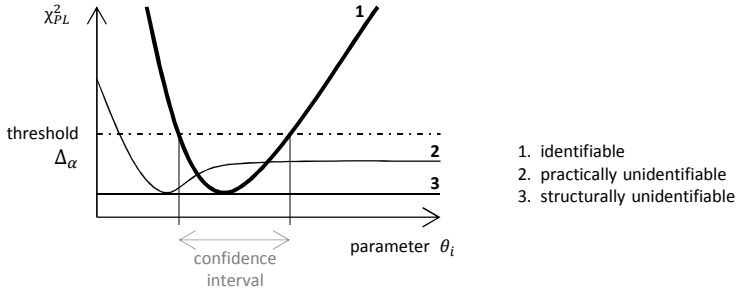

Figure 3.3: Graphical representation of χ^2_{PL} for parameter θ_i. A flat curve staying below the threshold Δ_α corresponds to a structurally unidentifiable parameter (3). A curve showing a minimum but staying below the threshold Δ_α in at least one direction of θ_i corresponds to a practically unidentifiable parameter (2). A curve crossing the threshold Δ_α in both directions of θ_i corresponds to an identifiable parameter (1). The intersections between the threshold Δ_α and χ^2_{PL} determines the confidence interval of parameter θ_i.

was introduced in section 3.1.1 and is used in this section to characterise the studied cavity wall. Hereby, first till fourth order models are considered, further denoted M1ref till M4ref, respectively. Their full model descriptions can be found in appendix D. The models are estimated by the maximum likelihood approach as implemented in CTSM-R. In order (to try) to avoid the estimation being trapped in a local minimum, each model estimation is repeated a 150 times for different initial parameter values. These initial values are randomly selected from a uniform or log-uniform distribution. Details about the latter are summarised in appendix D. From the set of 150 estimations, the final estimation result is then selected as the result with the highest log-likelihood value, on the condition that the estimation procedure reached convergence.

The next step towards guaranteeing a model's physical interpretability relates to the model's *identifiability*. For the considered model type, the structural identifiability has already been proven in section 3.1.4.1. However, to assess the models' practical identifiability, a profile likelihood analysis is performed. This is done for first till third order models. Since a profile likelihood assessment of these models is a data-based approach, a specific set of measurement data is assumed. Initially, the measurements of the entire winter peirod of the cavity wall are considered, as introduced in chapter 2. At a later stage, also the measurements of the summer measurements will be studied. By considering typical, realistic experimental conditions, the results can be interpreted quite generally. Hourly sampled data is assumed and both scenarios, i.e. the scenarios

with the constant and with the thermostatically controlled indoor temperature are considered. For both scenarios, the profile likelihood of the individual model resistances and capacitances is calculated. The resulting information then allows to discuss the identifiability of these individual model parameters. Although the latter might reveal information on the internal structure of the wall, it is actually the identifiability of the *total* thermal resistance that matters most, since this is the main parameter of interest. Therefore, also the influence of possible non-identifiable parameters on the physical interpretation of the the total thermal resistance is studied.

In parallel with the identifiability analysis, the estimated first till fourth models are validated based on the set of validation tools discussed in section 3.1.3. The tools assessing a model's descriptive capabilities are used to verify whether the assumed models perform in the expected physical way. Subsequently, the results of the statistical tests evaluating the individual parameter estimates are compared with the results of the identifiability analysis. A comparison of both allows to look for indications of non-identifiable parameters in the statistical evaluation criteria. Such indications would allow to decide on the identifiability of the model parameters based on the statistical validation criteria only. Even more, these would allow a more general approach to discuss the physical interpretability of the considered type of grey-box models for similar R-estimation problems of building components on-site.

3.2.2 Identifiability analysis

To visually assess the identifiability of the considered models, figure 3.4 depicts χ^2_{PL} in function of the different thermal parameters. The results for the two scenarios are distinguished from one another by a different colour and the results for the different order models are represented row wise by increasing model order. For the profile likelihood analysis, only first till third order models are examined. Note that the higher the model order, the more model parameters are present. The thresholds $\Delta_{0.862,df=1}$ and $\Delta_{0.95,df=1}$ are set for the evaluation of the profile likelihood based confidence intervals. They are represented in figure 3.4 as the dotted horizontal lines. Note that, when comparing profile likelihood based confidence intervals with asymptotic confidence intervals, the 86.2% profile likelihood bounds minus the estimated value can be compared to the standard deviation of asymptotic intervals and analogously, the bounds of the 95% intervals minus the estimated value can be compared to two times the standard deviation of asymptotic intervals.

In the first scenario, i.e. with constant indoor temperature, the results for the first order model (figure 3.4a) reveal that almost all thermal model parameters are practically non-

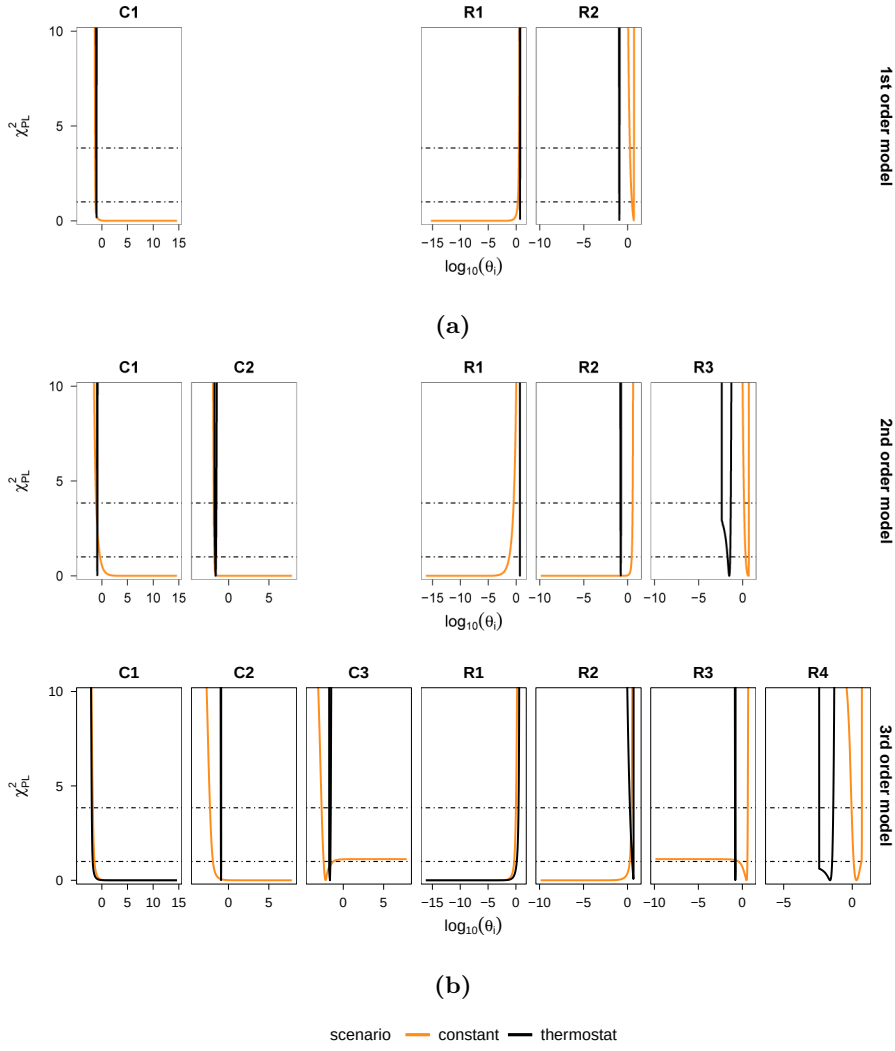

Figure 3.4: The profile likelihood, represented by χ^2_{PL}, of the thermal model parameters estimated from the winter measurements. The results for the different model orders are ordered row wise. The different model parameters are ordered column wise. Results for the two considered scenarios are shown in a different colour. The threshold for the point-wise confidence intervals $\Delta_{0.95}$ and $\Delta_{0.862}$ are represented by the dotted horizontal lines.

identifiable, except for the final internal thermal resistance R_2. As explained previously, the parameters C_1 and R_1 can be labelled non-identifiable based on the fact that χ^2_{PL} stays below the thresholds Δ_α in minimum one direction for these parameters. In contrast, for parameter R_2 the curve χ^2_{PL} crosses the threshold in both directions. Hence, this parameter is identifiable, nevertheless, with a large confidence interval given the logarithmic scale of the figure.

In the second scenario (figure 3.4a), i.e. with thermostatically controlled indoor temperature, the dynamic excitations come from both sides of the wall. These additional variations in input and output signals improve the identifiability of the first order model because, from figure 3.4a, it is now seen that all model resistances and capacitances are practically identifiable and have confined confidence intervals.

Similar observations are made for the higher order models (figure 3.4b). For the first scenario (constant), almost all thermal parameters are non-identifiable, except for some of the inner thermal resistances. For the second scenario (thermostat), the increased dynamics lead to more identifiable model parameters than in the first scenario. For the second order model in the second scenario all thermal parameters are identifiable. For the third order model, however, the additional dynamic information is not informative enough to estimate all parameters and R_1 and C_1 now appear to be practically non-identifiable. Nevertheless, in general, more parameters are identifiable in the scenario with a thermostatically controlled indoor temperature than in the scenario with a constant temperature.

The parameters C_3 and R_3 of the third order model in the first scenario deserve a more detailed analysis. As is seen from figure 3.4b, these parameters would be labelled identifiable when considering a $\Delta_{0.862}$-threshold and unidentifiable considering a $\Delta_{0.95}$-threshold. So, this parameter could be denoted *semi-identifiable* because its identifiability depends on the required reliability. Basically, these identifiability profiles should be interpreted as follows: assume that the considered model is estimated from different sets of very similar, but slightly different data, then 86.2% of the results would lie on the part of the profile below the $\Delta_{0.862}$-threshold; 95% of the results would lie on the part of the profile below the $\Delta_{0.95}$-threshold. So, although there is a preferred optimum in 86.2% of the cases, the optimum is not guaranteed in 95% of the cases. Even more, a wide variety of possible results is seen in 95% of the cases. So basically, the optimum is still sensitive to small changes in the data and thus is the estimated result not very certain. In essence, this means indeed that the present dynamics in the data are not optimal for a robust estimation of these parameters.

In sum, results so far revealed that the measurement data of the first scenario are not dynamically informative enough to estimate all model parameters separately. By contrast, the additional information embedded in the measurements of the second

scenario is sufficient to estimate all model parameters up till a second order model. The question raises, however, whether the presence of these non-identifiable parameters jeopardises the total thermal resistance estimation of those models.

Mathematically, the presence of non-identifiable parameters in a model does not automatically imply that the combined parameters are unidentifiable. Correlations between non-identifiable parameters can be as such that the variability of these parameters is cancelled out in the combined parameter. Or, the possible values of the unidentifiable parameters can be so small compared to the combined parameter, that their variability is insignificant. For the considered models, it is verified whether $R_{tot} = \sum R_i$ and $C_{tot} = \sum C_i$ can be robustly estimated by examining the behaviour of these combined parameters in the confidence regions of the model. Or, in other words, the behaviour of the combined parameters is examined in the regions where χ^2_{PL} is lower than $\Delta_{0.95,df=1}$. Since all the parameter values of θ_i in its confidence region are considered statistically equal, this region can be seen as the unidentifiable region of θ_i: no distinction between the parameter values can be made. Note that this unidentifiable region is infinite for unidentifiable parameters and finite for identifiable parameters. The behaviour of the combined parameters in these regions can be calculated by summing up the fixed parameter R_i or C_i and the remaining model resistances $R_{j\neq i}$ or capacitances $C_{j\neq i}$ that were optimised during the profile likelihood calculation of θ_i. Visually, this can be represented by plotting the calculated combined parameters R_{tot} and C_{tot} in function of the other model parameters in their confidence regions. Actually, this can also be done for the individual model parameters $\theta_{j\neq i}$. The profiles of these individual and combined parameters will vary in between their confidence bounds for every value of θ_i in the unidentifiable region. Hence, highly fluctuating profiles correspond to parameters with a large confidence interval, i.e. inaccurately estimated or possibly non-identifiable parameters. By contrast, nearly flat profiles correspond to parameters with small confidence bounds, i.e. most likely identifiable parameters.

Figure 3.5 depicts these functional relations for the third order model estimated on the winter measurements of the scenario with a constant indoor temperature. For clarity, the upper part of figure 3.5 repeats χ^2_{PL} for all thermal model parameters. The middle part represents the functional relations of the thermal resistances R_i and the total thermal resistance R_{tot} in function of the other model parameters in their confidence region. Analogously, the lower part of figure 3.5 represents the functional relations of the thermal capacitances C_i and the effective wall capacity C_{tot} in function of the other parameters in their confidence region.

Figure 3.5 (second row) shows clear correlations between most individual model resistances and the other model parameters in their 95% confidence region. Only R_4, the identifiable parameter of the model shows a flat profile in the confidence regions of all other parameters. R_3, the semi-identifiable parameter, shows a flat profile for the unidentifiable region of almost all parameters, except for parameter C_3 and R_4. This indicates a correlation between R_3 and these parameters. The other individual resistances R_1 and R_2, which are practically unidentifiable, vary strongly over the unidentifiable regions of the model. Nevertheless, despite these correlations, the total thermal resistance R_{tot} shows a flat profile and can thus be robustly estimated. Figure 3.5 (first row) shows that the unidentifiable regions of the parameters R_i span a range of very small values. Hence, the unidentifiable resistances' variability is insignificant for the value of R_{tot}. As a result, the total thermal resistance is not involved in the model's unidentifiability and is an identifiable parameter which can be robustly estimated.

Similarly, clear interactions are noticed between the model capacitances C_i and the other model parameters in their confidence region (figure 3.5 (third row)). Only the semi-identifiable C_3 shows a flat profile for the unidentifiable region of the other model parameters, except in the region of its correlated parameter R_3 and in the unidentifiable region of R_4. The profile of the total thermal capacity C_{tot} also shows large fluctuations in the unidentifiable regions of most thermal parameters, meaning that the parameter is involved in the model's unidentifiability. From the first row of figure 3.5 it is seen that the unidentifiable region of the individual parameters C_i cover large values. As such, the variability of the unidentifiable model capacitances has a significant influence on the combined parameter C_{tot}. The large fluctuations of C_{tot} indicate that the parameter cannot be estimated robustly. Hence, it implies that the estimated wall capacity of the unidentifiable model may not be physically interpreted, since its value depends on the estimated combination of the other model parameters. The fact that multiple model parameter combinations optimise the objective function can be physically explained by stating that time constants of the wall are estimated rather than separate R_i- and C_i-values.

Similar results are noticed for the other models estimated from the winter measurements of both scenarios. For completeness appendix E includes the figures depicting the behaviour of the model parameters in function of the unidentifiable regions of the model.

The previous findings can also be confirmed from figure 3.6, which compares the estimated thermal parameters with the system's *real* total resistance and total capacity.

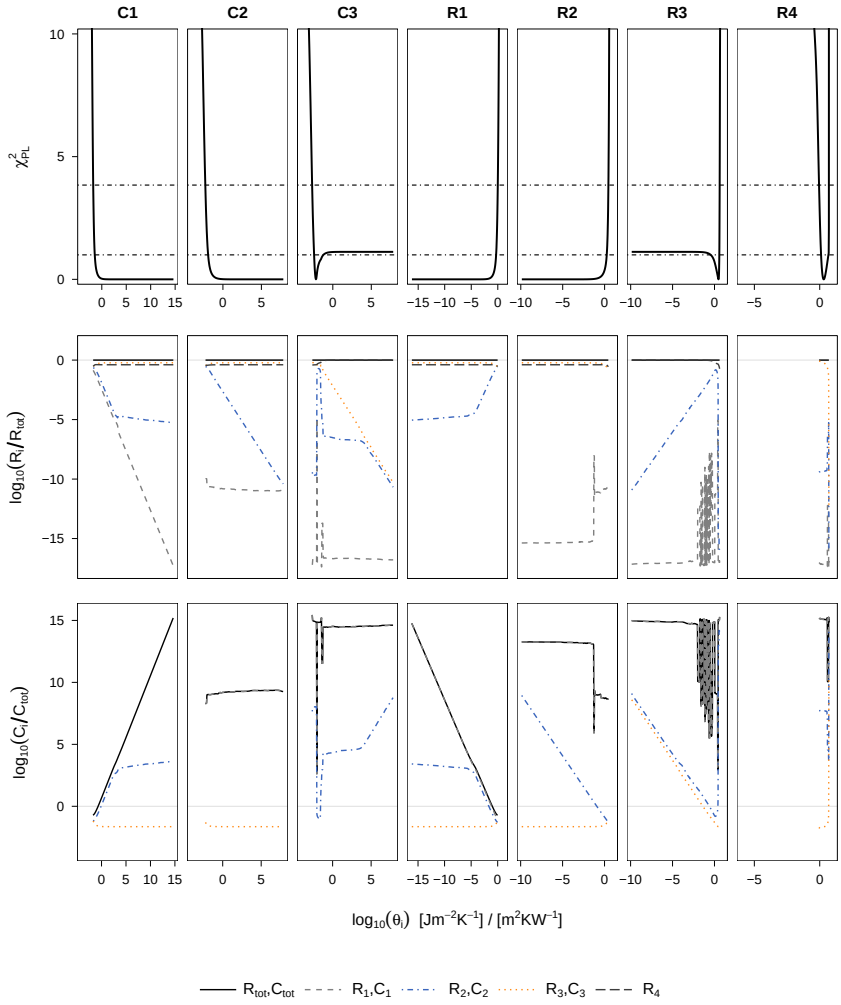

Figure 3.5: The behaviour of the thermal parameters in the non-identifiable regions of the third order model estimated on the winter measurements of the scenario with a constant indoor temperature. The top row repeats the χ^2_{PL}-profiles of the model's thermal parameters. The middle row represents the behaviour of the model resistances, divided by the total thermal resistance, R_i / R_{tot}, in the model's non-identifiable regions. The bottom row analogously represents the behaviour of the model capacitances, divided by the total thermal capacity, C_i / C_{tot}, in the model's non-identifiable regions.

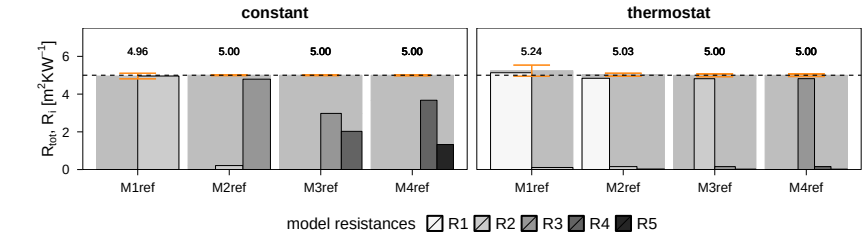

(a)

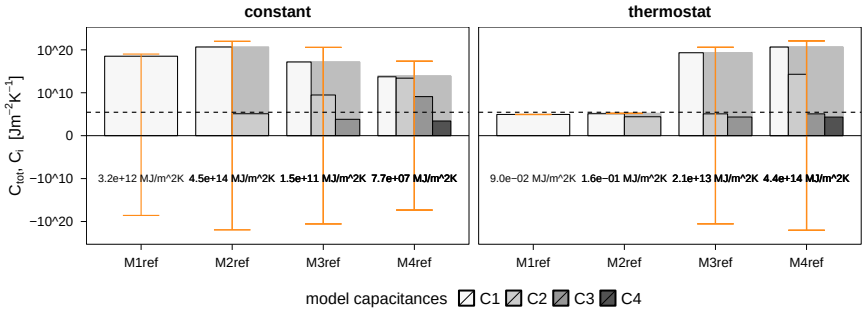

(b)

Figure 3.6: The thermal resistances (a) and capacitances (b) of the four different order models estimated from the winter measurements of both scenarios. The individual model resistances R_1 till R_5 are represented versus a solid grey block corresponding to the total estimated resistance R_{tot}. Analogously, the individual model capacitances C_1 till C_4 are represented versus the total estimated capacity C_{tot}. Note that the thermal capacitances are represented against a logarithmic y-axis in $Jm^{-2}K^{-1}$, while the labels of C_{tot} are represented in $MJm^{-2}K^{-1}$. The dotted lines represent the reference values of the wall calculated from the properties used to simulate the measurement data. The first till fourth order models are denoted M1ref, M2ref, M3ref and M4ref respectively.

The latter two are calculated from the properties used to simulate the cavity wall. It can be seen that for almost all models, in both scenarios, the total thermal resistance is robustly estimated since the reference value lies within the 95% asymptotic confidence intervals of the estimated parameters (see figure 3.6a). Only the first order model shows a less reliable thermal resistance estimation for the second scenario. The statistical validation criteria will, however, demonstrate that first order models are

not appropriate to explain all the dynamics present in the measurement data. Furthermore, it is noticed that the estimated total thermal capacities of the non-identifiable models systematically overestimate the wall capacity. Realistic C_{tot}-estimates are only obtained by the two fully identifiable models, i.e. the first and second order model in the second scenario (thermostat) (see figure 3.6b). Note, however, that the estimated total capacity of these two identifiable models underestimate the goal value. This has to do with the fact that the *effective* thermal capacity is estimated rather than the total thermal capacity. In a distributed system, often only a part of the total wall capacity is addressed by the perturbation signals [48, 86, 87]. Even more, the part of the wall that is addressed will depend on the excitation signals acting on this wall. Hence, instead of the total thermal capacity, it is this *active*, also called *effective*, part that is estimated by the characterisation method.

Furthermore, based on figure 3.6, the physical interpretation of the *individual* model parameters can be questioned. From a physical point of view, one would expect a model of an insulated cavity wall to have two capacitive nodes with small resistances on the inside and outside representing the inner and outer brick wall and a large thermal resistance in between the capacitances representing the insulation layer. The estimated internal distribution of the second order model's resistances and capacitances is, however, different. Also, from figure 3.4 it was seen that identifiable parameters of both scenarios do not always have the same optimum. The identifiable parameter R_3 of the second order model, for example, has an optimum in the first scenario that is different from the optimum in the second scenario. The same is seen for the parameters R_2 and R_3 in the first and second order model respectively. Thus, although a physical and identifiable model structure is assumed, the individual model parameters of a reduced order model can not be clearly pinpointed to the separate layers of the wall. A more complicated relation between the physical properties and the model parameters is playing as a consequence of the simplification that is made by modelling a distributed system by a lumped system [88]. Hence, the estimated internal distribution of the wall will be signal-dependent and difficult to interpret.

In sum, the main conclusions of the identifiability analysis reveal that, despite the presence of practically non-identifiable model parameters, the examined model structure always allows to estimate the total thermal resistance when a sufficient order model is selected. In contrast, it was seen thus far that the value of the total thermal capacity seems to be affected by the presence of non-identifiable parameters in the model structure and loses its physical meaning. Hence, identifiable models are required for an estimation of the total effective thermal capacity. In the next section, it is examined whether these conclusions are reflected in the model validation criteria.

3.2.3 Statistical validation

Before statistically examining the individual parameter estimates, the overall model performance is evaluated. Since a *physical* model is required to interpret its parameters, this evaluation basically verifies whether the model behaves in the physical way that it was designed. So, based on this analysis, inadequate models should be eliminated. Generally, for the statistical validation, first till fourth order models are considered.

To assess the overall model performance, the residuals are examined in the frequency domain by looking at the cumulated periodogram (CP). Figure 3.7a depicts the CP's for the residuals of all models and for both scenarios in a one-step prediction setting. All models show white noise residuals for the first scenario (constant) and nearly white noise residuals for the second scenario (thermostat). The absence of perfectly white noise in the second scenario is explained by the sudden heat changes occurring in the heat flux measurements. In figure 3.8, depicting the measured and predicted heat flux during the last 6 days of the winter period, it is seen that the largest deviations between models and measurements occur when the heating is switched on: the peak is not accurately modelled. It is generally known that sudden changes in capacitive components are hard to model with reduced order models, since a limited number of time constants is available. Moreover, due to the sampling, it might also be the measurement point at the peak that is biased. Therefore, it is treated as rather unimportant. In stochastic models, it is possible to implement a tolerance in the noise model that could allow higher residuals in the regions where the heating system is switched on, however, for this analysis, the CP is just judged in a more indulgent way. Note, furthermore, that is appears from figure 3.7a that the lower models in the second scenario perform better than the higher order models: the CP's of the first and second order model lie within the accuracy bands, while the CP's of the third and fourth order model do not. However, this can not be concluded so straightforwardly. The steep, vertical changes in the CP's of the first and second order model should be censured more severly than the deflections of the third and fourth order models' CP, since the steep changes indicate that the corresponding frequencies are not at all explained by the first and second order model.

Consequently, it can be concluded that all models show practically white noise residuals in a one-step prediction setting. This indicates an accurate imitation of the short-term input-output behaviour of the cavity wall. But, since the thermal parameters of interest are important for the long term behaviour of the system, the whiteness of the residuals is also assessed in a simulation setting (figure 3.7b). It is seen that the residuals of the first order models are autocorrelated for both scenarios. Thus, the long

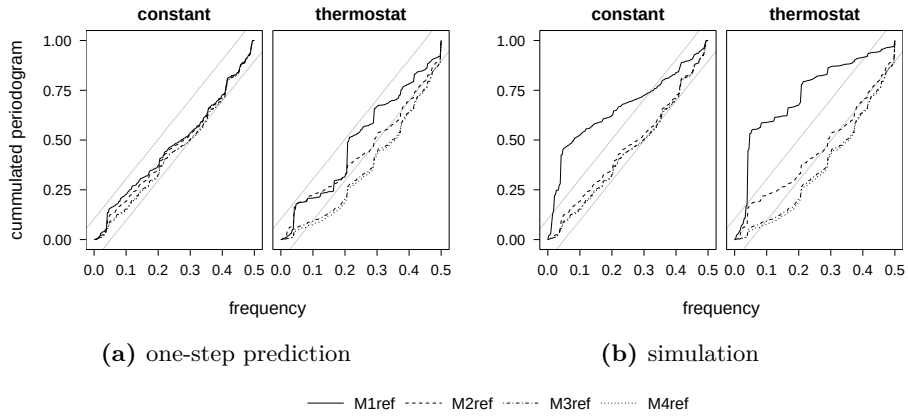

(a) one-step prediction **(b)** simulation

Figure 3.7: The cumulated periodograms of the first till fourth order models estimated on the winter measurements of both scenarios.

term input-output behaviour of the wall is not correctly modelled by a first order model. As an illustration, figure 3.9 represents the measured and modelled heat flux during the last 6 days of the winter period in simulation setting. It can be seen that the first order models do not capture all present dynamics. Based on this information, the first order models are falsified for both scenarios and should no longer be considered for the physical parameter estimation of the wall's thermal properties. Higher order models, however, do show white-noise residuals in a simulation setting. These models are thus considered to be physical models. The fact that even the second and third order models show white noise for the scenario with a constant indoor temperature proves that the non-identifiability of these models does not jeopardise their descriptive capabilities. Even more, it proves indeed that, in order to guarantee physical interpretability of the models, additional validation criteria are required.

Before regarding those additional validation criteria, first the optimal model order selection is discussed. Figures 3.10a and 3.10b represent the results from the AICc and log-likelihood ratio test, respectively, for the different order models. Both tests designate the third order model as the most optimal model to imitate the winter measurements of both scenarios. This shows that the tests select the model that best explains the observed measurements without reckoning with the model's identifiability, as otherwise the identifiable second order model would be preferred over the non-identifiable third order model in the second scenario.

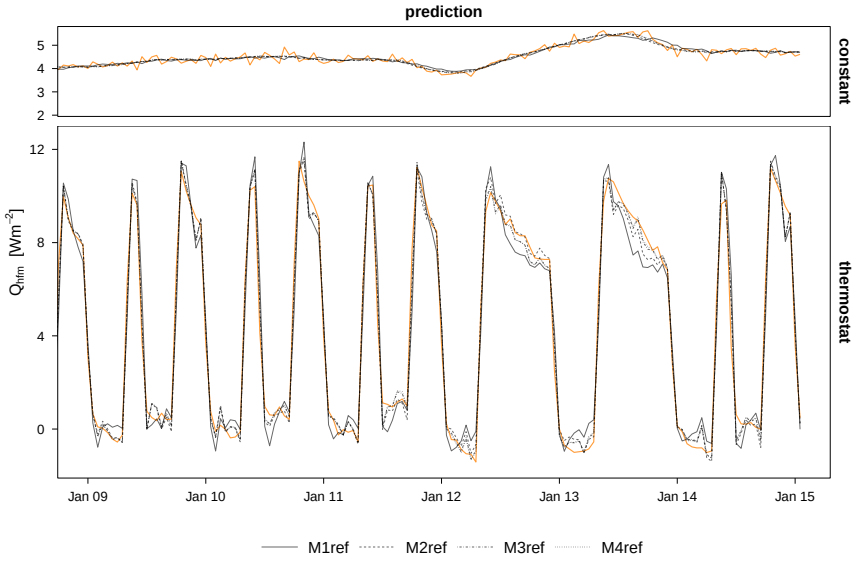

Figure 3.8: The measured heat flux (orange) and the heat flux predicted by the different order models during the last six days of the considered winter period.

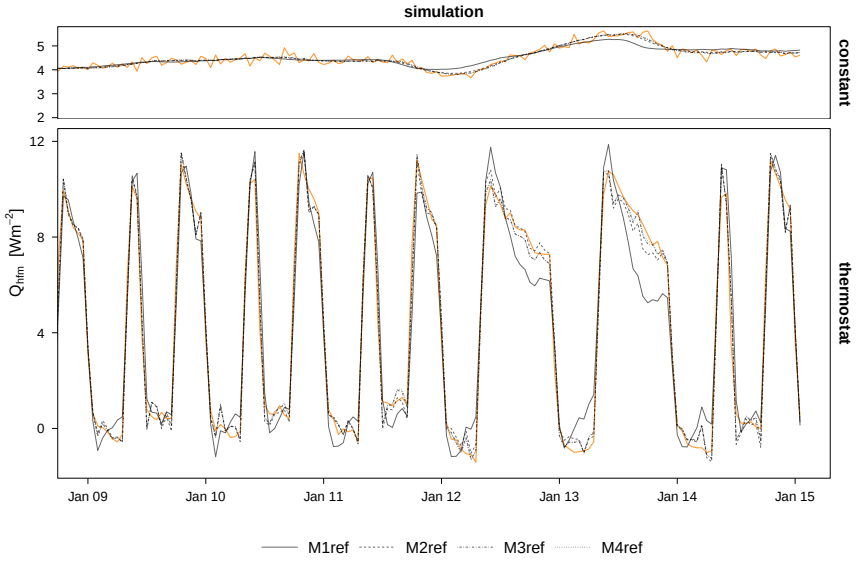

Figure 3.9: The measured heat flux (orange) and the heat flux simulated by the different order models during the last six days of the considered winter period.

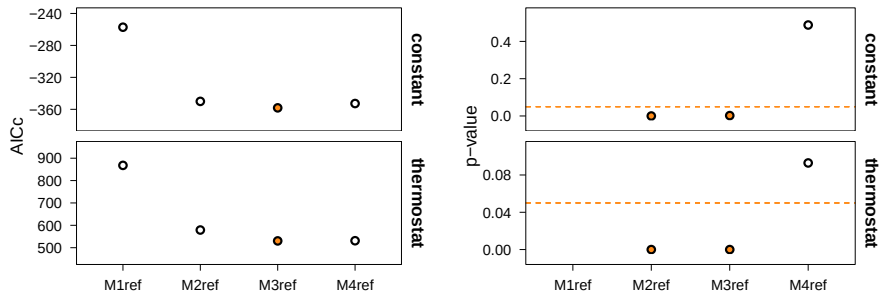

(a) AICc **(b)** Log-likelihood ratio test

Figure 3.10: Comparison of different order models estimated on the winter measurements of both scenarios. (a) The model with the lowest AICc-criterium is the preferred order model. (b) A model of order n is preferred over a model of order n-1, when the p-value, represented at the n-th order model, is lower than 0.05.

In general, it can be said that the selection of the optimal model order for physical parameter estimation purposes is not straightforward. Based on the observations for the considered cavity wall, a minimal and maximal model order can be set. The minimal order is the lowest possible model order corresponding to a model with white-noise residuals. The maximum model order is the order selected by the likelihood ratio test or AICc-criterion, as a further increase of model order does not significantly improve the model's descriptive capabilities. The optimal model order within these boundaries is then advised to be the model order that provides the desired accuracy levels for the parameters of interest.

Finally, to find indications of non-identifiable parameters, the individual estimated model parameters are statistically evaluated. Therefore, the significance testing and the approximate standard deviations, which are estimated together with the parameters, are studied. Both values are summarised in tables 3.1 and 3.2 for the different order models and for both scenarios. For comparison, the tables also mention which parameters were identifiable according to the profile likelihood analysis.

From tables 3.1 and 3.2, it can be seen that most non-identifiable parameters correspond to those model parameters that are insignificant. For the first order model in the first scenario (table 3.1a), for example, the only significant parameter is the only identifiable parameter R_2. In essence, a significance test performs a marginal t-test to check whether the estimated parameter is significantly different from zero [44]. Or,

(a) Parameter validation criteria for the first order model estimated on the winter measurements of the first scenario.

M1ref	value	$sd_{\alpha=0.68}$	p-test	significant?	identifiable?
Cw1	3.21E+12	3.51E+12	3.62E-01	N	N (+∞)
Ctot	**3.21E+12**	**3.51E+12**			
Rw1	2.24E-14	2.47E-14	3.66E-01	N	N (-∞)
Rw2	4.96E+00	7.35E-02	<2e-16	***	Y
Rtot	**4.96E+00**	**7.35E-02**			

(b) Parameter validation criteria for the second order model estimated on the winter measurements of the first scenario.

M2ref	value	$sd_{\alpha=0.68}$	p-test	significant?	identifiable?
Cw1	4.53E+14	4.58E+15	9.21E-01	N	N (+∞)
Cw2	1.27E-01	1.08E+00	9.06E-01	N	N (+∞)
Ctot	**4.53E+14**	**4.58E+15**			
Rw1	5.74E-17	5.79E-16	9.21E-01	N	N (-∞)
Rw2	2.13E-01	1.88E+00	9.10E-01	N	N (-∞)
Rw3	4.79E+00	1.89E+00	1.18E-02	*	Y
Rtot	**5.00E+00**	**1.09E-02**			

(c) Parameter validation criteria for the third order model estimated on the winter measurements of the first scenario.

M3ref	value	$sd_{\alpha=0.68}$	p-test	significant?	identifiable?
Cw1	1.45E+11	1.81E+14	1.0E+00	N	N (+∞)
Cw2	2.99E+03	2.13E+06	1.0E+00	N	N (+∞)
Cw3	6.46E-03	3.04E-03	3.4E-02	*	Y/N (+∞)
Ctot	**1.45E+11**	**1.81E+14**			
Rw1	7.60E-14	9.50E-11	1.0E+00	N	N (-∞)
Rw2	1.11E-05	7.94E-03	1.0E+00	N	N (-∞)
Rw3	2.98E+00	7.77E-01	1.5E-04	***	Y/N (-∞)
Rw4	2.03E+00	7.77E-01	9.5E-03	**	Y
Rtot	**5.00E+00**	**9.39E-03**			

(d) Parameter validation criteria for the fourth order model estimated on the winter measurements of the first scenario.

M4ref	value	$sd_{\alpha=0.68}$	p-test	significant?	identifiable?
Cw1	5.19E+07	7.27E+10	1.0E+00	N	NA
Cw2	2.47E+07	3.52E+10	1.0E+00	N	NA
Cw3	1.26E+03	1.05E+06	1.0E+00	N	NA
Cw4	2.64E-03	2.27E-03	2.4E-01	N	NA
Ctot	**7.66E+07**	**1.08E+11**			
Rw1	1.72E-10	2.41E-07	1.0E+00	N	NA
Rw2	1.21E-09	1.73E-06	1.0E+00	N	NA
Rw3	5.98E-06	5.01E-03	1.0E+00	N	NA
Rw4	3.67E+00	6.59E-01	5.4E-08	***	NA
Rw5	1.33E+00	6.58E-01	4.5E-02	*	NA
Rtot	**5.00E+00**	**1.02E-02**			

Table 3.1: The tables report the estimated model parameters with their estimated standard deviation. Resistances have the unity m^2KW^{-1}, capacitances $MJm^{-2}K^{-1}$. The p-value summarises the significance testing results. Parameters with a p-value < 0.001 are indicated as ***. Parameters with a $0.01 <$ p-value < 0.05 are indicated as * and insignifcant parameters are indicated with N. The identifiable and non-identifiable parameters are indicated with Y and N respectively. The infinite confidence bounds of the non-identifiable parameters are added in between brackets.

(a) Parameter validation criteria for the first order model estimated on the winter measurements of the second scenario.

M1ref	value	$sd_{\alpha=0.68}$	p-test	significant?	identifiable?
Cw1	8.74E-02	3.61E-03	< 2.2e-16	***	Y
Ctot	**8.74E-02**	**3.61E-03**			
Rw1	5.13E+00	1.48E-01	< 2.2e-16	***	Y
Rw2	1.10E-01	2.79E-03	< 2.2e-16	***	Y
Rtot	**5.24E+00**	**1.48E-01**			

(b) Parameter validation criteria for the second order model estimated on the winter measurements of the second scenario.

M2ref	value	$sd_{\alpha=0.68}$	p-test	significant?	identifiable?
Cw1	1.30E-01	4.69E-03	<2.2e-16	***	Y
Cw2	2.55E-02	3.13E-03	8.44E-15	***	Y
Ctot	**1.55E-01**	**3.87E-03**			
Rw1	4.84E+00	3.99E-02	< 2.2e-16	***	Y
Rw2	1.58E-01	5.83E-03	< 2.2e-16	***	Y
Rw3	3.04E-02	5.83E-03	8.45E-04	***	Y
Rtot	**5.03E+00**	**3.90E-02**			

(c) Parameter validation criteria for the third order model estimated on the winter measurements of the second scenario.

M3ref	value	$sd_{\alpha=0.68}$	p-test	significant?	identifiable?
Cw1	2.06E+13	1.83E+14	9.11E-01	N	Y (+∞)
Cw2	1.21E-01	5.00E-03	< 2.2e-16	***	Y
Cw3	2.22E-02	3.82E-03	1.49E-08	***	Y
Ctot	**2.06E+13**	**1.83E+14**			
Rw1	8.24E-16	7.34E-15	9.11E-01	N	N (-∞)
Rw2	4.82E+00	3.59E-02	< 2.2e-16	***	Y
Rw3	1.58E-01	8.56E-03	< 2.2e-16	***	Y
Rw4	2.41E-02	1.31E-02	6.69E-02	.	Y
Rtot	**5.00E+00**	**3.52E-02**			

(d) Parameter validation criteria for the fourth order model estimated on the winter measurements of the second scenario.

M4ref	value	$sd_{\alpha=0.68}$	p-test	significant?	identifiable?
Cw1	4.38E+14	5.81E+15	9.40E-01	N	NA
Cw2	2.02E+08	2.32E+11	9.99E-01	N	NA
Cw3	1.20E-01	5.29E-03	< 2.2e-16	***	NA
Cw4	2.15E-02	4.23E-03	6.04E-07	***	NA
Ctot	**4.38E+14**	**5.81E+15**			
Rw1	1.99E-17	2.61E-16	9.39E-01	N	NA
Rw2	4.32E-11	4.96E-08	9.99E-01	N	NA
Rw3	4.82E+00	3.36E-02	< 2.2e-16	***	NA
Rw4	1.59E-01	9.92E-03	< 2.2e-16	***	NA
Rw5	2.25E-02	1.50E-02	1.36E-01	N	NA
Rtot	**5.00E+00**	**3.28E-02**			

Table 3.2: The tables report the estimated model parameters with their estimated standard deviation. Resistances have the unity m^2KW^{-1}, capacitances $MJm^{-2}K^{-1}$. The p-value summarises the significance testing results. Parameters with a p-value < 0.001 are indicated as ***. Parameters with a $0.01 <$ p-value < 0.05 are indicated as * and insignifcant parameters are indicated with N. The identifiable and non-identifiable parameters are indicated with Y and N respectively. The infinite confidence bounds of the non-identifiable parameters are added in between brackets.

in other words, it is tested whether zero lies within the 95% asymptotic confidence interval of the estimated parameter. Hence, the results from the significance testing highly depend on the estimated standard deviations of the parameters.

The concept of standard deviations as indications for (non-)identifiable parameters is in line with the interpretation of the likelihood based confidence intervals. As stated previously, infinite or half-infinite likelihood based confidence regions indicate non-identifiable parameters. By contrast, asymptotic confidence bounds are never infinite, since these confidence regions, estimated along with the parameters by most software programs, are based on the Hessian of the goal function evaluated at its minimum. The estimated standard deviations of parameters θ_i are thus based on a quadratic approximation of the profile likelihood function for these parameters. As an illustration, figure 3.11 shows the χ^2_{PL}-profiles, calculated from the winter measurements of the scenario with a constant indoor temperature, and its second order approximation for the thermal resistances of the third order model. Note that the second order approximation has no parabolic shape because of the logarithmic scale of the x-axis. From this figure, but also from tables 3.1 and 3.2, it can be concluded that for the considered experimental conditions and model type, the nature of the identifiability is as such that the estimated standard deviations of the unidentifiable parameters will lead to insignificant parameters in most cases.

For example, the first order model of the first scenario (table 3.1a) showed a half-infinite profile likelihood confidence interval for the parameter C_1. The estimated standard deviation, derived from a second order approximation of the goal function is

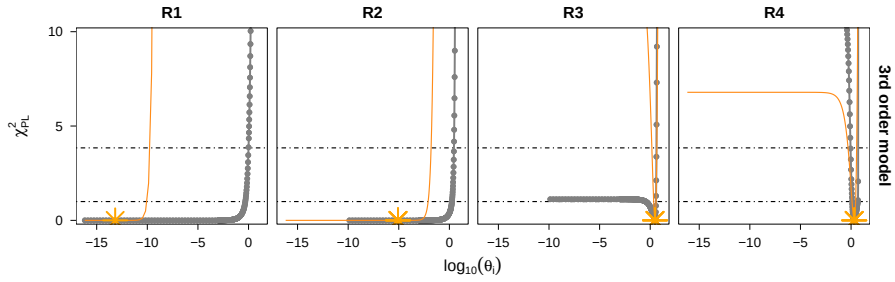

Figure 3.11: The χ^2_{PL}-profiles, calculated from the winter measurements of the scenario with a constant indoor temperature, for the thermal resistances of the third order model. A second order approximation of the χ^2_{PL}-profiles is represented in orange. The estimated thermal parameter is indicated by the asterisk.

$3.51E+12\ Jm^{-2}K^{-1}$. Due to the approximative character, the estimated standard deviation of C_1 is finite, but large. Moreover, the standard deviation is sufficiently large compared to the estimated value $3.21E+12\ Jm^{-2}K^{-1}$ so that C_1 is tested insignificant. Similar observations can be made for the other unidentifiable parameters of the models in both scenarios.

However, some exceptions are found. The parameters C_3 and R_3 of the third order model fitted on data of the first scenario, for example. These parameters are found significant by t-testing and show a very small estimated standard deviation compared to the estimated value (table 3.1c). From figure 3.11, it could be seen that a second order approximation of χ^2_{PL} in its minimum would indeed coincide only with the upper right part of the profile. Hence, the quadratic approximation is not able to portray the whole picture. As was discussed before, the estimated value might well be the preferred optimum for the considered experimental data, nevertheless, for very similar, but slightly different measurement data, the results might end up far from this optimum. Hence, the estimated accuracy of this parameter is estimated too optimistically.

Besides all that, the individual parameter evaluations do not inform about the identifiability of the combined parameters R_{tot} and C_{tot}. However, based on the standard deviations of the individual parameters and the correlations of the latter, combined standard deviations can be calculated for the combined parameters. This is done based on the rule that $Var(\sum_{i=1}^{n} R_i) = \sum_{i=1}^{n} Var(R_i) + 2\sum_{i<j} Cov(R_i, R_j)$ with Var the variance and Cov the covariance. The standard deviation of R_{tot} then equals the square of the variance $Var(\sum_{i=1}^{n} R_i)$. The combined standard deviations of R_{tot} and C_{tot} are calculated for all models and are summarised in tables 3.1 and 3.2. The combined standard deviations appear to be a good indication of the identifiability of the combined parameters. From tables 3.1 and 3.2 and from figure 3.6, it can be seen that the identifiable models of the first scenario, i.e. the first and second order model, result in total effective capacities with a reliable confidence region. By contrast, the non-identifiable models, i.e. t third order model in the second scenario and all models in the first scenario (tables 3.1 and 3.2) show very large confidence intervals indicating unreliable C_{tot}-estimates. The estimated total thermal resistances show small confidence intervals for all appropriate order models in both scenarios indicating reliable estimates (see figure 3.6 and tables 3.1 and 3.2). So, generally, it can be stated that the confidence intervals of R_{tot} and C_{tot} are a good indication to what extent these parameter estimates can be trusted.

In sum, the main findings of the statistical parameter evaluation reveal that the concept of identifiability is closely linked to the concept of statistical confidence bounds. This might not surprise, since they both essentially relate to the sensitivity of the

estimation's objective function to variations of the model parameters. By definition, profile likelihood intervals contain absolute information on a parameter's identifiability. But, from the previous analyses, it followed that also the approximate asymptotic confidence bounds contain valuable information and can function as indications for unidentifiability. For the considered model type and measurement data, it was observed that the character of the parameters' practical (non-)identifiability is as such that unidentifiable parameters can (mostly) be recognised as the insignificant parameters of the model. Hence, it is concluded that the asymptotic standard deviations of the individual and combined parameters are good indications of their identifiability. These results might not be ground breaking since insignificant parameters are known to indicate over-parametrised models, as such pointing in the direction of unidentifiable parameters in the model. However, the identifiability analysis brought more insight into the problem. It even slightly changed the interpretation of the statistical parameter criteria. Typically, insignificant or highly correlated parameters are seen as unnecessary parameters to adjust the model output to the measurements. They are consequently advised to be removed from the model. However, for the considered cases, removing these parameters would lead to a non-physical model structures. But, based on the results of the identifiability analysis, these parameters are no longer seen as unnecessary for the considered model structure. They are instead regarded as nuisance parameters: individually they have no specific physical meaning but combined they constitute the time constants necessary for accurately estimating the total thermal resistance of the studied building component.

3.3 **Whatever the circumstances?**

The physical interpretability analysis of the previous section was performed for specific measurements of a specific case study: winter measurements of an insulated cavity wall were regarded. In this section, it is shortly verified whether the conclusions are still valid under other circumstances. First, the summer measurements of the studied cavity wall are used to estimate the assumed stochastic grey-box models. Based on the results of a profile likelihood analysis, it is verified whether non-identifiable parameters are still indicated by insignificant parameters and whether the reliability of the total thermal resistance is still indicated by its standard deviation. Next, the estimation of stochastic grey-box models from measurement data of another wall type is studied: instead of simulations of a massive wall, simulations of a lightweight wall are envisaged. Here it is studied whether the estimation procedure also results in reliable thermal parameter estimates when other wall compositions are considered.

3.3.1 Summer conditions

Compared to the winter measurements of the cavity wall, the summer measurements are characterised by an increased dynamical behaviour of the external surface temperature. Furthermore, the heat flux does not longer hold a positive value over the entire measurement period, but has a fluctuating course around zero. Also, in the second scenario, no cooling is applied and consequently, the indoor temperature is a free-floating temperature at certain moments in time. Hence, the internal surface temperature is more correlated to the outdoor surface temperature than in the winter measurements, however, the correlations are still rather limited since the internal surface temperature is influenced by various other heat transfer phenomena.

Figure 3.12 represents the results of the profile likelihood analysis for the first till third order models which are estimated from the summer measurements of the cavity wall. Compared to the winter measurements, similar results are obtained: the same order models show the same non-identifiable parameters. Furthermore, it is seen that the shapes of the χ^2_{PL}-curves are of the same nature as the shapes of χ^2_{PL} of the winter measurements. Consequently, non-identifiable parameters will, in all probability, be tested as insignificant parameters. This can be verified based on tables F.1 and F.2 in appendix F, which summarise the estimation and statistical validation results for the summer models in both scenarios.

Only one curiosity is noticed: the parameter R_4 of the third order model in the first scenario (constant) is tested insignificant, although the profile likelihood analysis shows an identifiable parameter. Note, however, that, given the logarithmic scale of the x-axis, the parameter shows a large confidence region compared to its estimation value. Apparently, the unidentifiable region is that large that a second order approximation of the profile likelihood leads to 95% confidence bounds that include the value zero.This finding strengthens the conclusion that the estimated asymptotic standard deviations are only indications of their parameters' identifiability. They must be interpreted carefully and may not be seen as sufficient criteria to decide on the parameters' (non-) identifiability.

Figure 3.13 summarises the estimated thermal parameters of the different order models. The first and second order models in the constant scenario and the first order model in the second scenario show unreliable R-estimates. The periodograms in simulation setting show, however, that these models are falsified (see figure 3.14). Next to that, it is seen that the standard deviations of the combined parameters can be trusted as indications for their reliability. Note that in summer, the fourth order model in the second scenario shows a reliable C_{tot}-estimate despite some insignificant individual

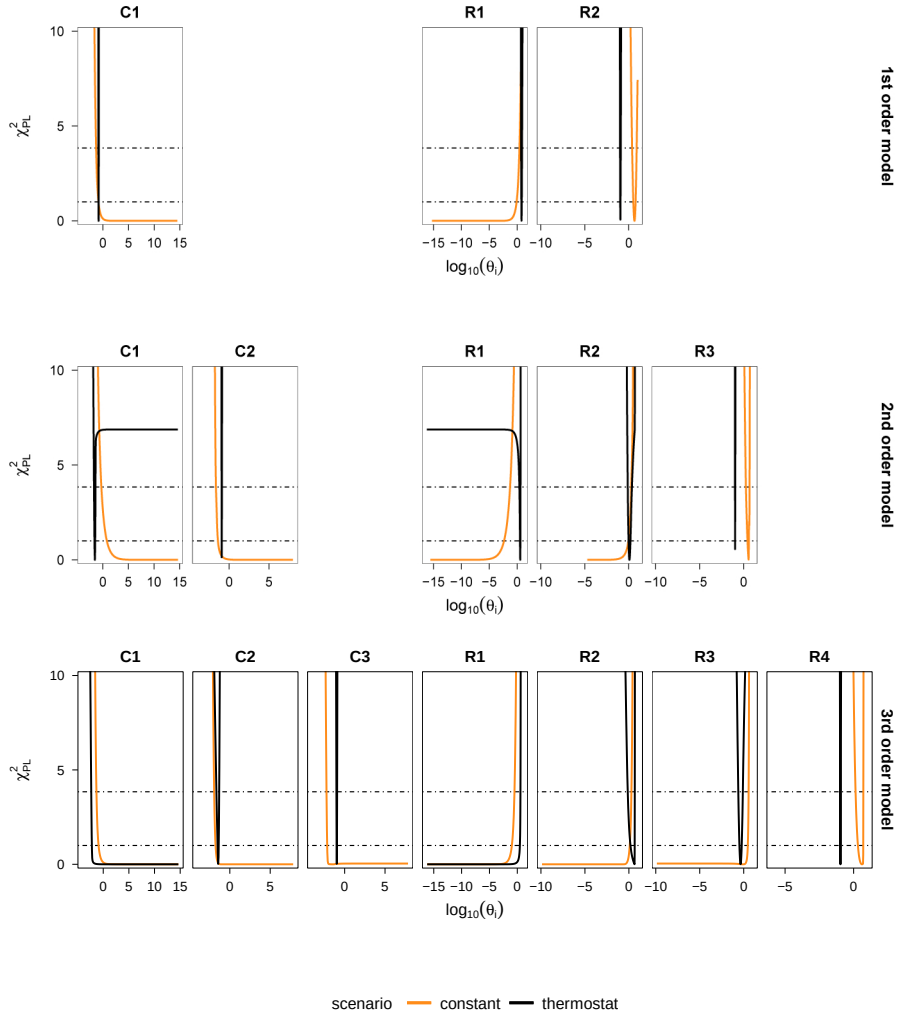

Figure 3.12: The profile likelihood, represented by χ^2_{PL}, of the thermal model parameters estimated from the summer measurements. The results for the different model orders are ordered row wise. The different model parameters are ordered column wise. Results for the two considered scenarios are shown in a different colour. The threshold for the point-wise confidence intervals $\Delta_{0.95}$ and $\Delta_{0.862}$ are represented by the dotted horizontal lines.

C_i-estimates (table F.2d in appendix F). Thus, in some cases, the correlations between the individual capacitances is as such that the total thermal capacity is estimated reliably. In that case, this will be indicated by the combined standard deviation of C_{tot}.

In sum, it can be stated that the seasonal differences between winter and summer measurements do not alter the analysis of the estimation results significantly. The conclusion that insignificant parameters are indications of non-identifiable parameters is still mainly valid, although it is added that insignificant parameters can also indicate parameters with a large unidentifiable region. Next to that, it is confirmed that the combined standard deviations indicate reliably estimated total thermal parameters.

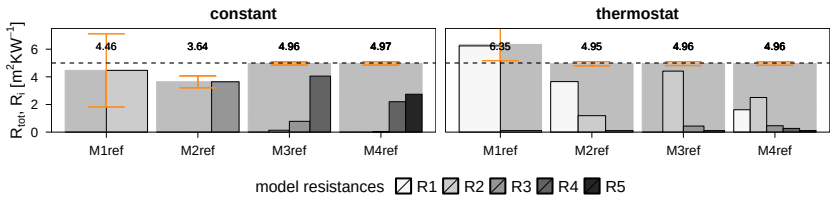

(a)

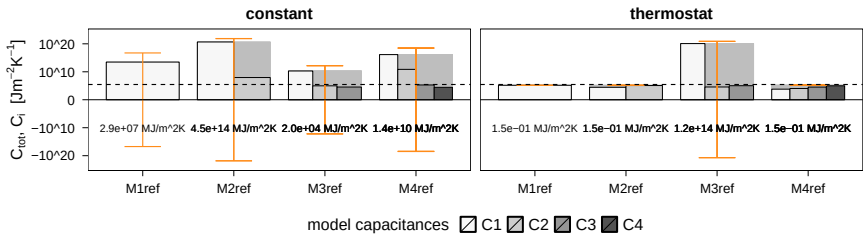

(b)

Figure 3.13: The thermal resistances (a) and capacitances (b) of the four different order models estimated from the summer measurements of both scenarios. The individual model resistances R_1 till R_5 and model capacitances C_1 till C_4 are represented versus a solid grey block corresponding to the total estimated resistance R_{tot} and to the total estimated capacitance C_{tot} respectively. Note that the thermal capacitances are represented against a logarithmic y-axis in $Jm^{-2}K^{-1}$, while the labels of C_{tot} are represented in $MJm^{-2}K^{-1}$. The dotted lines represent the reference values of the wall calculated from the properties used to simulate the measurement data. The first till fourth order models are denoted M1ref, M2ref, M3ref and M4ref respectively.

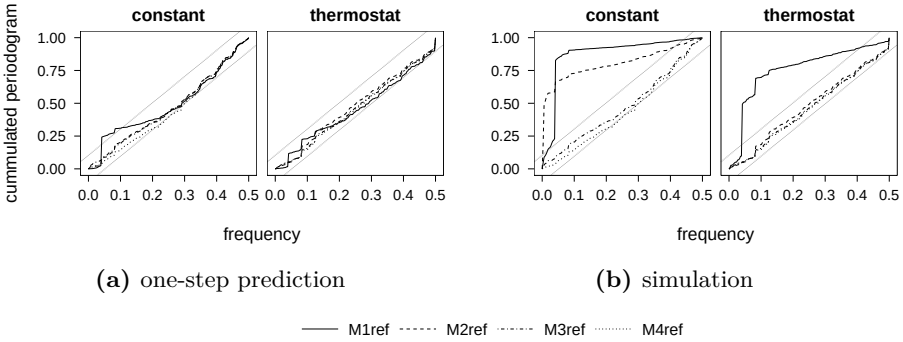

(a) one-step prediction **(b)** simulation

Figure 3.14: The cumulated periodograms of the first till fourth order models estimated on the winter measurements of both scenarios.

3.3.2 Other wall type

Thus far, the possibilities of stochastic grey-box modelling for R-estimation purposes were studied for the example of a heavyweight wall. To ensure that the successful results are not limited to the considered case study, another wall type is studied. As opposed to the heavyweight cavity wall, a lightweight timber frame wall is regarded.

Figure 3.15 represents the considered lightweight wall and table 3.3 summarises the assumed thermal properties. The wall is simulated with HAMFEM and both the scenario with a constant indoor temperature and with a thermostatically controlled indoor temperature are regarded. The simulations assume the same environmental conditions that were considered for the cavity wall, except for the imposed indoor temperature. For the lightweight wall, the indoor temperature is recalculated with TRNSYS, now assuming a two-zone model with lightweight wall-constructions instead of massive ones (see appendix A). Also, the same data periods in winter and summer are considered. System and measurement noise are applied as was done for the cavity wall. Note that the lightweight wall has a thermal resistance of 5.0 m^2KW^{-1}, equal to the R-value of the cavity wall, but that it has a significantly lower thermal capacity.

Figure 3.16 shows the thermal property estimates of the lightweight wall for the one hourly sampled data in winter and summer and for both scenarios. From this figure it is seen that the thermal resistance of the wall is accurately estimated in all cases when high enough order models are selected. As for the cavity wall, the lower order models are not capable of explaining all the dynamics present in the measurement data, so higher order models are needed. Figure 3.16 also shows that the effective thermal capacity is only accurately estimated for low order models and from dynamically informative

data. This is similar to the C_{tot}-estimation of the cavity wall. For the other cases, the large estimated standard deviations indicate that the unreliable C_{tot}-estimates result from the presence of unidentifiable parameters in the models.

Generally, the characterisation of the lightweight wall leads to estimation results similar to those of the previously studied cavity wall. Hence, it is concluded that stochastic grey-box modelling can be widely applied for the R-estimation of various wall types.

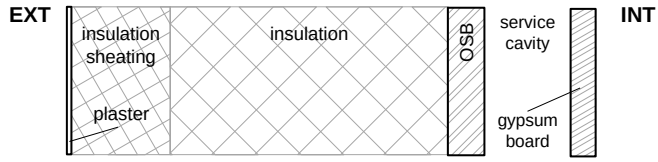

Figure 3.15: Section of the considered lightweight wall.

Table 3.3: Thermal properties of the considered lightweight wall.

	d $[m]$	**λ** $[W(mK)^{-1}]$	**ρ** $[kgm^{-3}]$	**c** $[J(kgK)^{-1}]$	**R** $[m^2KW^{-1}]$	**C** $[MJm^{-2}K^{-1}]$
exterior plaster	0.008	0.700	1300	1000	0.011	0.010
insulating sheating	0.040	0.044	180	840	0.909	0.006
mineral wool blankets	0.130	0.035	70	840	3.713	0.008
OSB	0.018	0.130	650	1880	0.138	0.022
vapour barrier						
service cavity	0.040	0.222	1.25	1000	0.180	5.00e-05
gypsum board	0.012	0.250	900	1050	0.048	0.011
TOTAL					**5.000**	**0.057**

3.4 **Fine-tuning settings for optimal R-estimation**

Stochastic grey-box modelling for R-estimation purposes is not a blindly applicable estimation method; it requires choices to be made by the modeller. This section discusses the influence of the main choices that are required. First, the influence of the averaging time of the measurement data is discussed. Subsequently, the consequences of the model order choice are addressed and finally, it is discussed how the assumption of other model structures influences the R-estimation results.

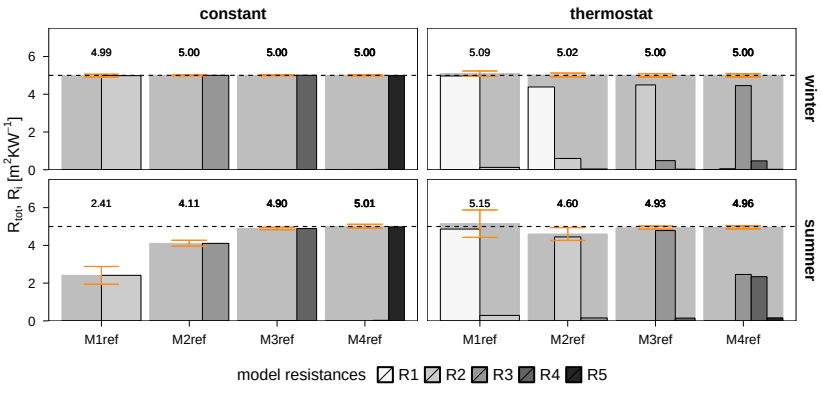

(a)

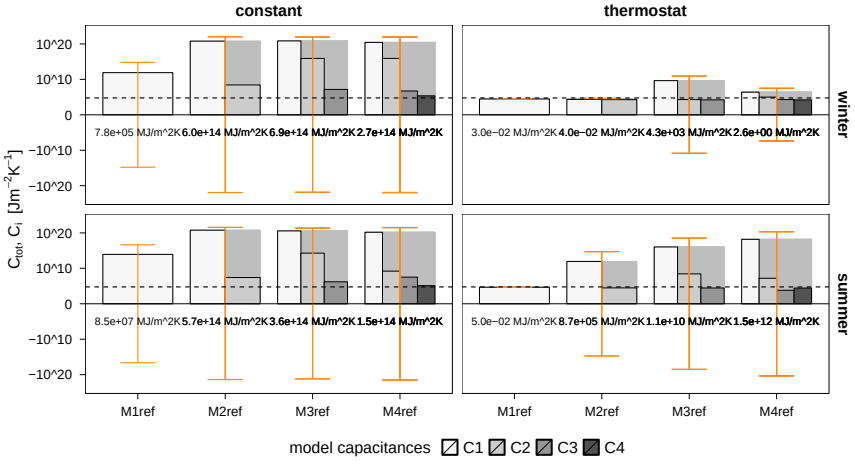

(b)

Figure 3.16: The thermal resistances (a) and capacitances (b) of the four different order models estimated from the winter and summer measurements of both scenarios for the lightweight wall. The individual model resistances R_1 till R_5 are represented versus a solid grey block corresponding to the total estimated resistance R_{tot}. Analogously, the individual model capacitances C_1 till C_4 are represented versus the total estimated capacity C_{tot}. Note that the thermal capacitances are represented against a logarithmic y-axis in $Jm^{-2}K^{-1}$, while the labels of C_{tot} are represented in $MJm^{-2}K^{-1}$. The dotted lines represent the reference values of the wall calculated from the properties used to simulate the measurement data. The first till fourth order models are denoted M1ref, M2ref, M3ref and M4ref respectively.

3.4.1 Influence of averaging time

First, it is examined to which extent the averaging time of the measurement data influences the thermal resistance estimation. Basically, by averaging, high frequency content is removed from the measurement data. This means that frequencies higher than the Nyquist frequency, which corresponds to variations with a period of two times the sampling period, are filtered out of the signal. For example, for hourly sampled data, only dynamics corresponding to a period longer than 2 hours will be represented accurately in the data. Dynamics corresponding to shorter periods will no longer be correctly modelled in the sampled data. Given that, the frequency spectrum of data with a larger sampling period (or lower sampling rate) contains less high frequency content than the frequency spectrum of data with a shorter sampling period (or higher sampling rate). Averaging can have both positive and negative consequences for the identification of systems. On the one hand, by averaging the data, high frequency content is removed and valuable information about the system's behaviour can be lost. Even more, the removed high frequency content is reproduced at lower frequencies when no low-pass filter is applied. This introduces additional noise on the signal or, in worst case, aliasing problems. On the other hand, high frequency phenomena do often not contribute to the estimation of stationary parameters. Hence, the removal of high frequencies, possibly complicating the estimation procedure, can be advantageous. The optimal averaging period of the data will have to balance between both arguments. In essence, the averaging period must reflect the use of the model and should be set depending on the required level of details [39]. Since the main focus of this dissertation lies on the estimation of the stationary thermal resistance, the averaging period can be relatively large.

To study the effects of the averaging period on the thermal resistance estimation, the case study of the insulated cavity wall is reconsidered. Therefore, different order models are estimated from the previously selected winter and summer data for the following averaging periods: 15 minutes (0.25 hours), 30 minutes (0.50 hours), 1 hour, 2 hours, 3 hours, 4 hours and 6 hours. Also, both scenarios defined in chapter 2 are considered.

First, the frequency spectrum of the measurement data is examined. Figure 3.17 represents the frequency spectrum, after eliminating the mean value, of the minutely simulated measurement inputs, i.e. the surface temperatures T_{si} and T_{se}, and output, i.e. the heat flux q_{hfm}. The vertical dotted lines in the figure indicate the frequencies that correspond to some important periods in the data. The figure shows that the most important frequencies in the data are associated to variations with a period larger than 12 hours. This means that, by averaging the data up to 6 hourly values,

no significant information is removed from the data. Only the winter period in the scenario with a thermostatically controlled indoor temperature shows some amplitude peaks corresponding to variations with smaller periods.

To verify whether averaging the data does indeed not influence the R-estimation of the considered wall, the thermal resistance estimates are examined. Figure 3.18 represents the total thermal resistance estimates and their accuracy for all models, both data periods and all averaging periods. The results for the different models are ordered row-wise; the results for the different averaging periods column-wise. Figure 3.18a summarises the results for the scenario with a constant indoor temperature and figure 3.18b for the scenario with a thermostatically controlled indoor temperature.

From figure 3.18a it can be seen that the averaging period does not influence the estimation results for the scenario with a constant indoor temperature. In winter only very small differences in R-estimates are noticed. In summer, it is seen that the accuracy of the estimates of the first and second order models increases for larger sampling periods. However, these findings are most likely linked to the decreasing measurement noise that results from averaging the data (white noise decreases when sampled). The fact that second order models underestimate the reference R-value of 5.0 m^2KW^{-1} is seen for all averaging periods and is hence not linked to the sampling periods.

For the scenario with a thermostatically controlled indoor temperature, the estimation results are summarised in figure 3.18b. Here, it is seen, that in winter, the accuracy of the R-estimates is lower for the 15 minutely sampled data than for the other considered averaging periods, resulting in unreliable R-estimates. In summer, the short averaging periods show even worse results: the 15- and 30-minutely sampled data result in incorrect thermal resistance estimates, while the data sampled with larger averaging periods do result in correct R-estimates. Although, the frequency spectrum of the perturbation signals showed no specific small frequency content, low sampling periods do hinder the estimation process for the second scenario. Possibly, this is due to the fact that changes in the internal surface temperature T_{si} are directly noticeable in the observed heat flux q_{hfm}. So, even high frequency variations with a small amplitude are important for the input-output characteristic of T_{si} to q_{hfm}. Hence, they need to be modelled carefully. Apparently, an accurate one-step ahead prediction of these short fluctuations is of more importance than the one-step ahead stationary behaviour.

So, although typical boundary conditions are mainly characterised by fluctuations with a period longer than 12 hours, small fluctuations can hinder the estimation process. Therefore, if the focus is entirely on the estimation of the stationary thermal resistance,

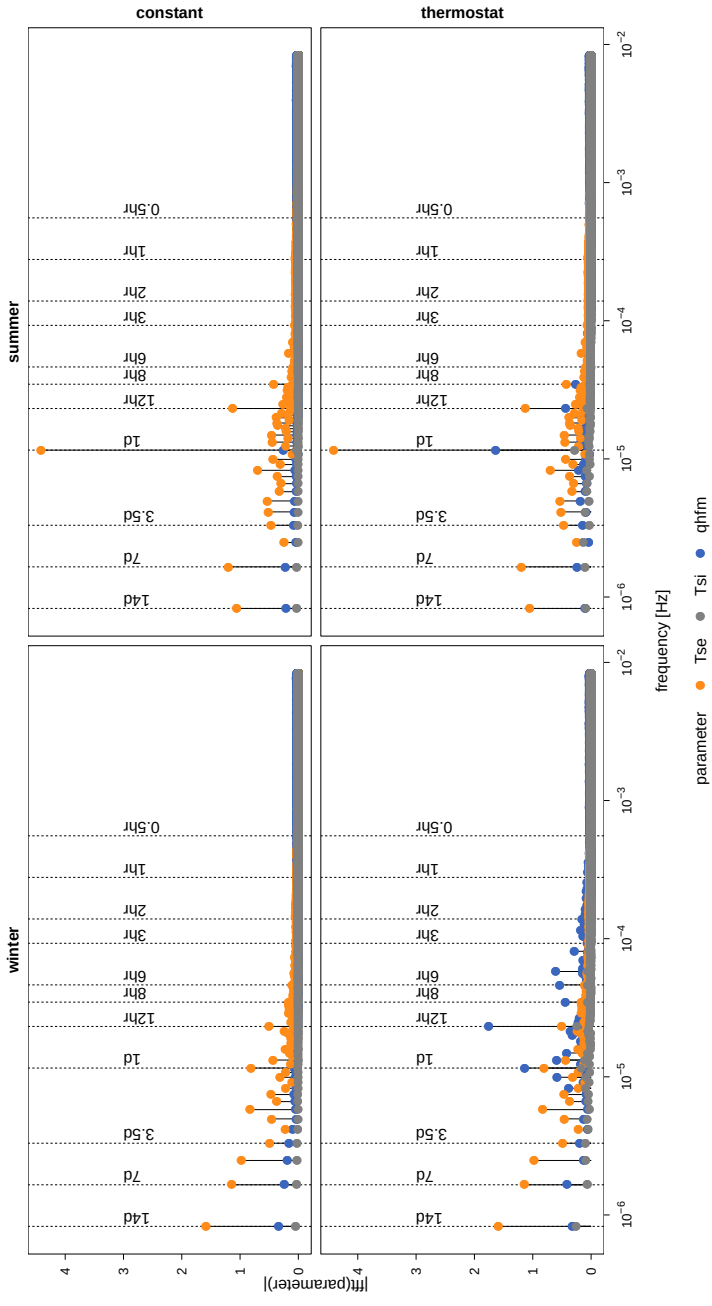

Figure 3.17: The frequency spectrum, after eliminating the mean value, of the minutely simulated inputs, i.e. the external and internal surface temperatures T_{se} and T_{si} respectively, and output, i.e. the heat flux q_{hfm}. The vertical dotted lines indicate the frequencies corresponding to some main periods in the data.

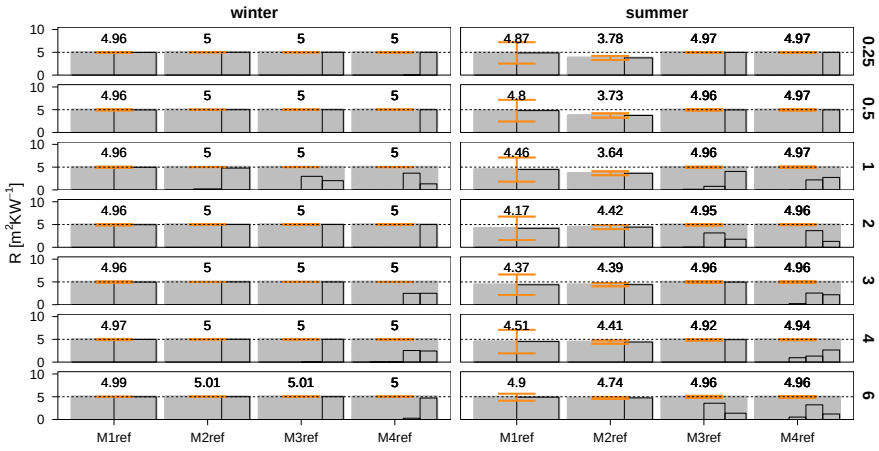

(a)

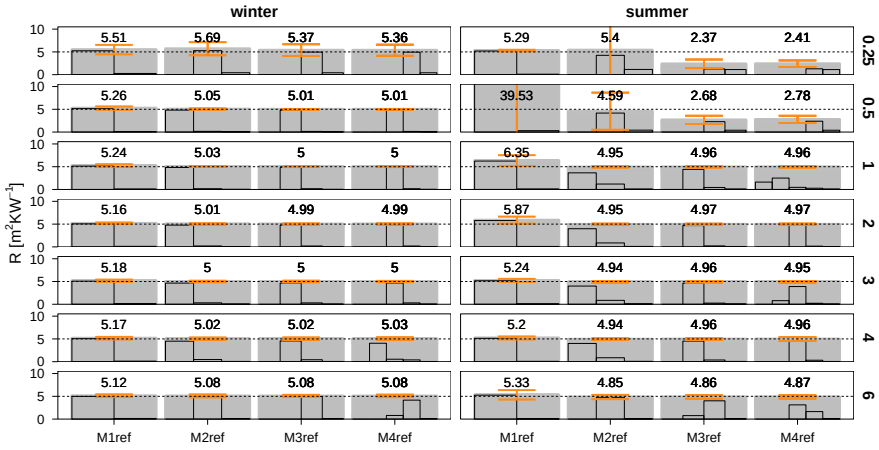

(b)

Figure 3.18: The thermal resistances of the four different order models estimated from the winter and summer measurements of (a) the scenario with a constant indoor temperature and (b) the scenario with a thermostatically controlled indoor temperature. Hereby different averaging period are considered: 15 minutes (0.25 hours), 30 minutes (0.50 hours), 1 hour, 2 hours, 3 hours, 4 hours and 6 hours. The dotted lines represent the reference value of the wall calculated from the properties used to simulate the measurement data. The first till fourth order models are denoted M1ref, M2ref, M3ref and M4ref respectively.

the averaging period can be assumed relatively long. In [39], an averaging period period between 1 and 6 hours is proposed for an application of the characterisation of buildings or building components.

3.4.2 Influence of model order

Previously, section 3.2.3 discussed the selection of the optimal model from a set of candidate models with a different order intended for physical parameter estimation purposes. This section does not further elaborate on this; it rather wants to shed a light on the different thermal behaviour of lower and higher order models. Therefore, Bode plots of different order models are examined.

Bode diagrams represent the frequency response of a model: they show the influence of the inputs on the model output as a function of the input frequencies. Both amplitude and phase shift of the frequency response are typically examined. Figure 3.19 represents the Bode diagrams of the first till fourth order models fitted on the one hourly measurement data of the scenario with a thermostatically controlled indoor temperature. As two inputs and one output are present in the model, two input-output characteristics must be considered. Figure 3.19 shows that the different order models coincide with each other over the lower frequency zones, but that from a certain frequency on, the models start to behave differently. Except maybe for the first order model which also behaves somewhat different for the lower frequencies. Nevertheless, the models distinguish themselves from one another by their performance in the higher frequency zones: the higher the order, the more accurate the description of the higher frequency harmonics.

Of course, a model only needs to be as precise as the normal operational conditions require. This often means that a model needs to be accurate only over a limited range of frequencies. If in this zone, the frequency response of a lower order model coincides with the response of a higher order model, than there is no need to select the higher order model. However, if this is not the case, than the higher order model could be preferred because of its increased accuracy.

The upper bound of this frequency range over which a model needs to be accurate is influenced by several aspects. The first aspect is the averaging time. As mentioned in the previous section, harmonics higher than the Nyquist frequency cannot be known from the sampled measurement data since these harmonics are masked by the averaging itself. Hence, the Nyquist frequency is the absolute upper boundary of the operational frequency range of the model. Consequently, data with a shorter averaging period are more likely to require higher order models. However, from the analysis in the

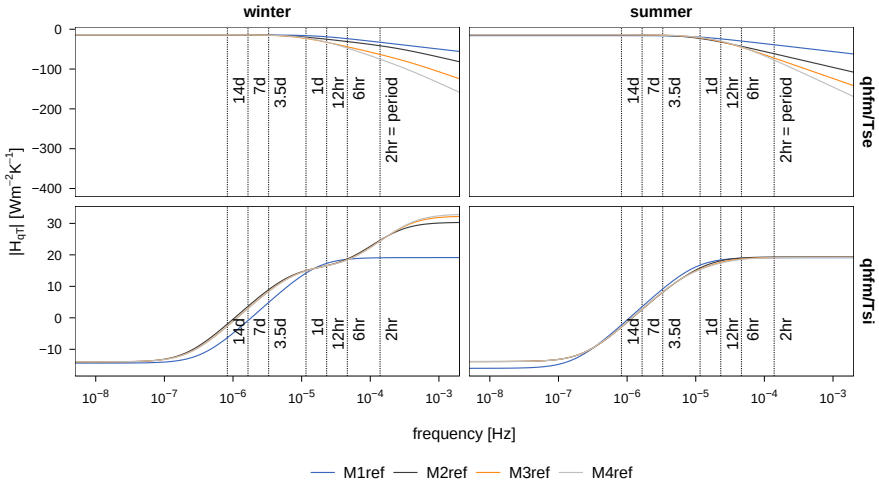

(a)

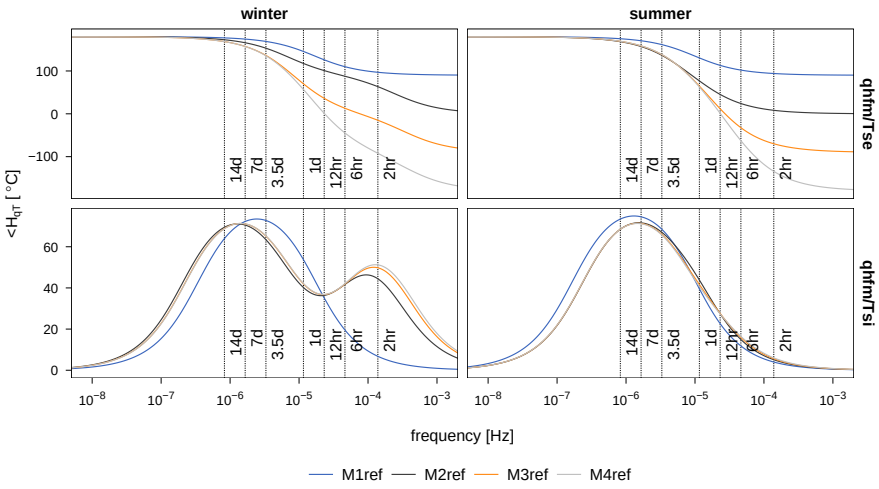

(b)

Figure 3.19: Bode diagram of (a) the amplitude and (b) phase angle of the input-output characteristics of the first till fourth order models estimated from the winter and summer measurements of the scenario with a thermostatically controlled indoor temperature.

previous section, this was not seen: the same order models were needed in order to obtain accurate R-estimates from the data with different averaging times. Hence, the upper bound of the operational frequency range must be restricted to a lower value by another aspect.

A second factor influencing the operational frequency range concerns the main harmonics of the input signals. It is logic that a model does not need to behave very accurate at high frequencies when the measurements have no high frequency content.

Next to that, the operational frequency range is influenced by a third aspect, which takes into account the achievable accuracy of the measurements. Let us assume for a moment that only variations higher than 1 Wm^{-2} can be measured by the indoor heat flux meter. To be able to measure such a variation as a result of a change in outdoor surface temperature, the variation of this surface temperature has to be large enough. If this is not the case, the signal will be damped out too much in order to be measurable at the inside. Capacitive building components will damp out the signals more than lightweight building components. Consequently, the operational frequency range is influenced by the achievable accuracy of the measurements and by the capacitive properties of the studied component. Figure 3.20 shows the minimal variations in amplitude of the surface temperatures that are required in order to measure a change in interior heat flux of 1 Wm^{-2}.

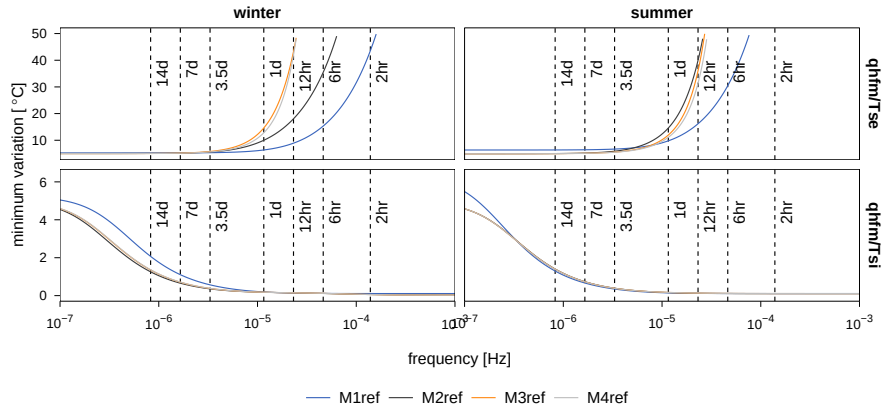

Figure 3.20: The minimum variation in °C of the external surface temperature (top row) or internal surface temperature (bottom row) required to be able to measure a variation of 1 Wm^{-2} with the internal heat flux sensor.

In sum, this section did not give practical guidelines on selecting an optimal model order, but gave a more detailed view on the factors influencing the required model order. Shortly, the sampling time, the main harmonics of the perturbation signals, the achievable accuracy of the measurements and the capacity of the studied component affect the range over which a model needs to be operational. Consequently, these factors also influence the required model order.

3.4.3 Influence of model type

From the identifiability analysis, it followed that the typical dynamic excitation conditions from the outdoor climate are often not informative enough to estimate fully identifiable models. In this section, it is studied whether simplifications of the considered model structure can improve the identifiability.

So far, the considered model structures relied on the analogy between heat transfer in materials and currents in electrical circuits. No further physical knowledge was used. However, in order to improve the reference models' identifiability, the insignificant parameters are advised to be removed. In order to reduce the number of model parameters, assumptions about the internal structure of the wall have to be made. Consequently, based on those assumptions, simplified models can be formulated. The model structures that are discussed in this section are all visually represented in figure 3.21.

Capacitance layer model

Thus far it is the identification process that determines the *location* of the model capacitances, since the values of the model resistances are estimated without any prespecified restrictions. It is, however, not illogical to assume that each model capacitance is placed between two resistances of the same size. In that case, it is assumed that the capacity of a layer is always lumped in the middle of a layer. Compared to the reference model, which has 2n+1 parameters for a model of order n, the new model structure has 2n parameters that need to be estimated.

The model structure, visually represented in figure 3.21, can be formulated as

$$dT_{i=1} = \frac{1}{C_1 \frac{R_1}{2}}(T_0 - T_1)dt + \frac{1}{C_1 \frac{(R_1+R_2)}{2}}(T_2 - T_1)dt + \sigma_i d\omega_i$$

$$dT_{i=2,..,n-1} = \frac{1}{C_i \frac{R_{i-1}+R_i}{2}}(T_{i-1} - T_i)dt + \frac{1}{C_i \frac{R_i+R_{i+1}}{2}}(T_{i+1} - T_i)dt + \sigma_i d\omega_i$$

$$dT_{i=n} = \frac{1}{C_n \frac{R_{n-1}+R_n}{2}}(T_{n-1} - T_n)dt + \frac{1}{C_n \frac{R_n}{2}}(T_{n+1} - T_n)dt + \sigma_i d\omega_i \quad (3.35)$$

$$q_{hfm} = \frac{2}{R_n}(T_{n+1} - T_n) \quad (3.36)$$

Since the reference model had most identifiability issues for the winter measurements of the scenario with a constant indoor temperature, this data is used to estimate the new model types. Table 3.4 summarises the results of the reference model (and of the model types studied hereafter) mentioning whether these models are fully identifiable, which parameters are not identifiable and what the total R- and C-estimates are. The identifiability results are derived from the significant tests of the individual model parameters. Table 3.4(first and second row) shows that the *capacitance layer model* does only improve the identifiability of the first order model. Second and higher order models of the new model type show to be not fully identifiable. Hence, this model type does not extensively improve the estimation results nor the identifiability compared to the reference model structure. So, more profound simplifications are studied.

Table 3.4: Summary of the estimation results of the different model types for the winter measurements of the scenario with a constant indoor temperature. The table represents which models are unidentifiable and which are the non-identifiable parameters based on the significance testing of the latter. The estimation results of R_{tot} $[m^2KW^{-1}]$ and C_{tot} $[MJm^{-2}K^{-1}]$ are also represented.

	identifiable? non-identifiable **Rtot**	**Ctot**	**identifiable?** non-identifiable **Rtot**	**Ctot**	**identifiable?** non-identifiable **Rtot**	**Ctot**	**identifiable?** non-identifiable **Rtot**	**Ctot**
	order 1		**order 2**		**order 3**		**order 4**	
Reference model	FALSE R1, C1		FALSE R1-2, C1-2		FALSE R1-2, C1-2		FALSE R1-3, C1-4	
	4.96	3.21E+12	5.00	4.53E+14	5.00	1.45E+11	5.00	7.66E+07
Capacitance layer model	TRUE /		FALSE R1, C1		FALSE R1-3, C1-3		FALSE R1-4, C1-4	
	4.96	5.69E-02	5.00	9.55E+04	5.00	8.23E+01	5.00	8.51E+06
Semi-homogeneous model	TRUE /		TRUE /		TRUE /		FALSE R2-3	
	4.96	5.69E-02	5.00	5.48E-02	5.00	5.66E-02	5.00	5.74E-02
Homogeneous model	TRUE /		TRUE /		TRUE /		TRUE /	
	4.96	5.69E-02	4.99	4.83E-02	5.00	5.00E-02	5.00	5.14E-02

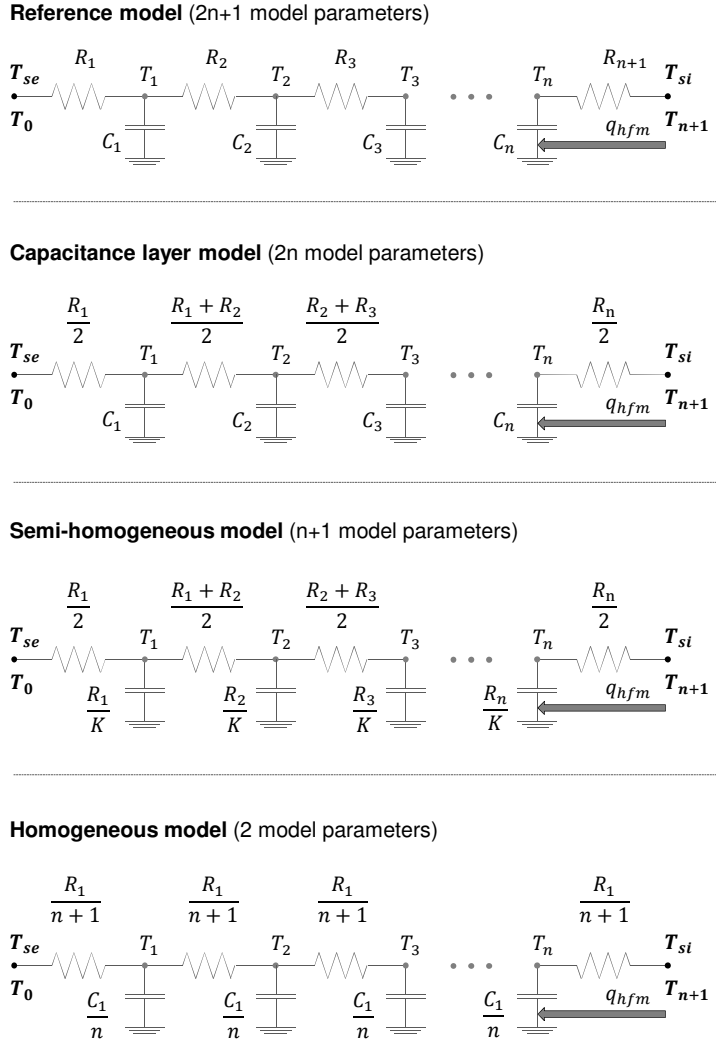

Figure 3.21: Different model types used to describe the heat transfer in building components represented as RC-networks.

Semi-homogeneous model

To further reduce the number of model parameters, a constant ratio between the thermal capacitance C_i and thermal resistance R_i of each layer can be assumed. As such, the diffusivity is considered equal over the entire wall. Given the considered cavity wall, it is clear that this assumption does not match the reality. However, due to the lack of dynamic information in the perturbation signals, it is justified to simplify the wall description and to represent it as an *equivalent* semi-homogeneous component. In [89], this model type is seen as an interpretation of a *homogeneous* model. However, in the present work, it is denoted as semi-homogeneous, since the next model structure still goes a step further towards representing homogeneous building components. For a model of order n, the semi-homogeneous RC-structure has n+1 model parameters. A visual representation of this model type is given in figure 3.21 and a mathematical description is given below

$$
\begin{aligned}
dT_{i=1} &= \frac{1}{R_1 K \frac{R_1}{2}}(T_0 - T_1)dt + \frac{1}{R_1 K \frac{(R_1+R_2)}{2}}(T_2 - T_1)dt + \sigma_i d\omega_i \\
dT_{i=2,..,n-1} &= \frac{1}{R_i K \frac{R_{i-1}+R_i}{2}}(T_{i-1} - T_i)dt + \frac{1}{R_i K \frac{R_i+R_{i+1}}{2}}(T_{i+1} - T_i)dt + \sigma_i d\omega_i \\
dT_{i=n} &= \frac{1}{R_n K \frac{R_{n-1}+R_n}{2}}(T_{n-1} - T_n)dt + \frac{1}{R_n K \frac{R_n}{2}}(T_{n+1} - T_n)dt + \sigma_i d\omega_i \\
q_{hfm} &= \frac{2}{R_n}(T_{n+1} - T_n)
\end{aligned}
$$

From table 3.4, it is seen that this model type improves the identifiability of the first, second and third order model. The fourth order model has too many parameters to be fully identifiable. Note that the estimated total effective capacities of the identifiable models are estimated quite low compared to the wall's reference. The value is, however, equal to the estimated value of the identifiable first order capacitance layer model.

Homogeneous model

The number of parameters can still be further reduced by assuming a fully homogeneous model to describe the cavity wall. In such a model, the total thermal resistance and effective capacity are evenly distributed over the wall. Hence, for a model of order n, only 2 parameters need to be estimated. Again, this is not in accordance with reality, however, the lack of information in the perturbation signals justifies to model the wall as an equivalent homogeneous structure. This homogeneous RC-model is visually represented in figure 3.21 and is mathematically described as

$$dT_{i=1,..,n} = \frac{1}{\frac{C_1}{n}\frac{R_1}{n+1}}(T_{i-1} - T_i)dt + \frac{1}{\frac{C_1}{n}\frac{R_1}{2}}(T_{i+1} - T_i)dt + \sigma_i d\omega_i \tag{3.37}$$

$$q_{hfm} = \frac{n+1}{R_1}(T_{n+1} - T_n) \tag{3.38}$$

Table 3.4 shows that all four order models are now fully identifiable. Furthermore, the total thermal resistance is correctly estimated by all model orders. The total effective C-estimates, on the other hand, are again estimated by the same value as for the previous model types. It is hard to say whether this rather low value is the true *effective* capacity of the wall in winter, or whether it is a result of the simplified model assumptions.

For completeness, let us also consider the application of these simplified models for a dynamically more informative data set, e.g. the winter measurements of the second scenario, i.e. with a thermostatically controlled indoor temperature. Table 3.5 summarises the results analogously to table 3.4. From this table, it is confirmed that the practical identifiability of the reference model improves by simplifying this model structure. But, for the considered scenario, this improved identifiability goes at the expense of the correctness of the R_{tot} and C_{tot}-estimates. The latter are wrongly estimated in a lot of cases. Basically, this results from the fact that, for more dynamically informative excitations, the assumption of, for example, an equivalent homogeneous wall does not longer hold. Luckily, the inappropriateness of such model assumptions are indicated by the periodograms of the residuals in simulation setting, as can be seen from figure 3.22.

In sum, thus far it is observed that simplified model structures can improve the structural identifiability of the reference model type. This knowledge can be useful when, for example, the effective thermal capacity needs to be estimated from measurement data that is not dynamically informative enough. Nevertheless, the estimated C_{tot}-values must be interpreted very carefully and it must be verified whether the assumptions for the internal model structure hold for the considered measurements. By contrast, when only the estimation of the total thermal resistance R_{tot} is of interest, the question can be raised why simplified models should be preferred: it has actually already been proven that the reference model structure always lead to reliable R_{tot}-estimates. Well, in most cases the simplified model structures are more robust in ways of optimisation. This might not surprise, since the goal function of an identifiable model has a clear optimum instead of an extensive set of optima.

Table 3.5: Summary of the estimation results of the different model types for the winter measurements of the scenario with a thermostatically controlled indoor temperature. The table represents which models are unidentifiable and which are the non-identifiable parameters based on the significance testing of the latter. The estimation results of R_{tot} $[m^2KW^{-1}]$ and C_{tot} $[MJm^{-2}K^{-1}]$ are also represented.

	identifiable? non-identifiable **Rtot**	**Ctot**	**identifiable?** non-identifiable **Rtot**	**Ctot**	**identifiable?** non-identifiable **Rtot**	**Ctot**	**identifiable?** non-identifiable **Rtot**	**Ctot**
	order 1		**order 2**		**order 3**		**order 4**	
Reference model	TRUE /		TRUE /		FALSE R1, R4, C1		FALSE R1-2, R5, C1-2	
	5.24	8.74E-02	5.03	1.55E-01	5.00	2.06E+13	5.00	4.38E+14
Capacitance layer model	FALSE C1		FALSE C1		FALSE R3		FALSE R1, R4, C1	
	0.32	3.58E+01	0.47	3.82E+01	5.00	1.55E-01	5.00	1.63E+03
Semi-homogeneous model	FALSE K		TRUE /		TRUE /		FALSE R1	
	0.32	3.58E+01	3.22	1.29E+00	23.07	1.01E+01	32.75	1.43E+01
Homogeneous model	FALSE C1		TRUE /		TRUE /		TRUE /	
	0.32	3.58E+01	0.47	1.24E+01	0.60	1.06E+00	0.69	6.83E-01

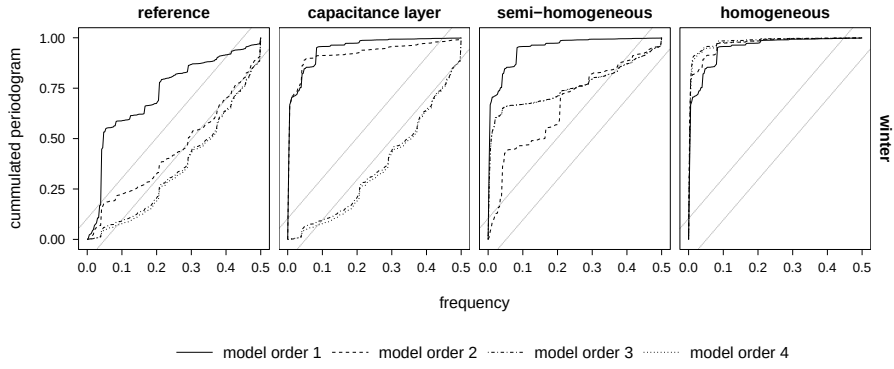

Figure 3.22: The cummulated periodograms in simulation setting of the first till fourth order models of the different model types estimated from the winter measurements of the scenario with a thermostatically controlled indoor temperature.

3.5 Guidelines for physical parameter estimation with stochastic state space models

The present chapter examined the potentials of stochastic grey-box modelling as a tool for the thermal characterisation of building components from on-site measurements. Hereby, typical lumped capacitance-resistance models were considered. Generally, the method was found successful for this purpose: the total thermal resistances of all the studied walls were accurately estimated, or, inaccurately estimated thermal resistances could be pinpointed based on the statistical validation criteria. However, in general the physical interpretability of the considered stochastic grey-box models was found to be not straightforward.

First, it was observed that the physical interpretability of the individual model parameters is uncertain. Although a physical model structure is assumed, the individual model resistances and capacitances of an (identifiable) lumped parameter model cannot be clearly pinpointed to the separate layers of the wall. A more complicated relation between the physical properties and the model parameters is playing [88] as a consequence of the simplification that is made by modelling a distributed system by a lumped system.

Nevertheless, the physical significance of the total thermal parameters $R_{tot} = \sum R_i$ and $C_{tot} = \sum C_i$ remains. Since the assumed model type is proven to be structurally identifiable, their physical interpretability is mainly influenced by the models' practical identifiability. The profile likelihood analysis revealed that the data-based identifiability of the considered models certainly is an issue for the considered characterisation problem. Common measurement data of building components often lack the dynamical information required to estimate the models' thermal parameters individually. For the considered case studies, however, it was seen that the presence of non-identifiable parameters in a model does not affect the total thermal resistance estimation. By contrast, it does affect, in most cases, the estimation of the effective thermal capacity C_{tot}.

Although it has been proven that the profile likelihood approach is an effective method to track structural and practical identifiability issues, it is a computationally time intensive method. Hence, it would be impractical to apply the method for every estimation process. Therefore, this chapter looked for indications of non-identifiability in the statistical validation criteria of the individual parameters. It was found that the asymptotic standard deviations are good indicators to detect a parameter's non-identifiability. This might not surprise since the asymptotic standard deviations are a second order approximation of the profile likelihood confidence bounds which are

linked to the identifiability concept. For the considered models and measurements, the profile likelihood analysis revealed that the nature of most parameters' unidentifiability is as such that the unidentifiable parameters are indicated by insignificant parameters. The latter implies that the asymptotic standard deviations have an equal or larger order of magnitude than the parameter estimate itself. So, basically, these findings say that the asymptotic standard deviations are a good measure of the unidentifiable region, or confidence region, of the model parameters. Hence they can be used to judge on the parameter's reliability. It was seen that the latter also applies for the combined standard deviations of the total thermal parameters. In essence, these findings are not ground breaking and might even seem rather trivial. However, without the understanding of the underlying identifiability issues, a lot of the considered estimated models would be labelled as inappropriate based on the parameter validation criteria. Typically, insignificant or highly correlated parameters are seen as unnecessary parameters to adjust the model output to the measurements and are advised to be removed from the model. Based on the identifiability analysis, these parameters are no longer seen as unnecessary for the considered model structure. They are instead regarded as nuisance parameters that, individually, have no specific physical meaning, but, when combined, are necessary tools for accurately estimating the total thermal resistance of the building component of interest.

The above conclusions were derived from the profound analysis of the stochastic grey-box estimation of an insulated cavity wall. The findings were verified for another wall type and for the most common experimental conditions of in-situ measurements of building components. As such, it is, in the author's opinion, justified to generalise the findings for similar estimation problems. So, based on the information from the previous analyses, a general framework is developed for the validation of models typically used for the estimation of building components from common on-site measurements. This general framework consists of the flowchart represented in figure 3.23.

The flowcharts follows a bottom-up approach, meaning that it starts with a first order model and gradually increases the model's complexity up to the moment that the validation criteria are met. Hereby, a distinction is made between the validation of the models for physical behaviour estimation and for physical parameter estimation. When models are used for physical behaviour estimation, only the accuracy of the modelled heat flux is important. Consequently, the validation can be limited to assessing the model's descriptive capabilities. By contrast, if models are used for physical parameter estimation, further validation is required, since now the identifiability of the parameters of interest is important. Hence, also the individual model parameters are evaluated.

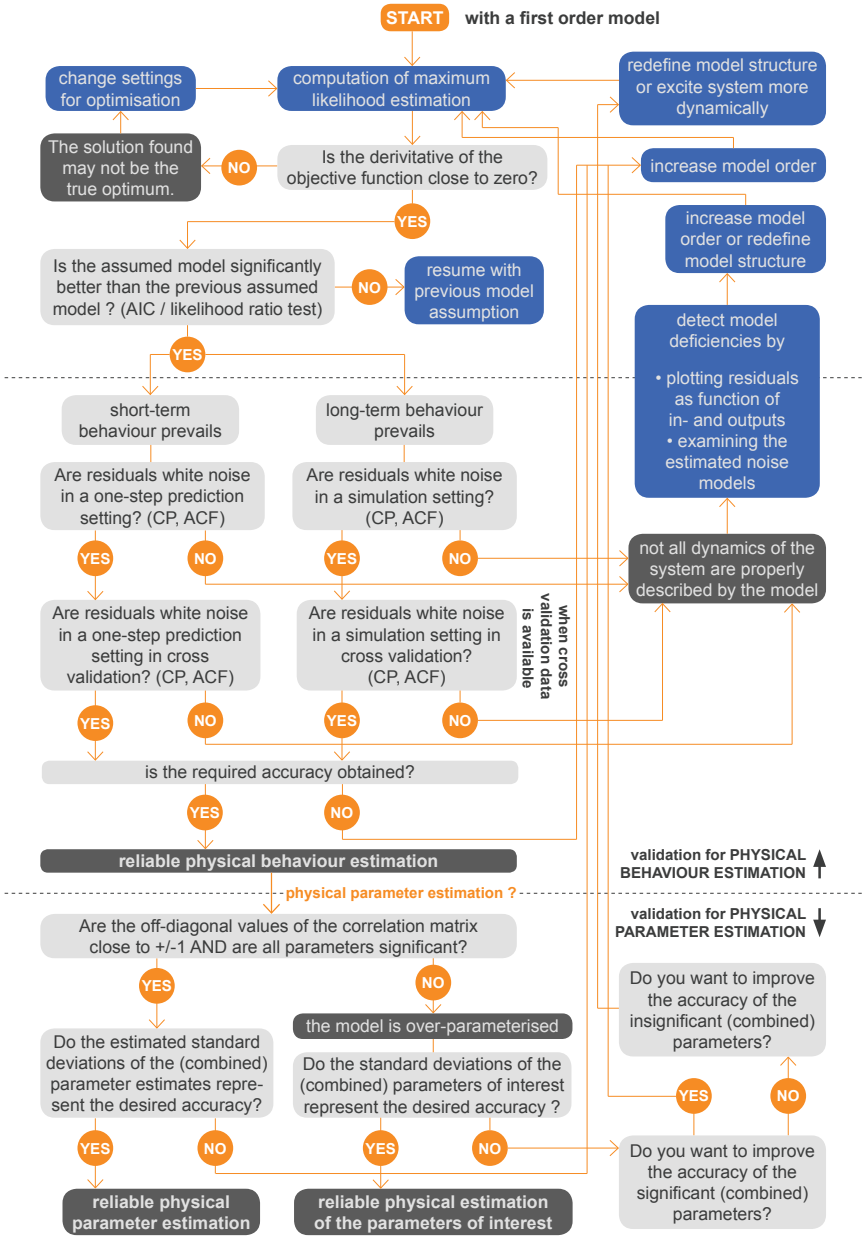

Figure 3.23: Flowchart for the physical behavior and physical properties estimation of typical lumped parameter models from common on-site measurements of building components.

Chapter 4

Comparison of characterisation methods

The main challenge of on-site characterisation methods is handling the influences from outdoor weather conditions in the measurement data. The intrinsically dynamic outdoor climate complicates the estimation of the in essence stationary thermal resistance. Besides, climatic perturbation signals have a seasonally different appearance, therefore demanding versatilely applicable analysis methods. The extent to which the characterisation methods are able to cope with the constantly varying climatic conditions determines their practical applicability, which is exactly what is studied in this chapter. By a large-scale comparison, the performances of all previously discussed characterisation methods are examined for various scenarios and boundary conditions.

4.1 **Methodology**

To evaluate and compare the performance of the different characterisation methods, they are all applied on various data sets of different case studies. In section 4.2, the methods are systematically compared when applied to *simulated* measurement data. In fact, the cases of the insulated cavity wall and timber frame wall, that were introduced in section 2.1 and 3.3.2 respectively, are considered again. By using these walls, the estimation methods' performances can be assessed for both massive and lightweight building element types. As mentioned previously, simulated data might be interesting from a research point of view because of the exact knowledge of the properties of the studied component and because of the controlled and error-free development of the experiments. However, these advantages are at the same time pitfalls: the resulting findings are inconclusive when they can not be validated for real-world experiments. That is why the step towards *actual* measurement data is taken in the third section.

The latter regards real-word experimental data of an insulated cavity wall subjected to a moderate European climate.

The comparative analysis in this chapter gives special attention to the reliability of the methods' estimation results when confronted with data sets of limited measurement time spans and in different seasonal boundary conditions. As such, the boundary condition dependency of the methods can be studied. In order to enable a large-scale comparison, a multitude of data sets with different lengths and from different periods are required. Such data sets are accommodated by constructing various subsets from the main experimental measurement periods of the studied cases. Each of the constructed subsets will be subjected to the different analysis methods and will result in a thermal resistance estimation. The ensemble of the results then allows to study the accuracy of the different methods in function of the measurement time span and of the measurement period throughout the year.

4.2 **Theoretical assessment: simulated measurement data**

4.2.1 Case study: massive vs. lightweight wall

At this stage, the simulated measurement data of the cavity wall and timber frame wall, introduced in sections 2.1 and 3.3.2 respectively, are regarded. This allows a comparison of the methods' performances for both massive and lightweight building components. Remind that the massive wall has a total thermal resistance of 5 m^2KW^{-1} and a total thermal capacitance of 0.284 $MJm^{-2}K^{-1}$, while the lightweight wall has the same total thermal resistance of 5 m^2KW^{-1}, but a much smaller total capacitance of 0.057 $MJm^{-2}K^{-1}$.

Data sets

To study the methods' performances for measurements in different seasons, three main data periods of 60 days are selected from the simulated year of measurements that is available. January and February represent winter data, July and August stand for summer data and April and March are selected to cover mid-seasonal periods. The heat flux and temperature simulations of the massive and lightweight wall are represented in figures 4.1 and 4.2 respectively for these main periods. For the analyses of the massive wall four hourly averaged data is considered, while for the analysis of the lightweight wall hourly averaged data is employed. The shorter averaging period

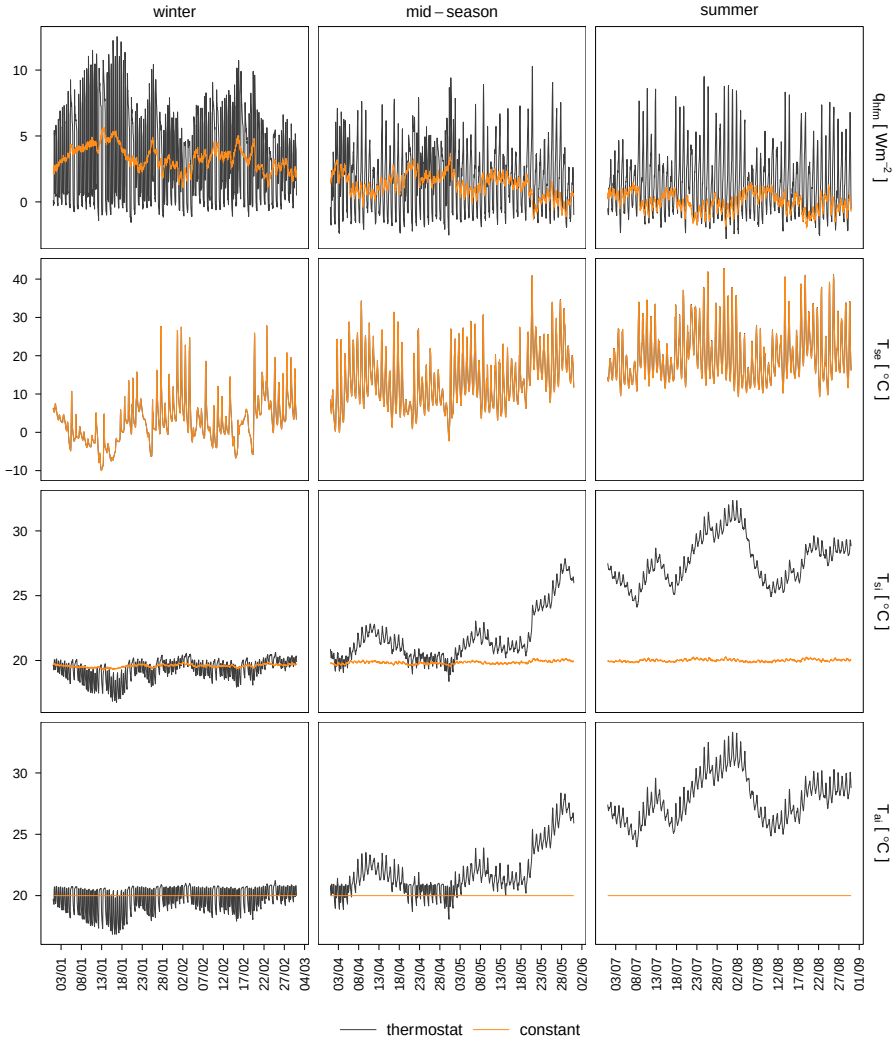

Figure 4.1: Measurement data and indoor temperature of the selected main periods for the massive wall. Data for the different scenarios is distinguished by colour.

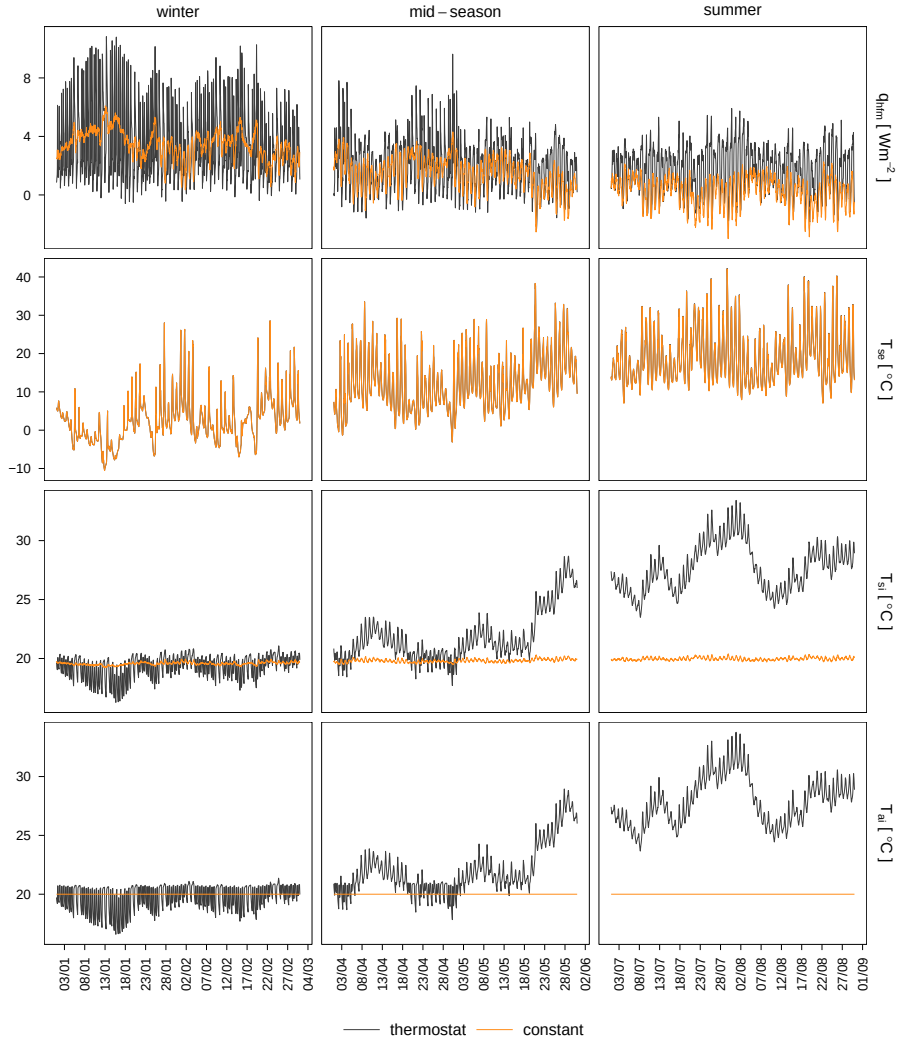

Figure 4.2: Measurement data and indoor temperature of the selected main periods for the lightweight wall. Data for the different scenarios is distinguished by colour.

for the lightweight wall is chosen because of the component's smaller thermal capacity: the wall will respond more rapidly to incoming signals and higher frequency content may be present compared to the massive wall.

To study the methods' performances in function of the measurement time span, various subsets are constructed from the selected main periods. Notably, data sets are considered with lengths ranging from 1 to 30 days, and data sets starting from the 1st of January, April and July till the 30th of these months. The different data sets are constructed by using a moving window approach. For the construction of the subsets, windows with lengths from 1 to 30 days are selected and are advancing with a one day step. This is illustrated in figure 4.3 for a window length of 10 days.

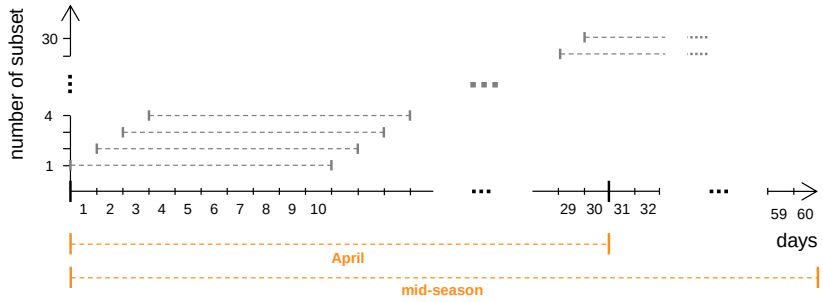

Figure 4.3: Construction of different subsets from the main mid-season period for a window length of 10 days.

Application of characterisation methods

The comparative assessment concerns all methods that were discussed in chapters 2 and 3, notably the average method, the average method corrected for storage effects, Anderlind's regression approach, ARX-modelling and stochastic grey-box modelling. Only the simple linear regression method is not considered. Since the latter showed in chapter 2 to have very similar results to those of the average method, it is left out of the comparative assessment.

Most methods require some assumptions to be made about their application. The choices that are made in the context of this chapter are reported hereafter. First of all, the average method corrected for storage effects demands the calculation of thermal mass factors. In the context of chapter 2, these factors were already calculated for the massive and lightweight wall in appendix B. They are reconsidered in this chapter for the application of the corrected average method.

Furthermore, the application of Anderlind-modelling requires the choice of an *influence time*. Based on the results of chapter 2, an influence time of 1 day is chosen. However, for short data sets, suffering from the fact that the amount of data points for the estimation itself is too little compared to the amount of historical data points in the regression, the influence time is decreased repetitively until a linear regression analysis can be computed.

The same is done for ARX-modelling. A fixed model order corresponding to an influence time of 1 day is initially assumed for all the polynomials in the model. But, when the presence of too many regressors prevents the regression analysis from being computed, then the order of all polynomials is decreased until a regression analysis is possible.

Concerning the stochastic grey-box models, the *reference* models as presented in chapter 3 are applied. Third order models are assumed to be fitted from the winter, mid-season and summer data sets. Similar to the application in chapter 3, each estimation is performed multiple times after which the final result is selected as the one with the highest maximum likelihood. The initial value selection and the boundaries set for the parameter estimation are equal to those applied in chapter 3 and were described in appendix D.

4.2.2 Results

To assess the robustness and reliability of the R-estimates characterised by the different analysis methods, *comparison plots* are constructed. Figure 4.4 is an example of such a *comparison plot*. The idea behind these figures is that each data point represents an R-estimate resulting from a different data set. By plotting the results in function of the length of the considered data set, i.e. the number of days included in the analysed measurement data, the influence of the measurement time span can be examined. To distinguish between the performances for different analysis methods and for different seasonal periods, the figures are organised as follows: the results for the different data periods throughout the year are ordered column wise, while the results for the different analysis methods are ordered row wise, with a repetition of the results for the average method in grey as a reference to the other methods' results. Furthermore, the reference R-value of the studied wall is indicated in each figure as the orange dotted line. The grey dotted lines represent the 5% and 10% accuracy bands around this goal value. On the other hand, the variable grey ribbon accompanying the estimation results represents the maximal estimated 95% confidence intervals, i.e. two times the maximal estimated standard deviation, that are found for every data set length. Note, furthermore, that the boundaries of the y-axis are adjusted to visually capture the

major estimation results. Hence, highly deviating data points might fall outside the boundaries of the graph.

Results for the massive wall: first scenario

Figure 4.4 renders the comparison plot for the case study of the massive wall subjected to an indoor environment with a constant temperature (scenario 1). The results of the **average method** can be examined from the top row of figure 4.4. The top left figure, for example, shows that the R-values estimated from the winter periods converge to the goal value when long enough data sets are considered. Short data sets display a rather large spread on the results. Only for data sets containing 4 days or more, all the results lie within a 10% accuracy band around the goal value. Data periods of around 10 days or longer are required to obtain 5% accurate results in winter. In mid-season (top centred figure), similar results are observed, although longer data sets are required to obtain the same accuracies on the R-estimates. Due to the increased capacitive working of the cavity wall, around 10 to 12 days, or longer are needed to obtain results in between the 10% accuracy band. Also, almost no long enough data periods are examined that result in all R-estimates within a 5% accuracy band. Finally, the R-estimates obtained from summer measurements (top right figure) clearly indicate the limited validity of the average method in summer: no meaningful estimates of the thermal resistance are acquired. That results from the fact that the summer measurements are characterised by small heat flow rates fluctuating around zero, indicating a highly alternating capacitive working of the wall.

If the **correction for storage effects** is applied on the data (second row of figure 4.4), an improvement of the estimation results in winter and mid-season is found compared to the average method. For winter measurements, data sets of around 2 to 3 days already lead to R-values lying within a 10% accuracy band and data sets of 5 days results in R-estimates in a 5% accuracy band around the goal value. For mid-season measurements, data sets containing around 6 and 13 days are required in order to obtain R-values with 10% and 5% accuracy levels. Hence, the correction for storage effects improves the results for winter and mid-season measurements. Note, however, that the correction is applied in an optimal way: the thermal properties that are required for the calculation of the thermal mass factors are exactly known for the studied wall. In reality, accurate thermal properties will rarely be known and hence the improvement of the correction will be less effective, as was studied in chapter 2. Besides, the results from the data sets in summer demonstrate that the correction is not able to improve the results for typical summer measurements with large fluctuations in heat storage.

Beneath the results of the semi-stationary methods in figure 4.4, the results of the dynamic data analysis methods are represented. It is shown that, in case of **Anderlind's regression method**, the R-estimates achieve a fast and accurate convergence to the true value for the measurements of all considered seasons. Data sets of 2 and 3 to 4 days are sufficient to obtain results that all lie within a 10% and 5% accuracy band in winter and mid-season. Data periods of around 4 and 6 days are required for 10% and 5% accurate results in summer. Although, when reckoning with the estimated standard deviations longer data sets are required for obtaining the same accuracies: minimum 6 days are needed in all seasons to obtain 10% accurate results. Nevertheless, figure 4.4 clearly demonstrates the advantage of a dynamic data analysis by the all-round applicability of the methods.

The estimates deduced from the **ARX-models** (figure 4.4) are very similar to the results of Anderlind's model, which might not surprise since they rely on the same principles. They are characterised by the same fast and accurate convergence to the reference value.

Finally, the R-estimates resulting from the **GREY-box modelling approach** are depicted in figure 4.4. It can be seen that data sets containing 1 or 2 days have no estimation results. This is due to the fact that those data sets contain too little data points for the analysis method to be operational. Besides that, very accurate estimation results are obtained in rather short data periods, although, compared to the previous two dynamic data analysis methods, the convergence to the goal value is somewhat slower. For winter and mid-season data sets, around 3 day periods allow to estimate the thermal resistance of the wall within a $\pm$ 5% accuracy band. For the summer measurements, 6 day periods are required to obtain that accuracy. Although, when accounting for the estimated standard deviations, longer data sets are required. More generally, it is seen for all dynamic estimation methods that the estimated standard deviations are larger for summer estimates than for mid-season estimates and that the accuracies of mid-season estimates are larger than for winter estimates. Hence, it looks like the estimation conditions are hardest in summer and best in winter.

Results for the massive wall: second scenario

A similar *comparison* plot (figure 4.5) is arranged for the measurement data of the second scenario, having a thermostatically controlled indoor temperature. Keep in mind that this scenario does only assume heating in the adjacent environment and no cooling. Consequently, the indoor temperature can exceed the set temperature during warm periods. From figure 4.1, it can be seen that this indeed happens. The assumption leads to a fully free-floating indoor temperature in the selected summer period and to a partly free-floating temperature during the mid-season period.

Compared to the results of the first scenario, several observations are made from figure 4.5. It is, for instance, noticed that the average method shows larger spreads on its results for winter and mid-season data sets. This is explained by the increased dynamic heat storage activity at the interior side of the cavity wall, induced by the changing indoor temperature of the second scenario. On the contrary, the average method's results in summer actually show more condensed results than in the first scenario. Although the scatter is still too large to speak of reliable R-estimates, a converging trend towards the goal value is noticed. This is a result of the free-floating indoor temperature of the second scenario. From figure 4.1 (top row) it can be derived that the net amount of heat going through the building components – this is the net surface under the heat flux curve – is larger in the second scenario (thermostat) than in the first (constant). Logical, since the indoor temperature is kept constant in the first scenario, meaning that the mean temperature difference over the wall is kept small and hence the net heat flux is small as well. While, by allowing a free-floating temperature, the mean temperature difference over the component is larger, and as such, also the net heat flux through the component. Since the increased net heat storage in the wall in the second scenario does not counterbalance this increased net heat transfer, the analysis is less hindered explaining the more condensed results of the average method in the second scenario.

This also explains the more effective application of the correction for storage effects in the second scenario. When the measured heat fluxes through the wall are rather small, as is the case in the first scenario, the correction of these heat fluxes is a delicate operation, while for increased values of heat flux measurements, as in the second scenario, the correction has more impact. This is indeed seen when comparing the results of the two regarded scenarios (figures 4.4 and 4.5). Whereas the correction for storage effects does not at all improve the summer results of the first scenario, it leads to reliable results for the summer measurements of the second scenario. For data sets of 12 and 17 days, accuracies of 10% and 5% are obtained.

Concerning the dynamic analysis methods, the results of the second scenario are deemed very similar to the results of the first scenario. The only thing noticed, is that the occurrence of interior dynamics renders the estimation conditions more difficult for the stochastic grey-box approach. This can be seen from the increased spread on the results and the increased estimated standard deviations. An explanation for this lies in the fact that the exciting dynamics come from both sides of the wall instead of coming from the exterior only. Hence, the assumed model has to balance its available time constants so that they explain the dynamics to both the interior and exterior.

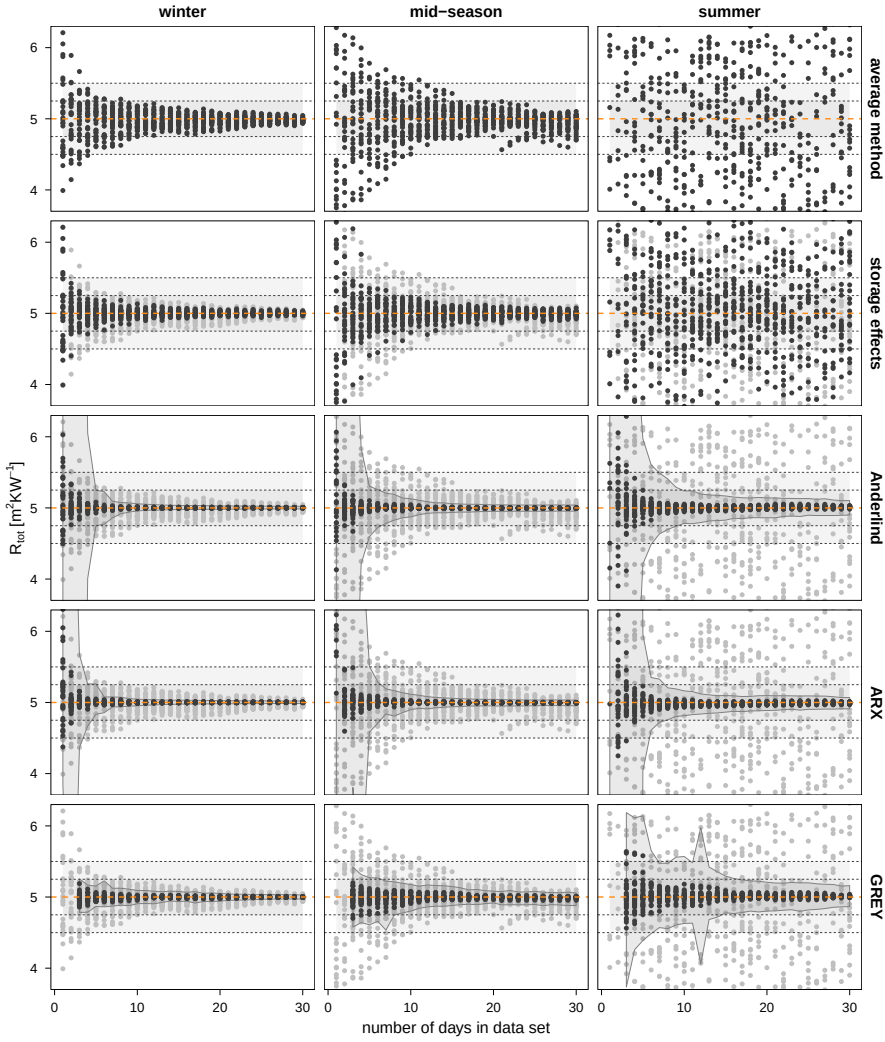

Figure 4.4: Comparison plot for the analyses of the massive wall in the first scenario (constant). Each data point represents an R-estimate resulting from a different data set. The results for the different seasons are ordered column wise, while the results for the different analysis methods are ordered row wise, with a repetition of the results for the average method in grey. The orange dotted line indicates the reference value and the grey dotted lines indicate the 5% and 10% accuracy bands. The variable grey ribbon represents the maximal 95% confidence intervals that are estimated for every data set length.

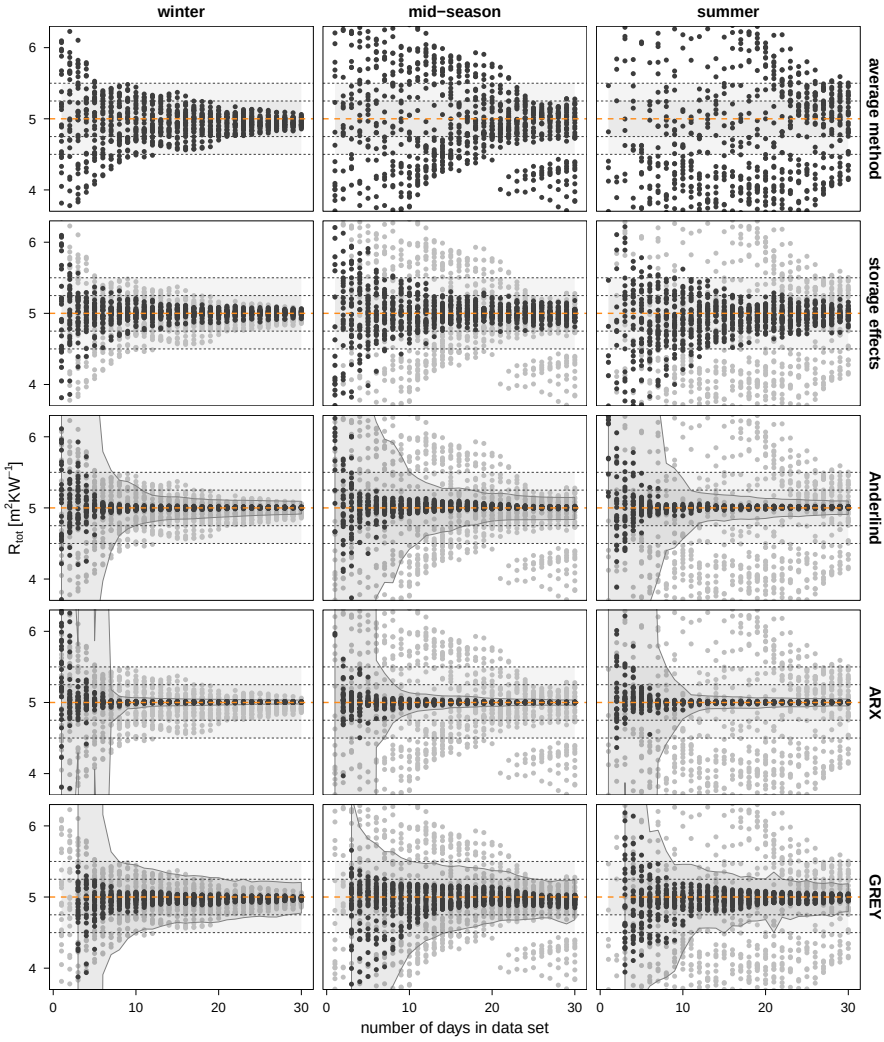

Figure 4.5: Comparison plot for the analyses of the massive wall in the second scenario (thermostat). Each data point represents an R-estimate resulting from a different data set. The results for the different seasons are ordered column wise, while the results for the different analysis methods are ordered row wise, with a repetition of the results for the average method in grey. The orange dotted line indicates the reference value and the grey dotted lines indicate the 5% and 10% accuracy bands. The variable grey ribbon represents the maximal 95% confidence intervals that are estimated for every data set length.

Results for the lightweight wall

Figure 4.6 reports the *comparison plot* for the lightweight wall. The figure includes the results for both the considered scenarios and distinguishes them by colour. The repetition of the average method's results as a reference for the other methods is omitted to avoid confusion.

Compared to the results of the massive wall, one main observation is made. Notably, figure 4.6 indicates that the average method enables correct R-estimations from summer measurements. The fact that the average method is able to do so, is linked to the wall's small total thermal capacity. Because of that, the wall has limited heat storage capacities and responds quite fast to the excitation signals. Hence, stationary conditions are more easily approximated by time-integrated values, which is in favour of the semi-stationary methods. Nevertheless, the measurement time that is required in order to obtain these reliable R-estimates is substantially longer than for the dynamic measurements. Or, put differently, the reliability of the semi-stationary methods can still not compete with the reliability of the dynamic estimation techniques.

Apart from that, similar conclusions can be drawn as for the massive wall. Figure 4.6 confirms that the semi-stationary methods benefit from the maintenance of a constant indoor temperature, at least in winter and mid-season. In summer, on the contrary, indoor environments that allow for increased temperature differences over the wall, such as free-floating temperatures do, enhance the semi-stationary estimation results.

Furthermore, concerning the dynamic characterisation methods, figure 4.6 demonstrates that these methods are all of approximately equal value when assessing their ability to reliably estimate the wall's thermal resistance, as was the case for the massive wall. Only stochastic grey-box modelling show a larger spread on its results compared to the other dynamic methods. Also note that the grey-box models result in slightly underestimated final R-values for the first scenario in summer and for the second scenario in mid-season. The underestimation, however, are smaller than 2% and the estimated standard deviations still include the reference value.

4.2.3 Discussion

For a general comparison between the analysis methods, figure 4.7 represents the spread on the estimated results as a function of the length of the analysed data sets for the different methods. The spread is calculated as the root mean square of the deviations between the estimated R-values and the *true* R-value, which is known to

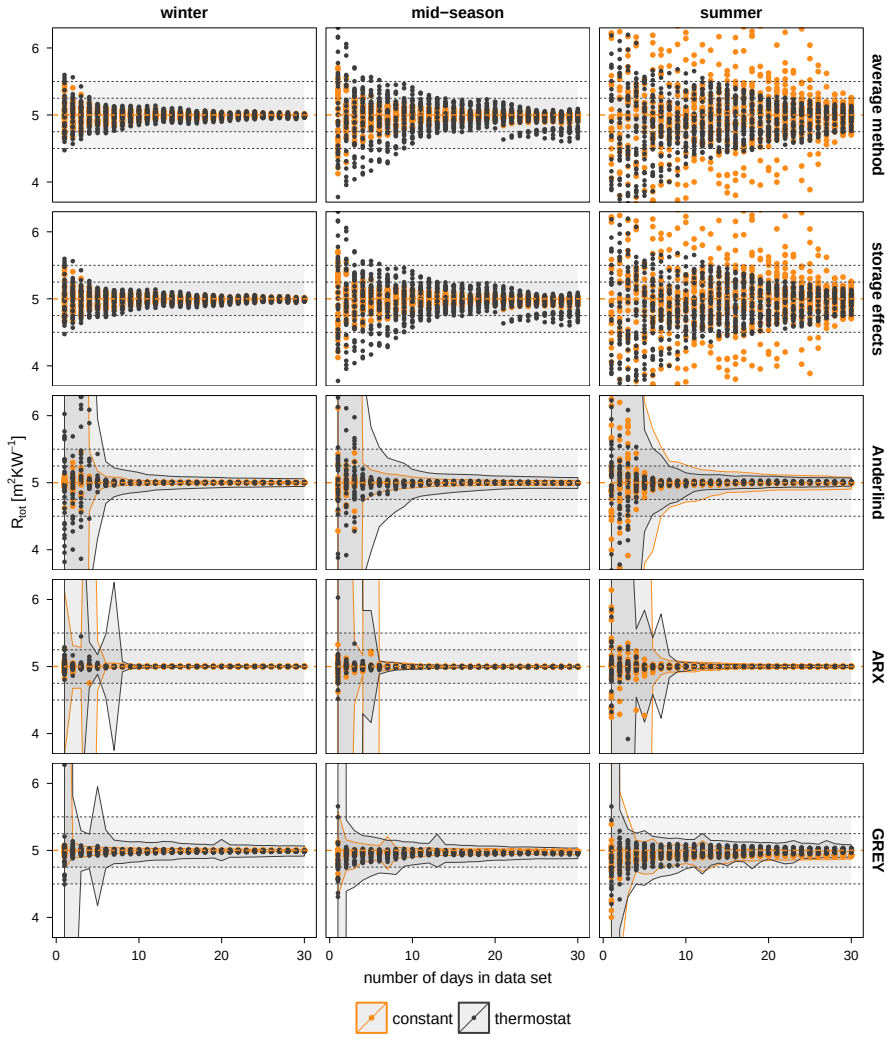

Figure 4.6: Comparison plot for the analyses of the lightweight wall in the first and second scenario. Each data point represents an R-estimate resulting from a different data set. The results for the different seasons are ordered column wise, while the results for the different analysis methods are ordered row wise. The orange dotted line indicates the reference value and the grey dotted lines indicate the 5% and 10% accuracy bands. The variable grey ribbon represents the maximal 95% confidence intervals that are estimated for every data set length.

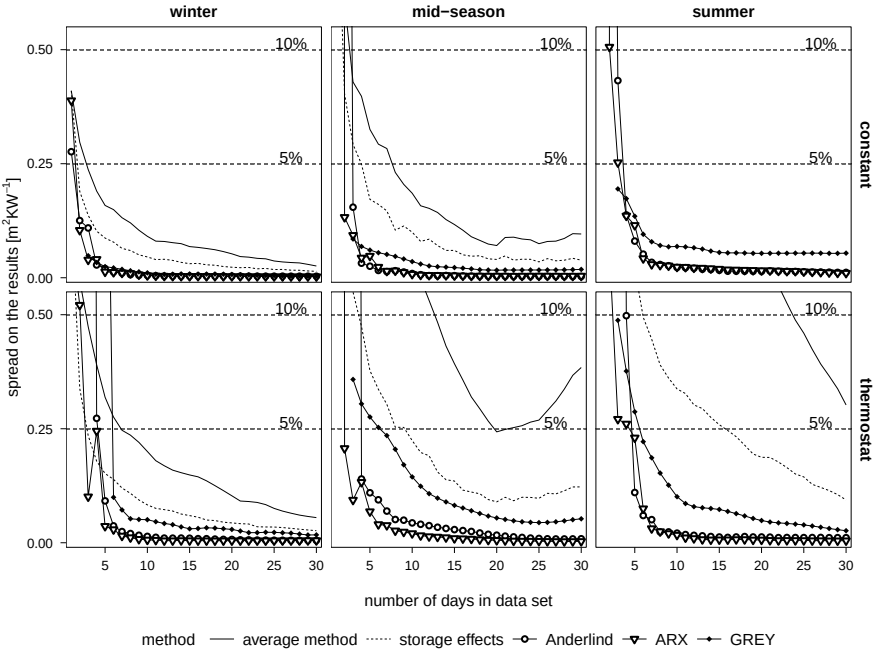

Figure 4.7: The spread on the results as a function of the data set lengths for the different methods. The grey dotted lines correspond to 5% and 10% deviations from the reference value.

be 5 m^2KW^-1. This quantity is typically referred to as the RMS error. The latter is calculated for the estimated R-values per data set length, per analysis method and for each seasonal period and scenario separately. Note, thus, that these standard deviations are calculated for the results of both wall types together. Hence, the general applicability of the different methods is studied.

Figure 4.7 clearly shows the advantage of the dynamic data analysis methods compared to the semi-stationary methods. For all data periods, the dynamic methods converge must faster to a reliable estimation result. Even more, the dynamic analysis methods result in accurate resistance estimates for summer data sets, while the semi-stationary methods do not lead to reliable results. Figure 4.7 also demonstrates that the correction for storage effects is an efficient adaptation of the average method. It must be repeated, however, that knowledge about the studied structure is needed in order to apply the correction. Next to that, the performance among the different dynamic analysis

methods appears to be of almost equal quality when situations are considered with a constant indoor temperature (top row of figure 4.7) Only in summer, the grey-box results are somewhat less accurate than the other dynamic methods, although the difference is limited. For the second scenario, figure 4.7 (bottom row) demonstrates that the grey-box models suffer most from a controlled, but varying indoor temperature. The variation on the estimated results is larger than for the other dynamic methods and diminishes at a slower rate. Nevertheless, note that the observed variation is still below 5% for most of the considered data set lengths. The performance of Anderlind- and ARX-modelling again appear to be of similar quality in case of the second scenario.

4.3 **The real deal: actual measurement data**

4.3.1 Case study: Vliet cavity wall

Thus far, the analysis methods have been applied and examined solely on numerically simulated data. This enabled a comparison between the estimation results and the *real* reference value, but it also neglected factors that possibly complicate the data analyses, such as temperature and moisture dependent thermal properties, measurement inaccuracies, etc. Therefore, in this section, the step towards actual measurement data is taken. Hence, it can be examined whether the discussed estimation methods also function in reality.

The different characterisation methods are applied on actual measurement data of the internal heat flux and surface temperatures of a south-west oriented insulated cavity wall. The measurements are performed in the VLIET test building of the KU Leuven, located in Leuven, Belgium [90]. This building was explicitly constructed to study the hygrothermal behaviour of building components under real climatic conditions. Measurements of 12 cavity walls are available from experiments performed during the late nineties and have previously been used to investigate the performance of brick cavity walls [10]. The wall considered in this dissertation is situated in the south-west façade of the building and is very similar to the previously simulated wall. The studied wall has a hight of 2.70 m and a width of 1.80 m. The interior and exterior surface temperatures, as well as the interior heat flux are measured at the centre of the wall. Figure 4.8 represents the Vliet building with the considered test wall. Measurements are obtained with a five minute interval but are averaged to four hourly values for the analyses performed in this section. Similar as for the simulations, averaging is performed by taking the arithmetic mean of the measurements in the intervals that correspond to the new sampling time, without prefiltering the data. The test wall consists of an inner and outer brick leaf of 0.140 m and 0.090 m respectively and

is insulated with 0.140 m glass wool blankets. Furthermore, the brick façade has a light colour. The thermal properties of the wall materials are summarized in table 4.1 and are obtained experimentally, except the materials' specific heat capacity that is obtained from literature. As the thermal conductivity of the insulation layer and brick façade is known to be temperature dependent, a different insulation resistance is calculated for the main winter and summer periods that will be considered in this section. Therefore, the overall insulation temperature is assumed to equal the mean of the two surface temperatures averaged over the considered periods. Resulting mean insulation temperatures of 13.7°C and 21.1°C are found for winter and summer respectively. The overall temperature of the inner and outer brick leaves are assumed to equal the mean temperature of the interior and exterior surface temperatures respectively. Hence, for the inner brick, mean temperatures of 21.3°C and 23.0°C are assumed in winter and summer respectively. For the exterior brick leaf, mean temperatures of 6.1°C and 19.2°C are assumed in winter and summer respectively. Hence, the theoretical total thermal resistance of the wall amounts to 4.56 m^2KW^{-1} for winter periods and to 4.45 m^2KW^{-1} for summer periods. These values are used as reference values in the following, although they do not pretend to embody the actual as-built thermal resistance of the wall. In fact, these *theoretical* values are liable to many possible errors, as was already stated in the introduction of this work. Uncertainties on the component's material properties, or, uncertainties induced by workmanship issues, etc. will render these theoretical values deviating from the *actual* thermal resistance of the wall. A simple calculation of the impact of errors in the assumed material properties learns the following: when relative errors of 5% are assumed for the materials' measured lambda-values and when absolute errors of 5 mm are assumed for the layers' thicknesses, a relative error of ± 5 to 7 % is found on the total thermal resistance of well-insulated cavity walls. Other uncertainty sources, such as different conditions during the property measurements compared to the conditions during the outdoor experiment, etc. can even broaden these accuracy intervals.

Table 4.1: Thermal properties of the considered massive wall.

	d $[m]$	**ρ** $[kgm^{-3}]$	**c** $[J(kgK)^{-1}]$	**R winter / summer** $[m^2KW^{-1}]$	**C** $[MJm^{-2}K^{-1}]$
brick	0.090	2261	840	0.115 / 0.112	0.171
air cavity	0.015	/	/	0.170	/
glass wool blankets	0.140	40.50	840	4.002 / 3.895	0.005
brick	0.140	1757	840	0.275 / 0.274	0.207
TOTAL	0.385			**4.561 / 4.451**	**0.382**

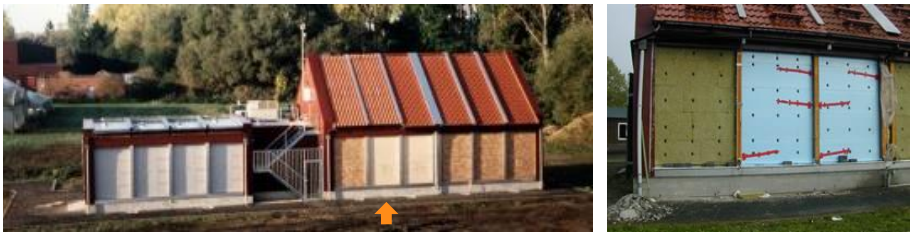

Figure 4.8: (left) Picture of the north-east façade of the Vliet test building in 1996. The considered test wall is located in the south-west façade, but is similar to the wall indicated in the picture by the orange arrow. (right) Picture of the construction of some of the walls in the south-west façade before the installation of the outer brick leaf.

The test wall is subjected to the outdoor climate and to an indoor environment that is heated to a constant set temperature of 23°C. No cooling is applied in the building so that during warmer periods, the indoor air temperature often exceeds the set temperature and acts as a free-floating temperature. Two main data sets of 40 days are selected: one in winter from 14/12/1997 till 23/01/1998 and one in summer from 22/04/1998 till 01/06/1998. The measurement data is represented in figure 4.9. Similar as to the simulation research, data sets with different lengths, starting on different days are constructed from these two main data periods. Therefore, a moving window with lengths ranging from 1 to 30 days is considered. However, since the total time span of the measurement data is now limited to 40 days, less larger data sets can be constructed compared to the simulation analysis. For example, only 10 data sets containing 30 days will be analysed in winter, notably, the data set starting on the 14th of January till the data set starting on the 24th of January.

The different characterisation methods were applied with the same assumptions that were made for the simulated measurement data of the cavity wall. Only for the analysis of the summer data a fourth order grey-box model was assumed instead of a third order model. This higher order was required to explain the hihgly varying heat flux in the periods with a free-floating indoor air temperature.

4.3.2 Results

The *comparison plot* for the estimation results from the actual measurement data of the Vliet cavity wall is represented in figure 4.10. Note hereby that the reference value is represented as one fixed line. Keep in mind, however, that this value is rather uncertain, as was stated previously.

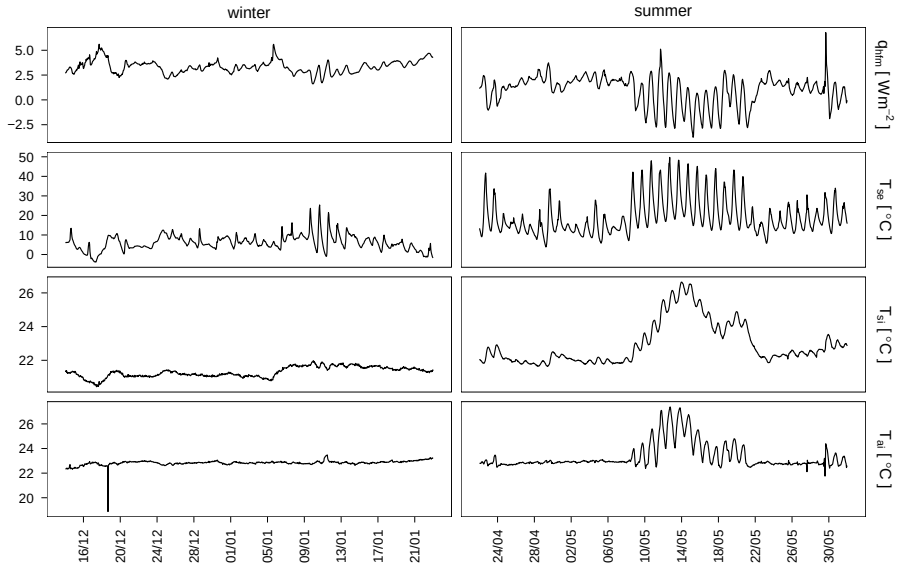

Figure 4.9: Actual measurement data of the selected main periods for the insulated cavity wall.

By examining the **winter** results from figure 4.10, it is seen that all analysis methods lead to reliable R-estimates for the cavity wall. Nevertheless, a few considerable differences are observed compared to the simulation results. First, it is noted that the correction for storage effects does not really reduces the spread on the estimation results of the average method, as was the case for the simulated measurements. Yet, its application results in a slight, but well-placed correction that shifts the R-estimates towards the reference value. However, the representativeness of the reference value can be questioned since the three dynamic estimation methods slightly underestimate this value after 30 days, although the differences are less than 5%. A more striking observation concerns the standard deviations that are estimated from the ARX-models. According to figure 4.10, the estimated confidence bounds are very large and even fall outside the boundaries of the graph, while the R-values appear to be rather accurate estimates. This probably results from an overfitting of the ARX-models. Since fixed model orders are assumed, redundant or highly correlated parameters are not removed from the model and might negatively influence the estimated standard deviation of the derived thermal resistance estimate. This may be avoided by using an automatic model order selection. However, this is not treated in this dissertation, as was mentioned in

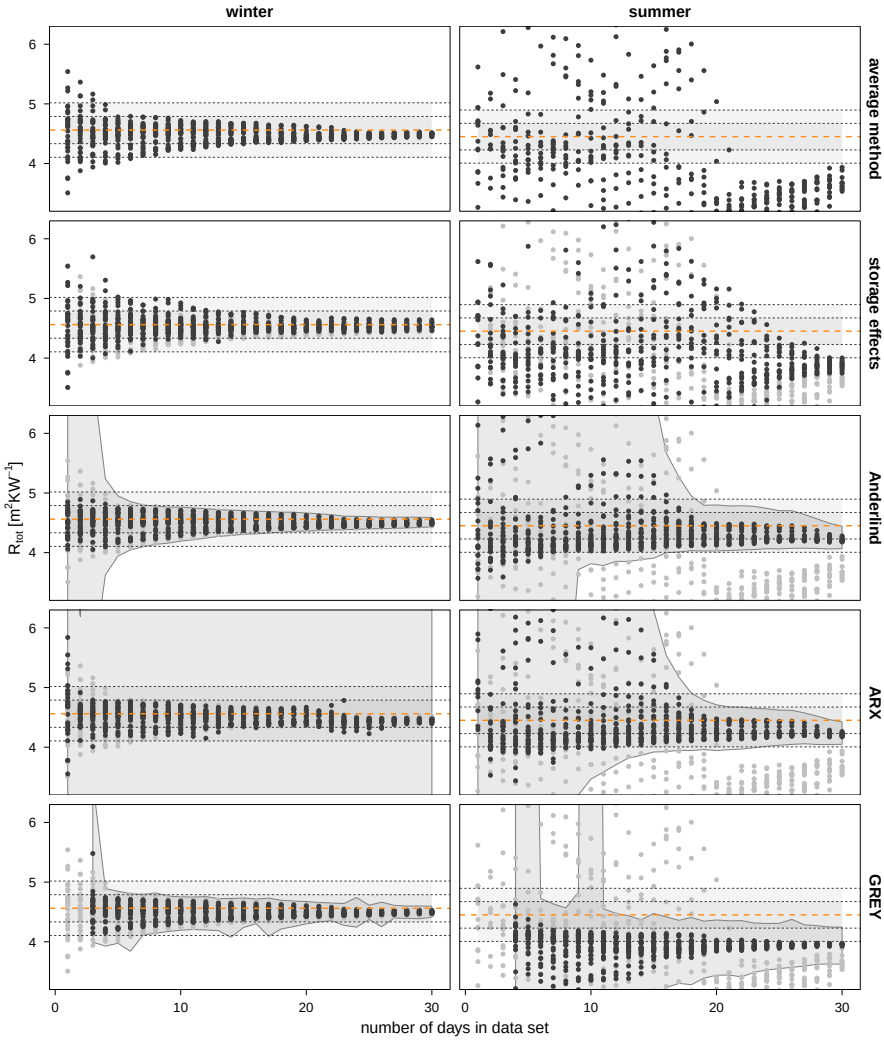

Figure 4.10: Comparison plot for the analyses of the insulated cavity wall from actual measurement data. Each data point represents an R-estimate resulting from a different data set. The results for the different seasons are ordered column wise, while the results for the different analysis methods are ordered row wise, with a repetition of the results for the average method in grey. The orange dotted line indicates the reference value and the grey dotted lines indicate the 5% and 10% accuracy bands. The variable grey ribbon represents the maximal 95% confidence intervals that are estimated for every data set length.

chapter 2. Furthermore, it is seen for all methods that the spread on the results is consistently wider than it was for the simulated data. This might not surprise, since the actual noise of real-world measurements is probably larger than the noise that was assumed for the simulated data. Nevertheless, estimation results with an accuracy of 5% and 10 % are feasible. In general, it can be stated that all analysis methods perform almost equally well for winter data sets.

The estimation results from the **summer** data sets, however, lead to more peculiar observations and ask for a more detailed discussion. The semi-stationary methods show wide-spread estimation results, as can be seen from figure 4.10. However, they do converge to a common R-estimate when long enough data sets are considered. This was also seen for the second scenario of the simulated measurements of the cavity wall: by allowing a (partly) free-floating indoor temperature, the amount of net heat storage is better balanced compared to the net amount of heat transfer and enables hence a better R-estimation when using semi-stationary methods. Figure 4.10 also proves the effectiveness of the correction for storage effects: compared to the average method's results, a more robust convergence is noticed and the results are adjusted in the right direction, although long measurement time spans are still required. But, the final R-estimates that are obtained differ significantly from the theoretically calculated reference value.

This is observed generally: the dynamic estimation methods also converge to final R-estimates underestimating the reference value. This can indicate that the actual wall's thermal resistance is lower than the theoretically calculated one. As was mentioned previously, the reference R-value is only an indication for the *actual* thermal resistance and errors in the order of magnitude of $\pm$ 5 to 7% are reasonable. Other sources might partly be at the origin of the underestimated R-values, such as phenomena disturbing the one dimensional heat transfer that is assumed in the wall for example. It is, for instance, possible that buoyancy driven ventilation takes place in the air cavity in summer [91], although no data is available to proof this assumption. Yet, such phenomena are not taken into account in this chapter, but are dealt with in chapter 5. Here, the assumption of models describing one dimensional heat transfer in building components is maintained. Among the dynamic analysis methods, significant differences are also noticed. Anderlind-modelling and ARX-modelling lead both to final R-values of approximately 4.22 m^2KW^{-1}, while the grey-box modelling approach lead to final R-values of 3.96 m^2KW^{-1}, which is a drop of $\pm$ 7% compared to the previous two. A possible explanation for this deviating result relates to the model formulation. Stochastic state space models have a pre-specified, and hence, more rigid model structure than black-box models, which manifests itself in a limited amount of degrees of freedom. Furthermore, the assumed grey-box model has a reduced order

compared to the assumed black-box models. The grey-box models are of fourth order while the ARX-models can have a maximum order up to 6 (the maximum model order corresponds to one day of historical data with a sample time of four hours). Increasing the grey-box model order, however, would lead to unidentifiability issues hindering the estimation procedure. Consequently, the decreased flexibility of the more rigid grey-box model structure might result in small variations that are discarded to the noise models, without disturbing the white noise behaviour, rather than that they are contributing to the model's stationary behaviour. Nevertheless, from a statistical point of view, the difference between the methods' estimation results is not alarming. Even more, the final R-estimates are statistically the same. This can be seen from figure 4.11, which depicts the final R-estimates and two times their estimated standard deviation from the 11 data sets containing 30 days. It can be seen that the confidence intervals of all methods are overlapping so that the results are statistically equal.

A last thing to notice is the frequent appearance of outlier R-estimates resulting from the dynamic analyses in summer. When these outliers are traced, they are found to correspond to data sets with a mainly free-floating indoor air temperature. This can be seen from figure 4.12 which depicts the estimation results of the data sets containing 10 to 15 days by plotting their R-value as a line over the entire period from which the values are estimated. As a reminder, the interior air temperature curve is added at the bottom in grey. The figure clearly demonstrates that the presence of large parts of free-floating data in the measurements jeopardizes the estimation results more than was found from the simulation research. In figure 4.13, it is examined whether these outliers are characterised by larger estimated standard deviations. Therefore,

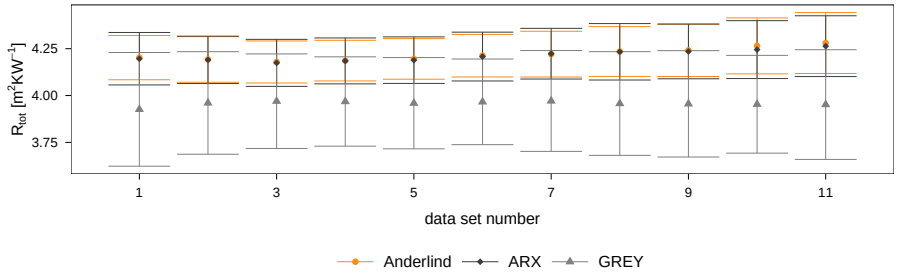

Figure 4.11: Estimated thermal resistances accompanied by their 95% confidence interval of the 11 summer data sets contain 30 days. The estimation results for the ARX-model, Anderlind's regression model and stochastic grey-box model are represented.

the figure plots the R-values estimated from summer data sets longer than three days in function of their estimated standard deviations. The figure shows indeed that the more deviating results have the lowest estimated accuracies, especially in the case of grey-box models.

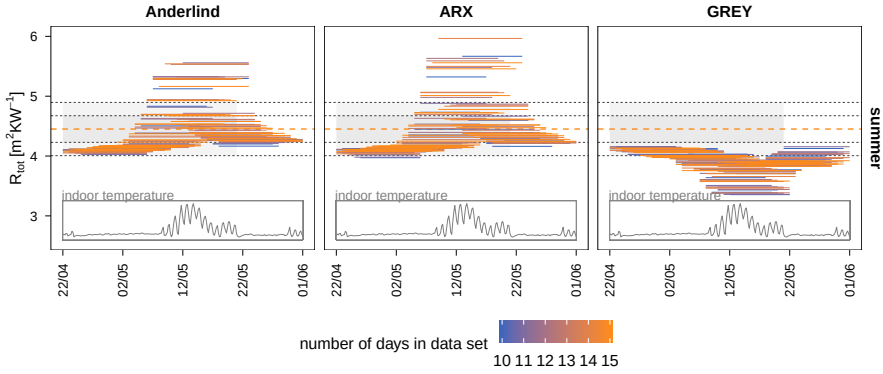

Figure 4.12: Representation of the estimation results of data sets containing 10 to 15 days. The obtained R-values are plotted as a line over the entire period from which the values are estimated. The interior air temperature is represented as the grey curve at the bottom. The R-estimates are coloured according to the number of days present in the estimation data set.

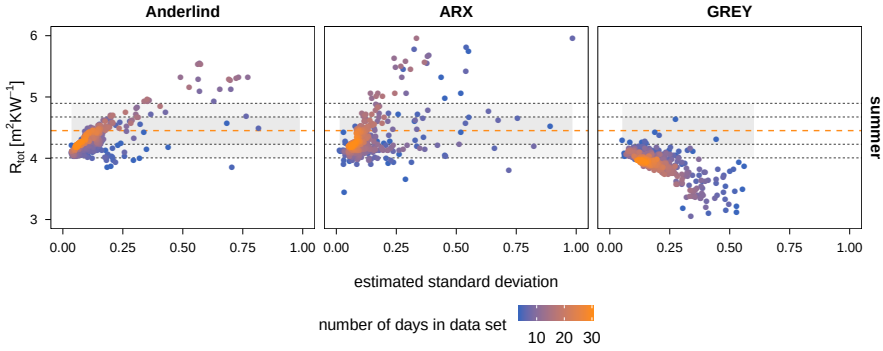

Figure 4.13: Estimated thermal resistances resulting from summer data sets larger than 3 days in function of their estimated standard deviations.

4.4 Conclusion

In this chapter, a large-scale comparison of the available characterisation methods for building components in-situ is performed. Thereby, special attention is given to the reliability of the methods estimation results when confronted with data sets of limited measurement time spans and different seasonal boundary conditions. First, the methods' performances are assessed for simulated measurements of a massive and a lightweight wall in a moderate European climate. Subsequently, the performances are examined for actual measurement data of an insulated cavity wall located in Leuven, Belgium.

From the simulation research, it followed that the dynamic data analysis methods generally have an improved performance compared to the semi-stationary methods. Indeed, the reliability of the average method proved to be boundary condition dependent: only when the heat storage activities of the studied walls were limited, reliable R-estimates were obtained. This was the case, for example, for the winter measurements of the massive wall in the first scenario, or, for the winter measurements of the lightweight walls in both scenarios. However, when solar activities or varying indoor temperatures started addressing the storage capacity of the walls, the obtained R-estimates turned unreliable, or, very long measurement times were required to obtain reliable results. This could be seen, for instance, for the results of the summer measurements of both walls and scenarios. The correction for storage effects, though, proved to be an efficient adjustment of the average method in many cases. Only in situations where the heat flux is largely fluctuating around zero, so that the net heat transfer through the wall is very small, the correction does not significantly improve the average method's results. Moreover, the correction method has a major pitfall, notably its dependence on prior information about the structure and thermal properties of the studied component. Since the method is employed in the context of thermal resistance estimation, it is doubtful that this knowledge is readily available.

In contrast with the semi-stationary methods, dynamic estimation methods proved to be more versatilely applicable from the simulation research. All studied dynamic estimation methods led to reliable R-estimates in all of the considered cases. Among the different dynamic methods, no real preference is shown for a particular method although Anderlind-modelling and ARX-modelling showed a faster convergence to more condense results than stochastic grey-box modelling did. Nevertheless, the increased validation criteria of this method might plead in the latter method's cause. Next to that, it was observed that, despite the versatile usability of the dynamic estimation methods, the methods still showed boundary condition dependencies. It was indeed seen that the different boundary conditions had an influence on the spread of the

estimation results and on the estimated standard deviations, which was most noticeable for results of the stochastic grey-box models. For winter conditions, for example, the estimation results were more condensed than for summer conditions and also the estimated standard deviations were smaller. The results for the mid-season periods lied in between. Hence, summer conditions will require longer measurement time spans than winter conditions in order to obtain results of equal accuracy. Generally, for the considered cases it was found that winter measurements required ± 3 to 6 days to obtain results within 5% accuracy of the reference value, while summer measurements required ± 10 to 14 days.

The results from the actual measurement data have cast a critical glance over the previous conclusions. For instance, from the experimental research, it was concluded that the semi-stationary methods perform almost equally well as the dynamic analysis methods when winter data is considered. The *in theory* improved performance of the dynamic methods in winter is thus less noticeable when real measurements are considered. By contrast, the improved performances of the dynamic methods for summer conditions are perceived. It was indeed seen that the results of the three dynamic methods converged vastly to a final R-estimate. The final values that are obtained are, however, in al three cases lower than the calculated R-value. Hence, the *theoretical* value is probably over estimated. However, which one of the three dynamically estimated values best approaches the *true* value, is unknown making it hard to assess the methods' reliability. Grey-box models are found to consistently estimate lower R-values than Anderlind's model or ARX-models. This might be due to the more rigid model structure of grey-box models. Nevertheless, from a statistical point of view, the differences are not alarming since the obtained results are statistically equal. Next to that, many outlier results were noticed from data sets containing around 8 to 16 days. These outliers are linked to measured data that has a mainly free-floating indoor temperature. So, apparently, the presence of large parts of free-floating data in the measurements jeopardizes the estimation results more than was found from the simulation research.

Generally, it can be concluded that semi-stationary methods are easy-to-use and that they are reliable characterisation methods when applied for winter measurements, whereas the dynamic methods are found to be more complex in use, but offer a more versatile applicability. Nevertheless, actual measurement data appeared to be more challenging than expected, especially when indoor free-floating temperatures are present. Hence, if possible, a controlled indoor environment can positively influence the analysis conditions.

Chapter 5

The challenge of characterising a variable thermal resistance

The thermal resistance of building components is typically seen as a stationary parameter, although in reality, the quantity is often time varying. Several phenomena can lie at the origin of this: some of them are bound to the heat conduction mechanisms in building materials and can not be prevented from occurring, while others are induced by external factors that can and should be avoided. Poor workmanship issues, for instance, can induce phenomena such as buoyancy driven air flows or wind washing that interact with the regular heat transfer mechanisms in building components and hence affect their apparent thermal resistance [9, 10, 92, 93]. In this chapter, it is examined whether the technique of stochastic grey-box modelling is able to identify the presence of such phenomena from measurement data and, if so, whether it can identify a variable thermal resistance indicator quantifying the thermal impact of these phenomena. This is investigated for the specific scenario of an insulated cavity wall that suffers from rotational air looping around its hard insulation boards, due to a poor installation of the latter.

5.1 **Thermal resistance: not always a stationary parameter**

5.1.1 Several causes for time dependent R-values

As aforementioned, the thermal resistance of a building element is typically regarded as a stationary parameter, while, in reality, it is often a time varying quantity. It is, for instance, generally known that building materials have a temperature and/or

moisture dependent thermal conductivity. In case of the former, the temperature profile that is established in the material will no longer be linear. Furthermore, the thermal resistance that could be determined is only an *apparent* thermal resistance and will depend on the average temperature of the material. Consequently, if a wall is subjected to dynamic boundary conditions, its *apparent* thermal resistance will be time varying. As an illustration, figure 5.1 depicts the impact of a temperature dependent thermal conductivity on the mean thermal resistance of a 0.100 m thick polyurethane insulation board. The figure demonstrates that the thermal resistance changes by 16.67% when mean material temperatures are considered ranging from 10°C to 40°C.

Moisture or temperature dependent thermal properties thus alter the linear behaviour of the temperature profile in building materials. Nevertheless, the heat transfer from one side to the other remains one dimensional and mainly conductive. A more thorough change of the regular heat transfer mechanisms in building components occurs when heat sources or sinks are present in the construction. This can, for instance, be the case when moisture condensates or evaporates internally in the construction, or, when air flows start moving through the construction. Sometimes such air flows are desired: for example, ventilation behind rain screen claddings is intended to evacuate excessive moisture between the cladding and the inner part of the structure. Or, air flows in active façades are often designed to evacuate heat from the cavity. However, typically, air flows in constructions are induced by workmanship deficiencies and are unwanted, because they largely influence the thermal performance of the affected building components. For instance, due to unsatisfactory airtightness of roof constructions, wind driven air flows might enter the construction and move through or under the roof insulation, hence short-cutting its thermal quality by a large extent [9, 93]. Or, poorly installed hard insulation panels in cavity walls might cause air looping around them, short-cutting their insulating quality [10, 92].

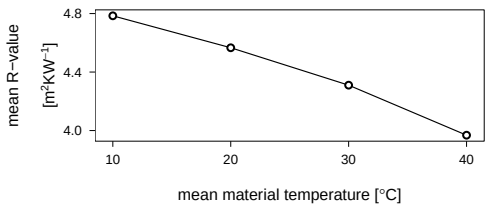

Figure 5.1: The impact of a temperature dependent thermal conductivity on the mean thermal resistance of a 0.10 m thick polyurethane insulation board.

As was demonstrated in figure 1.2 of chapter 1, workmanship deficiencies are still occurring regularly in the current building practice. Hence, the question should be asked what the impact of these deficiencies is on the actual thermal quality of the affected building components. Knowledge of this would furnish quantitative data that could be used to sensitise the building industry about the importance of good workmanship and to enforce better building practices. Therefore, in this chapter it is studied whether the impact of workmanship issues can be quantified by stochastic grey-box modelling. This is done for the specific case of an insulated cavity wall where a poor installation of the hard insulation panels causes air looping around them. In particular, it is studied whether stochastic grey-box modelling holds the ability to indicate the presence of this phenomenon from the measurement data and, if so, whether it can identify a variable thermal resistance indicator quantifying the component's variable thermal behaviour. Before discussing how this problem is approached, a short introduction on rotational air looping in cavity walls is given.

5.1.2 Variable R-value due to rotational air flow in a cavity wall

In cavity walls, heat is typically transferred by conduction through the material layers and by convection and radiation through the air cavity. When a homogeneous wall is considered, and there is no proximity of cold bridges, the heat flux through the wall is one dimensional and is equal at every position on the wall. However, this picture drastically changes when air starts flowing around or through the insulation. Such air flows can be induced by natural convection when small air cavities are present at both sides of the insulation. Due to temperature differences across the insulation layer, pressure differences are created in these flanking air layers, constituting a driving force for the air to loop around the insulation. The flanking air will, however, only actually loop when apertures are present at the top and bottom joints of an insulation board, unless air permeable insulation is used. In that case, the flanking air will loop through the insulation itself and apertures in the insulation are no prerequisites for the air to start looping. In this dissertation the focus lies on rotational air looping around hard, airtight insulation panels, since this scenario induces the largest additional heat losses through a cavity wall [92].

When residual air cavities are present in combination with apertures at the bottom and top joints of an insulation board, the air in the warmer cavity, having a lower density and hence being more buoyant than the air in the colder cavity, will flow upwards, leaving the warmer cavity through the upper openings in the insulation layer. Subsequently, the air in the colder cavity will flow downwards, entering the warmer cavity via the lower apertures. There it is warmed up again, so that the air

loop continues to exist. In theory, rotational air looping is explained by introducing a neutral plane, which is defined as the vertical position where the warmer cavity's air pressure equals the colder cavity's pressure (in absence of wind). When the pressure at the neutral plane is set to zero, the pressures in the warm air cavity above this plane are positive, indicating that air will flow out of any intermediate aperture. Below the neutral plane, the pressures in the warm cavity are negative, indicating that air from the cold cavity will be drown into the warm cavity through any intermediate aperture. This is illustrated in figure 5.2.

When a cavity wall is affected by rotational air looping, the heat flux measured at the interior side of the wall is no longer the same at every position, but varies over the height of the wall. The same can be said about the surface temperatures at both sides of the wall. Next to that, the definition of the traditional thermal resistance, as used thus far in this dissertation, is no longer valid. Although a local R-value can still be calculated by dividing the measured interior heat flux by the surface temperature difference across the component at a certain position, the obtained value can not be interpreted in the traditional way: it is no longer a unique and constant property characterising the thermal quality of the wall, but it is a varying property, depending on the location of the measured data as well as on the temperature difference over the wall. Therefore, this quantity is further denoted as the local, apparent thermal resistance R_{app}.

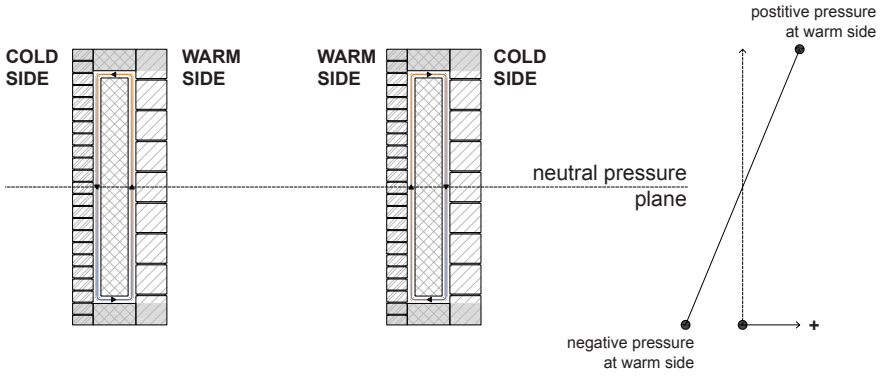

Figure 5.2: Conceptual representation of rotational air looping around the insulation of a cavity wall. The looping air is coloured according to a temperature scale that varies from warm (orange) to cold (blue).

To illustrate the concept of local, apparent R-values, a cavity wall affected by rotational air looping is simulated in Delphin, a software program that models heat, air and moisture transfer in building components (www.bauklimatik-dresden.de/delphin). More details about the simulations and wall are given in section 5.2.1, but, in order to illustrate the concept of apparent R-values, it is only important to know that the rotational air looping is developed over a total wall length of 1.48 m and that the wall is simulated under stationary conditions. The indoor temperature is fixed at 20°C, while the outdoor temperature is fixed at values ranging from 0°C to 30°C. Hence, heat fluxes and surface temperatures are calculated for several temperature differences across the wall. Rotational air looping is included by modelling continuous air channels around the insulating layer. Widths of 5 mm and 10 mm are assumed for the latter. For the smaller cavity, the air flow resistance is larger and smaller air flows will be developed.

Figure 5.3 represents the interior heat fluxes that are measured over the total height of the component in case of the various temperature differences that are assumed over the wall. The represented heat fluxes are normalised by dividing them by the heat flux that would be measured when no natural convection was occurring. This situation is further referred to as the reference situation. Several things stand out

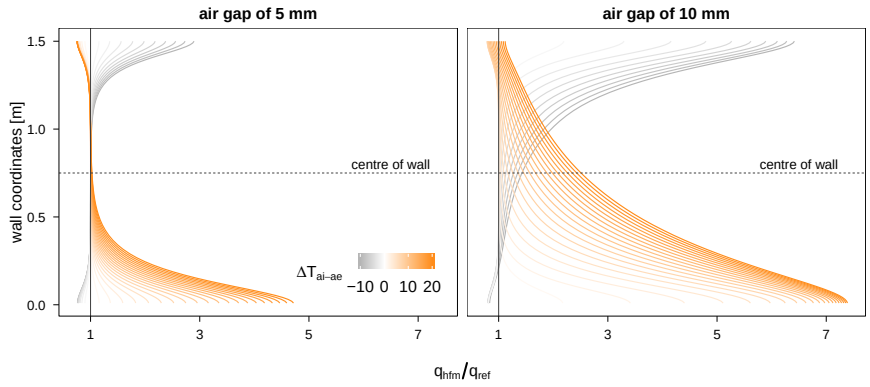

Figure 5.3: Interior heat fluxes measured over the total length of a cavity wall with rotational air looping. Two walls are considered: one with a continuous air channel of 5 mm around the insulation (left) and another with a continuous air channel of 10 mm (right). The heat fluxes are represented for various temperature differences accross the component and are normalised by dividing them by the heat flux that would be established in a wall without rotational air looping.

from figure 5.3. First, it is noticed that the impact of rotational air looping increases with increasing temperature differences across the wall. Furthermore, it seen that the impact of rotational air looping increases with decreasing air flow resistances in the cavity: the interior heat fluxes are much larger for the wall with residual cavities of 10 mm than of 5 mm. Next to that, for situations where the interior environment is warmer than the exterior environment (positive temperature differences), it is noticed that the impact of rotational air looping is largest for the lower part of the wall. Near the bottom, the heat flux is larger than would be the case in the reference scenario. This results from the fact that cold air enters the cavity at the bottom of the wall, cools down the exterior face of the inner construction layer and hence increases the measured interior heat flux at that position. For instance, for a temperature difference of 20°C, the measured heat flux at the bottom is four to seven times larger than in the reference situation, depending on the air channel's width. At the top, the impact of natural convection depends on the magnitude of the developed air flux. When a residual air cavity of 5 mm is assumed, the heat flux measured at the top is smaller than would be the case in the reference situation, for all temperature differences. This means that the exterior face of the inner construction layer is warmed up by the moving air to a temperature that is higher than would be the case in the reference situation. Conversely, when a cavity of 10 mm is regarded, the heat flux can be both smaller and larger than in the reference scenario, depending on the temperature difference over the wall. This has to do with the magnitude of the air flux. When larger air flows are being developed in the cavity, the air has less time to warm up and hence, the temperature of the exterior face of the inner construction layer will not warm up to a higher surface temperature than in the reference situation.

When negative temperature differences are considered, i.e. when the exterior environment is warmer than the interior environment, the behaviour of the heat flux profiles is mirrored: now the largest impact is seen at the top of the wall, where the heat flux is always larger than in the reference situation, while, at the bottom, the impact is variable. Finally, note that the heat flux profiles for positive and negative temperature differences are not symmetrical. This results from the fact that the construction layers flanking the residual air cavities to the inside or to the outside have different thermal properties.

Based on the simulated surface temperatures and heat flux measurements, the apparent thermal resistance can be calculated at every height of the considered walls. If this is done for the various assumed temperature differences, temperature dependent R(ΔT)-profiles can be composed (further simply denoted R-profiles). This is done in figure 5.4, which depicts the apparent thermal resistance for different locations on the wall in function of the surface temperature differences across the component. Three profiles

are represented in colour to indicate which profiles correspond to regions near the bottom, centre and top parts of the wall. Note that for a temperature difference of 0°C, all R-profiles intersect at the same R-value. The value for which this happens corresponds to the thermal resistance of the wall in the reference situation, i.e. when no air is looping around the insulation. This *stationary* R-value is further referred to as R_0 and equals, for the considered wall, 3.85 m^2KW^{-1}. Generally, it is noted that R_{app} is smaller than R_0 at the bottom of the wall and larger at the top for positive temperature differences. For negative temperature, the observations are reversed.

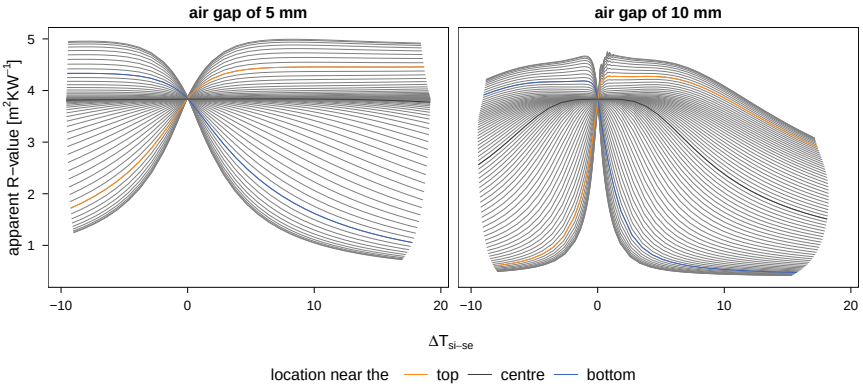

Figure 5.4: Representation of the temperature dependency of apparent thermal resistances measured at different positions on a cavity wall suffering from rotational air looping. Three profiles are represented in colour to indicate which profiles correspond to top, centre or bottom positions on the wall.

5.2 Methodology

The current chapter tries to answer two main questions. Initially, it is ascertained whether stochastic grey-box models are able to detect the presence of air looping around a cavity wall's insulation from local, on-site measurements, i.e. heat flux and surface temperature measurements. Secondly, it is examined whether specific grey-box models can be formulated that estimate a variable thermal resistance indicator, quantifying the impact of rotational air looping on the wall's thermal behaviour. To answer both questions, measurement data of a cavity wall with good and poor workmanship – i.e. a cavity wall without and with air looping around its insulation

– is required. Therefore, two cavity walls have been constructed in the VLIET test building of the KU Leuven, located in Leuven, Belgium [90]. To avoid the analyses to depend on measurement errors or experimental set-up deficiencies, both walls are also simulated by a HAM-model including natural convection phenomena. Further information on these simulations and on the experimental test set-up of the cavity walls can be found in section 5.2.1.

To answer the question if local measurement data holds information on whether natural convection is occurring or not, the next approach is followed: the reference stochastic grey-box models, as introduced in chapter 3, are fitted to the heat flux and surface temperature measurements by means of a maximum likelihood estimation. The models are fitted on data of the walls with and without rotational air looping. Therefore, local measurements are considered at three positions on the wall: near the top, at the centre and near the bottom of the wall. By comparing the statistical validation criteria for the estimation results of both walls, it is prospected whether indications for the presence of air looping can be found.

To answer the second question, grey-box models which include temperature dependent thermal resistances are estimated from the on-site measurements of the cavity walls with buoyancy driven air flows. From figure 5.4, it was seen that when a cavity wall with rotational air looping is subjected to stationary boundary conditions, the apparent R-value at a specific location will take a fixed value that depends on the settled temperature difference. However, when the wall is subjected to dynamic boundary conditions, the apparent R-value at a specific location will vary accordingly to the R-profile of that location. The range of this profile that will be observable from the measurement data logically depends on the range of temperature differences that is present in the considered data set. In winter, for example, the indoor environment is typically heated so that mainly positive indoor-outdoor temperature differences will occur across the wall. Thus, local R-values will behave accordingly to the right part of the R-profiles in figure 5.4. Over this temperature difference region, the R-profiles can be approximated by exponential curves. In summer, on the other hand, the indoor environment is typically not controlled so that both positive and negative temperature differences will occur. Hence, the local apparent R-values will behave accordingly to the middle part of the R-profiles in figure 5.4. In this region, the R-profiles can be approximated by s-shaped, logistic functions. To include this exponentially or logistically temperature dependent behaviour in stochastic grey-box models, one or more model resistances of the reference model can be replaced by temperature dependent functions, such as equations 5.1 or 5.2. These models can be fitted to the data by a maximum likelihood estimation and the behaviour of these models can then be examined by assessing their statistical validation criteria and their descriptive capabilities.

$$R_{exponential} = f(\Delta T) = R_i + b\ exp(-d\ \Delta T) \tag{5.1}$$

$$R_{logistic} = f(\Delta T) = R_i + \frac{a}{1 + b\ exp(-d\ \Delta T)} \tag{5.2}$$

5.2.1 Case study: cavity wall with rotational air looping around its insulation

Measurement data of a cavity wall with and without natural convection around its cavity insulation is provided by simulations as well as experiments. Both set-ups assume a similar wall configuration.

Simulation set-up

To provide on-site *measurements* of a cavity wall that is affected by buoyancy driven air flows, a wall with residual air cavities around its insulation is simulated in Delphin. The latter software program is a control volume method that models transient heat, air and moisture transport in porous building materials. Initially, only a simplified forced air convection model was included in the software, but in the context of the research project of Langmans [94], Delphin was further extended with a model for natural convection.

The assumed cavity wall consists of a 0.10 m thick brick façade layer, a 0.10 m thick polyurethane insulation board and a 0.09 m thick interior layer that is constituted of several wood cement boards. The latter replaces the typical interior brick leaf of a cavity wall, since wood cement boards allow to install an airtight inner construction layer without plastering. This was preferred in the experimental test set-up.

The rotational air flow around the insulation is simulated by including a 5 mm thick air channel at the four sides of the insulation board, which is assumed to be 1.50 m high. The channel's air flow permeability has to be specified by the user and can be calculated based on its thickness [94], which is in fact the channel's hydraulic diameter. For the 5 mm wide air channel, the air permeability is set to 0.116 s. To compose the temperature dependent R-values of figure 5.4, the wall is also simulated for a 10 mm wide air channel. Therefore, an air permeability of 0.46 s was selected. Furthermore, the air permeabilities of the used materials are set to 1E-14 s, 1E-20 s and 4E-6 s for the insulation board, wood cement boards and exterior brick layer respectively. Hence, the insulation and wood cement boards are treated as airtight, while the brick façade is simulated with a realistic, more permeable value [95]. A detailed discussion on how

the heat transfer in, from and to the air channel is calculated can be found in [94]. A representation of the assumed simulation grid for the wall can be found in appendix G.

The cavity wall is simulated for the typical moderate climate of Uccle (Belgium) which was already previously adopted for the simulations with HAMFEM. Figures 2.1a till 2.1d in chapter 2 represented the main outdoor boundary conditions for the considered reference year. Concerning the exterior heat balance, a convective heat transfer coefficient of 20 $Wm^{-2}K^{-1}$ is assumed in Delphin. For the calculation of short and long wave radiation, an absorption coefficient α_S of 0.75 and an emissivity ϵ_L of 0.9 is assumed for the brick façade. This corresponds to a brick with a rather dark colour.

Concerning the interior heat balance, Delphin assumes a constant interior heat transfer coefficient of 8 $Wm^{-2}K^{-1}$ to model the heat transfer from the wall to the indoor temperature node. The latter is assumed to be maintained at a constant temperature of 20°C throughout the whole year. Hence, a building with both ideal heating and cooling system is assumed.

The measurements will be analysed for two periods of 15 days: a winter period in December and a summer period in June. Figure 5.5 represents the heat flux and temperature measurements during both periods. Since these quantities are variable over the height of a wall, when affected by rotational air looping, the measurements are represented for three locations: near the bottom (at 0.19 m), at the centre (at 0.75 m) and near the top (at 1.30 m). These locations will be further denoted as the bottom, centre and top position. Figure 5.5, shows a clear shift, most noticeable at the bottom, between the heat flux and interior surface temperatures at the different positions on the wall. Generally, two-hourly averaged data will be considered. The averaging is performed by taking the arithmetic mean of the measurements in the intervals that correspond to the new sampling time, without prefiltering the data.

The cavity wall's *stationary* R_0-value equals 3.85 m^2KW^{-1}, as was already deduced from figure 5.4. This value is calculated from Delphin simulations which assumed a very high air flow resistance in the air channel, hence preventing buoyancy driven flows from occurring. On the other hand, local, temperature dependent R-values were previously presented in figure 5.4 (left). The profiles that correspond to the selected bottom, centre and top location are represented in colour and will be used as reference for the estimated variable thermal resistance indicators.

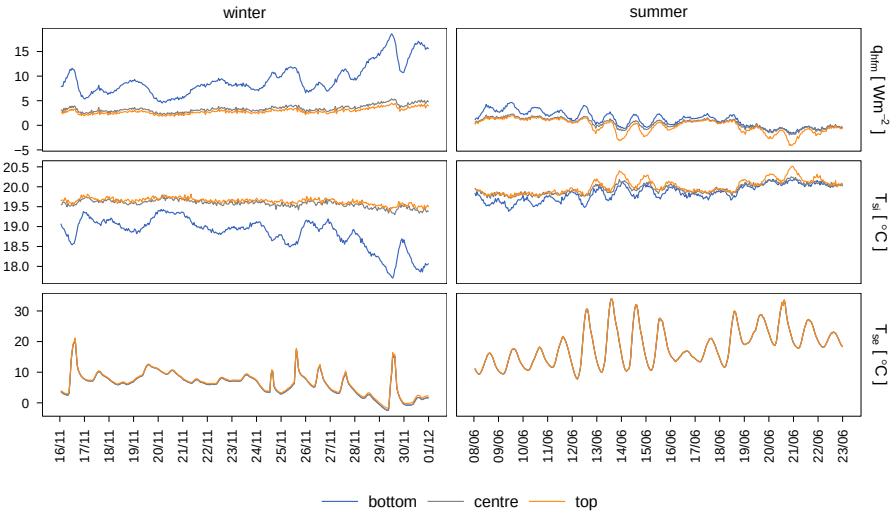

Figure 5.5: The surface temperature and heat flux measurements of the winter and summer periods that are simulated for a cavity wall with rotational air looping in its insulated cavity. The measurements are represented for three locations on the wall: near the top, at the centre and near the bottom of the wall.

Experimental set-up

In the VLIET test building, two cavity walls have been constructed: one with good workmanship and one with poor workmanship including air gaps around the insulation board. Figure 5.6 represents the cross sections of both test walls and the location of the measurement sensors. Note that the wall with good workmanship has an insulation layer that is attached against the wood cement boards, i.e. without residual air cavity behind the insulation. On the other side of the insulation, towards the brick façade, an air cavity of 0.04 m is created. Open head joints are not installed in the outer brick layer so that the air cavity is unventilated. For the wall with poor workmanship, an insulation board of 1.50 m high is deliberately shifted towards the exterior so that residual air cavities of 0.01 m are present behind the insulation and at the top and bottom joints. Towards the exterior an air cavity of 0.03 m is left over. Note that the insulation board is not shifted over the total length of the wall. This is done to avoid influences coming from the wooden frame that borders the test wall and that would influence measurements taken at the bottom of the wall.

Figure 5.7 (left) displays pictures of both test walls before the brick façade was built. The wall with good workmanship shows carefully installed insulation boards that are taped off at all boundaries to ensure airtightness. The wall with poor workmanship shows an airtight installation of all insulation boards, except for the middle boards. Figure 5.7 (left) also illustrates how wooden strips of 0.01 m thick are placed behind the insulation and between the separate insulation boards to ensure a continuous air channel along which the rotational air loop can be developed. An infrared picture of the walls (figure 5.7 (right)) demonstrates that rotational air looping is indeed occurring. The temperature gradient that is seen on the exterior face of the brick façade of the affected wall visualises the warm air that enters the exterior cavity and that flows downwards as it cools down. Conversely, at the interior face of the poorly installed wall, the cold air entering and rising in the interior cavity is visualised.

Experimental measurement data will by analysed for a specific winter period of 8 days. Figure 5.8 represents the most important boundary conditions for this period. Note that the indoor environment of the test building is maintained at a constant temperature of $\pm$ 18.4°C throughout the whole period. Figure 5.9 represents the heat flux and temperature measurements that are recorded throughout the selected 8 days for both walls. Two-hourly averaged data will be used to analyse the data. From figure 5.9 it is seen that the heat flux and interior surface temperatures are shifted relatively to each other for the wall with poor workmanship. Note furthermore, that for the wall with good workmanship, the interior surface temperature at the bottom differs from the other measurements, while the exterior surface temperatures and interior heat fluxes do coincide. This indicates a measurement error.

Based on the thermal properties of the used materials (see table 5.1), a theoretical R-value can be calculated for the wall with good workmanship. This value will be used as reference value for the wall, although it does not pretend to embody the actual thermal resistance. As was mentioned previously, many sources of error can affect this value. Next to that, note that the reference value of the test wall is higher than for the simulated wall. This mainly results from the fact that the simulations assume an insulation material with a thermal conductivity of 0.028 $W(mK)^{-1}$, while the experiments installed insulation boards with a thermal conductivity that was measured to be 0.021 $W(mK)^{-1}$. The remaining difference can be attributed to some specificities of Delphin's implementation of heat transfer and natural convection.

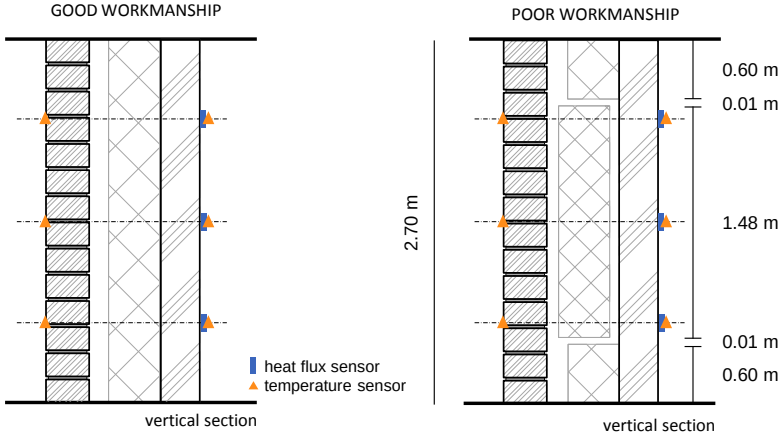

Figure 5.6: Cross sections of the test walls that are built in the VLIET test building. Note that the wall with good workmanship has an insulation layer that is attached closely against the wood cement boards, i.e. without residual air cavities, while the wall with poor workmanship has an insulation layer that is installed with residual air cavities of 10 mm at the joints and behind the middle insulation panel.

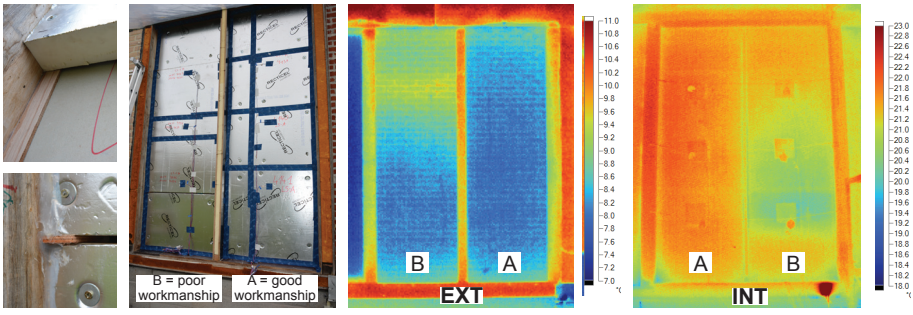

Figure 5.7: Left: Picture of both test walls with good and poor workmanship before the brick façade was built. Right: Infrared pictures of the exterior (EXT) and interior (INT) faces of the cavity walls with both good and poor workmanship that have been built in the VLIET test building.

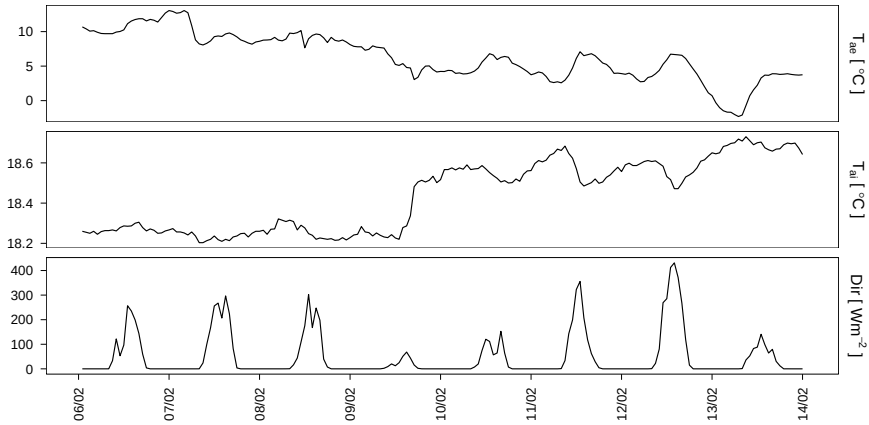

Figure 5.8: Outdoor air temperature, indoor air temperature and solar radiation measurements occurring during the winter experiments.

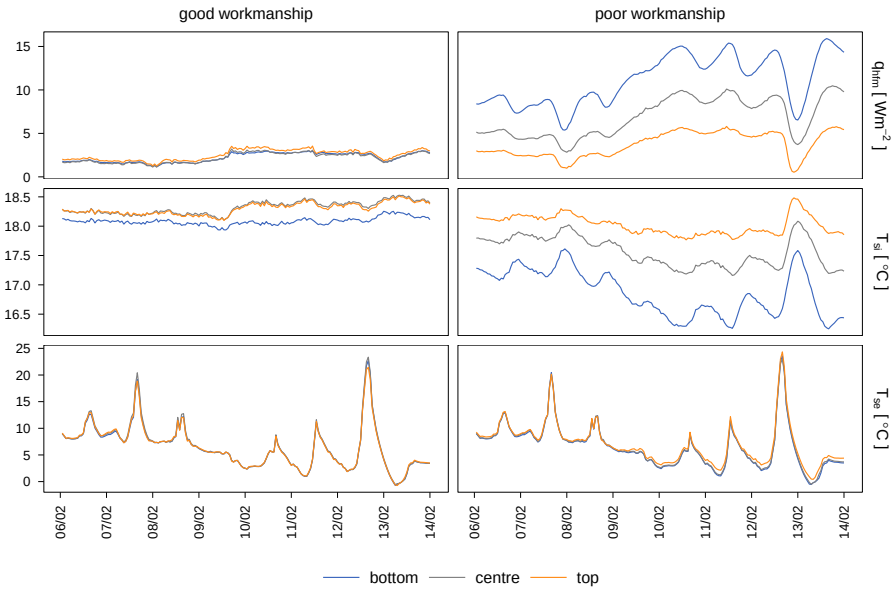

Figure 5.9: The surface temperature and heat flux measurements of both test walls with good and poor workmanship that are built in the VLIET test building. The measurements are represented for three locations on the wall: near the top, at the centre and near the bottom of the wall.

Table 5.1: Thermal properties of the considered cavity wall.

	d $[m]$	**λ** $[W(mK)^{-1}]$	**ρ** $[kgm^{-3}]$	**c** $[J(kgK)^{-1}]$	**R** $[m^2KW^{-1}]$	**C** $[MJm^{-2}K^{-1}]$
facing brick	0.100	0.900	2087	87	0.111	0.018
air cavity	0.040	/	/	/	0.180	/
polyureathane boards	0.100	0.021	35	1320	4.762	0.005
wood cement boards	0.090	0.350	1250	1470	0.257	0.165
TOTAL					**5.310**	**0.188**

5.3 Can a variable R-value be estimated by stochastic grey-box modelling?

5.3.1 Simulation research

In a first stage, the simulated wall with good workmanship is analysed to verify whether the wall behaves as assumed and to determine which model order is required to accurately predict the wall's interior heat flux. Therefore, the reference models, as presented in chapter 3 and described in appendix D, are fitted on the selected winter and summer data set by means of maximum likelihood estimation. First till fourth order models are regarded. Figure 5.10 shows the AICc for these different models when fitted on both data sets. As can be seen, in winter, third order models hold the lowest AICc, whereas in summer, fourth order models are assigned as optimal. Nevertheless, the AICc of the third order model in summer is very close to the AICc of the fourth order model. Hence, third order models are selected to analyse the measurement data of both winter and summer periods. This model order selection can also be justified from the periodograms in prediction and simulation setting which are depicted in figure 5.11: third order models are characterised by white-noise residuals for winter and summer data in both prediction and simulation setting.

The R-estimates resulting from the different models are represented in figure 5.12. The figure shows that reliable R-values can be estimated from both data periods when high enough model orders are selected. Furthermore, note that all fitted models locate the major part of the wall's thermal resistance in their inner model resistance. Analogous to what was demonstrated in chapter 3, the outer model resistances and capacitances are correlated, forming time constants explaining the dynamics coming from the outside. Since the interior temperature is kept constant, no dynamics coming from the inside have to be explained so that the inner thermal resistance can be allocated to capture the main part of the total thermal resistance.

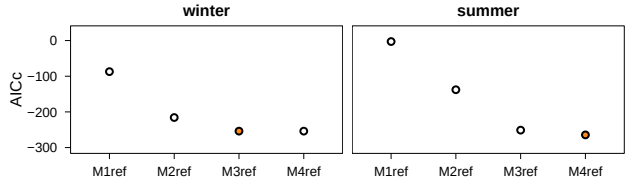

Figure 5.10: Comparison of different order models estimated from winter and summer measurements of the simulated cavity wall with good workmanship. The model with the lowest AICc-criterium indicates the preferred order model.

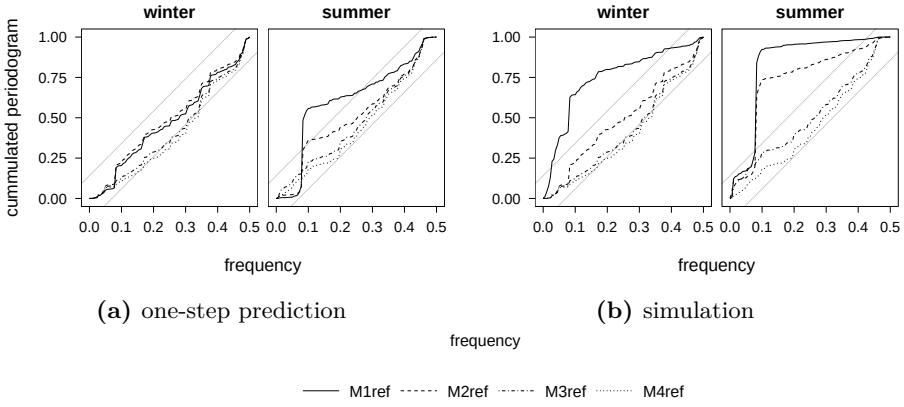

Figure 5.11: The cummulated periodograms of the first till fourth order models estimated both the winter and summer measurements of the simulated cavity wall with good workmanship.

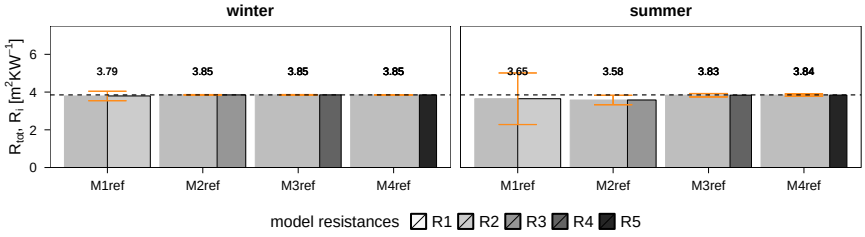

Figure 5.12: The thermal resistances of the four different order models estimated from both winter and summer measurements of the simulated cavity wall with good workmanship. The dotted lines represent the reference value of the wall deduced from the Delphin-simulations. The first till fourth order model are denoted by M1ref till M4ref respectively. The individual model resistances R_1 till R_5 are represented versus a solid grey block corresponding to the total estimated resistance R_{tot}.

To illustrate the third order model's descriptive capabilities, its behaviour in prediction and simulation setting is represented in figure 5.13. Note that the model behaves identical in both prediction and simulation setting. In general, the figure demonstrates that the selected third order model is able to accurately reproduce the wall's interior heat flux measurements in winter and summer periods.

In sum, the previous analyses demonstrated that the assumed third order model is suited for estimating the thermal resistance of the carefully installed cavity wall and that the validation criteria, as described in chapter 3, are fulfilled. In a next step, it is studied how this model behaves when applied to measurement data of a poorly installed cavity wall that is affected by rotational air looping around its insulation. In particular, it is examined whether the validation criteria are able to indicate that something peculiar is going on. To study this, the third order reference model is fitted on winter and summer measurements of the wall. Since rotational air flow has a different impact on the wall's thermal behaviour depending on the position of the measurements, the model is fitted to data at the top, bottom and centre of the wall. The exact locations of these positions were previously specified (see section 5.2.1).

Do stochastic validation criteria hold indications for rotational air looping?

One way of looking for indications of rotational air looping in the wall, is assessing the residuals of the fitted reference model for white noise. Figure 5.14 depicts the periodograms of the third order model's residuals in prediction and simulation setting when fitted on the winter and summer data measured at the three selected locations

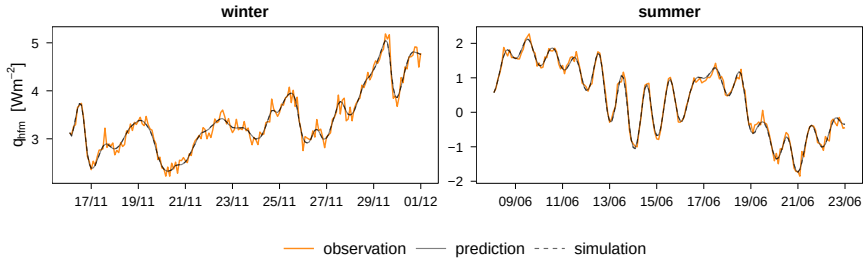

Figure 5.13: Observed, predicted and simulated heat flux in winter and summer. The results are represented for the third order reference model estimated from measurements at the centre of the simulated cavity wall with good workmanship.

on the wall. The figure demonstrates that the residuals are not significantly auto-correlated in a one-step ahead prediction mode: at all positions, the periodogram indicates white noise residuals. When looking at the residuals in simulation setting, however, auto-correlated residuals are found at some positions on the wall. In winter, only at the bottom, the long term descriptive behaviour of the model is found to be deficient. In summer, both top and bottom measurements show a poor long term model behaviour. Hence, the importance of inspecting the models' long term behaviour for validation purposes is underlined again. The fact that the impact of rotational air looping is poorly noticeable in a one-step prediction setting is linked to the unidentifiability issues of the considered identification problem. Due to the typical presence of practically unidentifiable parameters in the reference model (which was demonstrated in chapter 3), the uncertainty of certain states is large. Hence, the Kalman filter is forced to put its weight largely on the measurement data rather than on the model itself. As such, the modelled states are *corrected* at each prediction step according mainly to the measurements so that the influence of a variable thermal resistance is difficult to notice. Next to that, the fact that model deficiencies are observed only at some positions on the wall, might not surprise. When reconsidering figure 5.4 (left), it is clear that in winter – characterised by large, positive surface temperature differences – the rotational air looping is only observable at the bottom position: since the variable R-value is rather constant at the centre and top position over the temperature difference range that accords to winter, the air looping is not observed from the top and centre measurements. The summer period (see figure 5.4 (right)), on the other hand, corresponding to surface temperature differences located around zero, is characterised by a highly varying R-value at top and bottom, but by a

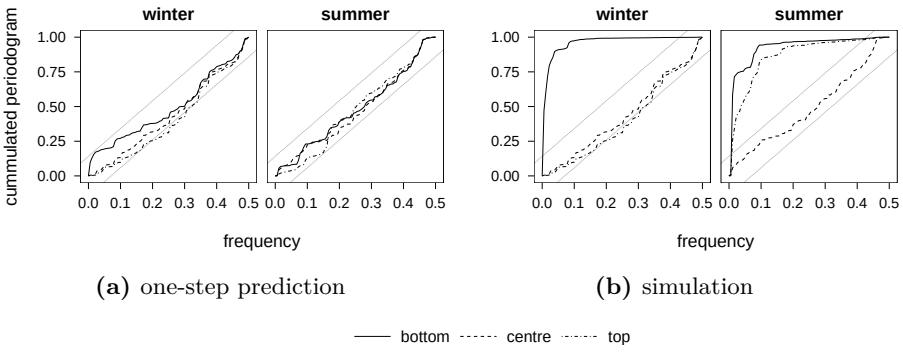

Figure 5.14: The cumulated periodograms of the third order reference models, estimated from measurements at the top, centre and bottom of the simulated wall with rotational air looping.

rather constant R-value at the centre. Hence, only the residuals at the centre behave as white noise.

The behaviour of the model versus the measurements is further illustrated in figure 5.16. It depicts the observed heat flux together with the predicted and simulated heat flux by the estimated third order models. The bottom figure also renders the residuals in one-step ahead prediction and in simulation mode. The representation of the observed and modelled flux and residuals confirms the conclusions drawn from the periodograms: the predicted heat flux mimics the measured flux quite accurately, while the simulated heat flux illustrates the impact of the rotational air looping more clearly, although only at certain positions on the wall.

Before assessing a second way of looking for indications of rotational air looping in the wall, the estimated thermal resistances of the reference models are examined when fitted on data of a wall with rotational air looping. Figure 5.15 represents the estimated model resistances for the three locations on the wall and for winter and summer periods. It is noticed that the apparent resistances that are estimated from winter measurements increase with the height of the measurement position on the wall. The estimates correspond to what was observed in theory: the R_{app}- at the bottom is typically lower than the stationary R_0-value, while the R_{app} at the top is higher, when positive indoor-outdoor temperature differences are occurring. Hence, the estimated constant R_{app}-values behave as an averaged value of their actual temperature dependent profiles. Next to that, note that the estimated R_{app}-value at the centre correspond to R_0. This is also seen for the R_{app}-value estimated from the

Figure 5.15: The thermal resistances of the third order reference model estimated from winter and summer measurements at the top, centre and bottom of the simulated cavity wall with rotational air looping. The individual model resistances R_1 till R_5 are represented versus a solid grey block corresponding to the total estimated resistance R_{tot}. The dotted line represents the stationary R_0-value of the considered wall.

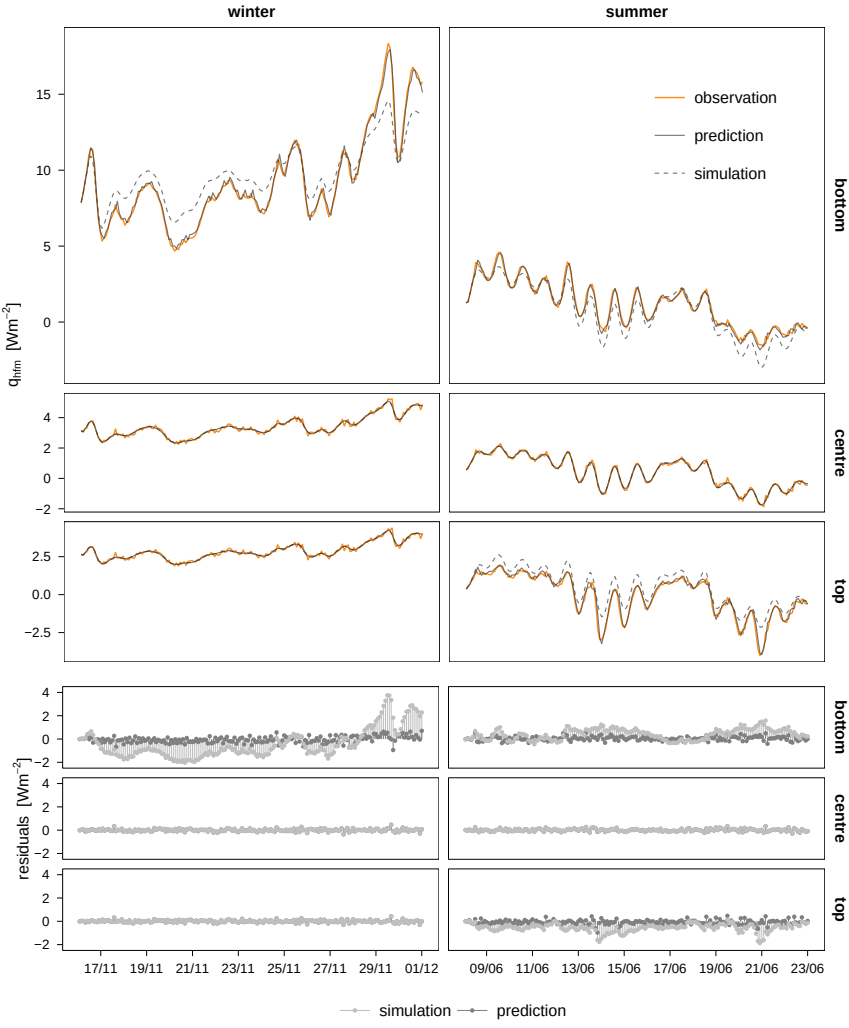

Figure 5.16: Observed, predicted and simulated heat flux in winter and summer (top) together with the corresponding residuals (bottom). The results are represented for the third order reference model, estimated from measurements at the top, centre and bottom of the simulated cavity wall with poor workmanship.

summer measurements at the centre and corresponds to the theoretical observations: at the centre of the wall, the influence or rotational air looping is negligible for air flows below a certain value. The bottom and top resistances that are estimated from summer measurements do not show any correlation between the position of the measurements and the obtained values.

Another way of looking for indications of rotational air looping in the wall, concerns the assessment of correlations between the residuals and the *driving force* of the natural convection. Theoretically, this driving force is the temperature difference over the insulation panel at the neutral pressure plane. However, in reality, the location of the neutral line is not known and the cavity temperatures are not typically measured. Therefore, the driving force is approximated by the difference between the measured surface temperatures. Furthermore, due to the thermal capacity of the studied wall, the rotational air flow induced by a momentaneous temperature difference, will not instantly affect the measured heat flux. Only after a certain time, the influence will be visible in the measured heat flux. Therefore, correlations will be analysed between momentary residuals and temperature differences that are lagged in time. Before analysing the residuals' cross correlations for the wall with poor workmanship, the correlations for the wall with good workmanship are assessed. Figure 5.17 depicts the residuals of the third order models fitted on the measurements of the carefully installed wall in function of the temperature difference over the wall, lagged in time or not. In the figure, the different columns correspond to temperature differences with a different time lag, while the different rows correspond to winter and summer results. Note that the residuals are represented in both one-step ahead prediction and simulation mode. From a statistical point of view, the latter are irrelevant, because residuals determined in an output error mode are very likely to be auto-correlated. However, since it was seen from figures 5.15 and 5.16 that the estimated models simulate the heat flux in an average way, their residuals might also illustrate the correlation with the driving force. Figure 5.17 demonstrates that no correlations are found between the residuals and the rotational air looping's driving force when a carefully installed cavity wall is analysed.

Conversely, when considering a cavity wall that is affected by rotational air looping around it's insulation, correlations between the residuals and the (approximated) driving force are found, as can be seen from figure 5.18. Analogously to figure 5.17, it depicts the residuals in prediction and simulation mode, and for winter and summer measurements, in function of the surface temperature differences which are lagged in time or not. For the winter measurements (figure 5.18a), a clear correlation between the residuals and temperature differences can be observed for the bottom measurements.

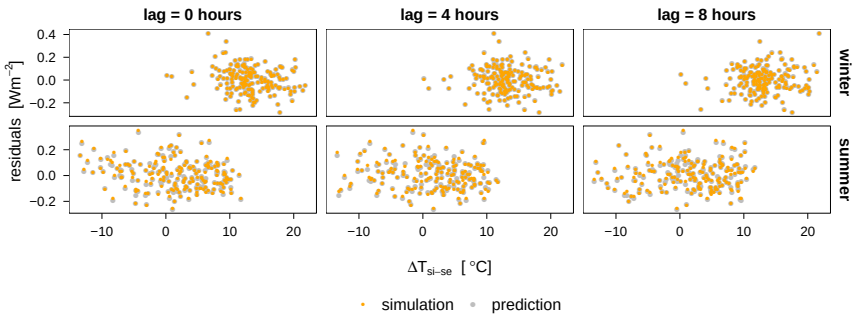

Figure 5.17: Residuals of the third order model, fitted on the measurements of the cavity wall with good workmanship, in function of the temperature difference over the wall, lagged in time or not. The residuals are grey when prediction errors are considered and orange when output errors are regarded. The results in the different columns correspond to temperature differences with a different time lag, while the results in the different rows correspond to winter and summer analyses.

Although the correlation is more pronounced in simulation setting, it is also perceivable in one-step ahead prediction mode: a linear correlation between the residuals and temperature differences can be observed. Note, furthermore, that the correlation is best pronounced when a time lag of 8 hours is considered, although also visible when smaller time lags are considered. From the top and centre measurements, no correlations are observed. This corresponds to the findings from the periodograms and confirms the explanation that the local, apparent thermal resistances at the top and bottom are quasi constant for the occurring range of temperature differences in winter. In summer, correlations are perceived for top and bottom measurements, although their trend is less pronounced than in winter. Even more, the correlation is not seen when the residuals are plotted in function of the momentary temperature differences (lag = 0 hours). Only when the latter are lagged over 4 or 8 hours, a correlation is installed. In prediction mode, a slightly concave relation is seen for the residuals at the top, while at the bottom, a convex correlation is noticed. In simulation mode, the correlation is more pronounced and a downward and upward v-shaped correlation is seen from top and bottom measurements respectively.

Overall, the previous analyses demonstrated that the impact of rotational air looping in the wall can, in some cases, be perceived from validation tests. It was shown that testing for white noise residuals, as well as testing for correlations between residuals and temperature differences, held indications for the presence of rotational air looping.

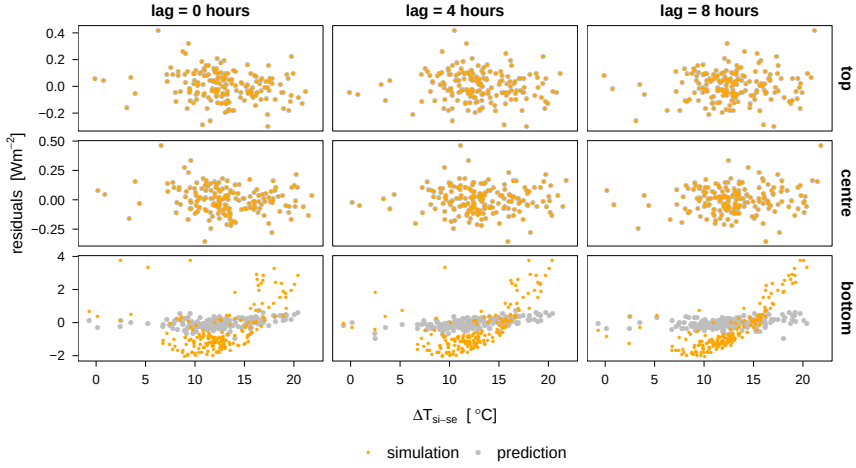

(a) winter

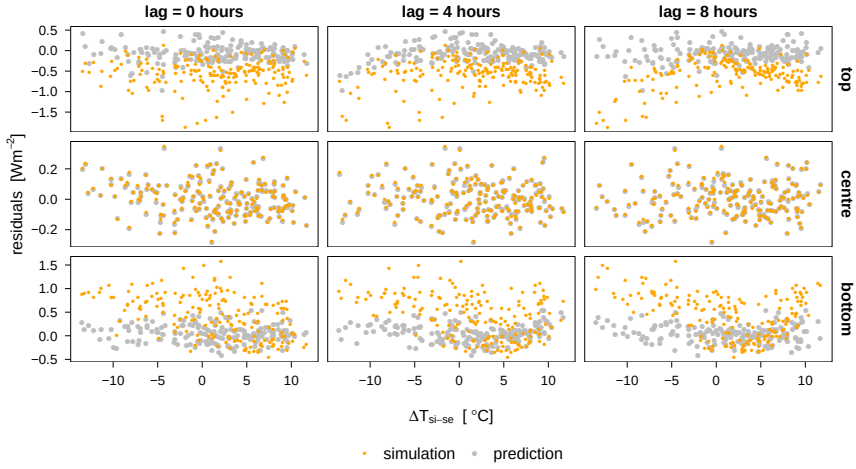

(b) summer

Figure 5.18: Residuals of the third order model, fitted on the measurements of the cavity wall with good workmanship, in function of the temperature difference over the wall, lagged in time or not. The residuals are grey when prediction errors are considered and orange when output errors are regarded. The results in the different columns correspond to temperature differences with a different time lag, while the results in the different rows correspond to top, centre and bottom analyses. The correlations are represented for both winter (a) and summer (b) periods.

However, these indications were not found at all positions on the wall: when the surface temperature differences occurring during the measurements correspond to a region where the apparent, local thermal resistance is quasi constant, than obviously, no indications are observed. Furthermore, for these measurements, the reference model behaves accurately and fulfil the main validation criteria as set in chapter 3, since the occurring dynamics can be explained by a time invariant thermal resistance. The estimated thermal resistance will, however, depend on the measurements' location on the wall. In sum, although stochastic grey-box modelling can indicate the presence of rotational air looping at some positions, the technique is not able to guarantee that no natural convection is occurring in the wall.

A next step in this study focusses on whether a variable R-value can be estimated from measurements that are affected by rotational air looping. Since the previous section showed that the largest impact of natural convection is seen at the bottom of the considered wall, the measurements at this position are analysed initially.

Can a variable R-value be estimated from measurements at the bottom?

Previously, figure 5.4 (left) depicted the temperature dependent R-profiles, calculated from stationary conditions, at different vertical positions of the considered wall. It was also mentioned that these variable R-values can be approximated by exponential or logistic curves, parametrised in function of a certain temperature difference. Hence, if the total model resistance of a grey-box model can be formulated as an exponential or logistic curve, a variable thermal resistance that quantifies the impact of rotational air looping can be estimated from measurements. In order to include such an exponentially or logistically varying R-value in a stochastic state space model, two questions have to be handled: first, it has to be decided which model resistance(s) will comprise the temperature dependent function and secondly, it must be chosen to which temperature difference this function will be linked. If the chosen temperature difference is linked to the modelled states, which is very likely, the model becomes non-linear.

From the previously considered analyses of measurement data of the wall with good workmanship, it was seen that the estimated third order models were of sufficient order to explain the occurring dynamics. Hence, a third order is also selected for the *non-linear* models used in this chapter. Furthermore, from the previously conducted analyses of the wall with buoyancy driven air flows, it was seen that the estimated reference models located the major part of their total thermal resistance in the inner resistance (see figure 5.15). The other model resistances were assumed to function, together with the outer model capacitances, as time constants explaining the dynamics coming from the exterior. Hence, it is chosen to include the exponentially or logistically, time dependent aspect in the inner thermal resistance of a third order model. The

temperature difference to which this variable resistance is then logically linked, is the temperature difference over this internal resistance, i.e. the difference between the interior surface temperature and the most internal state. This leads to the following non-linear, third order models, further denoted as exponential and logistic models:

$$dT_1 = \frac{1}{C_1 R_1}(T_{se} - T_1)dt + \frac{1}{C_1 R_2}(T_2 - T_1)dt + \sigma_1 d\omega_1 \tag{5.3}$$

$$dT_2 = \frac{1}{C_2 R_2}(T_1 - T_2)dt + \frac{1}{C_2 R_3}(T_3 - T_2)dt + \sigma_2 d\omega_2 \tag{5.4}$$

$$dT_3 = \frac{1}{C_3 R_3}(T_2 - T_3)dt + \frac{1}{C_3 R_{var}}(T_{si} - T_3)dt + \sigma_i d\omega_i \tag{5.5}$$

$$q_{hfm,t_k} = \frac{1}{R_{var}}(T_{si,t_k} - T_{3,t_k}) + \epsilon_{t_k} \tag{5.6}$$

with

$$R_{var} = b\ exp(-d\ (T_{si,t_k} - T_{3,t_k}))) \text{ for the exponential model} \tag{5.7}$$

or with

$$R_{var} = \frac{a}{1 + b\ exp(-d\ (T_{si,t_k} - T_{3,t_k})))} \text{ for the logistic model} \tag{5.8}$$

The parameters a, b and d are scaling factors that determine the shape of the exponential or logistic R-profiles. The total thermal resistance and capacity of the building component are calculated as $R_{app} = \sum R_i + R_{var}$ and $C_{tot} = \sum C_i$ respectively.

Since winter measurements are mainly characterised by positive indoor-outdoor temperature differences, the exponential model is the most obvious choice to be estimated to this data. The logistic function can also be fitted, although it is possible that winter measurements might not contain enough information to estimate the entire shape of the function. Nevertheless, both logistic and exponential models are estimated from winter measurements. Since summer measurements are characterised by both positive and negative surface temperature differences, only the logistic model is estimated from these measurements. Similar to the application of stochastic grey-box models in chapter 3, each model is estimated multiple times by a maximum likelihood estimation and afterwards the result with the highest maximum likelihood is selected as final result.

Figure 5.19 represents the temperature dependent R-profiles that are estimated from the bottom measurements of the simulated wall in winter and summer. The estimates resulting from the logistic and exponential models are shown, together with the constant thermal resistances that were estimated by the third order reference model. In orange, the theoretical R-profile of figure 5.4 is represented for the bottom location. Since this profile is calculated from stationary simulations of the same wall that is used

for the dynamic simulations, it serves as goal value for the estimated apparent model resistances. At the bottom of figure 5.19, a histogram represents the distribution of the surface temperature differences that occur during the considered winter and summer measurements. Finally, it must be noted that the estimated temperature dependent R-values are estimated as a function of ΔT_{si-3}, as could be seen from the model descriptions. In figure 5.19 they are represented in funtion of ΔT_{si-se}. The translation between both formulations can be made once a non-linear model is estimated: since all model resistances are known, the state temperature can iteratively be calculated for every pair of surface temperatures. In all further representations, the estimated temperature dependent R-values will be translated to functions of ΔT_{si-se}.

Figure 5.19 shows that the reference profile (orange) is approximated closely by both exponential and logistic R-estimates in winter, although only for temperature differences that occur regularly in the measurements. For other temperature differences,

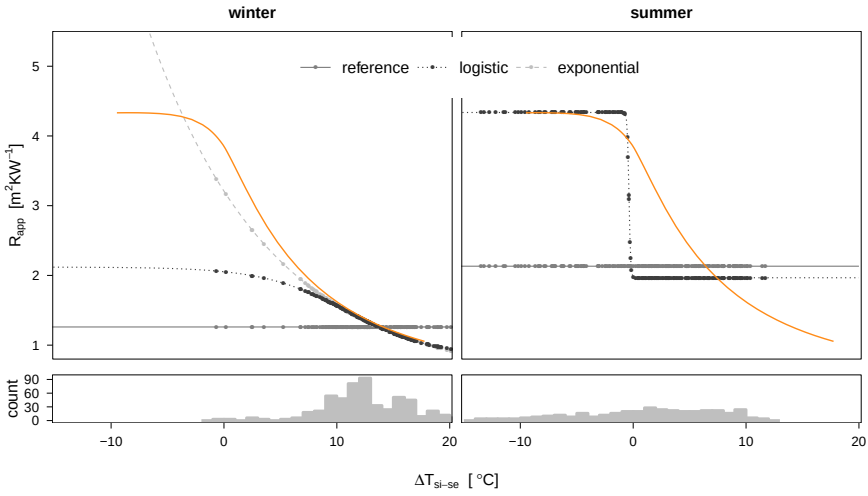

Figure 5.19: Temperature dependent, apparent R-values estimated from the bottom measurements of the simulated wall with poor workmanship in winter and summer. Estimates resulting from the logistic and exponential models are shown together with the constant R-values that were estimated by the reference model. In orange, the theoretical R-profile is represented as reference. The bottom graphs depict the distribution of the surface temperature differences that occur during the winter and summer measurements.

the estimated logistic and exponential profiles deviate from each other and from the reference profile. This might not surprise, since the data does not contain information on the behaviour of the variable apparent resistance in this temperature region. Hence, the estimated R-profiles might only be trusted for the range of temperature differences that occur in the measurements. This implies that the stationary R_0-value, which can be determined as the value of the estimated R-profile at a temperature difference of zero, can not be reliably estimated from the considered winter measurement, or, in general from measurements with merely positive temperature differences.

In summer, the estimated logistic R-profile differs significantly from the reference profile, even for temperature differences that are covered by the measurement data, as can be seen in figure 5.19. In particular for temperature differences around zero, the estimated R-profile deviates significantly from the goal curve. A possible explanation for this can be linked to the fact that the reference R-profile is calculated under stationary boundary conditions, which never occur when on-site measurements are considered. Whereas under stationary boundary conditions, every surface temperature difference corresponds to a fixed air flux in the cavity, this is not the case for dynamic boundary conditions, under which the developed air fluxes are constantly changing. Even more, for temperature differences fluctuating around zero, the air flow is regularly changing directions. Hence, in this region it is difficult to link a certain occurring temperature difference to a fixed air flow or apparent thermal resistance, especially because averaged data is used and because the considered surface temperature differences are only an approximation of the actual forces that drive the natural convection. Hence, also for summer measurements, the determination of the wall's stationary R_0-value from its apparent R-profile results is an unreliable estimate. However, although the estimated R-profile does not follow the shape of the reference profile exactly, it does fluctuate over the same range of R-values when considering the temperature differences that are present in the data, which is valuable information.

To assess the non-linear models' behaviour, the predicted and simulated heat fluxes are compared with the measured heat flux in figure 5.20. In parallel with the depicted heat fluxes, the time dependent R-values that are adopted by the different models are represented. The results of the reference model, and both logistic and exponential models are shown. From figure 5.20a it is seen that the heat fluxes modelled in a one-step ahead prediction setting do not differ significantly from each other: by the eye, no clear deviations are observed between the heat flux predicted by the reference model or by the non-linear models in winter nor in summer. Nevertheless, the thermal resistances that are adopted by the models are different, as can be seen from the bottom graphs of figure 5.20a. In winter, the time dependent R-values

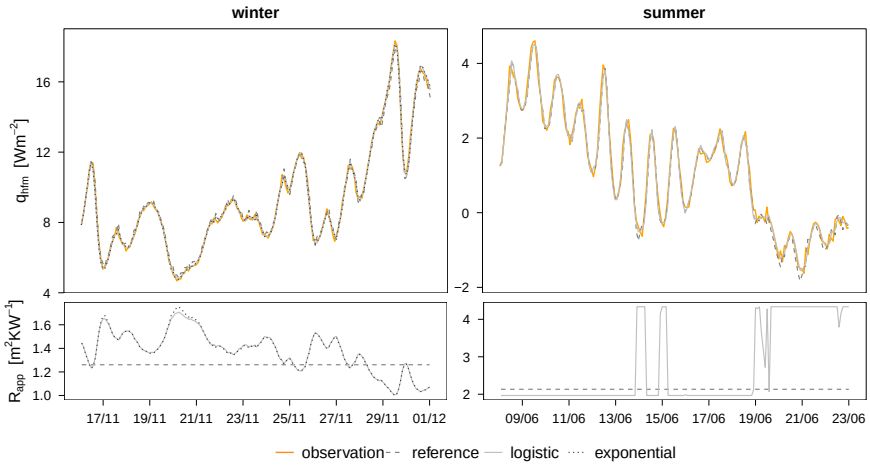

(a) prediction setting

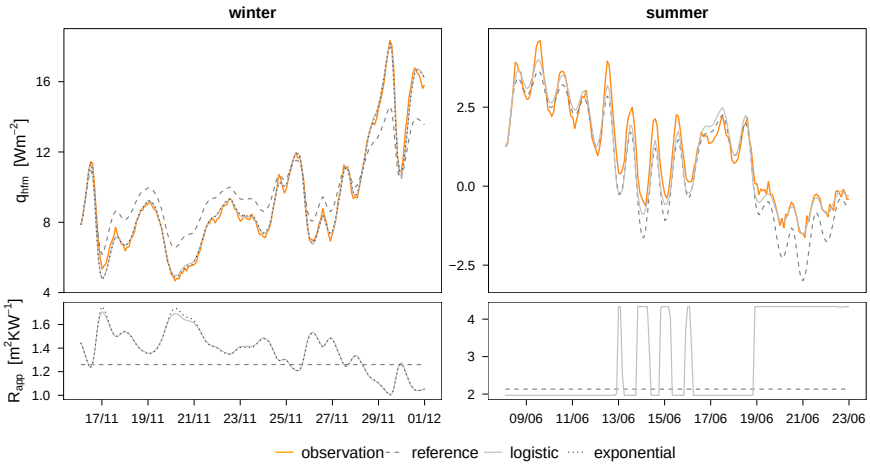

(b) simulation setting

Figure 5.20: Observed, predicted (a) and simulated (b) heat flux for winter and summer measurements. The results are represented for the third order reference model and for the logistic and exponential models, estimated from measurements at the bottom of the simulated cavity wall with poor workmanship.

(exponential and logistic) fluctuate smoothly between 1 and 1.7 m^2KW^{-1}, while the constant thermal resistance of the reference model behaves as an averaged value. In summer, the variable R-value shows a more abruptly changing pattern due to its steeply shaped temperature dependency. When observing the models' output in simulation setting (see figure 5.20b), their distinct behaviour can be seen more clearly. For winter measurements, the figure demonstrates that the reference model is not able to accurately simulate the observed heat flux, whereas the non-linear models are. Also in summer, the logistic model behaves more accurately than the reference model, although its simulation is far from perfect. The figure demonstrates that the heat flux is more or less accurately estimated by the logistic model during the first four days, when the heat flux is continuously positive, and during the last four days, when the heat flux is continuously negative. For the first period, the models adopted R-value is small but constant, while for the last period, the R-value is large but also constant. In the intermediate period, when the heat flux alters between positive and negative values, the model behaves inaccurately. As explained before, for temperature differences around zero, it is hard to pinpoint one specific apparent thermal resistance to a certain temperature difference.

By analysing the periodograms of the estimated models in figure 5.21, it is verified whether the above conclusions can also be retrieved from analysing the model's residuals. Figure 5.21a demonstrates that all models obtain white noise residuals in a one-step ahead prediction setting, which corresponds to the almost perfectly predicted heat fluxes that were previously observed in figure 5.20a. Notwithstanding all models' white noise residuals, the steeper regions in the periodogram of the reference model can not be found in the periodograms of the exponential and logistic models, indicating their improved performance. In simulation mode (see figure 5.21b), not any model shows white noise residuals, not even the exponential or logistic model in winter. A small improvement in the periodograms of the non-linear models is, however, observed compared to the periodograms of the reference model. Nevertheless, although the non-linear models appeared to predict and simulate the observed heat flux quite accurately in the time domain, this is not confirmed in the frequency domain: the periodograms indicate that the non-linear models are not able to explain all dynamics in the data. As such, although the non-linear models showed improved modelling capacities as well as an improved thermal characterisation, this can not be endorsed by all validation criteria.

Taken all this into account, it can be concluded that the considered exponential and logistic models hold the ability to characterise a temperature dependent R-value from local on-site measurements of a cavity wall that is affected by natural convection. The

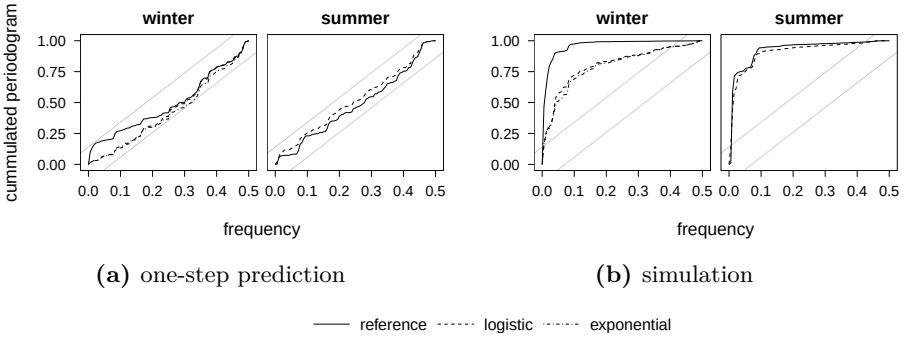

(a) one-step prediction **(b)** simulation

Figure 5.21: The cumulated periodograms of the reference, logistic and exponential model estimated from measurements at the bottom of the simulated wall with rotational air looping in winter and summer.

accuracy with which these variable apparent thermal resistances can be estimated depends highly on the considered measurement period. From the performed analyses, it was found that winter measurements, covering mainly positive indoor-outdoor temperature differences, enabled to accurately estimate apparent R-profiles, although only for the range of temperature differences occurring in the data set. From summer measurements, mainly covering temperature differences around zero, it was learnt that R-profiles are unreliably estimated for temperature differences around zero. Hence, from these findings it was concluded that a reliable estimate of the wall's stationary R_0-value can not be obtained. In a next step, it is verified whether temperature dependent R-values can also be estimated from other locations on the wall, where the impact of rotational air looping was found to be smaller than at the bottom of the wall.

Can a variable R-value be estimated from measurements at the centre or top?

Similar as for the measurements at the bottom position, the logistic and exponential model are fitted from winter measurements at the top and centre of the wall, while only the logistic model is fitted from summer measurements at these locations. Figure 5.22 depicts the R-profiles that are estimated from the on-site measurements at the top and centre of the cavity wall with poor workmanship. The results from the third order reference model are also represented. When examining the results for the measurements at the centre (bottom row of figure 5.22), it can be seen that the estimated R-profiles are flat in the region of the most frequently occurring temperature differences. In

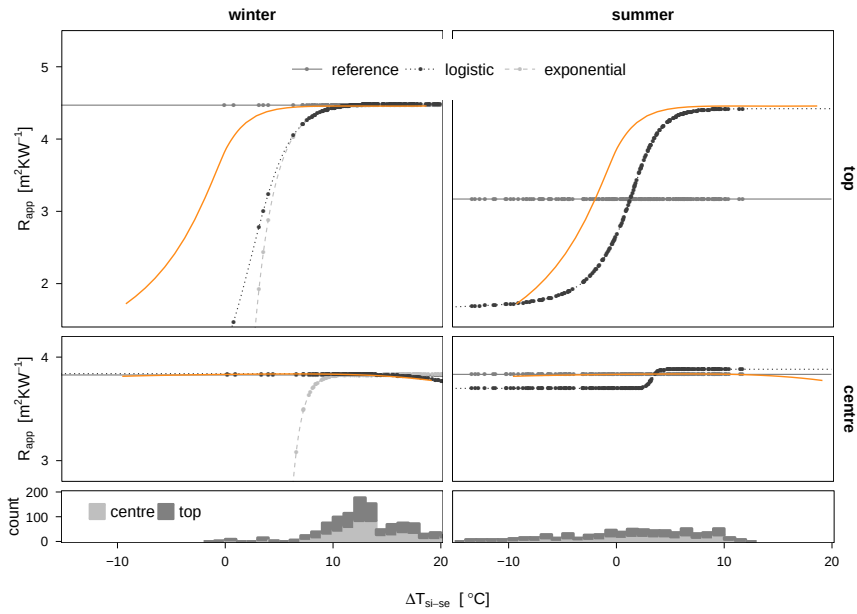

Figure 5.22: Temperature dependent, apparent R-values estimated from the top and centre measurements of the simulated wall with poor workmanship in winter and summer. Estimates resulting from the logistic and exponential models are shown together with the constant R-values that were estimated by the reference model. In orange, the theoretical R-profile is represented as reference. The bottom graphs depict the distribution of the surface temperature differences that occur during the winter and summer measurements.

summer, an s-shaped logistic R-function can be noticed, although the range of R-values this profile is covering is rather limited given the scale of the y-axis. In general, it is noticed that the model parameters are estimated in such a way that the *variable* parts of the logistic and exponential functions are discarded towards temperature differences that are not occurring in the measurements. Since the location of these variable parts is rather random, the models are very likely to contain unidentifiable parameters. This was also noticed from the fitted models which regularly hit the prespecified boundaries of their parameters, no matter how large they were set. The fact that the estimated R-profiles are quasi-stationary for the occurring temperature differences could be expected since the reference R-profile also indicates a quasi-constant apparent thermal resistance at the centre of the wall. These observations

lead to the conclusion that the estimated profiles can still be trusted, when evaluated for temperature differences that occur in the measurements, even for measurements that do not indicate to be affected by natural convection. Similar results are observed for the non-linear models that are estimated from the winter measurements at the top of the wall (top row of figure 5.22): since the impact of rotational air looping is rather constant for the considered measurements, a flat R-profile is estimated for the occurring temperature differences. Summer measurements obtained at the top of the wall, on the other hand, did indicate to be affected by rotational air looping in previous analyses. Correspondingly to this finding, a variable apparent thermal resistance is estimated by the logistic model. Similar as to the estimates from the bottom measurements, the R-profile behaves unreliably when temperature differences around zero are considered, but estimates accurately the range over which the apparent R-value fluctuates during the course of the measurements.

For completeness, the observed and modelled heat fluxes are shown in figure 5.23. Note that the modelled outputs are only represented in simulation mode since possible differences in model behaviour are best observed in this setting. As could be expected, only for the summer measurements at the top, the non-linear model shows an improved behaviour compared to the reference model. However, the simulated heat flux does not yet perfectly mimics the observed heat flux. Similar as to the analysis at the bottom, the heat flux of the first and last four days of the measurements are explained rather accurately by the logistic model, while the heat fluxes of the intermediate period, which fluctuate around zero, are predicted less accurately. For the centre measurements and for the winter measurements at the top, both the reference model and non-linear models simulate the heat flux in an accurate way. The R-values that are therefore adopted by the non-linear models behave in a quasi-constant way.

The periodograms in figure 5.24 confirm the previous observations. In simulation mode, both the reference models and non-linear models show white noise residuals for winter measurements and for summer measurements at the centre, confirming that all dynamics in the measurements are explained. Only for the summer measurements at the top, no white noise residuals are obtained. This means that the improved, yet not perfect, performance of the logistic model is not reflected by the periodogram. It is, however, reflected by the Akaike Information Criterion. Figure 5.25 represents the AICc-values for the reference model and non-linear models that are fitted at the top, centre and bottom measurements of the wall. The figure clearly indicates that the reference model is the preferred model to estimate models that are affected by the rotational air looping in a constant way.

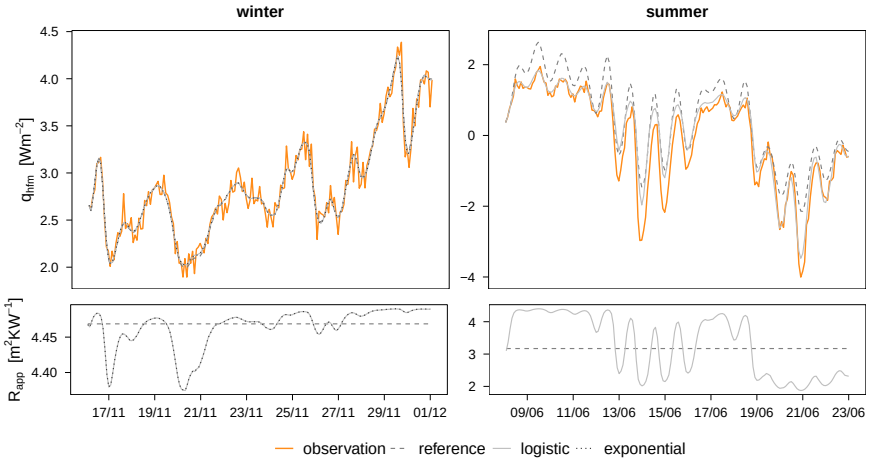

(a) top

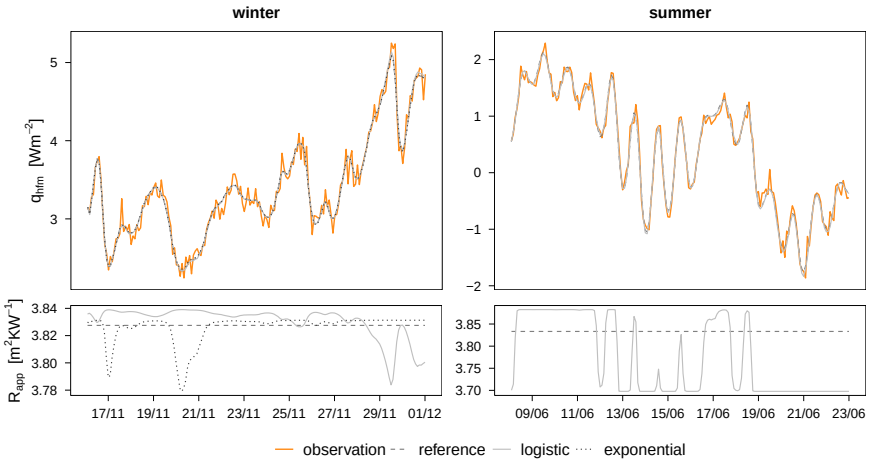

(b) centre

Figure 5.23: Observed and simulated heat flux for winter and summer measurements. The results are represented for the third order reference model and for the logistic and exponential models, estimated from measurements at the top (a) and centre (b) of the simulated cavity wall with poor workmanship.

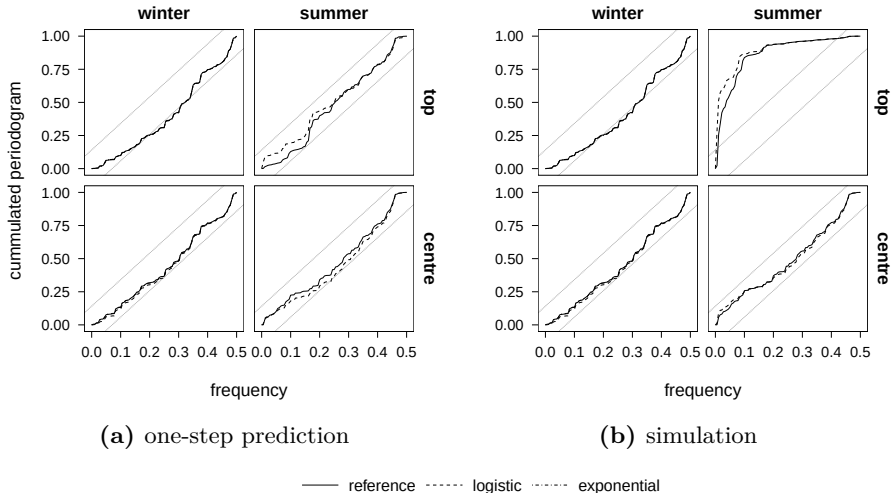

(a) one-step prediction **(b)** simulation

Figure 5.24: The cumulated periodograms of the reference, logistic and exponential models estimated from measurements at the top and centre of the simulated wall with rotational air looping in winter and summer.

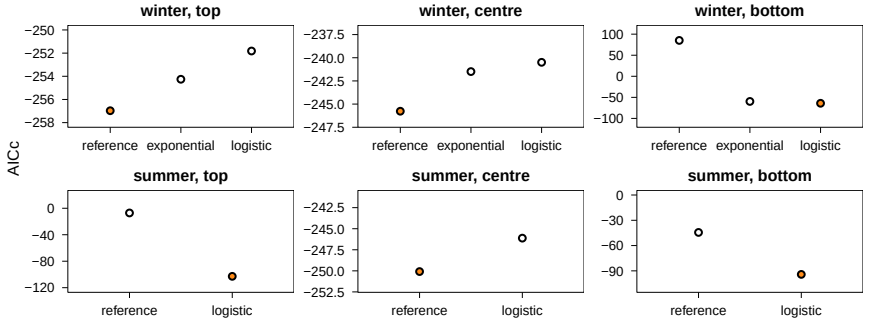

Figure 5.25: Comparison of different models estimated on the simulated winter and summer measurements at the top, centre and bottom of the cavity wall with poor workmanship. The model with the lowest AICc-value (orange) is the preferred model.

So, in general, from the previous analyses it can be concluded that the findings from the analyses at the bottom are still valid, but must be extended. First, it was observed that the non-linear models can be applied to all data sets. However, only for measurements that are affected by rotational air looping in a variable way, time invariant R_{app}-

values will be estimated. For data sets that are affected by natural convection in a quasi constant way, the variable part of the exponential and logistic R-profiles will be shifted to temperature differences that do not occur in the data. Consequently, in all probability, practical identifiability issues start hindering the estimation procedure. Hence, the use of non-linear models is redundant because reference models can be used just as well. The latter can be judged based on the Akaike information criterion, which proved to make an appropriate selection of optimal model for the considered data sets: the reference model was selected for measurements that are affected by the rotational air looping in a constant way, while the non-linear models where selected for measurements that were affected in a variable way. Secondly, the previous analyses confirmed that the logistic or exponential R-curves are not able to accurately capture the dynamic thermal resistance that is occurring around zero temperature differences. It is, however, doubted if any other function can, since the dynamic R-value at a specific temperature difference will, in all probability, take a different value every time this temperature difference occurs, depending on the wall's thermal history.

5.3.2 Experimental research

In this section, the step towards real measurements is taken. Therefore, the measurement data of the cavity walls, with both carefully and poorly installed insulation panels, that are constructed in the VLIET building are studied. Similar to the simulation research, initially, the wall with good workmanship is examined. Figure 5.26 represents the total thermal resistance that is estimated from the selected winter period for the three different measurement locations on the wall. The represented R-values are estimated by a third order, reference model. Note from figure 5.26 that, although much care was attributed to the installation of this wall and of its measurement devices, significant differences in estimated R-values are found. Especially, the estimate at the top in winter alters significantly from the other estimates. This underlines that the achievable measurement accuracy might play an important role in the final accuracy that can be obtained by the estimation results. This aspect is, however, not further studied in this dissertation.

Figure 5.27a represents the observed and modelled heat flux at the centre of the wall for the selected winter data period. The graph shows that a good approximation of the measured flux is obtained by the assumed reference model, although the periodogram in figure 5.27b demonstrates that no fully uncorrelated residuals are obtained in simulation setting.

In a next step, the reference model is fitted to measurement data of the wall that is affected by rotational air looping. Figure 5.28 represents the observed, predicted and simulated heat flux as well as the residuals at all three locations on the wall. Similar as to the simulation research, the one-step ahead predicted heat flux mimics the observed heat flux quite accurately, while the simulated heat flux deviates more

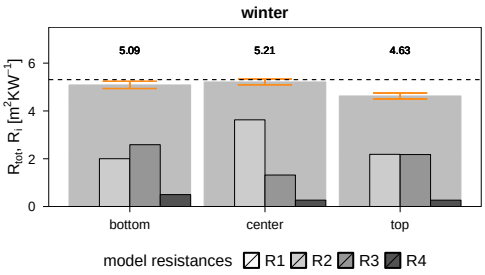

Figure 5.26: The thermal resistances of the third order reference model estimated from the selected winter measurements of the cavity wall with good workmanship. The individual model resistances R_1 till R_4 are represented versus a solid grey block corresponding to the total estimated resistance R_{tot}. The dotted line represents the theoretical R-value of the wall.

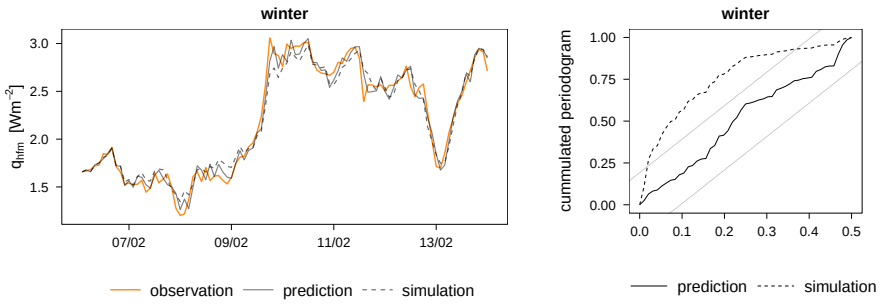

(a) **(b)**

Figure 5.27: (a) Observed, predicted and simulated heat flux for winter measurements. The results are represented for the third order reference model estimated from measurements at the centre of the cavity wall with good workmanship.
(b) The cumulated periodograms of the third order reference model estimated from winter measurements of the cavity wall with good workmanship.

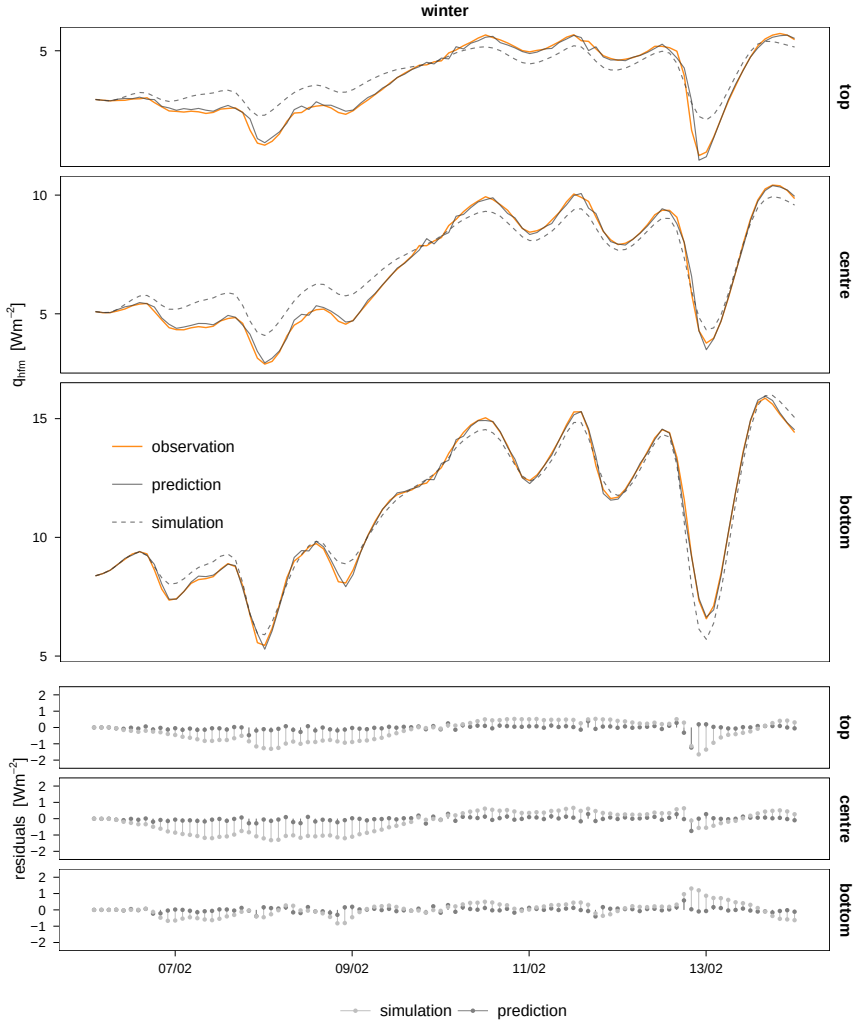

Figure 5.28: Observed, predicted and simulated heat flux in winter and summer (top) together with the corresponding residuals (bottom). The results are represented for the third order reference model, estimated from measurements at the top, centre and bottom of the cavity wall with poor workmanship.

clearly from the heat flux measurements. In winter, the largest deviations are seen for the measurements at the top and centre and not at the bottom, as was the case for the simulated cavity wall. This results from the fact that the developed air flows in the actual cavity wall are in all probability larger than in the simulated wall, since the cavities around the insulation are larger (10 mm instead of 5 mm). When the stationary R-profiles in function of temperature differences are reconsidered (see figure 5.4), it is noticed that the R-profiles corresponding to the wall with the larger air cavities (10 mm) behaves in a rather constant way at the bottom and in a more variable way at the top. For the wall with a smaller air gap (5 mm), it is the other way around. This explains why the impact of natural convection is recognised most distinctly at different locations when comparing the simulated and actual affected cavity wall. Yet, this also means that it is very hard to determine at which location should be measured to capture the influence of natural convection the best.

Figure 5.29 depicts the thermal resistances that are determined by estimating the third order reference model from the measurements of the poorly installed cavity wall. It shows that the lowest *stationary* R-value is established for the bottom position and the highest for the top position. This is as expected since the occurring temperature differences ΔT_{si-se} are mainly positive in the selected winter period. However, it stands out that all the R-estimates take a value that is largely below the theoretical value R_0 which would be obtained by a wall without rotational air flow. These lower estimates are an indication that rather small air flow resistances are established in the wall. From figure 5.4, it was seen that decreasing air flow resistances (10 mm compared to 5 mm of air gap) caused the temperature dependent R-profiles to drop in regions of higher temperature differences. When the air flow resistances in the cavities would be reduced even further, this region would shift to the left. Consequently, for temperature differences between 10°C and 20°C, the local, apparent R-values would always be lower than the theoretical R_0-value, even at the top. Another explanation for the *stationary* R-values being estimated below R_0 could be linked to the fact that exterior air can enter the cavity through (openings in) the brick wall. As a result, the rotational air loop could be decoupled into a loop around the insulation layer and into a loop around the ensemble of insulation and exterior brick veneer. The latter explanation is, however, less plausible because no open head joints were installed in the cavity wall and because the edges were carefully sealed.

Since deviations were observed between the modelled and observed heat flux, in particular in simulation setting, it is verified whether the residuals are correlated to the inputs. Figure 5.30 represents the residuals in function of the occurring surface temperature differences, lagged in time or not. Again, similar results as for the simulation

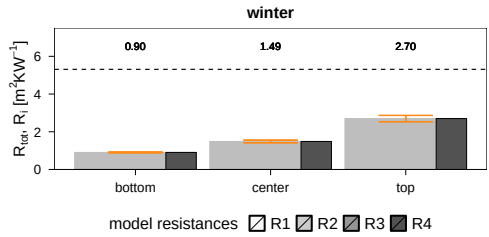

Figure 5.29: The thermal resistances of the third order reference model estimated from the selected winter measurements of the cavity wall with poor workmanship. The individual model resistances R_1 till R_4 are represented versus a solid grey block corresponding to the total estimated resistance R_{tot}. The dotted line represents the reference value of the considered wall.

research are obtained: a linear correlation between the one-step ahead predicted residuals and the temperature differences is found. This correlation is more pronounced when the temperature differences are lagged in time and the correlation is enlarged when represented in simulation mode. Because of the reasons explained above, the correlation is especially present for the residuals resulting from measurements at the top and centre of the wall. Note that no clear deviations were seen between the modelled and observed heat flux in a one-step ahead prediction mode. Nevertheless, a correlation between the prediction error and the surface temperature differences is observable. To be sure that the correlations are induced by the rotational air looping, it is verified whether the residuals resulting from the measurements at the centre of the carefully installed wall show this correlation with surface temperature differences. Figure 5.31 indicates that this is not the case.

Subsequently, non-linear models, which contain model resistances that are written as a function of temperature differences, are fitted to the data measured at the top, bottom and centre of the poorly constructed cavity wall. Since the R-estimates in figure 5.29 indicated that the major part of the apparent thermal resistance is located in the inner model resistance, the temperature dependent function is attributed to this resistance. Hence, identical models as those that were estimated in the simulation research are used. In figure 5.32, the modelling capabilities of the non-linear models, i.e. the exponential and logistic model, are illustrated. Note that the heat fluxes are only represented in simulation mode, since this setting illustrates the differences in model behaviour best. The results of the reference model are also added to enable a comparison between the stationary and non-linear models. In particular at the centre

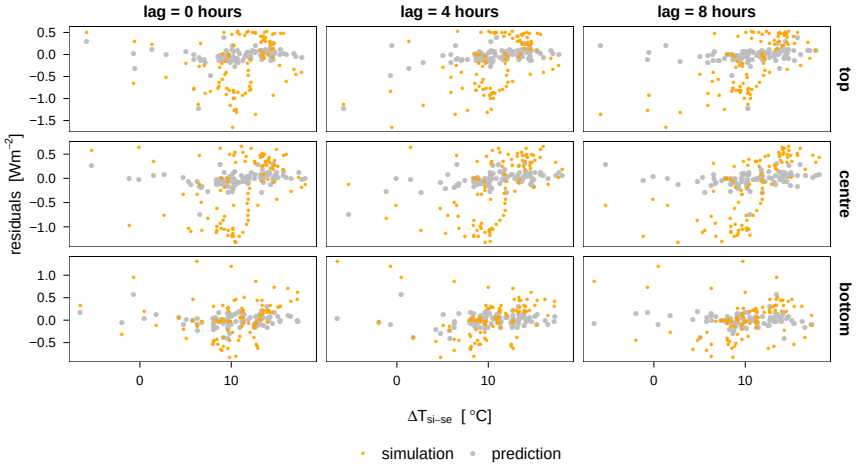

Figure 5.30: Residuals of the third order reference model, fitted on the measurements of the cavity wall with poor workmanship, in function of the temperature difference over the wall, lagged in time or not. The residuals are grey when prediction errors are considered and orange when output errors are regarded. The results in the different columns correspond to temperature differences with a different time lag, while the results in the different rows correspond to top, centre and bottom analyses.

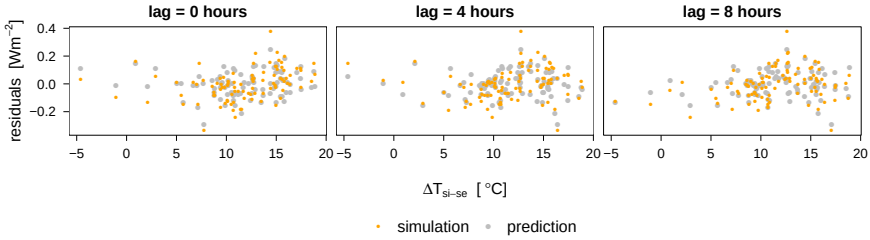

Figure 5.31: Residuals of the third order reference model, fitted on the measurements at the centre of the cavity wall with poor workmanship, in function of the temperature difference over the wall, lagged in time or not. The residuals are grey when prediction errors are considered and orange when output errors are regarded. The results in the different columns correspond to temperature differences with a different time lag.

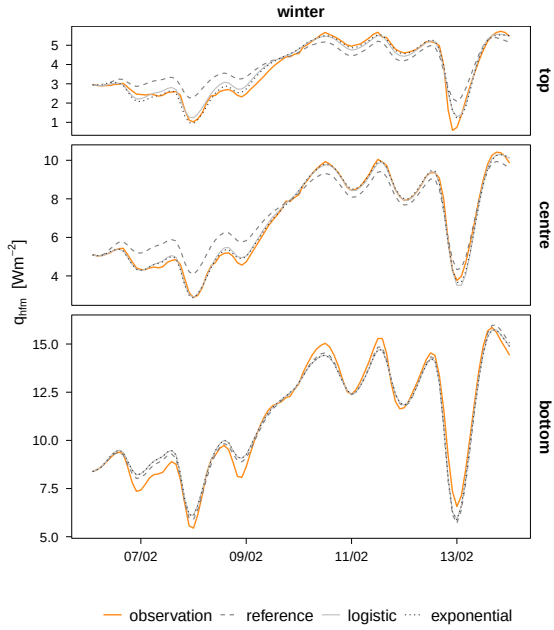

Figure 5.32: Observed and simulated heat flux for the third order reference model and for the logistic and exponential models, estimated from measurements at the top, centre and bottom of the cavity wall with poor workmanship.

of the wall, the use of the non-linear models entails an improved forecasting of the wall's heat flux. But also at the top, improvements are seen. Nevertheless for the top measurements, although the non-linear models mimic the observed heat flux better than the stationary model, discrepancies are still found. This might not surprise, since the modelled temperature dependent R-value is forced to take a certain shape, which is essentially only an approximation of the actual temperature dependent R-value. At the bottom of the wall, no improvement is seen: models with a variable or constant total thermal resistance behave very similarly. This could be expected, since limited correlations were seen at the bottom between the residuals and surface temperature differences. The AICc-criterion also indicates that the use of a reference model is preferred (see figure 5.33). For the other data sets, the exponential model is indicated as most suited.

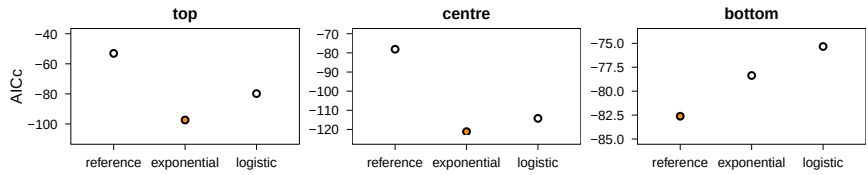

Figure 5.33: Comparison of different models estimated on the winter measurements at the top, centre and bottom of the cavity wall with poor workmanship. The model with the lowest AICc-value (orange) is the preferred model.

The estimated temperature dependent R-values are represented, together with the estimated stationary R-values, in figure 5.34. The histogram at the bottom shows that the bulk of temperature differences in the winter measurements occurs around 8°C to 20°C. In this region the R-value varies between ± 2.5 m^2KW^{-1} and 3.8 m^2KW^{-1} at the top of the and between 1.2 m^2KW^{-1} and 2 m^2KW^{-1} at the centre. At the bottom, the variability of the non-linear models' R-value is negligible. Although no *actual* temperature dependent R-profiles are available to validate the obtained variable estimates, they show a realistic course compared to the theoretical profiles that were drafted in figure 5.9. In theory, all estimated R-profiles should intersect around a zero temperature difference, indicating the wall's actual thermal resistance R_0 when no rotational air flow would be present. Figure 5.34 clearly indicates that this is not the case. The chance that R_0 is identifiable from on-site measurements is actually rather small. First, only if the measurement data would contain enough data points around zero, this part of the curve could be estimated. If this is not the case, only an extrapolation of the fitted R-curve can be used to approximate R_0. The chance that this extrapolated function accurately approximates the actual R-profile around zero is rather low, since the profiles change drastically in this region. Furthermore, even if the data set contains a bulk of temperature differences around zero, it was previously demonstrated that it is hard to obtain reliable results for these temperature differences. This has to do with the fact that the temperature difference Δ_{si-se} under dynamic boundary conditions does not correspond to a stationary situation.

5.4 Conclusion

The current chapter handled two main issues. A first one questioned whether it is possible to identify the presence of rotational air looping from local measurements of a

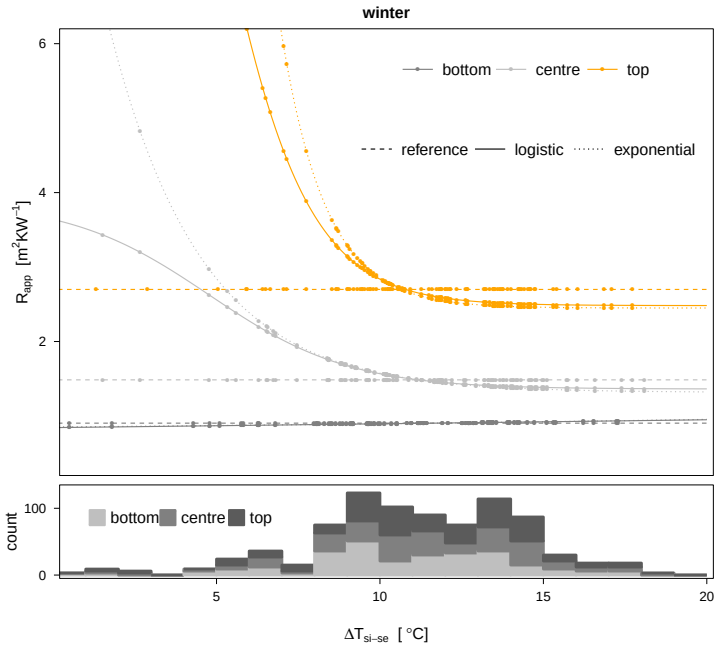

Figure 5.34: Temperature dependent, apparent R-values estimated from the top, centre and bottom measurements of the simulated wall with poor workmanship. Estimates resulting from the logistic and exponential models are shown together with the constant R-values that were estimated by the reference model.

cavity wall by using stochastic grey-box modelling. This was studied by applying the reference stochastic grey-box models, as defined in chapter 3, to a rigorously insulated wall and to a wall having buoyancy driven air flows around its cavity insulation. The application of these models learnt that the presence of rotational air looping can not be identified with complete certainty from every set of local measurements. This mainly results from the fact that rotational air looping can have a rather constant influence on the thermal behaviour of the wall at some locations and for some boundary conditions. Or, in other words, at some locations and for some boundary conditions – read, for some range of occurring temperature differences in the measurements – the local apparent thermal resistance has a shifted, but mainly constant temperature dependent profile. Hence, grey-box models with a constant R-value are able to explain the measured heat fluxes without warning for particularities. The estimated R-values will, however, depend on their location on the wall and will often deviate from the

wall's R_0-value. The locations on the wall for which natural convection has a rather constant influence are different for every other case. Hence, in order to assure the absence or presence of rotational air looping, it is advised to analyse multiple sets of local data sets, measured at different vertical positions on the wall.

When measurements are considered that do experience a time varying impact of rotational air looping, it was observed that indications for the occurrence of this phenomena could be found. First of all, the long-term performance of the estimated reference models was found to be unsatisfactory and resulted in auto-correlated model residuals in simulation setting. Note that this indicates the disability of the model to accurately simulate the measured heat flux. However, it does not link this inability to the presence of natural convection in the wall. Therefore, a more pinpointing indication was found to be the analysis of cross correlations between the model residuals and the driving forces for the natural convection. The latter was found to be best approximated by the measured surface temperature differences across the wall lagged in time. For several studied cases, the cross correlations between the model residuals and lagged surface temperature differences correctly indicated the presence of rotational air looping. Furthermore, when analysing these cross correlations for a wall without natural convection, no clear correlations could be appointed.

The second issue that was handled in this chapter studied whether it is possible to formulate stochastic grey-box models which characterise local apparent thermal resistance indicators for a cavity wall that is affected by natural convection. For several sets of measurements, it was found that models including temperature dependent R-values could be estimated from the data. Even more, they were preferred above the reference models. The data sets for which these variable thermal resistance indicators could be estimated corresponded to the locations on the wall where the influence of the rotational air looping was variable. The estimated variable R_{app}-values seemed to behave in a realistic way compared to the theoretically calculated R-profiles. Only for temperature differences around zero, the R-profiles showed to be less reliable. For the other locations on the wall, the variable resistance indicators were estimated as a flat profile over the temperature differences that were present in the measurements. The variable part of the curve was shifted towards a range of temperatures that was not present in the measurements. Consequently, the practical identifiability of these models is sensitive and they should be estimated carefully. However, for those data sets, the AICriterion indicated the reference models as optimal.

In sum, although the presence of rotational air looping could not be identified for every set of local measurements, the further conclusions of this chapter were rather optimistic: indications for rotational air looping could be found and variable thermal resistance indicators could be estimated. Nevertheless, a critical eye must be cast

on the obtained results. It must be noted that the data analyses are applied to measurements that result from highly controlled simulations or experiments: in the simulation research, the simulations are conducted in such a way that the rotational air looping in the cavity is the only phenomenon interacting with the regular heat transfer mechanisms in the wall. Hence, natural convection has an isolated impact on the considered measurement data. The experimental data, on the other hand, are more realistic, although they are still obtained in a very controlled way: the residual air cavities are carefully designed to induce proper rotational air loops around the insulation, the location of the measurements is rigorously selected to observe the influence of the natural convection in its optimal way, no open head joints are built to avoid ventilation in the exterior air cavity, etc. Hence, the considered experimental data are still rather *easy* to analyse compared to real-world measurements. Actual measurement data will experience a combination of several phenomena that influence the regular heat transfer mechanism in the wall. Hence, the ability of recognising what is going on will be impeded. Furthermore, the behaviour of the apparent thermal resistances will be influenced by more than rotational air looping alone. It can hence be questioned whether an exponential or logistic curve will still be able to explain what is going on. Thus, it is recognised that the study in this chapter took only a first step towards quantifying a variable thermal resistance indicator that characterises non-linear heat transfer in building components. In order to develop a more general framework to identify and quantify the impact of workmanship issues, further research is required.

Chapter 6

Conclusions

The present work recognised the importance of understanding the actual, on-site thermal performance of building components. Therefore, it has studied essential tools for characterising the thermal performance from typical on-site measurements, which consist of surface temperature and interior heat flux measurements. More specifically, the main aim of this dissertation was *to investigate the reliability of characterisation methods determining the thermal resistance of building components based on on-site measurements.* In essence, the characterisation methods studied in this work are not new: both semi-stationary methods as well as inverse modelling techniques are *established* approaches. Yet, the conducted research provided new insights concerning the application and interpretation of these methods and contributed as such to the current discourse on in-situ thermal characterisation. The main contributions of this work are twofold: first, the originality of this works lies in the in-depth study of stochastic grey-box modelling for thermal resistance estimation purposes (chapter 3 and 5) and secondly, added value is provided by the assembly of the different characterisation methods' performances and the resulting comprehensive and systematic comparison (chapter 2 and 4). The current chapter recapitulates the main conclusions of this work and casts a critical view on the topic of stochastic grey-box modelling used for characterising building components on-site. Furthermore, suggestions for a logic continuation of the initiated research are formulated.

Summary of the main conclusions

Potentials and limitations of established characterisation methods. Since the nineteen eighties, interest has been shown in characterising the as-built thermal performance of building components. As a result, several methodologies for on-site

thermal resistance estimation have been proposed in the literature. In chapter 2, we introduced the most important methods among these and systematically demonstrated their application. Thereby, a distinction was made between semi-stationary and dynamic methods. Among the semi-stationary methods, the average method – with and without correction for storage effects – and a simple linear regression technique were studied. The considered dynamic techniques consisted of Anderlind- and ARX-modelling.

Generally, the semi-stationary methods were found to be more restricted in their application than the dynamic methods because of their assumption of steady state principles while analysing inherently dynamic data. On the other hand, the semi-stationary methods shined through their simplicity: except for the average method corrected for storage effects, the methods were found to be very straight-forward to apply and to interpret. Dynamic analysis methods, by contrast, were found to be more complicated. Actually not because of their mathematical implementation – they rely on multiple linear regression techniques – but because of their model formulation: it was noticed that both Anderlind's model and the ARX-model relied on decisions to be made by the user. This introduced an additional step in the estimation procedure, taking time and being susceptible to mistakes. Next to that, ARX-modelling was found to require a theoretical understanding of time series analysis and the involved statistics in order to deduce a thermal resistance from the analysed measurements. This increased complexity, however, came along with an enlarged ability to describe the accuracy of the estimated thermal resistance. Whereas the average methods were found to hold no information about the reliability of their estimated R-values, and the simple linear regression technique and Anderlind's model to hold only limited information, ARX-models were noticed to be more informative. Being a prediction error method, ARX-modelling enabled the use of a set of statistical validation criteria that do not hold for deterministic techniques or output error methods.

What about stochastic grey-box modelling? Stochastic grey-box modelling is an even more advanced dynamic characterisation method. Although the technique is an analysis method with an impressive track record in identifying systems and their parameters in various disciplines, it is rather new in the context of thermally characterising building components. Therefore, the method has been re-contextualised in chapter 3: the possibilities of the method, as defined in [43, 44], have been studied for the new, specific context of in-situ thermal resistance estimation from surface temperature and heat flux measurements.

Generally, the method was found successful for this purpose: the total thermal resistance of all considered case studies were accurately estimated, or, inaccurately estimated thermal resistances could be pinpointed based on the models' statistical

validation criteria. Nevertheless, a comprehensive analysis uncovered that the physical interpretability of the considered stochastic grey-box models is not straightforward. It revealed the importance of identifiability issues when physically interpreting model parameters. This work is one of the first to have considered both structural and data-based identifiability aspects in the context of in-situ resistance estimation by grey-box modelling. Although the followed approach for the identifiability analysis is not original, its results in the considered context are: they contributed largely to unravelling the method's obtained estimation results and settled a new perspective on the interpretation of the estimation results' statistical properties. It was observed that the identification problem as posed suffers from data-based identifiability issues. Apparently, typical on-site measurements of building components lack the dynamical information required to estimate the assumed models' thermal parameters individually. Consequently, different sets of parameter values optimise the same identification problem, which obviously jeopardises the physical interpretation of the estimated parameters. For the considered case studies, however, it was observed that the presence of non-identifiable parameters in the models did not affect the value of their total thermal resistance estimate. By contrast, it did affect, in most cases, the estimate of the effective thermal capacity. Hence, it was learnt that for the identification problems at hand, non-identifiable parameters should be regarded as nuisance parameters that have no individual specific physical meaning, but that are, when combined, necessary tools for accurately estimating the total thermal resistance of the building components.

Non-identifiable parameters were found to be indicated by their profile likelihood confidence intervals: infinite, or half-infinite confidence bounds indicated non-identifiability. However, profile likelihood confidence intervals are computationally time-intensive to determine. That is why we looked for indications of unidentifiable parameters in the statistical validation criteria of the models. It was ascertained that the non-identifiability of most parameters was of such nature that it could also be indicated by the parameters' asymptotic standard deviations, which essentially approximate the profile likelihood confidence intervals. The above conclusions were derived for several wall types and experimental boundary conditions. Hence, based on these findings, a general framework could be developed for the validation of the reference models used for estimating building components from common on-site measurements.

Comparison of different thermal characterisation methods. The existence of various on-site thermal characterisation methods, handling the R-estimation problem in different ways, encourages to ask which method performs best. To answer this question, a comparison of the studied on-site characterisation methods has been performed in chapter 4. The added value of this comparative assessment lies in its comprehensive and systematic approach. As was mentioned in the literature review,

a comparison between different methods has, up till now, mainly been established by isolated studies, focussing on demonstrating the specific advantages of one studied method with regard to one or more other methods. In this work, the scope of the comparison was broadened: the focus of the comparative assessment shifted towards a systematic search for the method that is most generally applicable throughout the year and that obtains the most accurate results in the shortest time spans, and this for various scenarios and boundary conditions. The considered data sets covered simulated and experimental on-site measurement data of a massive and lightweight wall in moderate European climates.

In general, dynamic data analysis methods were observed to have an improved performance compared to semi-stationary methods. Nevertheless, for winter measurements, the differences were found to be rather limited. Hence, in those situations, the simplicity of the semi-stationary methods' application might favour their use and counterbalance the slightly more accurate R-estimates obtained by dynamic analysis methods. Users only need to be aware of the fact that the average method can lead to biased results when the amount of heat storage in the studied component has changed significantly during the measurement period. A correction for storage effects can remedy this, although an application of this rectification requires good assumptions about the studied construction and its layers' thermal properties. Furthermore, for summer measurements, semi-stationary methods were found to result in unreasonable R-estimates for most studied cases. By contrast, dynamic methods were able to result in correct R-estimates both for winter as well as for summer conditions. However, the experimental research proved that it was harder to obtain reliable results for *actual* measurement data than it was for the *simulated* measurement data. The experimental indoor boundary conditions, changing between a constant and free-floating indoor temperature, seemed to complicate the analysis.

In sum, it was concluded that, if possible, winter measurements should always be preferred above summer measurements, since they incurred the highest accuracies in the shortest measurement times. Next to that, concerning an appropriate method selection, it was concluded that the user must always balance the required accuracy with the amount of effort he wants to spend. Generally, Anderlind- and ARX-modelling seemed to balance these two aspects quite well in most situations. When indications of non-linear heat transfer are present, or when a more advanced model validation is required, stochastic grey-box modelling might be the better solution.

The challenge of characterising a variable thermal resistance. In the final chapter, it has been examined whether the advanced possibilities of stochastic state space modelling could be deployed to identify and characterise phenomena that interact with the intended heat transfer mechanisms in building components. This

was investigated for the specific scenario of an insulated cavity wall that suffered from rotational air looping around its hard insulation boards.

The analyses in chapter 5 showed that buoyancy driven air flows could be identified from the validation criteria of reference models fitted to those local measurements that were affected by the air looping in a variable way. Furthermore, from those sets of measurements, a logistic or exponential R-profile could be estimated. The accuracy of these temperature dependent R-profiles was found to rely on the range of temperature differences that occurred in the measurements. On the other hand, for many data sets of local measurements, no indications were found for the buoyancy driven air flows in the component's cavity. This resulted from the fact that, for those measurements, the rotational air looping influenced the local, apparent thermal resistance in a constant way. Hence, grey-box models with a constant thermal resistance were able to accurately mimic the observed measurements and to fulfil all validation criteria.

Generally, it was concluded that, although stochastic grey-box models hold the ability to identify and characterise disturbing phenomena such as rotational air looping or wind washing, their proper functioning might be hindered by many practicalities when real-world measurement data are considered. Actual measurement data will experience a combination of several phenomena that influence the regular heat transfer mechanism in the wall. Hence, the ability of recognising what is going on might be impeded.

A critical view on stochastic state space modelling

If one thing is demonstrated by the present work, it is that a building component's on-site thermal resistance is harder to determine than would be expected. What was thought to be a simple characterisation exercise from field measurements, turned out to be requiring more care and understanding than was readily apparent. The research in this work has mainly been driven by the search for characterisation methods that overcome the restrictions of the commonly used average method. Or, in other words, we have been looking for characterisation methods that are generally applicable, independently from the occurring dynamic boundary conditions. Thereby, the main focus was on stochastic grey-box modelling.

The expectations of stochastic grey-box modelling were high, since it is an extremely powerful method with many possibilities for model validation and pinpointing deficiencies. However, in retrospect, the specific use of this powerful method for characterising a wall from simple measurements, might seem like taking a sledgehammer to crack a nut. Although the method has proved its usefulness, several aspects indicate that its advanced statistical properties can not be benefited from, making it hard to justify its time-intensive use.

A first discussion point is the *physical* formulation used by grey-box models to describe the wall's observed heat flux. Although, an RC-representation is able to model the internal structure of building components, the idea of modelling the latter is redundant if this structure can not be identified from the available data. In practice, we can only collect a limited amount of data and, as was proven in chapter 3, typical on-site measurement data is generally not sufficiently informative to estimate the internal model resistances and capacitances individually. Even more, it was seen that the estimated model parameters of models that were identifiable could not be pinpointed to the separate layers of the wall: a more complicated relation between the physical properties and the model parameters is playing as a consequence of the simplification that is made by modelling a distributed system by a lumped system. Hence, if only the total thermal resistance of grey-box models can be reliably estimated, then there is no need to model the internal structure of the wall. Models such as Anderlind's model or ARX-models can just as well do the job.

A next discussion point deals with stochastic grey-box models' property of decomposed noise. According to the definition, stochastic state space models are characterised by both process noise and measurement noise. The Kalman filter then balances these estimated uncertainties to come up with an *optimal* estimate of the future state variables. In essence, process noise is intended to accommodate for random, but continuous disturbances that are induced by the system. As such, by specifically accounting for these random system disturbances, it is prevented that the latter are absorbed in the system's parameters or output. Although this is a very useful feature, it is, for the considered systems, hard to image a phenomenon that would continuously, but randomly disturb the temperature distribution in walls (and that could not be accounted for in the measurement noise). Hence, the practicability of this feature might be rather limited. Next to that, the frequent presence of non-identifiability issues does largely influence the functioning of the Kalman filter: due to the presence of unidentifiable parameters, the uncertainty of certain states in the model will be very large. Hence, the Kalman filter is forced to put its weight largely on the measurement data rather than on the model itself and the modelled states are *corrected* at each prediction step according mainly to the measurements. As such, the longer-term behaviour of the model is neglected.

Generally, stochastic grey-box modelling was found to be a satisfactory method for characterising building components from on-site measurements. However, taken all the previous comments into account, it must indeed be recognised that the method might be an overkill for estimating the thermal resistance from the elementary heat flux and temperature measurements considered in this dissertation. Especially when less time-intensive approaches such as Anderlind- and ARX-modelling have proved

to result in R-estimates of similar quality. The use of stochastic grey-box modelling might be more relevant for identifying the dynamic behaviour of building components than it is for characterising their stationary properties. One can imagine applications such as charactering the performance of double-skin façades or building integrated photovoltaics where the strengths and possibilities of the method will be accorded their full weight.

Recommendations for future research

The present work tried to give an extensive overview of the potentials and limitations of different methods characterising the on-site thermal resistance of building components. Inevitably some aspects have been ignored or could have been studied more thoroughly. Consequently, a number of fields for future research are identified.

On ARX-modelling. This dissertation treated ARX-modelling as an established method. However, in the specific context of thermally characterising on-site building components, only a few in-depth studies on this methods have been conducted [18, 21]. There is still need for future research. Especially, the issue of an automatic model order selection could be further investigated, including the possibility of adopting separate orders for the individual model polynomials. Furthermore, the potentials of extending the approach towards ARMAX- or seasonal models could be examined.

On optimising stochastic grey-box models' identifiability. Chapter 3 demonstrated that typical on-site measurements are often not informative enough to imply practically identifiable grey-box models. Also the previous section indicated that many of the method's shortcomings resulted from a lack of dynamic information in the elementary on-site measurements. Nevertheless, the question can be posed whether other perturbation signals would optimise these models' practically identifiability. Although the outdoor boundary conditions can not be altered, one could easily imagine a fully controlled indoor environment. Hence, the impact of specific indoor temperature or heat input signals, such as PRBS- or ROLBS-signals, on a grey-box model's identifiability could be studied. Furthermore, it could be examined whether specific interior perturbation signals can be designed that enable the characterisation of the internal structure of the affected building component.

On deterministic or multiple-step ahead grey-box modelling. Thus far, stochastic state space models have been considered that are estimated by a one-step ahead prediction estimation procedure. The latter has, on the one hand, the advantage of being embedded in a statistical framework. On the other hand, it has the property of estimating a model according to its one-step ahead predictive performance rather than to its long-term descriptive performance. The latter might be a disadvantage

when retrieving the in essence stationary thermal resistance from such models. An alternative can be found in deterministic grey-box models. Such models can be identified from measurement data by means of least squares estimation. As such, they leave the statistical framework behind, but they have the advantage of being estimated based on their overall descriptive performance. Another alternative can be found in stochastic state space models that are estimated in a multiple-step ahead environment. Instead of estimating an optimal model based on its one-step ahead predictive capabilities, such estimation procedure focusses on their performance over a horizon of multiple steps. As such, these methods are benefiting from two worlds. Neither deterministic, nor multiple-step ahead grey-box models have been investigated in this dissertation. Hence, their potentials and limitations are a topic for study and their performances could be compared to the performances of the other characterisation methods.

On automatising on-site characterisation of building components. Performing on-site measurements only requires a limited amount of sensors, notably two temperature sensors and one heat flux sensor, all connected to a data logger. Currently, *R-value measurement kits* including these sensors have been brought to the market for the purpose of characterising as-built thermal resistances from building components (see figure 6.1). The kit is accompanied by software for an on-board calculation of thermal resistances. However, this software only includes the average method. Hence, one could easily imagine to extend the software's analysing possibilities by including several other characterisation methods. Therefore these methods must be fully automated and user interferences must be omitted as much as possible. Hence, future research is needed in order to translate some of the more advanced dynamic methods into a robust and fully automated characterisation software.

Figure 6.1: Measurement kit for performing on-site measurements of building components in order to estimate their thermal resistance. Source: http://u-value.greenteg.com

Appendix A

Specifications of dwelling model

This appendix defines the dwelling that is used to generate the thermostatically controlled indoor temperature which is imposed, among others, as indoor boundary condition for the simulation of building components in this dissertation.

For the simulations of the different wall types in this dissertation, one of the indoor environment scenarios considers a realistic indoor temperature regime, notably, a varying indoor temperature as common in dwellings with a thermostatically controlled heating system. Since HAMFEM, used to simulate the thermal behaviour of the wall, does not include a dwelling model, TRNSYS is used to generate the data.

For the TRNSYS simulations, an existing two-zone model, developed in [56], is used. The model is based on a real dwelling, which was previously depicted in figure 2.3 of chapter 2. It concerns a well insulated, detached house with a total volume of 431 m^3. The ground floor, with a volume of 243 m^3, is considered as day-zone, while the first floor is regarded as night-zone. The dwelling has a total heat loss area of 349 m^2.

The dwelling is simulated twice: (1) a first time with the assumption of the cavity walls as introduced in section 2.1 as outer walls and (2) a second time with the assumption of the lightweight timber frame walls, as introduced in section 3.3.2. For the roof and floor, R-values of 5.166 m^2KW^{-1} and 7.303m^2KW^{-1}, respectively, are assumed according to their composition represented in tables A.1 and A.2. The floor is simulated as a slab on ground. Furthermore, wooden windows and high insulating glazing with a U-value of 1.06 $Wm^{-2}K^{-1}$ are assumed.

Table A.1: Thermal properties of the pitched roof.

	d $[m]$	**λ** $[W(mK)^{-1}]$	**R** $[m^2KW^{-1}]$
tiles	/	/	/
wind shiedling	0.015	0.230	0.065
insulation layer between beams	0.200	0.041	4.878
service cavity	/	/	0.18
gypsum board	0.015	0.350	0.043
TOTAL			**5.166**

Table A.2: Thermal properties of the floor.

	d $[m]$	**λ** $[W(mK)^{-1}]$	**R** $[m^2KW^{-1}]$
tiles	0.020	0.810	0.025
screed	0.080	1.700	0.047
insulation layer	0.200	0.028	7.143
concrete	0.150	1.700	0.088
TOTAL			**7.303**

The outdoor boundary conditions of the TRNSYS simulations are those used for the wall-simulations with HAMFEM and were represented in figure 2.1 of section 2.1.

For the indoor boundary conditions, a heating and ventilation system are implemented. The heating system is assumed to be ideal and has a maximal heating power of 5 kW in the day zone and of 2 kW in the night zone. The indoor air temperature is thermostatically controled and the assumed heating profiles for week and weekend days are represented in figures A.1. Note that no cooling is implemented so that the summer periods can be characterised by a free-floating indoor air temperature and hence overheating may occur.

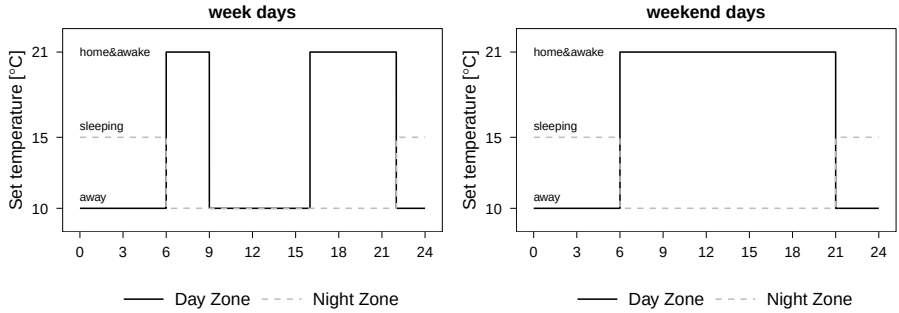

Figure A.1: The implemented heating profile during week and weekend days.

Considering the ventilation, a balanced system with mechanical air exhaust and mechanical air supply is assumed, corresponding to a system D in the Belgian standard. For a dwelling with a total volume of V_{tot}, the ventilation rate is calculated as

$$n_{vent} = (0.20 + 0.50e^{-V_{tot}/500}) * m \tag{A.1}$$

with

m = 1 during winter

m = 1.5 during summer (including open windows and doors)

From October till March, the intake air is preheated by a heat exchanger with an efficiency of 0.70. An infiltration rate n_{inf} of $0.04 * n_{50} = 0.04 * 1h^{-1}$ is assumed.

Internal gains in the dwelling are implemented as described in section 3.3.8 of [56].

Appendix B

Calculation of thermal mass factors

This appendix calculates the thermal mass factors of the massive cavity wall introduced in chapter 2, of the lightweight timberframe wall introduced in chapter 3 and of the massive cavity wall built in the VLIET test building introduced in chapter 4. The thermal mass factors are essential for the R-estimation of these walls by means of the average method corrected for storage effects. The latter is implemented in chapters 2 and 4 for the massive wall and in chapter 4 for the lightweight wall and the VLIET cavity wall. Thereby the thermal mass factors as calculated in this appendix are used.

As mentionned in section 2.2.2, for a building component with total resistance R and consisting of M layers, numbered from m=1 to m=M with layer 1 at the interior side of the component, the thermal mass factors F_i and F_e are calculated as

$$F_i = \sum_{m=1}^{M} F_{im} = \sum_{m=1}^{M} C_m \left[\frac{R_{em}}{R} + \frac{R_m^2}{3R^2} - \frac{R_{im} R_{em}}{R^2} \right] \tag{B.1}$$

$$F_e = \sum_{m=1}^{M} F_{em} = \sum_{m=1}^{M} C_m \left[\frac{R_m}{R} \left\{ \frac{1}{6} + \frac{R_{im} + R_{em}}{3R} \right\} + \frac{R_{im} R_{em}}{R^2} \right] \tag{B.2}$$

with (B.3)

$$R_{im} = \sum_{j=1}^{m-1} R_j \tag{B.4}$$

$$R_{em} = \sum_{j=m+1}^{M} R_j \tag{B.5}$$

(B.6)

Hereby R_m $[m^2 K W^{-1}]$ and C_m $[J m^{-2} K^{-1}]$ are the thermal resistances and capacitances, respectively, of each separate layer m.

Thermal mass factors of massive wall

The cavity wall as introduced in chapter 2 consists of four layers and the calculation of its thermal mass factors is summarised in table B.1.

Table B.1: Calculation of the thermal mass factors of the massive wall.

	m	**Rm**	**Cm**	**Rim**	**Rem**	**Fim**	**Fem**
interior							
plaster	1	0.079	1.19E+04	0	4.921	11663.880	92.568
building brick	2	0.233	1.35E+05	0.079	4.688	124889.604	5059.427
insulation layer	3	4.582	4.62E+03	0.312	0.106	1384.456	829.465
facing brick	4	0.106	1.32E+05	4.894	0	19.709	1376.312
exterior							
		R =				**Fi =**	**Fe =**
		5.000				**137957.65**	**7357.773**

Thermal mass factors of lightweight wall

The timber frame wall as introduced in chapter 3 consists of six layers (since the vapour barier is neglected) and the calculation of its thermal mass factors is summarised in table B.2.

Table B.2: Calculation of the thermal mass factors of the lightweight wall.

	m	Rm	Cm	Rim	Rem	Fim	Fem
interior							
gypsum board	1	0.048	1.13E+04	0.000	4.952	11231.484	54.084
service cavity	2	0.180	5.00E+01	0.048	4.772	47.283	1.337
vapour barrier		/	/	/	/	/	/
OSB	3	0.138	2.20E+04	0.228	4.634	19459.981	1228.441
insulation layer	4	3.713	7.64E+03	0.366	0.921	2708.344	1535.730
insulating sheating	5	0.909	6.05E+03	4.079	0.011	69.190	494.453
plaster	6	0.011	1.04E+04	4.989	0.000	0.018	11.868
exterior							
		R =				**Fi =**	**Fe =**
		5.000				**33516.300**	**3325.912**

Thermal mass factors of massive wall built in the VLIET test building

The cavity wall as introduced in chapter 4 consists of four layers and the calculation of its thermal mass factors is summarised in table B.3.

Table B.3: Calculation of the thermal mass factors of the massive wall built in the VLIET test building.

	m	Rm	Cm	Rim	Rem	Fim	Fem
interior							
building brick	1	0.280	2.16E+05	0	4.270	203154.3	6388.505
insulation layer	2	4.000	4.76E+03	0.280	0.270	11492.156	883.927
air cavity	3	0.159	1.29E+01	4.280	0.111	0.02391	0.516
facing brick	4	0.111	1.71E+05	4.439	0	33.980	2053.170
exterior							
		R =				**Fi =**	**Fe =**
		5.000				**204977.40**	**9326.12**

Appendix C

Structural identifiability of stochastic grey-box models

This appendix demonstrates the structural identifiability of the second and third order model of the main stochastic state space model structure that is assumed in this dissertation to describe the heat transfer in building components.

Second order model

The second order model can be represented by the RC-network in figure C.1.

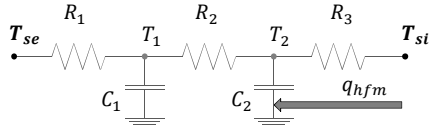

Figure C.1: Graphic representation of a second order stochastic grey-box model used to describe the heat transfer in building components.

The input, output and state space matrices of this model, i.e. $\boldsymbol{u}$, $\boldsymbol{y}$ and $\boldsymbol{x}$ respectively, can be formulated as

$$\boldsymbol{x} = \begin{bmatrix} T_1 & T_2 \end{bmatrix}^T \quad \text{(C.1)} \qquad \boldsymbol{y} = \begin{bmatrix} Q_{hfm} \end{bmatrix} \quad \text{(C.2)} \qquad \boldsymbol{u} = \begin{bmatrix} T_{se} & T_{si} \end{bmatrix}^T \quad \text{(C.3)}$$

$$\boldsymbol{A} = \begin{bmatrix} \frac{-1}{C_1R_1} - \frac{1}{C_1R_2} & \frac{1}{C_1R_2} \\ \frac{1}{C_2R_2} & \frac{-1}{C_2R_2} - \frac{1}{C_2R_3} \end{bmatrix} \quad \text{(C.4)} \qquad \boldsymbol{B} = \begin{bmatrix} \frac{1}{C_1R_1} & 0 \\ 0 & \frac{1}{C_2R_3} \end{bmatrix} \quad \text{(C.5)}$$

$$\boldsymbol{C} = \begin{bmatrix} 0 & \frac{-1}{R_3} \end{bmatrix} \quad \text{(C.6)} \qquad \boldsymbol{D} = \begin{bmatrix} 0 & \frac{1}{R_3} \end{bmatrix} \quad \text{(C.7)}$$

Based on the equality $\boldsymbol{H}_{input}(s) = \Big(\boldsymbol{C}(\boldsymbol{\theta})(s\boldsymbol{I} - \boldsymbol{A}(\boldsymbol{\theta}))^{-1}\boldsymbol{B}(\boldsymbol{\theta}) + \boldsymbol{D}(\boldsymbol{\theta})\Big)$, the transfer function of this model in its zero-pole-gain form is calculated as

$$H_{input,11}(s) = \quad \text{(C.8)}$$
$$\frac{1}{R_3} \frac{s^2 + \frac{C_1R_1+C_2R_1+C_2R_2}{C_1C_2R_1R_2}s + \frac{1}{C_1C_2R_1R_2}}{s^2 + \frac{C_1R_1R_2+C_1R_1R_3+C_2R_1R_3+C_2R_2R_3}{C_1C_2R_1R_2R_3}s + \frac{R_1+R_2+R_3}{C_1C_2R_1R_2R_3}}$$
$$H_{input,12}(s) = \quad \text{(C.9)}$$
$$\frac{-1}{C_1C_2R_1R_2R_3} \frac{1}{s^2 + \frac{C_1R_1R_2+C_1R_1R_3+C_2R_1R_3+C_2R_2R_3}{C_1C_2R_1R_2R_3}s + \frac{R_1+R_2+R_3}{C_1C_2R_1R_2R_3}}$$

The latter results in the following set of eight equations from which 5 are independent

$$K_{11} = \frac{1}{R_3} \quad \text{(C.10)}$$
$$K_{12} = \frac{-1}{C_1C_2R_1R_2R_3} = -K_{11}a_{11,2} \quad \text{(C.11)}$$
$$a_{11,1} = \frac{C_1R_1 + C_2R_1 + C_2R_2}{C_1C_2R_1R_2} \quad \text{(C.12)}$$
$$a_{11,2} = \frac{1}{C_1C_2R_1R_2} \quad \text{(C.13)}$$
$$b_{11,1} = \frac{C_1R_1R_2 + C_1R_1R_3 + C_2R_1R_3 + C_2R_2R_3}{C_1C_2R_1R_2R_3} \quad \text{(C.14)}$$
$$b_{11,2} = \frac{R_1 + R_2 + R_3}{C_1C_2R_1R_2R_3} \quad \text{(C.15)}$$
$$b_{12,1} = \frac{C_1R_1R_2 + C_1R_1R_3 + C_2R_1R_3 + C_2R_2R_3}{C_1C_2R_1R_2R_3} = b_{11,1} \quad \text{(C.16)}$$
$$b_{12,2} = \frac{R_1 + R_2 + R_3}{C_1C_2R_1R_2R_3} = b_{11,2} \quad \text{(C.17)}$$

Hence, the five model parameters C_1, C_2, R_1, R_2 and R_3 can be uniquely defined from the transfer function and are, therefore, structurally identifiable.

Third order model

The third order model can be represented by the RC-network in figure C.2.

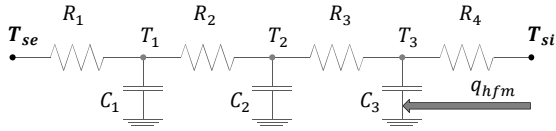

Figure C.2: Graphic representation of a third order stochastic grey-box model used to describe the heat transfer in building components.

The input, output and state space matrices of this model, i.e. $\boldsymbol{u}$, $\boldsymbol{y}$ and $\boldsymbol{x}$ respectively, can be formulated as follows

$$\boldsymbol{x} = \begin{bmatrix} T_1 & T_2 & T_3 \end{bmatrix}^T \quad \text{(C.18)} \qquad \boldsymbol{y} = \begin{bmatrix} Q_{hfm} \end{bmatrix} \quad \text{(C.19)} \qquad \boldsymbol{u} = \begin{bmatrix} T_{se} & T_{si} \end{bmatrix}^T \quad \text{(C.20)}$$

$$\boldsymbol{A} = \begin{bmatrix} \frac{-1}{C_1 R_1} - \frac{1}{C_1 R_2} & \frac{1}{C_1 R_2} & 0 \\ \frac{1}{C_2 R_2} & \frac{-1}{C_2 R_2} - \frac{1}{C_2 R_3} & \frac{1}{C_2 R_3} \\ 0 & \frac{1}{C_3 R_3} & \frac{-1}{C_3 R_3} - \frac{1}{C_3 R_4} \end{bmatrix} \quad \text{(C.21)} \qquad \boldsymbol{B} = \begin{bmatrix} \frac{1}{C_1 R_1} & 0 \\ 0 & 0 \\ 0 & \frac{1}{C_3 R_4} \end{bmatrix} \quad \text{(C.22)}$$

$$\boldsymbol{C} = \begin{bmatrix} 0 & 0 & \frac{-1}{R_4} \end{bmatrix} \quad \text{(C.23)} \qquad \boldsymbol{D} = \begin{bmatrix} 0 & \frac{1}{R_4} \end{bmatrix} \quad \text{(C.24)}$$

Based on the equality $\boldsymbol{H}_{input}(s) = \Big(\boldsymbol{C}(\boldsymbol{\theta})(s\boldsymbol{I} - \boldsymbol{A}(\boldsymbol{\theta}))^{-1}\boldsymbol{B}(\boldsymbol{\theta}) + \boldsymbol{D}(\boldsymbol{\theta})\Big)$, the transfer function of this model in its zero-pole-gain form is calculated as

$$H_{input,11}(s) = K_{11}\frac{s^3 + a_{11,1}s^2 + a_{11,2}s + a_{11,3}}{s^3 + b_{11,1}s^2 + b_{11,2}s + b_{11,3}} \quad \text{(C.25)}$$

$$H_{input,12}(s) = K_{12}\frac{1}{s^3 + b_{12,1}s^2 + b_{12,2}s + b_{12,3}} \quad \text{(C.26)}$$

with

$$K_{11} = \frac{1}{R_4} \tag{C.27}$$

$$a_{11,1} = \frac{\begin{array}{c} C_1C_2R_1R_2 + C_1C_3R_1R_2 + C_1C_3R_1R_2 \\ + C_1C_3R_1R_3 + C_2C_3R_1R_3 + C_2C_3R_2R_3 \end{array}}{C_1C_2C_3R_1R_2R_3} \tag{C.28}$$

$$a_{11,2} = \frac{C_1R_1 + C_2R_1 + C_2R_2 + C_3R_1 + C_3R_2 + C_3R_3}{C_1C_2C_3R_1R_2R_3} \tag{C.29}$$

$$a_{11,3} = \frac{1}{C_1C_2C_3R_1R_2R_3} \tag{C.30}$$

$$b_{11,1} = \frac{\begin{array}{c} C_1C_2R_1R_2R_3 + C_1C_2R_1R_2R_4 + C_1C_3R_1R_3R_4 \\ + C_1C_3R_1R_3R_4 + C_2C_3R_1R_3R_4 + C_2C_3R_2R_3R_4 \end{array}}{C_1C_2C_3R_1R_2R_3R_4} \tag{C.31}$$

$$b_{11,2} = \frac{\begin{array}{c} C_1R_1R_2 + C_1R_1R_3 + C_1R_1R_4 + C_2R_1R_3 + C_2R_1R_4 \\ C_2R_2R_3 + C_2R_3R_4 + C_3R_1R_4 + C_3R_2R_4 + C_3R_3R_4 \end{array}}{C_1C_2C_3R_1R_2R_3R_4} \tag{C.32}$$

$$b_{11,3} = \frac{R_1 + R_2 + R_3 + R_4}{C_1C_2C_3R_1R_2R_3R_4} \tag{C.33}$$

$$K_{12} = \frac{-1}{C_1C_2C_3R_1R_2R_3R_4} = -K_{11}a_{11,3} \tag{C.34}$$

$$b_{12,1} = b_{11,1} \tag{C.35}$$

$$b_{12,2} = b_{11,2} \tag{C.36}$$

$$b_{12,3} = b_{11,3} \tag{C.37}$$

From this set of 11 equations, only 7 equations are independent. Consequently, the 7 parameters of the third order model, i.e. C_1, C_2, C_3, R_1, R_2, R_3, R_4, can be uniquely defined from the transfer function and are thus structurally identifiable.

The previous set of equations demonstrates that even for simple models of a small order the symbolic formulation can already become quite cumbersome. Therefore the transfer function analysis is not applied on the fourth order model of this model structure. Nevertheless, from studying the transfer functions of the first, second and third order models, an analogy in the equations can be seen. It is, therefore, justified to extend the conclusion of structurally identifiable models to the fourth order model and even to higher order models. Hence, this model structure is assumed to be structurally identifiable.

Appendix D

Specification of stochastic grey-box models

In this appendix the model equations and observation equations of the stochastic grey-box models used in chapter 3 are listed. The equations are formulated as continuous-discrete stochastic state space models and are presented in the way that they are implemented in CTSM-R. Thereby, the conventions listed in table D.1 are used. Furthermore, the bounds set for the parameter estimation, as well as the initial value selection are also discussed.

Table D.1: Names and parameter description of the conventios for variables used in the stochastic grey-box model implementation in CTSM-R.

Name	parameter description	Unit
Tsi	internal surface temperature	$^{\circ}C$
Tse	external surface temperature	$^{\circ}C$
qhfm	internal heat flux	Wm^{-2}
Twi	state temperature	$^{\circ}C$
Rwi	model resistance	m^2KW^{-1}
Cwi	model capacitance	$MJm^{-2}K^{-1}$
pii	incremental variance of Wiener process	$^{\circ}C$
eii	measurement error	Wm^{-2}
0	indicates initial values of the relevant parameter	$^{\circ}C$

The implementation of the models in CTSM-R requires a specification of the lower- and upperbounds for every estimable parameter or state in the model. The boundaries that are set for the estimations in this dissertation are listed in the table below (table D.2). Note that the boundaries might seem physically unrealistic. However, due to the non-identifiabilities in the model, the parameters do not necessarily adopt physical values.

Table D.2: Upper- and lowerbounds set for the parameter estimation of the stochastic grey-box models in chapter 3.

Name	Lowerbound	Upperbound	Unit
Twi	-10	60	$^{\circ}C$
Rwi	1E-25	60	m^2KW^{-1}
Cwi	1E-10	1E15	$MJm^{-2}K^{-1}$
pii	-500	50	$^{\circ}C$
eii	-500	50	Wm^{-2}

Furthermore, every estimation in this dissertation is repeated a 150 times for different initial values. This is done in order to avoid the estimation procedure to be trapped in a local minimum. The initial values are randomly selected from a uniform or log-uniform distribution. The latter are listed for every parameter in the table below.

Table D.3: Every estimation is repeated a 150 times with different initial values. The initials values are randomly selected from the uniform or log-uniform distrubtions described in this table.

Parameter	Range	a	b	Unit
Twi0	$\in$ [a,b]	min(Tse.t0,Tsi.t0)	max(Tse.t0,Tsi.t0)	$^{\circ}C$
Rwtot0	$\in$ [a,b]	1	10	m^2KW^{-1}
Cwtot0	$\in 10^{[a,b]}$	-2.3	0.48	$MJm^{-2}K^{-1}$
Rwi0	$\in$ [a,b]*Rwtot0	0	1	$MJm^{-2}K^{-1}$
Cwi0	$\in$ [a,b]*Cwtot0	0	1	$MJm^{-2}K^{-1}$
pii0	$\in$ [a,b]	-15*model order	10	$^{\circ}C$
eii0	$\in$ [a,b]	-15	10	Wm^{-2}

REFERENCE MODEL

M1ref

```
Linear state space model with 1 state, 1 output and 2 inputs
System equations:
        dTw1 ~ (1/(Cw1 * 10^6 * Rw1) * (Tse - Tw1) + 1/(Cw1 * 10^6 *
             Rw2) * (Tsi - Tw1)) * dt + exp(p11) * dw1
Observation equations:
        Qhfm ~ 1/(Rw2) * (Tsi - Tw1)
Inputs:  Tse, Tsi
```

M2ref

```
Linear state space model with 2 states, 1 output and 2 inputs
System equations:
        dTw1 ~ (1/(Cw1 * 10^6 * Rw1) * (Tse - Tw1) + 1/(Cw1 * 10^6 *
                   Rw2) * (Tw2 - Tw1)) * dt + exp(p11) * dw1
        dTw2 ~ (1/(Cw2 * 10^6 * Rw2) * (Tw1 - Tw2) + 1/(Cw2 * 10^6 *
            Rw3) * (Tsi - Tw2)) * dt + exp(p22) * dw2
Observation equations:
        Qhfm ~ 1/(Rw3) * (Tsi - Tw2)
Inputs:  Tse, Tsi
```

M3ref

```
Linear state space model with 3 states, 1 output and 2 inputs
System equations:
        dTw1 ~ (1/(Cw1 * 10^6 * Rw1) * (Tse - Tw1) + 1/(Cw1 * 10^6 *
            Rw2) * (Tw2 - Tw1)) * dt + exp(p11) * dw1
        dTw2 ~ (1/(Cw2 * 10^6 * Rw2) * (Tw1 - Tw2) + 1/(Cw2 * 10^6 *
            Rw3) * (Tw3 - Tw2)) * dt + exp(p22) * dw2
        dTw3 ~ (1/(Cw3 * 10^6 * Rw3) * (Tw2 - Tw3) + 1/(Cw3 * 10^6 *
            Rw4) * (Tsi - Tw3)) * dt + exp(p33) * dw3
Observation equations:
        Qhfm ~ 1/(Rw4) * (Tsi - Tw3)
Inputs:  Tse, Tsi
```

M4ref

```
Linear state space model with 4 states, 1 output and 2 inputs
System equations:
        dTw1 ~ (1/(Cw1 * 10^6 * Rw1) * (Tse - Tw1) + 1/(Cw1 * 10^6 *
            Rw2) * (Tw2 - Tw1)) * dt + exp(p11) * dw1
        dTw2 ~ (1/(Cw2 * 10^6 * Rw2) * (Tw1 - Tw2) + 1/(Cw2 * 10^6 *
            Rw3) * (Tw3 - Tw2)) * dt + exp(p22) * dw2
```

```
        dTw3 ~ (1/(Cw3 * 10^6 * Rw3) * (Tw2 - Tw3) + 1/(Cw3 * 10^6 *
            Rw4) * (Tw4 - Tw3)) * dt + exp(p33) * dw3
        dTw4 ~ (1/(Cw4 * 10^6 * Rw4) * (Tw3 - Tw4) + 1/(Cw4 * 10^6 *
            Rw5) * (Tsi - Tw4)) * dt + exp(p44) * dw4
Observation equations:
        Qhfm ~ 1/(Rw5) * (Tsi - Tw4)
Inputs:  Tse, Tsi
```

CAPACITANCE LAYER MODEL

M1clm

```
Linear state space model with 1 state, 1 output and 2 inputs
System equations:
        dTw1 ~ (1/(Cw1 * 10^6 * 0.5 * Rw1) * (Tse - Tw1) + 1/(Cw1 * 10^6 *
            0.5 * Rw1) * (Tsi - Tw1)) * dt + exp(p11) * dw1
Observation equations:
        Qhfm ~ 1/(0.5 * Rw1) * (Tsi - Tw1)
Inputs:  Tse, Tsi
```

M2clm

```
Linear state space model with 2 states, 1 output and 2 inputs
System equations:
        dTw1 ~ (1/(Cw1 * 10^6 * 0.5 * Rw1) * (Tse - Tw1) + 1/(Cw1 * 10^6 *
                    0.5 * (Rw1 + Rw2)) * (Tw2 - Tw1)) * dt + exp(p11) * dw1
        dTw2 ~ (1/(Cw2 * 10^6 * 0.5 * (Rw1 + Rw2)) * (Tw1 - Tw2) + 1/(Cw2 *
            10^6 * 0.5 * Rw2) * (Tsi - Tw2)) * dt + exp(p22) * dw2
Observation equations:
        Qhfm ~ 1/(0.5 * Rw2) * (Tsi - Tw2)
Inputs:  Tse, Tsi
```

M3clm

```
Linear state space model with 3 states, 1 output and 2 inputs
System equations:
         dTw1 ~ (1/(Cw1 * 10^6 * 0.5 * Rw1) * (Tse - Tw1) + 1/(Cw1 * 10^6 *
             0.5 * (Rw1 + Rw2)) * (Tw2 - Tw1)) * dt + exp(p11) * dw1
         dTw2 ~ (1/(Cw2 * 10^6 * 0.5 * (Rw1 + Rw2)) * (Tw1 - Tw2) + 1/(Cw2 *
             10^6 * 0.5 * (Rw2 + Rw3)) * (Tw3 - Tw2)) * dt + exp(p22) *
            dw2
        dTw3 ~ (1/(Cw3 * 10^6 * 0.5 * (Rw2 + Rw3)) * (Tw2 - Tw3) + 1/(Cw3 *
            10^6 * 0.5 * Rw3) * (Tsi - Tw3)) * dt + exp(p33) * dw3
Observation equations:
        Qhfm ~ 1/(0.5 * Rw3) * (Tsi - Tw3)
Inputs:  Tse, Tsi
```

M4clm

```
Linear state space model with 4 states, 1 output and 2 inputs
System equations:
        dTw1 ~ (1/(Cw1 * 10^6 * 0.5 * Rw1) * (Tse - Tw1) + 1/(Cw1 * 10^6 *
                   0.5 * (Rw1 + Rw2)) * (Tw2 - Tw1)) * dt + exp(p11) * dw1
        dTw2 ~ (1/(Cw2 * 10^6 * 0.5 * (Rw1 + Rw2)) * (Tw1 - Tw2) + 1/(Cw2 *
                   10^6 * 0.5 * (Rw2 + Rw3)) * (Tw3 - Tw2)) * dt + exp(p22) *
            dw2
        dTw3 ~ (1/(Cw3 * 10^6 * 0.5 * (Rw2 + Rw3)) * (Tw2 - Tw3) + 1/(Cw3 *
            10^6 * 0.5 * (Rw3 + Rw4)) * (Tw4 - Tw3)) * dt + exp(p33) *
            dw3
        dTw4 ~ (1/(Cw4 * 10^6 * 0.5 * (Rw3 + Rw4)) * (Tw3 - Tw4) + 1/(Cw4 *
            10^6 * 0.5 * Rw4) * (Tsi - Tw4)) * dt + exp(p44) * dw4
Observation equations:
        Qhfm ~ 1/(0.5 * Rw4) * (Tsi - Tw4)
Inputs:  Tse, Tsi
```

SEMI-HOMOGENEOUS MODEL

M1shm

```
Linear state space model with 1 state, 1 output and 2 inputs
System equations:
        dTw1 ~ (1/(Rw1/K * 10^6 * 0.5 * Rw1) * (Tse - Tw1) + 1/(Rw1/K *
            10^6 * 0.5 * Rw1) * (Tsi - Tw1)) * dt + exp(p11) * dw1
Observation equations:
        Qhfm ~ 1/(0.5 * Rw1) * (Tsi - Tw1)
Inputs:  Tse, Tsi
```

M2shm

```
Linear state space model with 2 states, 1 output and 2 inputs
System equations:
dTw1 ~ (1/(Rw1/K * 10^6 * 0.5 * Rw1) * (Tse - Tw1) + 1/(Rw1/K *
    10^6 * 0.5 * (Rw1 + Rw2)) * (Tw2 - Tw1)) * dt + exp(p11) *
        dw1
dTw2 ~ (1/(Rw2/K * 10^6 * 0.5 * (Rw1 + Rw2)) * (Tw1 - Tw2) +
    1/(Rw2/K * 10^6 * 0.5 * Rw2) * (Tsi - Tw2)) * dt + exp(p22) *
        dw2
Observation equations:
        Qhfm ~ 1/(0.5 * Rw2) * (Tsi - Tw2)
Inputs:  Tse, Tsi
```

M3shm

```
Linear state space model with 3 states, 1 output and 2 inputs
System equations:
        dTw1 ~ (1/(Rw1/K * 10^6 * 0.5 * Rw1) * (Tse - Tw1) + 1/(Rw1/K *
            10^6 * 0.5 * (Rw1 + Rw2)) * (Tw2 - Tw1)) * dt + exp(p11) *
            dw1
        dTw2 ~ (1/(Rw2/K * 10^6 * 0.5 * (Rw1 + Rw2)) * (Tw1 - Tw2) +
                    1/(Rw2/K * 10^6 * 0.5 * (Rw2 + Rw3)) * (Tw3 - Tw2)) * dt +
            exp(p22) * dw2
        dTw3 ~ (1/(Rw3/K * 10^6 * 0.5 * (Rw2 + Rw3)) * (Tw2 - Tw3) +
            1/(Rw3/K * 10^6 * 0.5 * Rw3) * (Tsi - Tw3)) * dt + exp(p33) *
            dw3
Observation equations:
        Qhfm ~ 1/(0.5 * Rw3) * (Tsi - Tw3)
Inputs:  Tse, Tsi
```

M4shm

```
Linear state space model with 4 states, 1 output and 2 inputs
System equations:
        dTw1 ~ (1/(Rw1/K * 10^6 * 0.5 * Rw1) * (Tse - Tw1) + 1/(Rw1/K *
            10^6 * 0.5 * (Rw1 + Rw2)) * (Tw2 - Tw1)) * dt + exp(p11) *
            dw1
        dTw2 ~ (1/(Rw2/K * 10^6 * 0.5 * (Rw1 + Rw2)) * (Tw1 - Tw2) +
            1/(Rw2/K * 10^6 * 0.5 * (Rw2 + Rw3)) * (Tw3 - Tw2)) * dt +
            exp(p22) * dw2
        dTw3 ~ (1/(Rw3/K * 10^6 * 0.5 * (Rw2 + Rw3)) * (Tw2 - Tw3) +
            1/(Rw3/K * 10^6 * 0.5 * (Rw3 + Rw4)) * (Tw4 - Tw3)) * dt +
            exp(p33) * dw3
        dTw4 ~ (1/(Rw4/K * 10^6 * 0.5 * (Rw3 + Rw4)) * (Tw3 - Tw4) +
            1/(Rw4/K * 10^6 * 0.5 * Rw4) * (Tsi - Tw4)) * dt + exp(p44) *
            dw4
Observation equations:
        Qhfm ~ 1/(0.5 * Rw4) * (Tsi - Tw4)
Inputs:  Tse, Tsi
```

HOMOGENEOUS MODEL

M1hom

```
Linear state space model with 1 state, 1 output and 2 inputs
System equations:
        dTw1 ~ (1/(Cw1/1 * 10^6 * Rw1/(1 + 1)) * (Tse - Tw1) + 1/(Cw1/1 *
            10^6 * Rw1/(1 + 1)) * (Tsi - Tw1)) * dt + exp(p11) * dw1
Observation equations:
        Qhfm ~ (1 + 1)/(Rw1) * (Tsi - Tw1)
Inputs:  Tse, Tsi
```

M2hom

```
Linear state space model with 2 states, 1 output and 2 inputs
System equations:
        dTw1 ~ (1/(Cw1/2 * 10^6 * Rw1/(2 + 1)) * (Tse - Tw1) + 1/(Cw1/2 *
            10^6 * Rw1/(2 + 1)) * (Tw2 - Tw1)) * dt + exp(p11) * dw1
        dTw2 ~ (1/(Cw1/2 * 10^6 * Rw1/(2 + 1)) * (Tw1 - Tw2) + 1/(Cw1/2 *
            10^6 * Rw1/(2 + 1)) * (Tsi - Tw2)) * dt + exp(p22) * dw2
Observation equations:
        Qhfm ~ (2 + 1)/(Rw1) * (Tsi - Tw2)
Inputs:  Tse, Tsi
```

M3hom

```
Linear state space model with 3 states, 1 output and 2 inputs
System equations:
        dTw1 ~ (1/(Cw1/3 * 10^6 * Rw1/(3 + 1)) * (Tse - Tw1) + 1/(Cw1/3 *
            10^6 * Rw1/(3 + 1)) * (Tw2 - Tw1)) * dt + exp(p11) * dw1
        dTw2 ~ (1/(Cw1/3 * 10^6 * Rw1/(3 + 1)) * (Tw1 - Tw2) + 1/(Cw1/3 *
            10^6 * Rw1/(3 + 1)) * (Tw3 - Tw2)) * dt + exp(p22) * dw2
        dTw3 ~ (1/(Cw1/3 * 10^6 * Rw1/(3 + 1)) * (Tw2 - Tw3) + 1/(Cw1/3 *
           10^6 * Rw1/(3 + 1)) * (Tsi - Tw3)) * dt + exp(p33) * dw3
Observation equations:
        Qhfm ~ (3 + 1)/(Rw1) * (Tsi - Tw3)
Inputs:  Tse, Tsi
```

M4hom

```
Linear state space model with 4 states, 1 output and 2 inputs
System equations:
        dTw1 ~ (1/(Cw1/4 * 10^6 * Rw1/(4 + 1)) * (Tse - Tw1) + 1/(Cw1/4 *
            10^6 * Rw1/(4 + 1)) * (Tw2 - Tw1)) * dt + exp(p11) * dw1
        dTw2 ~ (1/(Cw1/4 * 10^6 * Rw1/(4 + 1)) * (Tw1 - Tw2) + 1/(Cw1/4 *
            10^6 * Rw1/(4 + 1)) * (Tw3 - Tw2)) * dt + exp(p22) * dw2
        dTw3 ~ (1/(Cw1/4 * 10^6 * Rw1/(4 + 1)) * (Tw2 - Tw3) + 1/(Cw1/4 *
                   10^6 * Rw1/(4 + 1)) * (Tw4 - Tw3)) * dt + exp(p33) * dw3
        dTw4 ~ (1/(Cw1/4 * 10^6 * Rw1/(4 + 1)) * (Tw3 - Tw4) + 1/(Cw1/4 *
                   10^6 * Rw1/(4 + 1)) * (Tsi - Tw4)) * dt + exp(p44) * dw4
Observation equations:
        Qhfm ~ (4 + 1)/(Rw1) * (Tsi - Tw4)
Inputs:  Tse, Tsi
```

Appendix E

Parameter behaviour in the unidentifiable regions of the estimated stochastic grey-box models

This appendix displays the behaviour of the thermal parameters in the unidentifiable regions of the different reference stochastic grey-box models considered in in chapter 3 of this dissertation.

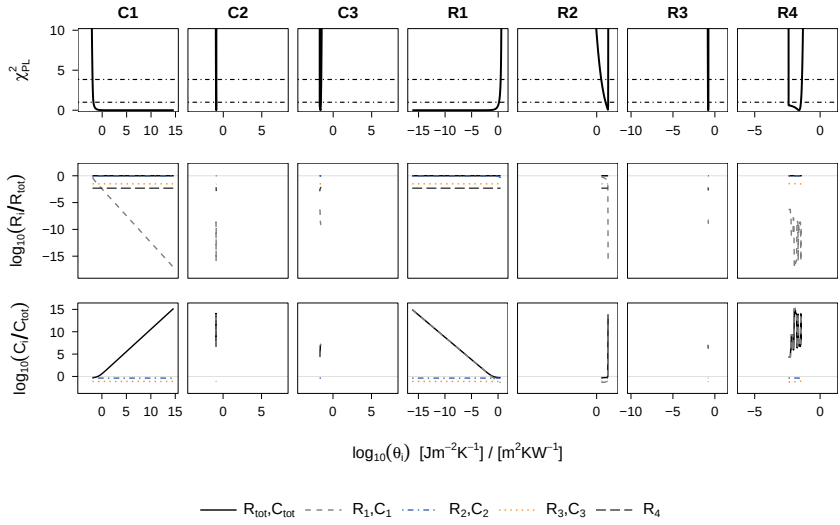

Figure E.1: The behaviour of the thermal parameters in the non-identifiable regions of the third order model estimated on the winter measurements of the scenario with a thermostatically controlled indoor temperature. The top row repeats the χ^2_{PL}-profiles of the model's thermal parameters. The middle row represents the behaviour of the model resistances, divided by the total thermal resistance, R_i/R_{tot} in the model's non-identifiable regions. The bottom row analogously represents the behaviour of the model capacitances, divided by the total thermal capacity, C_i/R_{tot} in the model's non-identifiable regions.

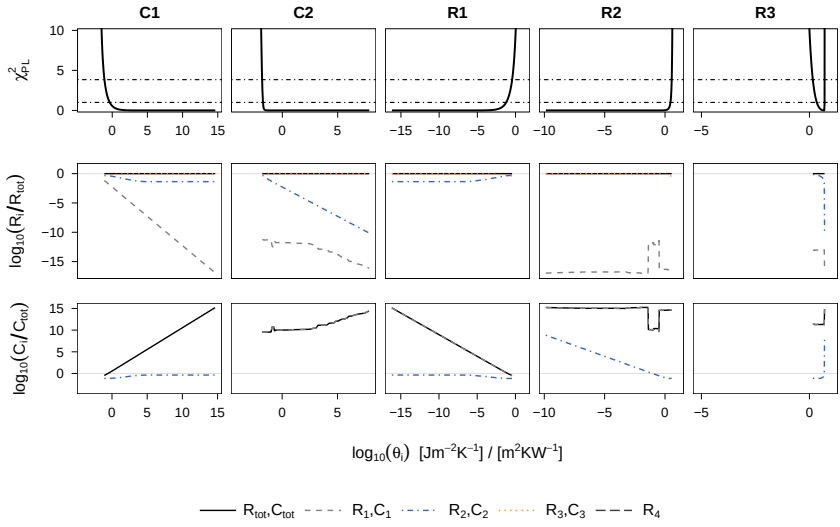

(a)

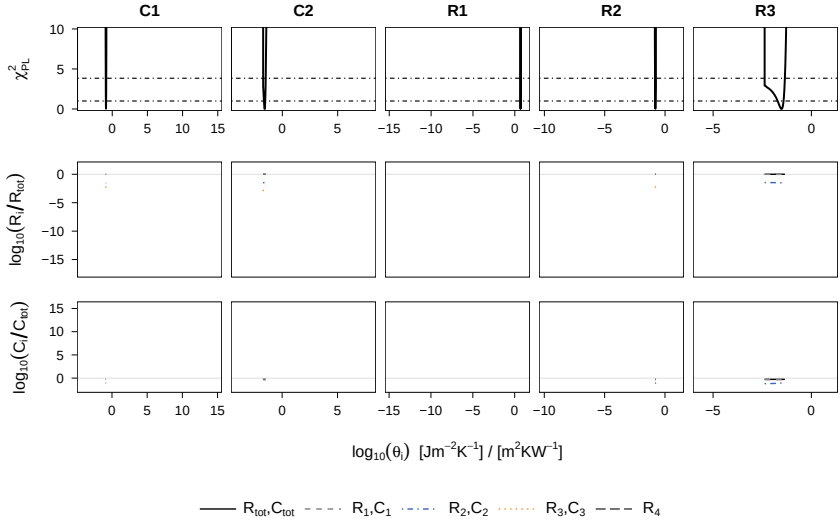

(b)

Figure E.2: The behaviour of the thermal parameters in the non-identifiable regions of the second order model estimated on the winter measurements of (a) the scenario with a constant indoor temperature and (b) the scenario with a thermostatically controlled indoor temperature. The top row repeats the χ^2_{PL}-profiles of the model's thermal parameters. The middle row represents the behaviour of the model resistances, divided by the total thermal resistance, R_i / R_{tot} in the model's non-identifiable regions. The bottom row analogously represents the behaviour of the model capacitances, divided by the total thermal capacity, C_i / R_{tot} in the model's non-identifiable regions..

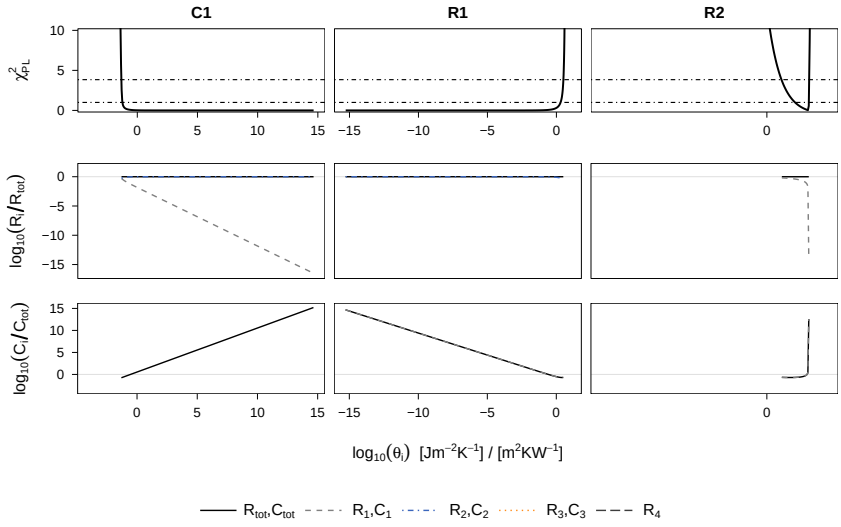

(a)

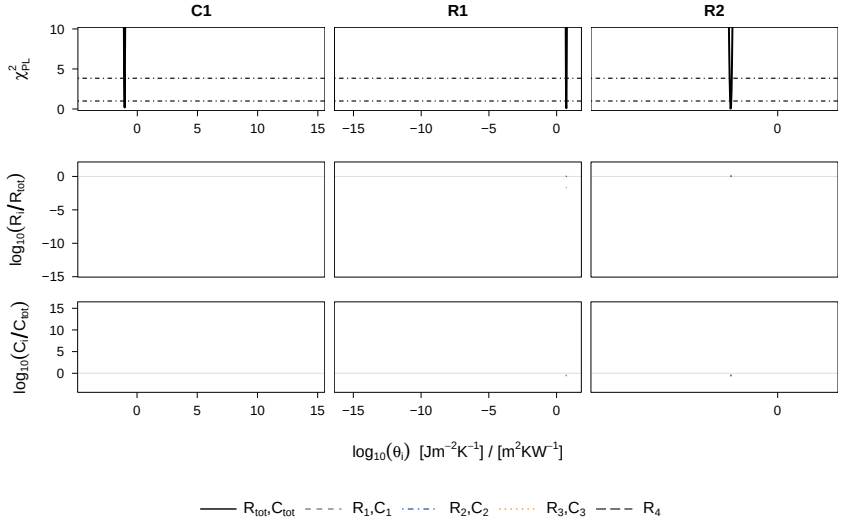

(b)

Figure E.3: The behaviour of the thermal parameters in the non-identifiable regions of the first order model estimated on the winter measurements of (a) the scenario with a constant indoor temperature and (b) the scenario with a thermostatically controlled indoor temperature. The top row repeats the χ^2_{PL}-profiles of the model's thermal parameters. The middle row represents the behaviour of the model resistances, divided by the total thermal resistance, R_i / R_{tot} in the model's non-identifiable regions. The bottom row analogously represents the behaviour of the model capacitances, divided by the total thermal capacity, C_i / R_{tot} in the model's non-identifiable regions.

Appendix F

Individual parameter validation of the estimated stochastic grey-box models from summer measurements

This appendix summarises the parameter validation criteria of the different stochastic grey-box models estimated from the summer measurements of the cavity wall.

(a) Parameter validation criteria for the first order model estimated on the summer measurements of the first scenario.

M1m	value	$sd_{\alpha=0.68}$	p-test	significant?	identifiable?
Cw1	2.95E+07	2.72E+10	9.99E-01	N	N (+∞)
Ctot	**2.95E+07**	**2.72E+10**			
Rw1	3.54E-09	3.27E-06	9.99E-01	N	N (-∞)
Rw2	4.46E+00	1.32E+00	8.34E-04	***	Y
Rtot	**4.46E+00**	**1.32E+00**			

(b) Parameter validation criteria for the second order model estimated on the summer measurements of the first scenario.

M2m	value	$sd_{\alpha=0.68}$	p-test	significant?	identifiable?
Cw1	4.45E+14	3.59E+15	0.901	N	N (+∞)
Cw2	8.74E+01	5.19E+03	0.987	N	N (+∞)
Ctot	**4.45E+14**	**3.59E+15**			
Rw1	6.25E-17	5.07E-16	0.902	N	N (-∞)
Rw2	3.18E-04	0.019	0.987	N	N (-∞)
Rw3	3.64E+00	0.216	<2.2e-16	***	Y
Rtot	**3.64E+00**	**2.15E-01**			

(c) Parameter validation criteria for the third order model estimated on the summer measurements of the first scenario.

M3m	value	$sd_{\alpha=0.68}$	p-test	significant?	identifiable?
Cw1	1.95E+04	7.71E+05	9.80E-01	N	N (+∞)
Cw2	9.46E-02	2.15E+00	9.65E-01	N	N (+∞)
Cw3	3.52E-02	1.87E-01	8.51E-01	N	N (+∞)
Ctot	**1.95E+04**	**7.71E+05**			
Rw1	5.05E-07	2.00E-05	9.80E-01	N	N (-∞)
Rw2	1.33E-01	4.17E+00	9.75E-01	N	N (-∞)
Rw3	7.79E-01	3.53E+00	8.25E-01	N	N (-∞)
Rw4	4.05E+00	2.98E+00	1.74E-01	N	Y
Rtot	**4.96E+00**	**6.13E-02**			

(d) Parameter validation criteria for the fourth order model estimated on the summer measurements of the first scenario.

M4m	value	$sd_{\alpha=0.68}$	p-test	significant?	identifiable?
Cw1	1.39E+10	1.52E+12	9.93E-01	N	NA
Cw2	7.24E+04	7.78E+06	9.93E-01	N	NA
Cw3	1.94E-01	3.51E+00	9.56E-01	N	NA
Cw4	2.76E-02	3.63E-03	3.27E-13	***	NA
Ctot	**1.39E+10**	**1.52E+12**			
Rw1	4.15E-13	4.55E-11	9.93E-01	N	NA
Rw2	7.95E-08	8.54E-06	9.93E-01	N	NA
Rw3	2.93E-02	5.40E-01	9.57E-01	N	NA
Rw4	2.20E+00	1.70E+00	1.96E-01	N	NA
Rw5	2.74E+00	1.41E+00	5.32E-02	.	NA
Rtot	**4.97E+00**	**6.61E-02**			

Table F.1: The tables report the estimated model parameters with their estimated standard deviation. Resistances have the unity m^2KW^{-1}, capacitances $MJm^{-2}K^{-1}$. The p-value summarises the significance testing results. Parameters with a p-value < 0.001 are indicated as ***. Parameters with a $0.01 <$ p-value < 0.05 are indicated as * and insignifcant parameters are indicated with N. The identifiable and non-identifiable parameters are indicated with Y and N respectively. The infinite confidence bounds of the non-identifiable parameters are added in between brackets.

(a) Parameter validation criteria for the first order model estimated on the summer measurements of the second scenario.

M1m	value	$sd_{\alpha=0.68}$	p-test	significant?	identifiable?
Cw1	1.48E-01	5.74E-03	<2.2e-16	***	Y
Ctot	**1.48E-01**	**5.74E-03**			
Rw1	6.23E+00	5.85E-01	<2.2e-16	***	Y
Rw2	1.11E-01	5.36E-03	<2.2e-16	***	Y
Rtot	**6.35E+00**	**5.87E-01**			

(b) Parameter validation criteria for the second order model estimated on the summer measurements of the second scenario.

M2m	value	$sd_{\alpha=0.68}$	p-test	significant?	identifiable?
Cw1	2.82E-02	4.82E-03	1.26E-08	***	Y
Cw2	1.19E-01	3.03E-03	<2.2e-16	***	Y
Ctot	**1.47E-01**	**3.23E-03**			
Rw1	3.65E+00	3.08E-01	<2.2e-16	***	Y
Rw2	1.19E+00	2.94E-01	6.70E-05	***	Y
Rw3	1.08E-01	2.31E-03	<2.2e-16	***	Y
Rtot	**4.95E+00**	**7.52E-02**			

(c) Parameter validation criteria for the third order model estimated on the summer measurements of the second scenario.

M3m	value	$sd_{\alpha=0.68}$	p-test	significant?	identifiable?
Cw1	1.20E+14	3.04E+14	6.94E-01	N	N ($+\infty$)
Cw2	3.63E-02	5.53E-03	2.24E-10	***	Y
Cw3	1.06E-01	4.93E-03	<2.2e-16	***	Y
Ctot	**1.20E+14**	**3.04E+14**			
Rw1	6.35E-17	1.55E-16	6.83E-01	N	N ($-\infty$)
Rw2	4.41E+00	1.53E-01	<2.2e-16	***	Y
Rw3	4.37E-01	1.28E-01	7.03E-04	***	Y
Rw4	1.10E-01	2.94E-03	<2.2e-16	***	Y
Rtot	**4.96E+00**	**7.09E-02**			

(d) Parameter validation criteria for the fourth order model estimated on the summer measurements of the second scenario.

M4m	value	$sd_{\alpha=0.68}$	p-test	significant?	identifiable?
Cw1	5.98E-03	3.65E-03	1.03E-01	N	NA
Cw2	1.07E-02	1.03E-02	2.96E-01	N	NA
Cw3	3.33E-02	1.35E-02	1.43E-02	*	NA
Cw4	9.78E-02	6.87E-03	<2.2e-16	***	NA
Ctot	**1.48E-01**	**5.17E-03**			
Rw1	1.62E+00	1.88E+00	3.90E-01	N	NA
Rw2	2.50E+00	1.84E+00	1.75E-01	N	NA
Rw3	4.62E-01	3.51E-01	1.89E-01	**N**	NA
Rw4	2.69E-01	8.96E-02	2.88E-03	**	NA
Rw5	1.10E-01	3.26E-03	<2.2e-16	***	NA
Rtot	**4.96E+00**	**6.95E-02**			

Table F.2: The tables report the estimated model parameters with their estimated standard deviation. Resistances have the unity m^2KW^{-1}, capacitances $MJm^{-2}K^{-1}$. The p-value summarises the significance testing results. Parameters with a p-value < 0.001 are indicated as ***. Parameters with a $0.01 <$ p-value < 0.05 are indicated as * and insignifcant parameters are indicated with N. The identifiable and non-identifiable parameters are indicated with Y and N respectively. The infinite confidence bounds of the non-identifiable parameters are added in between brackets.

Appendix G

Simulation grid for the cavity wall with rotational air looping

This appendix shows the grid that is assumed in the Delphin simulations for the cavity wall with rotational air looping around its insulation.

Figure G.1 represents the grid that is assumed in Delhin to simulate the cavity wall with rotational air looping around its insulation (see chapter 5). The grid contains a total of 1960 elements. The total height of the wall (1.50 m) is subdivided into 70 elements. The latter have a minimum height of 10 mm and a maximum height of 30 mm. In the horizontal direction, the wall is subdivided into 28 elements varying between 10 and 12 mm. The air channel is modelled as a series of elements with a width of 10 mm (for the vertical channel elements) or with a height of 10 mm (for the horizontal channel elements).

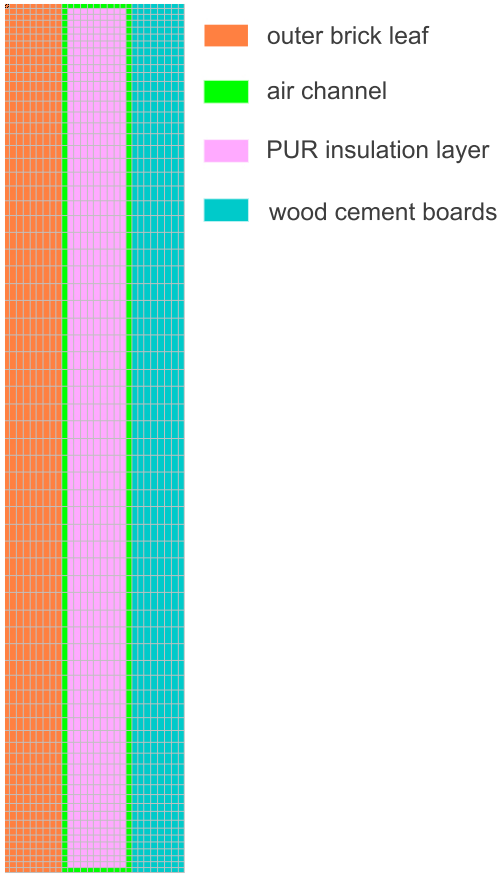

Figure G.1: Grid assumed in the Delphin simulations for the cavity wall with rotational air looping.

Curriculum vitae

An-Heleen Deconinck
Kortrijkstraat 98
B - 3210 Linden
0032 472 97 86 97
ahdeconinck@gmail.com

Education

2011 - 2012 **KU Leuven - Master of Civil Engineering**
MSc Thesis: *Co-heating: a critical evaluation of data analysis methods.* (Supervisor: Staf Roels)

2009 - 2011 **KU Leuven - Master of Engineering: Architecture**
MSc Thesis: *Analyse de sensibilité et d'incertitude de logiciel de bilan thermique à l'aide des plans d'expériences.* (Supervisor: Frank Detroyer)
Exchange program with *Ecole Polytechnique Federale de Lausane (EPFL)*, in Lausanne, Switserland, during the autumn semester.

2006 - 2009 **KU Leuven - Bachelor of Engineering: Architecture**

2000 - 2006 **Lyceum Ieper - ASO Science and Mathematics**

Scientific Experience

2012 - 2017 PhD Candidate at the Building Physics Section, Department of Civil Engineering, KU Leuven
PhD Thesis: *Reliable thermal resistance estimation of building components from on-site measurements.* (Supervisor: Staf Roels)
Research funded by a PhD grant (grant number 121167) of the Agency for Innovation by Science and Technology (IWT)

2011 - 2016 IEA EBC Annex 58-project:
Reliable building energy performance characterisation based on full scale dynamic measurements

Publications

All publications are presented in a-chronological order from new to old, and sorted per type of publication.

Articles in international journals

Deconinck A-H, Roels S (2017). Is stochastic grey-box modelling suited for physical properties estimation of building components from on-site measurements? *Journal of Building Physics*. DOI:10.1177/1744259116688384

Deconinck A-H, Roels S (2016). Comparison of characterisation methods determining the thermal resistance of building components from onsite measurements. *Energy and Buildings* 130:309-320. DOI:10.1016/j.enbuild.2016.08.061

Peer reviewed papers at international conferences

Deconinck A-H, Roels S (2017). The as-built thermal quality of building components: characterising non-stationary phenomena through inverse modelling. Accepted for *Nordic Symposium on Building Physics (NSB) 2017*.

Deconinck A-H, Roels S (2015). A maximum likelihood estimation of the thermal resistance of a cavity wall from on-site measurements. *Energy Procedia* 78:3276-3281. DOI:10.1016/j.egypro.2015.11.723

Deconinck A-H, Roels S (2014). Comparative assessment of in-situ thermal characterisation techniques. *Proceedings of the 10th Nordic Symposium on Building Phycics* 525-532.

Academic books

Madsen H, Bacher P, Bauwens G, **Deconinck** A-H, Reynders G, Roels S, Himpe E, Lethé G (2016). IEA EBC Annex 58 - Reliable building energy performance characterisation based on full scale dynamic measurements. Report of subtask 3, part 2: Thermal performance characterisation using time series data - statistical guidelines. Belgium: KU Leuven. ISBN:9789460189869

Papers presented at project meetings

Deconinck A-H, Roels S (2014). Measurement noise due to incident solar radiation on heat flux sensors: white or coloured? *IEA/EBC Annex 58 Meeting, 14-16 April 2014, Ghent.*

Deconinck A-H, Roels S (2013). Dynamic parameter estimation of different wall types' thermal characteristics: influence of indoor dynamics. *IEA/EBC Annex 58 Meeting, 14-16 October 2013, Hong Kong.*

References

Bibliography

1 Eurostat. Consumption of energy. 2016. URL: (http://ec.europa.eu/eurostat/statistics-explained/index.php/Consumption_of_energy) [Accessed: 22 February 2017].

2 D. Marchio and A. Rabl. Energy-efficient gas-heated housing in France: predicted and observed performance. *Energy and Buildings*, 17(2):131–139, jan 1991.

3 H. Jeeninga, M. Uyterlinde, and J. Uitzinger. Energieverbruik van energiezuinige woningen. Effecten van gedrag en besparingsmaatregelen op de spreiding in en de hoogte van het reële energieverbruik. Technical report, IVAM Environmental Research, jun 2001.

4 G. Branco, B. Lachal, P. Gallinelli, and W. Weber. Predicted versus observed heat consumption of a low energy multifamily complex in Switzerland based on long-term experimental data. *Energy and Buildings*, 36(6):543–555, jun 2004.

5 O. G. Santin. *Actual Energy Consumption in Dwellings. The Effect of Energy Performance Regulations and Occupant Behaviour*. Doctoraal proefschrift, TU Delft, 2010.

6 D. Majcen, L. Itard, and H. Visscher. Theoretical vs. actual energy consumption of labelled dwellings in the Netherlands: Discrepancies and policy implications. *Energy Policy*, 54:125–136, mar 2013.

7 J. Fang and R. Grot. In Situ Measurement of the Thermal Resistance of Building Envelopes of Office Buildings. In *ASHRAE Transactions*, volume 91, pages 543–557, Chicago, 1985.

8 S. Flanders. Confidence in Heat Flux Transducer Measurements of Buildings. In *ASHRAE Transactions*, volume 91, Chicago, 1985.

9 G. Houvenaghel and H. Hens. Pitched roofs with a vapour permeable underlay. Technical report, KU Leuven, Internal Report. Leuven, 2003.

10 H. Hens, A. Janssens, W. Depraetere, J. Carmeliet, and J. Lecompte. Brick Cavity Walls: A Performance Analysis Based on Measurements and Simulations. *Journal of Building Physics*, 31(2):95–124, oct 2007.

11 J. Wingfield, M. Bell, D. Miles-Shenton, T. South, and Lowe Bob. Lessons from Stamford Brook. Understanding the Gap between Designed and Real Performance. Technical Report 8, Leeds Metropolitan University, Leeds, 2009.

12 P. G. Cesaratto and M. De Carli. A measuring campaign of thermal conductance in situ and possible impacts on net energy demand in buildings. *Energy and Buildings*, 59:29–36, 2013.

13 S. Ahvenainen, E. Kokko, and A. Aittomäki. Thermal Conductance of Wall Structures. *LVI-Tekniikan Laboratorio, Report 54, Espoo*, 1980.

14 A. Aittomäki. Determination of the Overall Heat Transfer Coefficient of Multilayer Structures under Non-Steady Conditions. *CIB W 40, Holzkirchen-meeting*, 18-20 Sept, 1972.
15 G. Anderlind. Multiple Regression Analysis of in situ Thermal Measurements – Study of an Attic Insulated with 800 mm Loose Fill Insulation. *Journal of Building Physics*, 16(1):81–104, jul 1992.
16 B. Anderson. SITE-TESTING THERMAL PERFORMANCE: a CIB survey. *Batiment International, Building Research and Practice*, 12(3):147–149, jan 1984.
17 P. Fazio and R. Zmeureanu. Simplified procedure to estimate the dynamic thermal performance of existing walls. In *Buildings III Conference*, pages 255–271, 1985.
18 M. Jiménez, H. Madsen, and K. Andersen. Identification of the main thermal characteristics of building components using MATLAB. *Building and Environment*, 43(2):170–180, feb 2008.
19 C. Kupke. Unteruchungen über ein Wärmedämm - Schnellmesverfahren. *Institut für Bauphysik, Stuttgart, BW 148/76*, 1976.
20 D. A. McIntyre. In situ measurement of U-values. *Building Services Engineering Research and Technology*, 6(1):1–6, jan 1985.
21 I. Naveros, C. Ghiaus, D. Ruíz, and S. Castaño. Physical parameters identification of walls using ARX models obtained by deduction. *Energy and Buildings*, 108:317–329, dec 2015.
22 U. Norlén. Determining the Thermal Resistance from In-Situ Measurements. In J. Bloem, editor, *Workshop on Application of System Identification in Energy Savings in Buildings*, pages 402–429. commission of the European communities, 1994.
23 G. Stamatiou. *An investigation into the insitu "U" values of wall constructions*. PhD thesis, University of Newcastle Upon Tyne, 1991.
24 M. Modera, M. Sherman, and R. Sonderegger. Determining the U-value of a wall from field measurements of heat flux and surface temperatures. In *ASTM workshop on heat flow sensors*, Philadelphia, 1986.
25 C. Roulet, J. Gass, and I. Markus. In-Situ U-Value Measurement : Reliable Results in Shorter Time By Dynamic Interpretation of Measured Data. In *Buildings III Conference*, 1985.
26 W. C. Brown and G. D. Schuyler. In Situ Measurements of Frame Wall Thermal Resistance. In *ASHRAE Transactions*, number Vol. 88, Part 1, pages 667–676, 1982.
27 W. Brown and G. Schuyler. A calorimeter for measuring heat flow through walls. In *Conference on Thermal Performance of the Exterior Envelopes of Buildings. ASHRAE SP28*, pages 262–268, Kissimmee, Florida, 1979.
28 M. H. Sherman, R. C. Sonderegger, and J. W. Adams. The determination of the dynamic performance of walls. Number ASHRAE Transactions Vol. 88 Part I, pages 689–712, Atlanta: American Society of Heating, Refrigerating and Air Conditioning Engineers, 1982.
29 M. Modera, M. Sherman, and S. de Vinuesa. In-situ measurement of wall thermal performance: data interpretation and apparatus design recommendations. In *American Society for Testing Materials Symposium*, Dallas, Texas, 1984.
30 A. Rasooli, L. Itard, and C. I. Ferreira. A response factor-based method for the rapid in-situ determination of wall's thermal resistance in existing buildings. *Energy and Buildings*, 119: 51–61, may 2016.
31 S. J. Treado and D. M. Burch. Evaluation of Hand-Held Infrared Thermometers for Wall Thermal Resistance Determinations. *ACS Symposium Series*, pages B99–B109, 1979.
32 H. Trethowen. Measurement errors with surface-mounted heat flux sensors. *Building and Environment*, 21(1):41–56, jan 1986.
33 B. R. Anderson. The measurement of U-values on site. In *Buildings III Conference*, pages 3–19, 1985.
34 G. Anderlind. Dynamic thermal models. Two dynamic models for estimating thermal resistance and heat capacity from in situ measurements. Technical report, The Swedish Council for Building Research, Stockholm, 1996.
35 L. Ljung. *System Identification: Theory for the User*. Prentice Hall PTR, Upper Saddle River, NJ, USA, 2nd editio edition, 1999.
36 P. Baker and H. van Dijk. PASLINK and dynamic outdoor testing of building components.

Building and Environment, 43(2):143–151, feb 2008.

37 O. Gutschker. Parameter identification with the software package LORD. *Building and Environment*, 43(2):163–169, feb 2008.

38 J. Bloem, G. Fracastoro, R. Gicquel, S. Hammarsten, J. Kreider, A. Lindfors, H. Madsen, F. Neirac, E. Nino, U. Norlén, A. Rable, V. Richalet, T. Söderström, and D. van Dijk. *System identification applied to building performance data*. Office for Official Publications of the European Communities, Luxembourg, 1994.

39 H. Madsen, P. Bacher, G. Bauwens, A.-H. Deconinck, G. Reynders, S. Roels, E. Himpe, and G. Lethé. Thermal performance characterisation using time series data - statistical guidelines. In *Reliable building energy performance characterisation based on full scale dynamic measurements*, chapter Report of. IEA EBC Annex 58, 2015.

40 G. Bauwens. *Thermal performance characterisation of building envelopes*. Doctoral dissertation, KU Leuven, 2015.

41 P. Young. Parameter estimation for continuous-time models: A survey. *Automatica*, 17(1): 23–39, 1981.

42 J. N. Nielsen, H. Madsen, and P. C. Young. Parameter estimation in stochastic differential equations: An overview. *Annual Reviews in Control*, 24:83–94, 2000.

43 N. R. Kristensen, H. Madsen, and S. B. Jørgensen. Parameter estimation in stochastic grey-box models. *Automatica*, 40(2):225–237, feb 2004.

44 N. R. Kristensen, H. Madsen, and S. B. Jørgensen. A method for systematic improvement of stochastic grey-box models. *Computers & Chemical Engineering*, 28(8):1431–1449, jul 2004.

45 H. Madsen and J. Holst. Estimation of continuous-time models for the heat dynamics of a building. *Energy and Buildings*, 22(1):67–79, mar 1995.

46 P. Bacher and H. Madsen. Identifying suitable models for the heat dynamics of buildings. *Energy and Buildings*, 43(7):1511–1522, jul 2011.

47 P. D. Andersen, R. Juhl, T. H. Uffe, and H. Madsen. Parameter Identifiability in Greybox Models of Heat Dynamics of Buildings, 2013.

48 G. Reynders, J. Diriken, and D. Saelens. Quality of grey-box models and identified parameters as function of the accuracy of input and observation signals. *Energy and Buildings*, 82:263–274, oct 2014.

49 M. Jiménez, B. Porcar, and M. Heras. Estimation of building component UA and gA from outdoor tests in warm and moderate weather conditions. *Solar Energy*, 82(7):573–587, jul 2008.

50 I. Naveros, P. Bacher, D. P. Ruiz, M. J. Jiménez, and H. Madsen. Setting up and validating a complex model for a simple homogeneous wall. *Energy and Buildings*, 70:303–317, feb 2014.

51 P. Biddulph, V. Gori, C. a. Elwell, C. Scott, C. Rye, R. Lowe, and T. Oreszczyn. Inferring the thermal resistance and effective thermal mass of a wall using frequent temperature and heat flux measurements. *Energy and Buildings*, 78:10–16, 2014.

52 M. J. Jiménez, B. Porcar, and M. R. Heras. Application of different dynamic analysis approaches to the estimation of the building component U value. *Building and Environment*, 44 (2):361–367, 2009.

53 H. Janssen, B. Blocken, and J. Carmeliet. Conservative modelling of the moisture and heat transfer in building components under atmospheric excitation. *International Journal of Heat and Mass Transfer*, 50(5-6):1128–1140, mar 2007.

54 S. Sharples. Full-scale measurements of convective energy losses from exterior building surfaces. *Building and Environment*, 19(1):31–39, jan 1984.

55 G. Bauwens and S. Roels. Co-heating test: A state-of-the-art. *Energy and Buildings*, 82: 163–172, oct 2014.

56 M. Deurinck. *Energy savings in the residential building sector. An assessment based on stochastic modelling*. PhD thesis, KU Leuven, 2015.

57 ISO 9869: 2014 Thermal insulation - Building elements - In-situ measurement of thermal resistance and thermal transmittance, 2014.

58 A.-H. Deconinck and S. Roels. Measurement noise due to incident solar radiation on heat flux

sensors : white or coloured? Technical report, Report. EBC/IEA Annex 58. Ghent-meeting April 2014., 2014.

59 J. G. Eisenhauer. Regression through the Origin. *Teaching Statistics*, 25(3):76–80, sep 2003.

60 I. Naveros, M. Jiménez, and M. Heras. Analysis of capabilities and limitations of the regression method based in averages, applied to the estimation of the U value of building component tested in Mediterranean weather. *Energy and Buildings*, 55:854–872, dec 2012.

61 H. Madsen. *Time Series Analysis*. Chapman & Hall/CRC Taylor&Francis Group, 2008.

62 K. K. Andersen, H. Madsen, and L. H. Hansen. Modelling the heat dynamics of a building using stochastic differential equations. *Energy and Buildings*, 31(1):13–24, jan 2000.

63 P. D. Andersen, M. J. Jiménez, H. Madsen, and C. Rode. Characterization of heat dynamics of an arctic low-energy house with floor heating. *Building Simulation*, 7(6):595–614, dec 2014.

64 A.-H. Deconinck and S. Roels. Comparative assessment of in - situ thermal characterisation. In J. Arfvidsson, L.-E. Harderup, A. Kumlin, and B. Rosencrantz, editors, *Proceedings of the 10th Nordic Symposium on Building Physics*, pages 525–532, Lund, Sweden, 2014. 10th Nordic Symposium on Building Physics.

65 A. Androutsopoulos, J. Bloem, H. van Dijk, and P. Baker. Comparison of user performance when applying system identification for assessment of the energy performance of building components. *Building and Environment*, 43(2):189–196, feb 2008.

66 H. Melgaard. *Identication of Physical Models*. PhD thesis, DTU - Denmark, 1994.

67 M. J. Jiménez and H. Madsen. Models for describing the thermal characteristics of building components. *Building and Environment*, 43(2):152–162, feb 2008.

68 A.-H. Deconinck and S. Roels. A Maximum Likelihood Estimation of the Thermal Resistance of a Cavity Wall from On-site Measurements. *Energy Procedia*, 78:3276–3281, nov 2015.

69 G. Fraisse, C. Viardot, O. Lafabrie, and G. Achard. Development of a simplified and accurate building model based on electrical analogy. *Energy and Buildings*, 34:1017–1031, 2002.

70 I. Naveros and C. Ghiaus. Order selection of thermal models by frequency analysis of measurements for building energy efficiency estimation. *Applied Energy*, 139:230–244, feb 2015.

71 K. J. Kircher and K. Max Zhang. On the lumped capacitance approximation accuracy in RC network building models. *Energy and Buildings*, 108:454–462, dec 2015.

72 Jazwinski. *Stochastic Processes and Filtering Theory*. Academic Press, New York, 1970.

73 S. S. Wilks. The Large-Sample Distribution of the Likelihood Ratio for Testing Composite Hypotheses. *The Annals of Mathematical Statistics*, 9(1):60–62, mar 1938.

74 W. Q. Meeker and L. a. Escobar. Teaching about approximate confidence regions based on maximum likelihood estimation. *American Statistician*, 49(1):48–53, 1995.

75 H. Akaike. A new look at the statistical model identification. *IEEE Transactions on Automatic Control*, 19(6):716–723, dec 1974.

76 C. M. HURVICH and C.-L. TSAI. Regression and time series model selection in small samples. *Biometrika*, 76(2):297–307, 1989.

77 A. Raue, C. Kreutz, T. Maiwald, J. Bachmann, M. Schilling, U. Klingmüller, and J. Timmer. Structural and practical identifiability analysis of partially observed dynamical models by exploiting the profile likelihood. *Bioinformatics*, 25(15):1923–1929, 2009.

78 R. Bellman and K. Åström. On structural identifiability, apr 1970.

79 V. Avdeenko Tatyana. Problems of symbolic computation in testing of structural identifiability of state space models. In *Proceedings KORUS 2000. The 4th Korea-Russia International Symposium On Science and Technology*, volume 1, pages 24–29. IEEE, 2000.

80 L. Ljung and T. Glad. On global identifiability for arbitrary model parametrizations. *Automatica*, 30(2):265–276, feb 1994.

81 E. Walter and Y. Lecourtier. Global approaches to identifiability testing for linear and nonlinear state space models. *Mathematics and Computers in Simulation*, 24(6):472–482, dec 1982.

82 K. Glover. *Structural Aspects of System Identification*. Doctoral dissertation, Massachusetts Institue of Technology, 1967.

83 M. Grewal and K. Glover. Identifiability of linear and nonlinear dynamical systems. *IEEE Transactions on Automatic Control*, 21(6):833–837, dec 1976.

84 A. Raue, J. Karlsson, M. P. Saccomani, M. Jirstrand, and J. Timmer. Comparison of approaches for parameter identifiability analysis of biological systems. *Bioinformatics*, 30(10):1440–1448, 2014.

85 D. Venzon and S. Moolgavkar. A Method for Computing Based Confidence Intervals. *Journal of the Royal Statistical Society. Series C (Applied Statistics)*, 37(1):87–94, 1988.

86 K. Antonopoulos and E. Koronaki. Apparent and effective thermal capacitance of buildings. *Energy*, 23(3):183–192, mar 1998.

87 G. Reynders. *Quantifying the impact of building design on the potential of structural storage for active demand response in residential buildings.* PhD thesis, KU Leuven.

88 A. P. Ramallo-González, M. E. Eames, and D. A. Coley. Lumped parameter models for building thermal modelling: An analytic approach to simplifying complex multi-layered constructions. *Energy and Buildings*, 60:174–184, may 2013.

89 L. H. Hansen, J. L. Jacobsen, H. A. Nielsen, and T. S. Nielsen. Approximating building components using stochastic differential equations. In J. Bloem, editor, *System Identification Competition*, pages 149–162. Joint Research Centre, European Commission, Brussels, 1996.

90 A. Janssens, S. Roels, and L. Vandaele. *Full scale test facilities for evaluation of energy and hygrothermal performances.* Ugent. BFG, 2011.

91 M. Vanpachtenbeke, J. Langmans, S. Roels, and J. Van Acker. Modelling Cavity Ventilation Behind Brick Veneer Cladding: How Reliable are the Common Assumptions? *Energy Procedia*, 78:1467–1477, nov 2015.

92 J. Lecompte. *De invloed van natuurlijke convectie op de thermische kwaliteit van geïsoleerde spouwconstructies.* doctoral dissertation, PhD Thesis (in Dutch). KU Leuven, 1989.

93 S. Roels and J. Langmans. Highly insulated pitched roofs resilient to air flow patterns: Guidelines based on a literature review. *Energy and Buildings*, 120(April):10–18, 2016.

94 J. Langmans. *Feasibility of exterior air barriers in light weight construction.* PhD thesis, KU Leuven, 2013.

95 J. Langmans, T. Z. Desta, L. Alderweireldt, and S. Roels. Experimental Analysis of Cavity Ventilation Behind Residential Rainscreen Cladding Systems. *Energy Procedia*, 78:1750–1755, nov 2015.

FACULTY OF ENGINEERING SCIENCE
DEPARTMENT OF CIVIL ENGINEERING
BUILDING PHYSICS SECTION
ahdeconinck@gmail.com
http://bwk.kuleuven.be/bwf